Ultrasonic and acoustic emission studies of plasma sprayed coatings.

Moghisi, M.

Award date:
1985

Awarding institution:
University of Bath

ULTRASONIC AND ACOUSTIC EMISSION STUDIES OF PLASMA SPRAYED COATINGS

Submitted by M. Moghisi

For the degree of PhD of the University of Bath 1985

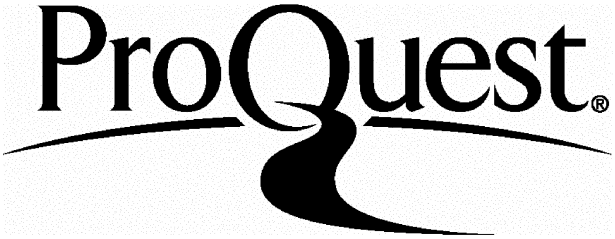

Dedicated to my parents

Abstract

This work assesses the potentials of two NDE techniques namely ultrasonic C-scan and acoustic emission for evaluating plasma sprayed coating quality. The coating materials used were aluminium (Metco 54), alumina (Metco 105), molybdenum (Mo63) and self-fusing molybdenum (Mo505).

It has been established that ultrasonic C-scan imaging can reliably detect thickness variations of the order of 0.05mm in plasma sprayed coatings. Also, by using this technique it is possible to detect the presence of delamination or lack of adhesion between the coating and substrate. Although it was only possible to produce aluminium and alumina coatings with artificially introduced adhesion defects, it has been shown that the presence of such defects in other coatings can also be detected. It has been established that an ultrasonic C-scan technique is not sensitive to the process parameters of plasma spraying. The process parameters investigated were; poor surface preparation, input power and surface cooling. Another major limitation of ultrasonic C-scan technique is the geometrical restrictions where components with high curvatures can not be tested.

Acoustic emission activities from plasma sprayed coatings were monitored during four point bend testing. Samples sprayed on poorly prepared surfaces or sprayed without coolant air could be distinguished from control samples using AE characteristics at low strain levels. Also the AE response of the alumina coatings reflected the thickness of the coatings. Thicker coatings produced more AE events. The AE response of the molybdenum (Mo63) and self-fusing molybdenum (Mo505) coatings were complex. It was found that they were related to the residual stresses in the coatings. Aluminium coatings showed very little acoustic emission activities.

CONTENTS

Acknowledgements

Special thanks are due to my tutors, Dr. D.P. Almond and Mr. H. Reiter for their helpful advice and constructive criticisms.

My gratitude is also extended to Professor B. Harris for allowing the use of the facilities provided in the School of Materials Science. I am also indebted to Mr. M. Phillips for the use of computing facilities.

I would like to thank all the technical and research staff, especially Mr. P. Taylor, Mr. P. Dicken and Miss J. Hayward.

I am grateful for the partial finacial assistance from the British Welding Institute.

Finally, I would like to thank my brother Hossein for his help, encouragement and his endless patience, because his complaints were never acoustically emitted.

Chapter 1

Introduction

1. INTRODUCTION

In general, coatings are desirable or may be necessary for various reasons, which include economics, ornamental, material-conservation, unique properties or engineering and design-flexibility. This is especially so in today's high technology, where components are required with combinations of various and sometimes conflicting properties, where the surface properties must differ from the bulk materials. These properties can be obtained by separating the near surface properties from those of the bulk materials. This near surface region is produced by depositing a coating on the substrate.

Various techniques and processes can be used to produce coatings. In general these processes fall between two extremes; the deposition of coatings and conversion coating. Conversion coating is achieved by altering the composition of the near surface region of the substrate by diffusion, such as carburizing , which produces a chemical bond with the substrate. In deposition coatings the bonding between coating and substrate is physio-chemical.

A high proportion of the coatings are produced by the thermal spraying technique. Thermal spraying provides a surface that may be resistant to heat, corrosion and wear. It is a technique which allows the manufacture of components from low cost, easily machinable metals which can then be given the required surface properties. Worn or damaged parts can be restored in situ. Thermal spraying is the build up of a coating by melting and projecting onto a substrate any heat-fusible material (1) to a cast-like structure. Coating can be sprayed from wire or rod, or from powdered materials. As the materials pass through the spray unit, they are heated to

a molten or semi molten state and then atomized and propelled against the substrate. Heating can be accomplished by a gas flame, electric arc, detonation, a combustible mixture or plasma.

Plasma spraying has developed from combustion flame spraying, the only essential difference being the higher gas temperature and velocities obtained in a plasma jet and the use of inert atmospheres. With this method highly adherent coatings with low porosity can be produced (1).

In an aero-gas turbine, coatings are essential features of the initial design. The majority of coatings used are either plasma, detonation or combustion sprayed (2). The aircraft industry has developed a high standard of quality which has forced both the suppliers of plants and spraying materials as well as coatings shops to observe strictly controlled production specifications(3). Similar specifications with strict tolerances also apply today for production of coated parts in nuclear power plants.

This group of users is normally prepared to meet the high financial cost of strict quality control. In many other branches of industry such willingness is not yet to be found.

Ideally, a surface coating should, when applied on expensive precision made components, have the following characteristics(4):

a- be easily applied and evaluated by practical methods

b- have no significant effect on substrate strength

c- improve component performance

d- be easily stripped i.e. without excessive reduction in substrate cross-section.

Thermal sprayed coatings can fulfil most of these demands. However, at present there is no established NDE technique to evaluate sprayed coatings. Also there must be a number of potential applications of the thermal sprayed coatings which have not been pursued due to lack of effective non-destructive evaluation (NDE) of the quality and integrity of the sprayed coatings. It is widely believed that for these applications there is an urgent need for an effective non-destructive evaluation technique to provide assurance of coating quality and integrity (5,6). In a review of possible NDE techniques, Bucklow(7) concluded that only those based on acoustics showed sufficient promise for the evaluation of sprayed coatings. Steffens (8) states that "ultrasonic techniques offer the greatest potential for transferring research achievements into practice". Also he added that other promising test methods are: optical holography, thermography and acoustic emission.

In a more recent review, Almond (5) discussed the effectiveness and limitations of the ultrasonic pulse echo technique for revealing adhesion defects, excess porosity and thickness variations in thermal sprayed coatings. Although all these may be detected, Almond(5) pointed out that in practice ultrasonic methods may prove to be unsuitable if components with high curvatures must be examined.

While not strictly a NDE technique, acoustic emission is particularly suitable for supervisory functions. Its potential for detecting phase transformations (10), crack initiation and crack propagation (11), plastic deformation (12) and frictional processes resulted in the employment of acoustic emission analysis for thermal spraying(9).

Although Shankar et al(13), Berndt and Herman (14), Ravishankar and

Herman(15), Safai and Herman(9) and Steffens(8) reported some correlation between the spraying parameters and spray materials with acoustic emission, there are still no concrete results on the acoustic emission behaviour of sprayed coatings.

The aim of this work has been to study the possibility of employing the ultrasonic pulse echo technique and acoustic emission as effective NDE techniques for evaluating sprayed coatings.

Chapter 2

Thermal spraying

2. Thermal spraying

Thermal spraying is a generic term given to a group of commonly used processes for depositing metallic or non-metallic coatings(16).

There are four main types of thermal spraying processes; flame spraying, plasma-arc spraying, electric arc spraying and detonation spraying .

2.1 Flame spraying

Flame spraying is the oldest thermal spraying technique developed around 1910 by Schoop. This process utilizes the heat from a chemical reaction. Four common fuel gases used in flame spraying are; acetylene, methyl-acetylene-propandiene (MAPP), propane and/or natural gas, all combined with oxygen(1). Acetylene is most widely used because it produces a higher temperature. Flame temperature and characteristics depend on the oxygen to fuel gas ratio as shown in table 2.1 .

Any material in the form of wire, rod or powder with a melting point below 3000^0 C (5000^0 F) can be flame sprayed(17). When wire or rod is the sprayed material, a set of drive rollers draw the material into the rear of the gun. Compressed gas, usually air, flows around the flame, atomizing the material as it melts at the tip of the wire or rod, and propelling it onto the substrate. A typical cross section of the flame spraying gun is shown in Fig 2.1 .

Flame spraying is cheap relative to other coating methods(17). However, particle velocities and temperatures are low, producing more porous coatings, of lower density and lower bond strength(16,17,18).

2.2 Detonation spraying

A detonation gun uses the energy of oxygen-acetylene explosion to blast powdered metal and ceramics onto the substrate. The detonation gun shown schematically in Fig 2.2 , resembles a small calibre cannon. In its chamber a sparking device ignites a mixture of air or oxygen and fuel gas (acetylene) along with the powder. The resultant detonation wave forces the molten or semi molten particles onto the workpiece. The detonations are repeated several times a second, followed by nitrogen purge pulses. Particle velocity reaches 760 m/s (2500 ft/s) as they exit from the barrel(16,17,18). Temperature in the gun reaches 6000°F and a gas,(usually CO_2), keeps the substrate temperature below 300°F. The resulting coating is strong, hard, dense and tightly bonded to the substrate(18).

2.3 Electric arc spraying

Electric arc spraying differs from the other thermal spraying techniques in which there is no external heat source such as the gas flame .This process requires two consumable wire electrodes which are insulated from each other meeting only where an arc strikes to melt them. A jet gas, (usually compressed air), flows across the arc, strips off the molten metal to form droplets and carries them onto the substrate. The wire to be sprayed is fed through wire guides into the electrode tips. Fig 2.3 shows a cross section of a typical electric arc spray gun.

Direct current is supplied to the electrodes at a potential of 18-35 volts DC (18), depending upon the spray material and the gun design. Larger

particles are formed when the arc gap is lengthened, and any voltage rise increases the arc gap (1). The voltage is always kept at the lowest level for a stable arc, to provide the smallest possible particles and the smoothest and most dense coatings. Smaller wire diameters provide denser and smoother coatings(1).

Due to the high temperature in the arc zone (10000°F) the coatings have much higher adhesive and cohesive strength than flame sprayed coatings (18). An Electric-arc spray uses about one ninth of the energy needed for gas flames (1), and also since no flame touches the substrate, temperature is low, thus minimizing the possibility of warping, distortion or other physical changes in precision parts (16).

Theoretically deposition rates are limited only by the electrical capacity available and the rate at which wires can be fed to the atomising head (18). The Electric-arc process is limited to relatively ductile, electrically conductive wire about 1.5 mm in diameter (16).

2.4 Plasma Spraying

2.4.1 Definition of plasma

Plasma can be broadly defined as a system of electric neutrality composed of positively and negatively charged carriers(19). This is a broad definition of plasma and does not imply any restriction to the density of charged particles, the presence of neutral species, the emission and absorption of radiation, etc. Plasma can be in the form of: solid, liquid or gas. In Plasma spraying, only plasmas in a gaseous state are of interest .

2.4.2 Formation of plasma gas

When an atom or molecule absorbs enough energy, one or more electrons are lost, and positively charged particles are formed, the particles are ionized . The ionized gas is conductive and the degree of conductivity depends on the concentration of the charged particles.

The most important ionization process is the ionization of gas particles by electron collision and by absorption of radiation. This can be best accomplished in a fully developed arc. Edels(20) defines a fully developed arc as " a steady state discharge having a positive column in thermal equilibrium and a cathode fall of small voltage and high current density ".

To produce a neutral plasma the arc is confined in a chamber in which the anode is a hollow nozzle. By introducing a gas into the arc chamber, the gas becomes dissociated and ionized in the arc stream, and the arc is forced down the nozzle. The gas emerging from the nozzle is a neutral plasma flame. The reason that the arc extends down the nozzle, instead of shorting out to the nearest edge of the nozzle, is because of what is known as thermal pinch effect. The relatively cold gas which is introduced around the arc stream tending to de-ionize and make it less conductive. This effect constricts the arc, raises its temperature and forces it down the nozzle. In the nozzle, which is relatively long, there is almost complete heat exchange between the arc stream and the gas used. The plasma flame, is a fairly uniform blast of dissociated and partially ionized gas which emerges from the nozzle.

2.4.3 Plasma spraying equipment

Plasma spraying equipment mainly consists of three parts;

a- Plasma spray gun

b- Control unit

c- Powder feed

A typical plasma spray gun is shown in Fig 2.4 The main components of the plasma spraying gun are two electrodes assembled coaxially in the housing of the gun. The cathode is copper tipped tungsten doped with thoria. Doping the tungsten with thoria lowers the electrodes work function and produces a more efficient electron emitter electrode. The energy required to raise an electron to its free state is known as the work function of the material(21). The anode is a hollow cylinderical copper nozzle. Both electrodes are water cooled to keep the temperature down and to prevent the electrodes from melting. The powder, arc gas and coolant are connected to the gun through a series of flexible tubes. The electrical cables supplying the potential difference between the electrodes are passed through the coolant tubes. A plasma forming gas such as nitrogen, argon, hydrogen or a mixture of these is forced into the arc chamber through the insulating block. This enterance can be either radial or tangential, depending on the arc gas and the anode protection techniques. The coating material in powder form is suspended in the carrier gas and is transmitted into the plasma flame either by an external feed tube or by a feed tube incorporated into the anode.

The arc is struck by superimposing a high frequency AC spark on the DC potential. After the arc is stabilised the AC is by-passed.

There are two basic types of powder feed units: aspirators and rotating slot feed hoppers(21). In this work the rotating slot hopper feed method

was used.

The control unit contains the on/off switch for ignition, voltmeters, ameters, gas flow meters, powder flow and monitoring devices.

2.4.4 Formation of plasma sprayed coatings

The main problem with the study of coating formation is that the flattening and solidification of each individual droplet, of which the coating is formed, occurs in an extremely short time, so that the direct observation is almost impossible and the structures formed are very different from those produced by conventional processing(22). Although there was considerable debate concerning the mechanism of formation of sprayed metal coatings, it is now accepted that they are formed by the build up of successive layers of liquid droplets which flatten and solidify on impact to give the lenticular microstructure usually observed (1,18,22,23). A schematic diagram of coating formation is given in Fig 2.5 . Complete melting of the particles is essential for efficient plasma spraying because solid particles will tend to bounce off the substrate or previously solidified materials. In practice, due to the large temperature and velocity gradients within the plasma jet, wide distributions of velocities and temperatures of injected particles are produced(18).

2.4.4.1 Heat transfer to injected particles

Both theoretical and experimental studies of the heat transfer to the injected particles have been reported (24,25,26,27). Due to the difficult nature of the problem and the complex interaction of variables no truly theoretical calculation of this problem has been reported. There are a number of difficulties associated with these calculations, for example;

since the thermal conductivity varies considerably with plasma temperature (24) , it is difficult to assess realistic values. Further complications in the DC plasma jet arise from the turbulent mixing which takes place within the plasma stream and with surrounding cold air (28).

Large temperature and velocity gradients exist in the plasma jet with peak values ranging up to 10000°K and 1000 m/s respectively(29). In practical plasma spraying, as suggested by Atkins (30), difficulty is experienced in applying a constant degree of melting to the individual powder particle. This is shown by Atkins diagram Fig 2.6 .

The energy available in the plasma must be transferred to the powder in a very short period of time. Estimates of the time required to melt a particle vary between .1 to 4 milliseconds(21).

From the possible mechanisms suggested by Fisher (29), whereby energy may be transferred to particles, the interface conduction across the interface between the plasma gas and the particle will have a decisive role. Engelke's (31) treatment of the heat transfer problem was based on interfacial heat transfer and assumed uniform heating of the particle. His model assumes that a spherical particle is heated in a plasma of known length, constant enthalpy and constant velocity. The powder particle size is assumed to be small and thermal gradients within the particles are neglected. Engelke shown the condition for the melting of a particle of powder to be

$$\left(\frac{S\,(\lambda\,\Delta\,T)^2}{\mu\,V}\right)_{plasma} = \left(\frac{L^2\,D^2}{16\,\rho}\right)_{particle} \qquad 2.1$$

Where S = length of the flame.

λ = interfacial heat transfer coefficient.

ΔT = temperature differential between the plasma and the powder.

V = plasma velocity.

μ = mean viscosity of the plasma and the gas.

L = enthalpy per unit volume of powder at the melting point.

D = particle diameter.

ρ = particle density.

It can also be deduced from this equation that the heat transfer characteristics of a system are strongly dependent on the plasma characteristics, since the right hand side of the equation is effectively constant (ρ and L are properties of powder material), and the powder diameter does not vary much within a powder batch. Engelke (31) has introduced a useful parameter ($L \rho^{-1/2}$), which indicates the difficulty of melting. Here (L) is the heat constant of the liquid material per unit volume at its melting point, which is a significant material parameter. Marynowski et al (32) suggested that as the accurate values for L are not always available and since L is proportional to the melting point of the material, the difficulty of melting can be expressed as ($T_m \times 10^{-3}$) $\rho^{-1/2}$, where T_m is the melting point in degrees centigrade.

Scott and Cannell (24) calculated both the drag and heat transfer coefficients on the basis of results accepted in gas dynamics at lower temperatures. They also assumed that the particles are spherical.

Fisher(29) and others point out that although their calculation is complex it remains a simplified model. Fizdon (25) and Pawlowski (26) calculated

the heat transferred to a spherical particle and its relation to the particles radius, taking into account the phase change and allowed the change of plasma jet parameters and the variation with temperature of the physical properties of the gas medium and the particle. Both authors have emphasised the relative simplicity of their calculations for any further application.

Other workers (27, 28) have measured the velocity and temperature distribution of the particles in a plasma jet. Particle temperature distributions are more difficult to measure than velocity distribution, because of emission problems when using radiation methods (22).

There are three methods of increasing the probability of melting. The enthalpy of the gas can be increased by controlling the performance of the arc. The heat transfer of the nitrogen or argon plasma gasses can be improved by the addition of 10% hydrogen (21). The powder particle size can be reduced , thus affecting the quantity of energy that needs to be transferred.

2.4.4.2 The impact of molten particles on the substrate and solidification

From the microstructure of the plasma sprayed coatings it is quite clear that coatings are formed from the individual liquid droplets flattening and solidifying on impact. There are three major factors controlling the microstructure and properties of the coating(22, 23). These factors are: particle velocity, temperature and size. The semi-molten particles should be included as well and obviously these particles would affect the coating microstructure.

When a liquid drop impinges on a flat surface at low velocity it flattens to a disc which then retracts, passing through the equilibrium shape and then spreads again to form the final equilibrium shape determined by the static surface tension force(33). However, at high impact velocities the flowing thin sheet of liquid disintegrates into many small droplets. Studying the deformation of liquid droplets impinging onto a hot metal surface Akao et al (34) suggest that the condition for break-up of an impinging droplet is that the Weber number W_e is greater than 80.

$$W_e = \rho V^2 d / \gamma \qquad 2.2$$

Where ρ is the density, γ the surface tension of the liquid, d the drop diameter and v the drop velocity. The Weber number for molten paricles in plasma spraying is in the order of several thousands therefore disintegration on impact would be expected. Madjeski (35) analyzed the solidification of droplets on a cold surface for plasma spraying and, neglecting solidification, he obtained the following equation for the spreading of the droplet;

$$\frac{3\xi_m^2}{W_e} + \frac{1}{R_e}\left(\frac{\xi_m}{1.2941}\right)^5 = 1 \qquad 2.3$$

Where ξ_m is a dimensionless radius of the disc, indicating the maximum area covered by the droplet. Under plasma spraying condition W_e and R_e are greater than 100, so $3\xi_m^2 / W_e$ is negligible, giving

$$\xi_m = 1.29\, R_e^{1/5} = 1.29\left(\frac{\rho d V}{\eta}\right)^{1/5} \qquad 2.4$$

The application of equation 2.4 to plasma sprayed alumina gave values for comparable with experimental values, suggesting that spreading is complete before significant solidification of the droplet(36).

As the liquid droplet spreads to form a thin film, its cooling rate will rapidly increase by conduction into the substrate. The liquid layer will cool to below its melting point, solidification starts and further spreading will be arrested. Ruhl (37) in his analysis of splat cooling, concluded that the variables with the greatest influence on the splat-cooling rate are the splat thickness, the interface heat transfer coefficient and the instantaneous splat temperature. Pawlowski (38) studied temperature distribution in plasma sprayed coatings. His model is based on the assumption that the substrate is a semi-infinite body. He concluded that the contact temperature at the grain substrate boundary markedly influences the adhesion of the sprayed coatings to the substrate. McPherson(22) in his study of the formation and microstructure of plasma sprayed coatings pointed out that if there were perfect contact between lamela and the substrate, the heat transfer coefficient would be infinite. While the contact between the lamela and substrate is not a perfect one, the value of the heat transfer coefficient obtained from the cooling rate may give an indication of the nature of the interface. The significance of these studies is their possible use for the modelling of residual stresses in plasma sprayed coatings.

The solidification and crystallization of the molten droplet is determined by the heat extraction rate. A perfect contact between the droplet and the substrate tends to encourage heterogeneous nucleation(22,23).

In a small volume of material, a high cooling rate will increase the undercool required for nucleation. For the highly undercooled melt the growth rate is not limited by the rate of heat removal as in most normal crystallization situations, unless the temperature increases to the equilibrium melting point. An increase in the temperature of the liquid

droplet, produced by release of the heat of fusion during rapid crystal growth, would tend to suppress further nucleation because of the large temperature dependence of nucleation rates, and columnar crystal growth from the interface into the droplet would be expected(23). However, if the rate of heat extraction through the substrate interface were greater than the rate of heat produced from the crystallization, the temperature would continue to decrease, the nucleation rate would increase and crystallization would be controlled by nucleation.

2.4.5 Parameters effecting the quality of plasma sprayed coatings

Parameters influencing the coating structure and properties of a particular coating are a complex function of torch operating conditions such as the nature and flow rate of gases, powder particle size distribution, torch substrate distance, electrical input to the torch and powder injection position, velocity and direction. Fisher (29) states that there are approximately 150 variables influencing plasma sprayed coatings, of which many are interrelated. Gerdeman and Hecht (39) have listed 24 variables in addition to those assosiated with the nature of the powder and substrate. Mash et al (40) categorized the variables associated with plasma spraying into five groups, as shown in table 2.2 . McPherson(22) in his review of the formation of plasma sprayed coatings concluded that plasma spraying has now probably reached that stage where empirical development is approaching its limit and any further improvement in coating performance will be gradual as a result of a better scientific understanding of the fundamental processes occurring during the coating formation.

2.4.5.1 Influence of process variables associated with plasma

Historically, variables are usually optimized with respect to spraying efficiency rather than coating characteristics (deposit efficiency is the ratio of the powder adhering to the substrate to that fed into the plasma). This is because, in the majority of cases, optimum spraying efficiencies produce the required coating characteristics(40).

Gun variables are usually fixed at the design stage, e.g. arc length. However, with flexible design some control over the plasma characteristics can be exercised. The arc length can be controlled by anode control: i.e. by changing the anode the arc length can be changed. The effect of nozzle diameter upon spraying efficiency and coating properties has been investigated by number of researchers (41). A decrease in nozzle diameter will further constrict the arc and hence increase the current density and specific enthalpy of the arc core (29). Also Andrews results show that changes in the nozzle diameter significantly affect the plasma velocity and hence the particle velocity. Nash et al (40) studied the effect of arc power on spraying efficiency. The arc power, for a set of spraying conditions will control the heat available in the arc . If the arc power is too low, particle melting will be incomplete resulting in a low spraying efficiency, while if it is too high the particles will vaporize. The optimum arc power will vary from powder to powder because the amount of heat required to melt a particle depends upon the properties of the materials.

Further control of the plasma can be achieved with the plasma forming gas. In selecting the arc gas, the following four factors should be taken into account: thermal and electrical properties, the enthalpy and the possibility of the gas reacting with powder or substrate. The energy available from a plasma arc depends upon the amount of dissociation and/or ionization of the gas molecules and atoms. This in turn will depend upon

the arc gas used. The heat content of diatomic gases is greater than that of inert gases at a given temperature (40). Some researchers and plasma equipment manufacturers have suggested the use of nitrogen with the addition of 10% hydrogen as a plasma forming gas. However Atkins (42) suggested that the enthalpy of the plasma was unimportant and the enthalpy per unit arc length should be considered. The enthalpy per unit arc length of argon is higher than that of nitrogen. Also the results of Mash et al (40) and Atkin (30) show that the deposition efficiency is a function of arc gas flow rate. The optimum arc gas flow rate varies for different materials.

2.4.5.2 Powder considerations

The present work has made use of commercially available powders. Although, powder variables are important they will not be extensively discussed here.

The most important powder variables are the physical and chemical properties of the powder, the particle size and size distribution, and the powder feed method.

2.4.5.3 Variables associated with the spraying procedure

It is believed that variables associated with the spraying procedure have extensive influence on plasma sprayed coatings. Mash et al (40) have reported that the extreme sensitivity of some of the spraying variables make it almost impossible to produce reproducible coatings with hand operated equipment.

Torch to substrate distance is one of the more sensitive spraying variables

(29,40). If the gun is too near to the work-piece extensive substrate heating will occur. This may produce distortions in a thin substrate or give rise to internal stresses at the interface for a thick substrate. It can also produce oxidization at the surface which weakens the adhesive bond(43). If the distance between the substrate and gun is greater than the optimum distance particles may partially solidify which will result in poor coating quality. There is a minimum spraying distance, beyond which an increasing number of particles solidify before striking the substrate. At greater distance the coating density and strength diminish rapidly(40).

Because of the high velocity of the arc gas, the surrounding air is drawn into the arc, resulting in a cooling of the flame(29). This contamination of the arc gas can result in oxidization and/or other chemical reactions with the powder. Two methods have been suggested to over come these problems. The first method is to use a cover gas. The plasma in this method is shield by an inert gas. The second method is to spray in an inert atmosphere.

According to Marynowski et al (32) the gun traverse speed or substrate rotation does not have a very significant effect, except when producing fine surface finishes. However, the temperature distribution within the substrate and coating during deposition is responsible for much of the difficulty in preparation of reliable coatings(32,38). Very slow traverse speed result in over heating of the substrate. The substrate receives heat from several sources: radiation from arc, heat from the impacting particles and from the plasma gas. The amount of heat contributed by the impacted particles is considerably more than the heat absorbed from radiation(29).

A temperature gradient exists through the substrate and coating, since heat is applied from the surface and mainly lost from the rear of the substrate.

Fig 2.7 shows the temperature and stress profile within the substrate and coating. The interfacial stress tends to reduce adhesive strength and the tensile stress at the surface may cause cracking at the coating surface (32).

2.4.5.4 Variables associated with the substrate

The selection of the substrate material is usually based on its physical and chemical properties or based on economic considerations(1,18,29,40).

It has been suggested that the thermal conductivity and hardness of the substrate affects the formation of the coatings (22,36). The mechanism of formation of the plasma sprayed coating has been discussed in section 2.4.4 . At the instant of collision, the particle experiences both elastic and plastic deformation, the substrate hardness plays a dominant role, after which thermal conductivity becomes dominant(22). It has been suggested that the ratio of the elastic to plastic deformation determines the amount of porosity of the coating (44). As the coating thickness increases the elastic properties of the substrate become masked and the coating density and porosity tend to a constant value(44).

Although the bonding mechanism of the sprayed coating to the substrate is not fully understood (45), it is widely accepted that substrate surface preparation has a significant affect on the adhesion of the plasma sprayed coatings (29).

Surface cleanliness is very important in all coatings (46). Surface roughness is the next critical factor. Degreasing is usually the most economical and safest way to remove lubricants and body oils. Rust , paint and other contaminations can be removed by machining or grit blasting.

Walker and Lewis (47) studied the adhesion of copper to nickel and presented results which showed that the adhesion was always greater for clean samples. He suggested that the increase in strength was due to an increase in the true area of contact.

British standards (48) suggest the pre-heating of 100°C to 200°C prior to spraying. The pre-heating removes water vapour from the surface of the substrate and stops condensation of water vapour on the surface of the substrate. Hasui et al (49) plasma sprayed alumina onto mild steel substrate at temperatures between 150°C and 380°C. They found that the bond strength increases markedly with preheating temperature.

Baxter and Reiter (50) studied the mechanism of adhesion of aluminium to a steel substrate. Their results show that oxide films formed during pre-heating can form an effective barrier between aluminium and the steel substrate. At pre-heat levels of 400° C to 700° C they found that aluminium can penetrate through oxide film and form intermetallic Al_5Fe_2 . Above this temperature the oxide films soften and resist spalling and the adhesion is via the iron/iron oxide interface. Baxter and Reiter suggest that below 400°C pre-heat level, grit blasting cosiderably improves the adhesion of aluminium coating to steel.

Of the many factors influencing the surface roughness the most important are the grit size, the speed of the grit, the angle of blasting and the hardness of the base material relative to the abrasive(18,51).

Grit blasting induces work hardening at the surface. The unit surface energy and the point defect concentration will both increase with the grit blasting(52), and the unit surface area will be increased. Endoh et al (53)

studied the influence of grit blasting parameters on the surface roughness and its effect on the bond strength of plasma sprayed zinc coating on steel. The grit blasting parameters studied were grit particle size, the length of blasting nozzle and grit density in the blasting column. Their results show that the surface roughness and density of anchor points reaches a maximum beyond which these values decrease for each of the parameters considered. The tensile bond strength increased with grit blasting density and nozzle length to a maximum beyond which a decrease in tensile bond strength was observed, but the tensile bond strength increased with grit size. However there was a small change in adhesive shear strength with grit size.

Mechanical bonding will depend on the number of anchoring points but physical and metallurgical adhesion will depend on the surface area and cleanliness(45,46,47,54).

From what has been discussed it is clear that the mechanism of the formation of plasma sprayed coatings is complex, and many parameters can influence the structure and properties of the coatings. Any changes in these parameters may effect the quality and integrity of the coatings. The main problems associated with sprayed coatings are porosity, lack of adhesion and delamination. It is also difficult to produce coatings of uniform thickness and to measure the thickness of these coatings accurately. Any NDE method which can assess the amount of porosity and indicate coating thickness will be useful. The availability of a reliable NDE method will increase the possible application of plasma sprayed coatings. A more detailed account of problems associated with plasma sprayed coatings, present methods of testing and a brief description of various NDE methods along with their potential application for plasma sprayed coatings is given in chapter 3.

Chapter 3

Properties and testing of plasma sprayed coatings

3 INTRODUCTION

In this chapter the general properties of plasma sprayed coatings are discussed. Also various common testing methods, both destructive and non-destuctive are reviewed and their potential application as a testing method for plasma sprayed coatings are assessed.

3.1 Properties and testing of Plasma Sprayed Coatings

Even for a fixed coating material the charateristics of a coating vary widely depending on the application. For example where wear-resistance or electrical insulation are desired the coating should be dense, but if it is to serve as a catalytic surface it should be highly porous (16).

Most metallic and ceramic coatings sprayed in air are dull grey in appearance, but some sprayed with an argon shield, can be reflective . The oxide coatings vary from black to white with the colour often different from the conventional ceramic of the same composition (16,18).

The mechanical properties of plasma sprayed coatings are sensitive to spraying parameters . Therefore any general tabulation of properties based on coating composition are not very meaningful. The mechanical and other properties of plasma sprayed coatings are anisotropic, because of the rapid quenching and directional solidification resulting from the spraying process. For example Safai and Herman (23) presented results for aluminium, which showed that the layers near the substrate contain highly oriented elongated grains, with the longitudinal axis perpendicular to the substrate.

Because of the rapid cooling a very fine structure is achieved within each particle, and non equilibrium phases can be present in the final coating. Microscopic irregularities of the surface affect the spreading of the impinging particle and hence the solidification behaviour. Safai and Herman(23) claimed that virtually defect-free and regular patterened grains were produced at the periphery of each lenticular platelet, and suggested that these thin regions were not fully in contact with the substrate surface (Fig 3.1).

The bonding mechanism of plasma deposited coatings is not always clear (24). Mechanical interlocking has been considered the most important mechanism by most investigators (29). Grit blasting as previously discussed provides an ideal surface for interlocking(45,46). Other mechanisms have been suggested as contributing to the bond strength including van der Waals forces, alloying, epitaxy, and surface reaction (45,52). Kitahara and Hasui(54) also reported that when the refractory metals, tungsten or molybdenum are sprayed on steel some metallurgical bond is formed.

The oxidation of the particles results in the formation of thin layer of oxide which can interfere with the spreading of the liquid droplets, resulting in the formation of interparticle stresses and providing a path for crack propagation. The bond strength and integrity of plasma sprayed coatings are sensitive to the residual stresses in the coating and coating substrate interface(24). The most important parameter which results in stress at the interface is the difference between the coefficient of expansion of the substrate and coating materials. The rapid cooling of the particle leads to high internal stresses in the individual particle as well as at the particle interface(24).

The most frequently quoted mechanical property is hardness. The nature of the sprayed coatings, is such that macrohardness techniques are not applicable and even microhardness measurements need careful interpretation (29). For a plasma sprayed coating with a given composition the hardness increases with coating density. Hardness is usually reduced for a given material if the coating is applied in an inert atmosphere(18), because of the absence of oxide.

3.2 Density and Porosity of Coatings

In the majority of applications, coatings with a high density are required and coating densities of up to 98% of the bulk density have been reported (29).

Generally there are two types of pore geometries in the plasma-sprayed coatings; 1- elongated pores, normally parallel to the substrate, formed between the particles, and 2- spherical pores formed by entrapped gases.

The basic requirements for high porosity are that the particle arrive at the substrate with a lower temperature or a lower velocity than that for the optimum conditions.

3.3 General Considerations in the Testing of Plasma Sprayed Coatings

At present it is difficult to test coated parts adequately, because established tests are destructive and some are of doubtful value (55). A variety of tests are used to establish the quality of coatings. Where destructive tests are used, these are usually performed on test-pieces, since components thermally sprayed are generally produced in small

quantities and may be expensive. Often in the case of reclamation only one component is coated and destructive testing is not possible. The problem is then to ensure that the components are coated under the same spraying condition as those used on the component and test coupon. Due to the differences in the shape and mass of the test piece compared with the component, differences in heating and cooling rate may exist between the coating on a test piece and the component, which may result in coatings with different quality.

A large number of properties or characteristics may be used to define the quality of a coating. Smart (55) has indicated some of the potential criteria for coatings table 3.1 . The precise criteria to be used depend upon the application.

Bucklow (7), has summarized the main defects encountered in sprayed coatings. The main problem is bond integrity. Also delamination of the coating layers (cracks parallel to the surface), and cracks normal to the substrate may be present. In most applications voids and porosity are not desirable and oxide inclusions can result in failure of coatings.

3.3.1 Current test methods

Kretzschmar (56) has reviewed the current destructive test methods and listed the advantages and disadvantages of the adhesion tests. There are many variations in these test methods. However in all these tests a test bar is coated and the bond strength calculated from the force required to detach the coating from the bar. Often adhesives are used to attach the coating to a suitable pulling device. In such cases, the result may be

affected by the type of adhesive, its degree of penetration into a porous coating, and its curing time and temperature (56). The alignment of specimens in the testing machine has a considerable effect and the results can vary up to one hundred per cent (57). Some of these methods will be discussed briefly .

3.3.2 Bend Test

In this test the coating is applied to a thin substrate and bent to a set radius. If the coating remains attached to the strip, adhesion is considered good, whilst the amount of bending required to produce cracks gives an indication of coating cohesion. This test mainly measures the coating ductility, and gives some measure of coating integrity. The bend test is not applicable to ceramic coatings, where even a good coating will not withstand any degree of bending.

3.3.3 Tensile Test

In a tensile test the coating is pulled off the substrate and the amount of force necessary to cause failure at the interface is a measure of adhesive strength. A quantitative test, for the adhesion of coatings is given by the ASTM standard C633-69. The test initially consists of flame spraying one face of the substrate and bonding it to the face of a loading part after which a tensile force is applied to the plane of the coating.

Although different types of tensile tests for plasma sprayed coatings have been developed, they cannot generally give information about the stress

values that coatings can withstand(45), because the stress pattern may not be as simple as in a tensile test. Also tensile loading of the sprayed coatings seldom occur in practice.

3.3.4 Shear Test

Because shear stresses on coatings are much more common than tensile stresses, it has been suggested that shear testing is more relevant and may give a better indication of the service life of plasma sprayed coatings (45).

Boehem (58) adapted a modified version of the tensile test, to measure the shear strength of plasma sprayed coatings. His arrangement of this test is shown in Fig 3.2 . Bohem pointed out that in the overlapped region, apart from the shear forces, forces normal to the surface are also present. Bohem proposed the torsion shearing test, where the stresses applied to the coating are pure shear stresses Fig 3.3 . In this test, the specimen is coated and bonded with the counter-stamp. Then the specimen is held in a rotating clamp and the counter-stamp fixed in jaws to prevent its rotation. A lever arm attached to the specimen clamp is used to apply a torsional force to the coating.

3.4 NDE Techniques

Sharpe (59) states that "NDE is not just looking for cracks, it is rather a branch of materials science and is concerned with all aspects of quality

and uniformity of materials.". An ideal non-destructive testing method should not only detect the defects but also determine their type and size . The position, orientation and shape of the flaw is usually more important than just its size .

Non-destructive testing of plasma sprayed coating can be expected to differ from that of metallic materials, because they are generally anisotropic, and have high acoustic attenuation. Bucklow (7) has reviewed the possible NDE methods for plasma sprayed coatings and concluded that only those based on acoustics showed promise for the evaluation of sprayed coatings. Steffens (8) has also reported several potential NDE candidates for plasma sprayed coatings and carried out tests on some of these methods. Bucklow(7) has also suggested that measured characteristics of a coating should be related to coating integrity. Several NDE methods are briefly discussed below.

3.4.1 Visual Examination

Visual inspection is the most widely used and cheapest of all the non-destructive methods available. The visual test is essentially a skill developed by the operator rather than being a routine specified by an engineer. The eye can distinguish colour changes, it is sensitive to patchiness of the surface and can detect uniformity of the surface (59). It can also provide information about the roughness. The results of visual observation can provide information for the more effective use of other nondestructive testing techniques.

In plasma spraying visual observation can be effective for good surface

preparation of the substrate.

3.4.2 Liquid Penetrant Test

Tests based on liquid penetrants may well be considered as an extension to visual inspection. In this method cracks or pores are made visible by impregnation with a low viscosity and low surface energy liquid and then revealed with the aid of a suitable developer.

The use of liquid penetrants is quick, inexpensive and a relatively reliable NDE technique for revealing cracks at the surface. While very few cracks can be revealed by liquid penetrant which a skilled operator could not find unaided, employing this technique reduces the human element in the inspection process. For plasma spraying this technique is of little help, because plasma sprayed coatings are porous and usually have rough surfaces. Also in most cases the bond integrity of substrate coating is the main concern and they cannot generally be detected by liquid penetrant.

3.4.3 Radiography

Radiography is a method of non-destructive testing which uses X-rays or gamma rays. The radiation passed through the work piece will suffer attenuation and scattering, not only diffraction. The record of transmitted intensity provides information about the structure and composition of the material through which it has passed. The intensity of the radiation is also modified by the passage through defects (59).

In radiography if the specimen is uniform in density and thickness, the radiation emerging from the opposite side of the specimen will have uniform intensity. If a specimen has variations in thickness or density due to inhomogenities, the intensity of emerging radiation will be modified. This emerging radiation can be used as an indicator of the soundness of the specimen. In conventional film radiography, emulsions sensitive to the radiation are used as recording devices. This process consists of making a record of the variation in intensity of the film and interpreting the density on the radiograph in terms of thickness and density variations in the specimen.

The disadvantages of X-ray and gamma ray radiography are that they are direction sensitive and have low depth of penetration in weld metals. For example a close tight crack if not oriented properly with respect to the incident radiation may not be detected(59).

The radiographic techniques are well developed and widely used NDE techniques in manufacturing and assembly of components. Bucklow (7) suggests that radiographic methods might be useful for non-metallic coating at microwave frequencies.

3.4.4 Magnetic test Methods

If a ferromagnetic material which contains cracks, pores or inclusions near the surface is magnetized, the path of the magnetic flux is disturbed, because the inhomogeneities have different magnetic properties than the bulk material. The distortion in magnetic flux is called leakage flux.

All magnetic NDE methods employ some means of detecting the leakage flux. The leakage flux can be detected by either a search coil or magnetic particles.

Magnetic particle inspection is a relatively simple technique. The magnetic particles or powder can be either dry or suspended in thin transparent liquid. If a flaw lies at or near the surface then there will be a set up of magnetic poles which act as small magnet. The magnetic powder is attracted by the leakage flux, thus forming a visible mark, indicating the position and extent of the defect.

In practice if the magnetic particle method is used, a clean and smooth surface is required, or particles tend to congregate in grooves and notches on the surface giving either false indication or masking the presence of any cracks.

For plasma sprayed coatings with a smooth surface finish, the magnetic flux method might be useful for investigating the presence of cracks normal to the surface.

3.4.5 Eddy Current

If a coil carrying alternating current is brought close to a metallic surface, the alternating magnetic field from the coil induces eddy currents in the surface of the metal. The eddy current induces a magnetic field

which is used either to alter the inductance of the generating coil, and hence the current flowing through it, or to generate a voltage in a search coil. As an eddy-current probe is brought close to a conductor the resistive and inductive components of the probe coil impedance are altered. When a probe passes over a defect the eddy-current flow distorts, resulting in a change in the probe coil impedance.

The magnitude of the induced eddy current depends on the magnitude and frequency of the alternating current, the electrical conductivity, the magnetic permeability and shape of the specimen, the relative position of the coil and presence of defects in the specimen (59).

Eddy-currents induced by a changing magnetic field concentrate near the surface, and decrease with increasing depth. This is because eddy-currents flowing in the sample at any depth produces a magnetic field which opposes the primary field, thus reducing the magnetic flux and thereby causing a decrease in current flow . The result is an exponential decrease in eddy current. This phenomenon is commonly known as skin effect and depends on test frequency, electric resistivity and magnetic permeability of the sample.

Application of the eddy current technique includes, detection of cracks, voids and inclusions, and measurement of coating thickness. Eddy-current testing is also very sensitive to surface roughness (60) which restricts its possible use in plasma sprayed coatings.

Since eddy-currents flow parallel to coil windings, certain probe designs are required for detecting different types of defects. A probe with a circumferential coil can only detect defects normal to the surface (60).

Theoretically, laminar defects can be made detectable with a horse-shoe type probe, however Van Drunen and Cecco (60) pointed out that at present there is no commercially available probe specifically designed for laminar defects.

The inability of eddy-current technique to detect laminar flaws, makes it unsuitable as an effective NDE method for sprayed coatings, because the main defects encountered in sprayed coatings are either delamination or lack of adhesion of the coatings to the substrate(7).

3.4.6 Thermal Testing

Thermal methods are also adopted for non-destructive evaluation of materials. In the literature there are many examples of the application of the thermal techniques e.g. in detecting cracks, pores in welded joints and defects in adhesive bounded joints. There are two types of thermal field in materials (59), 1- stress generated thermal fields, where localized hot spots are generated as a consequence of cyclic loading and maximum temperature rise can be expected where stress are the highest (around the flaws) and 2- externally applied thermal fields, where normally uniform isotherms are distorted as a result of a flaw or damaged region. All thermal methods are based on measuring temperature changes at the surface arising from these two thermal fields.

The means available for detecting the temperature rise at the surface range from masking the surface with temperature sensitive paint to the use of liquid crystals and infra-red detectors.

In plasma sprayed coatings the rate at which the heated surface of a coating loses heat depends on many factors, two of which are the conductivity of the coating , and its thermal contact with the substrate. Sayers (61) investigated the detectability of defects by thermal nondestructive testing method. His theoretical calculations were performed for heat flow through a material of rectangular cross section assumed to be of infinite length in one direction containing a linear defects of constant cross section down its length. From his theoretical calculation Sayers has concluded that in one sided inspection a large defect at the opposite side of the specimen may be mistaken for a small defect close to the surface investigated. Furthermore he concluded that although more accurate sizing of defects in two-sided inspection is possible, the magnitude of the signal is much smaller than that occuring in one-sided inspection, when the defect lies close to the heated surface. Almond et al (62) and Patel and Almond (63) investigated the potential application of photo thermal imaging for NDE of plasma sprayed coatings. They scanned the surface of the specimen using a one watt argon ion laser as the heat generating source and variation of the surface temperature was monitored by an infra-red detector. Their result for a poorly bonded region of alumina plasma sprayed coating is in good agreement with ultrasonic observation of the same part. However Almond suggests that photo thermal imaging has advantages compared with ultrasonic techniques. They are completly non contacting and the overall geometry of a bulk substrate has no effect on the photo thermal signals.

3.4.7 Ultrasonics

Szilard (64) in his review of conventional ultrasonic techniques pointed out that Soklov in 1929 was first to propose the use of ultrasound for

detecting defects in materials. Since then, as the potential of ultrasonic testing become apparent, its significance has grown, and it is now probably the most important NDE technique.

In general, ultrasonic waves are reflected from all solid gas interfaces because of large acoustic impedance mismatch between the two media. The mismatch between solids and liquids is not so large, hence liquids and greases are commonly used as acoustic couplants. If a beam of ultrasound is passed through a material with a defect (e.g. crack), the ultrasonic wave will be at least partially reflected from the flaw. Monitoring the reflected or transmitted beam can therefore provide information about the size and location of defect.

A detailed discussion of ultrasonic NDE techniques in general and possible application in plasma sprayed coatings in particular is given in chapter 4.

3.4.8 Acoustic Emission

Acoustic emission is defined by ASTM 610-77 as " the class of phenomena where by transient elastic waves are generated by the rapid release of energy from localized sources within a material, or the transient wave(s) so generated". The stress waves are usually detected by a piezoelectric transducer, which converts mechanical vibration into electrical signal. The AE signals can then be processed in a variety of ways. It has been claimed that AE monitoring of structures not only has the potential to locate sources of acoustic emission but also can be used for proof testing of

structures. A detailed study of acoustic emission techniques and its potential application for proof testing of plasma sprayed coatings is given in chapter 5.

Chapter 4

Principles of ultrasonics

4 Introduction

This chapter discusses the basic principles of ultrasonic testing of materials. Conventional ultrasonic testing methods are reviewed and possible application to plasma sprayed coatings are assessed. Finally a brief description of three special ultrasonic testing technique and their possible use for plasma spraying is given.

4.1 Physical principles of ultrasonics

In a solid each particle is held at its position by elastic restoring forces, which makes them, when displaced return to an equlibrium position and oscillate about it. In an elastic medium these vibrations are transferred to the adjacent particles or atoms, resulting in an elastic wave. Ultrasound is the name given to these waves when their frequency is higher than the audiable range i.e. more than 20 KHz.

In an infinite body the oscillation of particles may result in either pressure waves or shear waves. Pressure waves, are also called longitudinal waves because the particles are displaced along the direction of propagation Fig 4.1 . Shear waves are also called transverse waves, because particles are displaced perpendicular to the direction of propagation Fig 4.2. The transverse wave can only exist in a medium with shear elasticity, like solids.

In a body with boundaries, the propagation of sound wave is disturbed by reflection and refraction from boundaries. The reflection of longitudinal wave can transform them into transverse wave and vice versa. This

transformation of one kind of wave to another is called mode conversion.

The combination of pressure and shear wave at a boundary can also give rise to two different mode of wave propagation, namely surface waves and lamb waves. Fig 4.3 shows an instantaneous picture of a surface wave on steel. Surface waves travel along the surfaces of relatively thick materials. The disturbance occurs at the surface, attenuating rapidly within a depth of one wave length (64). Lamb or plate waves are generated in thin sheet or rod. They occur in two different modes, namely dilatational and bending waves . Transmission characteristics of lamb waves is dependent on the thickness of the plate, wavelength of the acoustic wave, and type of solid (64).

4.2 Generation of acoustic waves

Non-destructive evaluation of materials almost exclusively makes use of piezoelectric transducers. The piezoelectric effect is a property of a crystal structure and was first discovered by the Curie brothers. If a piezoelectric material is deformed by an external force, electric charges are produced on its surfaces. Also if they are placed between two electrodes, in an applied electric field, it will change its dimensions, and either contract or expand according to the polarity of the electric field, Fig 4.4 . Therefore if an alternating electrical signal acts on a piezoelectric crystal it vibrates producing sound. Similarly vibration of sound waves impinging on such crystals produce an alternating electric charge.

Of the known natural piezoelectric crystals, quartz is the most important one, because of its good piezoelectric properties combined with excellent

mechanical and dielectric strength, any pressure applied to the face of the crystal reduces its thickness. This shifts the electrically charged elements (silicon and oxygen ions) relative to each other, such that the plate becomes polarized Fig 4.4 .

The other class of materials which can be made to show piezoelectric properties are dielectric materials with an enhanced electrostrictive effect. When a dielectric material is placed in an electric field, the elementary dipoles align themselves. The polarization disappears when the electric field is removed. Certain ceramic materials can be permanently polarized when placed in a strong field.

Of the many crystals with piezoelectric properties mainly lead zirconate titanate (PZT), barium titanate ($BaTiO_3$), lead metaniobate ($PbNb_2O_6$)), lithium sulphate ($LiSO_4$) and lithium niobate ($LiNbO_3$) are the most widely used for non-destructive evaluation of materials (65). Table 4.1 gives some of the properties of these crystals.

The properties of transducer materials are characterized by a set of constants. The electromechanical coupling coefficient, K, is a measure of the proportion of the electrical or mechanical energy fed into the transducer which is converted into the other form. A constant d gives the electric charge produced on the electrodes on a transducer subjected to a given force, or the deformation caused by the applied voltage. A constant g denotes the field produced in a piezoelectric transducer by an applied stress. These constants are not independent, and according to Mason (66) are related in tensor notation as follows:

$$d_{ni} = (\varepsilon_{e} T_{e} g_{ei})/(4\pi) = e_{ni} S_{ij}^{E} \qquad m, n=1 \text{ to } 3 \qquad 4.1$$

$$g_{ni} = 4\pi\beta_{ss}T_{ss}d_{si} = h_{ni}S_{ij}^{D} \qquad i,j=1 \text{ to } 3 \qquad 4.2$$

where T, E and D are the stress, electric field and electric displacement respectively, ε is the permitivity, S is the elastic compliance C is the elastic stiffness and β is the dielectric impermeability. For a good transmitter a high d is desirable , which for a sensitive receiver g should be high. As can be seen from the constants given in table 4.1, lithium sulphate has the best properties, but is very expensive and extremely sensitive to water (65). Quartz is a reasonably good receiver, but because of its high Q factor should be damped to reduce its ringing and produce shorter pulses. The damping of a transducer reduces its sensitivity. PZT5 is the transducer material widely used in non-destructive evaluation of materials, since it is resonably good both as a receiver and transmitter. If it is to be used in water its high acoustic impedance prevents its sensitivity from being fully exploited.

4.3 Ulterasonic wave propagation

Since ultrasound is essentially of the same nature as audiable sound, the theory of its propagation is similar . Kinsler and Fry (67) give the equation for the propagation of a one dimentional flat wave as:

$$\frac{\partial^2 P}{\partial t^2} = C^2 \frac{\partial^2 P}{\partial x^2} \qquad 4.3$$

where P is the sound pressure, t is the time, x is the distance and C is the speed of sound. The general solution of this equation is :

$$P = A\, e^{j(\omega t - kx)} \qquad 4.4$$

where A is the amplitude , j is $\sqrt{-1}$, ω is the angular frequency and K is the wave number (ω/ C). In general the amplitude of the wave will not be constant, but will decrease as;

$$A = A_0 e^{-\alpha x} \qquad 4.5$$

where A_0 is the incident amplitude and α is the attenuation coefficient. The attenuation is due to two general processes, namely absorption, wherein the acoustic wave performs work as it propagates through the medium and thus loses energy, and scattering, whereby part of the energy in the wave is refracted or reflected out of the path of wave propagation.

The magnitude of the attenuation coefficient is a function of the material, its homogeneity, its temperature and the frequency of the acoustic wave. Truell et al (68) have listed ten different process where by a stress wave may interact with the various properties of a solid. Goebbles (69) named three of these processes as the most important absorption mechanisms in polycrystalline metals at room temperature with ultrasonic frequency in the range 1 to 50 MHz. Absorption in metals at room temperature for frequencies around 1 MHz, can be divided into losses due to hysteresis and losses due to relaxation process. Hysteresis means that in the interval of frequencies for which damping is appreciable the strain is out of phase with the stress. One example of hysteresis loss occurs when an ultrasonic wave interacts with the stress field of a pinned dislocation (69). Relaxation losses can occur when the structure is anisotropic causing a strain variation, or when heat flows from highly strained regions to lesser strained areas. For example when a longitudinal wave is propagated through a solid, a temperature gradient will be set up between regions of compression and rarefaction (69). Another form of relaxation is when the acoustic pressure forces atoms into vacant lattice positions against

resisting interatomic forces. Both of these relaxation processes are frequency dependent because of the finite relaxation time needed for energy to flow from one position to another. The losses due to relaxation effects are usually smaller than the dislocation effect (70). The total attenuation due to absorption will be the sum of the attenuations produced by each absorption mechanism.

The scattering of sound waves results when they encounter inhomogeneities such as inclusions, pores or flaws. In general, the scatterers have a different acoustic impedance from the matrix material (acoustic impedance is the product of density and the sound speed), and consequently reflection and refraction occurs which directs energy out of the path of the acoustic wave propagation. The amount of scattering which will occur in a given situation depends upon the frequency of the sound, the cross-sectional area of the scatterer normal to sound propagation direction, and the shape of the scatterer.

For frequencies around 1 MHz, the attenuation of most polycrystalline materials, is determined almost entirely by grain scattering. Mason and McSkimin (71) adapted Rayleigh's work for grain scattering in metal. Rayleigh originally analyzed the scattering caused by inhomogeneities in a fluid for the case $\lambda >> D$, where λ is the wave length of ultrasound and D is the diameter of the scatterer . The short coming of Mason and McSkimin's theory was it's failure to take into acount the energy lost through mode conversion (72).

Further theoretical and experimental work has shown that around 80% of the scattered energy from an incident longitudinal wave is lost to shear wave when $\lambda >> D$ (71).

In polycrystalline materials the attenuation due to scattering depend strongly on the ratio D/λ , where D is the diameter of the scatterer (i.e. grain size). Smith and Stephens (72) have summerized the relationship between attenuation frequency and grain size as follows:

For $\lambda > 2\pi D$ attenuation = $B_1 f + A_4 D^3 f^4$ 4.6

$\lambda < 2\pi D$ attenuation = $A_2 D f^2$ 4.7

$\lambda <= D_{min}$ attenuation = $B_1 f + B_2 f^2 + A_0/D$ 4.8

Where D is the average grain diameter, A and B are constant which are unrelated to each other, $B_1 f$ is elastic hysteresis loss, $B_2 f^2$ is thermoelectric loss. Fig 4.5 shows the attenuation of longitudinal ultrasonic wave versus frequency in SAE 4150 steel for various microstructures.

In polycrystalline materials the presence of preferred orientation, has a large effect on grain scattering, since it modifies the change in modulus from grain to grain by aligning the crystallographic axes. Of equal importance, is the grain size distribution, as the scattering depends strongly on the particle size.

For both $D/\lambda \rightarrow \infty$ and $D/\lambda \rightarrow 0$ the amount of microstructural scattering is small. Where D is much greater than λ ($D/\lambda \rightarrow \infty$), Pure reflection and refraction occurs at grain boundaries. In the case of $D/\lambda \rightarrow 0$ the diameter of the scatterer is much too small to scatter the sound wave.

The laws of reflection and refraction of sound are the same as for any other waves. However in case of acoustic waves, mode conversion can occur, a phenomenon which does not exist for other waves (e.g. electromagnetic

waves). For a normal incident of acoustic wave on boundaries the reflection and transmission coefficients for pressure and intensity are given by the following equations (64);

$$\alpha_{TP} = \frac{2}{(m+1)} \qquad \text{Pressure transmission coefficient} \qquad 4.9$$

$$\alpha_{TI} = \frac{4m}{(m+1)^2} \qquad \text{Intensity transmission coefficient} \qquad 4.10$$

$$\alpha_{RP} = \frac{(m-1)}{(m+1)} \qquad \text{Pressure reflection coefficient} \qquad 4.11$$

$$\alpha_{RI} = \frac{(m-1)}{(m+1)^2} \qquad \text{Intensity reflection coefficient} \qquad 4.12$$

Where m is the ratio of the characteristic impedances of the two media.

$$m = \frac{R_2}{R_1} = \frac{\rho_2 C_2}{\rho_1 C_1} \qquad 4.13$$

As an example the acoustic impedance of water and steel are:

$R_1 = \rho_1 C_1 = 1.5X10^6$ NS/m^3 water

$R_2 = \rho_2 C_2 = 45X10^6$ NS/m^3 steel

The reflection and transmission coefficients for the intensity of sound of the water/steel interface are:

$$\alpha_{TI} = \frac{4m}{(m+1)^2} = 0.125$$

$$\alpha_{RI} = 1 - \alpha_{TI} = 0.875$$

The intensity of the transmitted sound wave from water to steel is 12.5% of the incident wave whilst the reflected sound wave has 87.5% of the intensity of the incident wave.

Compared to liquid or solid materials, a gas has a very low acoustic impedances. For air the acoustic impedance is $4X10^2$ NS/m^3, so that for a steel/air interface the coefficient of reflection is approximately one .

In general for a solid material the boundary with air can be regarded as similar to a boundary with a vacuum and the reflection of sound can be taken to be 100% .

In addition to the problem of the interface between two materials, the double interface as in the case of a plate or a gap, is of interest in the testing of materials. Examples are transmission of sound through a sheet immersed in water, or through a crack in a solid body. For continuous waves, transmission and reflection through a plate or gap depends in addition to impedance ratios, on the ratio of layer thickness to wave length. This is due to the multiple reflection within the layer and their interfaces with each other. The transmission and reflection coefficients for an embedded layer is given by the following expressions (64):

$$\alpha_{TP\ layer} = \frac{1}{1 + 1/4(m-1/m)^2\ Sin^2(2\pi l/\lambda)} \qquad 4.14$$

$$\alpha_{RP\ layer} = \frac{1/4(m-1/m)^2\ Sin^2(2\pi l/\lambda)}{1+1/4(m-1/m)^2\ Sin^2(2\pi l/\lambda)} \qquad 4.15$$

Stumpf (144) has given an analytical solution for the case of three different layers. Cox (57) has calculated the total amplitude of the transmitted acoustic wave through a metal plate immersed in water, taking into acount the attenuation in the metal plate. Fig 4.6 shows the graphical presentation of his calculation.

The equations 4.14 & 4.15 are also valid for an air filled gap, which can be in the form of a crack in the test sample. Fig 4.7 shows the transmittance for an air and water filled gap in steel and in aluminium. Fig 4.8 shows the same result for reflectance. Comparison of the Fig 4.7 and Fig 4.8 shows that at a freqency of 1 MHz an air gap of 10^{-8} mm - 10^{-7} mm can be readily detected from the reflected signal, although no change

on the transmitted signal would occur.

4.4 Ultrasonic wave propagation in porous media

Porous media range from the porous rocks, various polymer foams to the water-saturated sediments of the ocean floor.

In architectural acoustics and noise control the interest is centred on the reflection and absorbtion of small amplitude, air-borne sound waves from porous surfaces in the audio-frequency range. Marine geophysicists use measurements of the reflection of low amplitude sound waves of low frequency (near the audio frequency range) to obtain information on the composition and history of the deep sedimentary layers.

Numerous workers have investigated the problem of wave propagation in porous media, to predict fundamental acoustic parameters of these materials. Most of the wave propagation models for porous materials suppose that the solid constituent is rigid and the behaviour of the fluid constituent is equivalent to that of a modified, homogeneous, isotoropic fluid. Attenborough (73) in a comprehensive review has given various theoretical models for characterizing the porous materials. Attenborough also reviewed models which take into account the elasticity of the solid constituent of porous materials.

All these models deal with the wave propagation in the low frequency range, taking into acount the interaction between the acoustic wave and solid constituent at the solid interface . The treatment of the wave propagation in porous media are of little help for an understanding of the ultrasonic

wave propagation in plasma sprayed coatings, because it is hard to believe that scale modeling could give any satisfactory answer. Where in the case of plasma sprayed coatings, some of the assumption made (e.g. pores are interconnected) are not strictly true. More importantly these models assume that the sound wave propagates through the fluid. However in plasma sprayed coatings the situation is reversed, and the sound travels through the solid constituent and the sound velocity and modulus of the coatings are close to their solid constituent (74).

In plasma sprayed coatings most of the pores are thin elongated with a typical thickness of less than 0.1 micrometer. The trapped gas in such gaps behaves like a two dimensional gas, where the thickness of the gaps is less than the mean free path of the air molecules. Therefore the freedom of movement of the air molecules is not the same across the gap as along it. Szilard (75) proposed that the three order of magnitude difference between the predicted theoretical calculation and his experimental results for the drop in transmission of ultrasound through a thin crack is due to the two dimensional behaviour of the entrapped gas. Where the number of collisions of the gas molecules with the walls of the crack is much more than usual, and the compressibility and density in a pressure wave become non-linear. However plausible this suggestion might be, Gustufson (76) could not measure any of the harmonic components of the sound wave, which would be associated with such a non linear effect. Gustufson concluded that harmonic generation effects were not significant, at least for his experiments.

The most relevant and illuminating experiments for the ultrasonic wave propagation through thin gaps were carried out by Tarnoczy (77) and Clark (78). Early experiments of Tarnoczy were designed to detect air gaps having thicknesses in the submicron range. He found that incident longitudinal

waves were able to propagate through air three orders of magnitude larger than perdicted by acoustic theory. Clark (78) refined Tarnoczy's experimental technique and showed that although Tarnoczy's experimental results for the transmission characteristics of a thin air gap was correct in principle , but his finding of the frequency dependence of the transmission coefficient was not correct.(Tarnoczy found that the amount of transmission of ultrasound through the gap increased with frequency).

Clark (78) in his experiments used polished fused silica glass discs, flat to 54 nm or less over their 5 cm diameter surface. After cleaning, the surfaces were clamped together and the air gaps between them were measured by optical interferometry . The schematic diagram of his experiments are shown in Fig 4.9 . The acoustic reflection coefficient of the air gap was measured using a pulse echo technique. The frequency range covered in his experiments were 2-10 MHz. and the thickness of the glass discs were 0.94 cm, Fig 4.10a shows the theoretical reflection coefficients for various gap thicknesses at a frequency of 2.5 MHz . Also shown in Fig 4.10a are the experimental results of Clark and Tarnoczy. Although Clark's experimental results were closer to the theoretical calculation, they were still about three orders of magnitude higher than theoretical predictions. The most interesting results of Clark's experiments are the relationship between the acoustic reflection coefficient of the thin air gap and the degree of cleanliness of the gap walls. Fig 4.10b shows his results for the reflection coefficients for discs of varying cleanliness. These results show that the gap cleanliness strongly influences the reflection. He did not attempt to explain this behaviour, although he noted that the physics behind this is unclear at present. It apears that for ultra thin gaps in solids a correction factor for the reflection and transmission coefficient of sound is essential.

It is noteworthy that the particle displacement in solids even for very energetic sound waves in the MHz region, are less than one or two nanometers (65). Therefore even in the case of very thin gaps (e.g. 0.1 micrometer thick) no sound would be transmitted due to the movements of the gap walls. The most likely reason for the transfer of sound energy through a thin gap, (especially in the light of Tarnoczy's and Clarck's experiments) is due to the contact points between the gap walls. These contact points could be caused by the trapped free particles in the gap or grease, etc. The contact points act like channels for sound waves, and a transducer because of its size would only detect the overall effect and the average signal level.

The nature of plasma sprayed coatings are such that cracks and pores are inherently unclean. In SEM micrographs of plasma sprayed coatings, even large entraped fragmented pieces of coating material can be seen (Chapter 7) . Fumes and dust are an inherent part of the stream of molten droplets impinging on the work piece.

4.5 Ultrasonic testing of materials

Krautkramer (65) attempted to classify all ultrasonic testing methods, his classification being given in table 4.2.

4.5.1 Intensity method

The principles of the intensity method is shown in Fig 4.11 . It is the

oldest of the ultrasonic testing technique. In this technique the intensity of the ultrasound is measured after it passes through the test piece. The smallest diameter of detectable defect must be more than the wavelength of the ultrasound (diffraction around the edges of defect). Good and consistent acoustic coupling is essential, otherwise the received ultrasound will vary regardless of the presence or absence of any defect. Also alignment of the transducers is of equal importance. If continuous waves are used, the transmission and reflection follows the rules given in section (4.3) for a wave propagating through a plate. In plates, continuous waves can generate standing waves. Small variations of thickness will cause considerable variation in the received signal intensity. This problem can be overcome by modulating the frequency of the transmitted ultrasound. This technique is suitable for applications where no great accuracy is required.

4.5.2 Ultrasonic holography

Holography is a method of producing the image of an object by utilizing the interference effects. Fig 4.12 illustrates the holographic principle. A laser beam is divided into two parts, one part is reflected by a mirror and forms the plane reference wave, while the other beam illuminates the object. The portion of the laser beam which is reflected by the object forms it's wave field. The hologram is the result of the interference pattern of the object wave and reference wave.

The formation of the hologram can be explained as follows; if one assumes that the object is formed from many point-shaped reflectors or secondary radiators, each point in the object radiates a spherical wave which

together with the plane reference wave produces in a reception plane a single interference pattern in the form of alternating bright and dark rings. The hologram results from a superposition of the individual interference patterns.

In testing of materials, optical holography can be used for the continuous measurement of surface deformations. The aim of acoustic holography is to produce the image of the inside of an object by means of acoustic waves. Compared with the conventional sound-imaging methods, it offers the possibility of producing a three-dimentional optical image.

The generation of an acoustic hologram is fairly straight forward, because sound waves can readily be made coherent. For instance, two sound transducers energised continuously by the same generator, produce coherent sound waves. The main problem with acoustic holography is linked to the properties of the sound field. In contrast to optics the wave length of ultrasonic sound waves are comparable with the dimensions of the objects to be investigated (e.g. flaws). Consequently, diffraction phenomena are very evident. Furthermore in highly attenuating media, the interference pattern may not be properly formed and actually blur the reproduction. The high sound attenuation in plasma sprayed coatings, would make the holographic techniques unsuitable.

4.5.3 Transit time method

Transit time methods are primarily used for wall thickness measurements. In this technique the transit time over a given distance is measured, for which either continuous or pulsed sound can be used. The application of

this technique to plasma sprayed coatings, might not be successful, because the transit time measurements are either based on resonance (for continuous waves) or multiple reflections when pulsed ultrasound is employed. Both of these techniques require multiple reflections which imposes a serious limitation on the application of this technique for materials with a high attenuation such as plasma sprayed coatings. Therefore these techniques will not be discussed any further.

4.5.4 Pulse-echoe technique

The pulse echo technique is the most widely used ultrasonic non-destructive evaluation method for testing materials. In this technique a short burst of ultrasound generated by a transducer, propagates through a sample and is reflected from interface (e.g. The interface between a solid and gas such as in crack) and the reflected or transmitted signal is captured by a receiver transducer. The transmitted and received signals are usually displayed on an oscilloscope screen. The generation of sound bursts is repeated at least 20 times a second to ensure a persistent image.

4.5.4.1 Reflection pulse-echo technique

Fig 4.13 shows the principles of the reflection pulse-echo technique. In this method usually the same transducer detects the reflected echo. The output from the transducer is displayed on an oscilloscope screen as a synchronous trace of echo amplitude versus time. In Fig 4.13 the echo (B) correspond to the back wall of the sample and echo (C) is the reflected echo from the crack in the body of the sample. The transit time between the

initial driving pulse and the crack echo can be used to determine the position of the crack in the sample. In practice the transducer is scanned across the sample and an ultrasonic image of the test piece is constructed. Signals such as (C) would be attributed to the defects. The main drawback of this technique is that the defects near the surface can not be detected, because the finite pulse width makes it difficult to resolve a sub-surface echo. The thickness of this layer for a pulse width of about 1 microsecond, is for most metals 1 or 2 mm . Consequently the reflection pulse echo technique can not be employed for the examination of sprayed coatings, as the thickness of the sprayed layer is usually much smaller than 1mm.

4.5.4.2 Back-face reflection technique

An alternative method is to make use of the back-face reflected echoes for testing of sprayed coatings. The basic principles of this technique are shown in Fig 4.14 . Here a single transducer is used to generate and receive the reflected echoes. The transit time of the back-face reflected echo corresponds to the thickness of the test piece but carries no information about the position of any potential defects, although the amplitude of the back-face reflected echo can provide information about the presence of defects. The attenuation of the back-face reflected echo not only depends on the existance of flaws in the test piece, but also is a function of material characteristics.

The most convenient coupling method is by immersion , where both the sample and transducer are immersed in a liquid filled tank. Because of the acoustic mismatch between the sample and liquid couplant, echoes from the front and back faces of the sample are produced. It is essential that these

two echoes are well resolved. For a pulse width of 1 microsecond the minimum thickness of steel sample to produce two well resolved echoes is 3 mm. For plasma sprayed coatings this means that the back-face reflection technique can be used if the thickness of the substrate is not less than 3 mm. The other requirements for the successful application of this technique are that the back-face of the sample should act as a good reflector for the ultrasonic wave and be perpendicular to the direction of wave propagation, otherwise the reflected echo can not be detected. This leads to geometric restrictions to the applicability of this technique. Fig 4.15 shows schematically the effect of back-face orientation on the received signal.

The main advantages of the back-face reflection technique are that it only requires access to one side of the component and its enhanced sensitivity to small defects (because the beam passes through the defect twice)

4.5.4.3 Transmission pulse-echo technique

The transmission pulse-echo technique can be used to reveal the presence of defects in the bulk or sub-surface of components. A schematic diagram of the principles of this technique is shown in Fig 4.16 . In this technique separate transducers are used to generate the ultrasonic waves and to receive them after passing through the sample. Here also, immersion is the most suitable way of coupling the ultrasonic wave between transducers and the sample. If the beam of ultrasound is intercepted by a defect, the amplitude of the received signal drops below its average value depending on the size and type of defect. Cracks or delaminations because of the high reflection coefficient of solid/gas interfaces, produce an acoustic shadow, Fig 4.16 . This technique is applicable for ultrasonic testing of sprayed coatings, because the thickness of the coating is usually less than 0.5 mm,

and the attenuation of ultrasound in sprayed coatings is very high (57).

4.5.5 Geometric restrictions imposed on ultrasonic testing

Oblique incidence of a plane sound wave on a plane boundary, results in reflection and refraction of sound waves. The direction of the reflected and the transmitted waves are determined by the general laws of refraction

$$\frac{\mathrm{Sin}\alpha_1}{\mathrm{Sin}\alpha_2} = \frac{C_1}{C_2} \qquad 4.16$$

Here C_1 and C_2 are the velocities of sound in medium 1 and 2, α_1 and α_2 are the angles of incidence and refraction respectively, Fig 4.15 . The ratio of C_1/C_2 for two mediums of steel and water is about 4, therefore for an incident angle greater than about 15^0 total reflection occurs and no sound can be transmitted through the sample.

In all the techniques described in the previous section, it was assumed that either the ultrasonic pulse travels straight through the parallel sided sample oriented normal to the ultrasonic beam, or it is echoed from a discountinuity in the sample. This restricts the shape of the components to either plates, cylinders or spheres.

Although it is possible to devise a scanning system for components with complex geometry, such that the transmitter transducer scans normal to the component's surface and adjust the position of the receiver to follow the ultrasonic beam, in most cases it would be impractical.

4.5.6 Special testing techniques

In cases where conventional testing methods fail to provide a satisfactory solution, special techniques can sometimes be employed. Many special techniques have been devised and some of which are commercially available . A brief description of some of these techniques and their potential application to plasma sprayed coatings are given below.

Kaule et al (65) developed a pulse resonance based technique and Krautkramer manufactured an instrument based on this method. In this method the test piece is excited to resonance by a long pulse. The transient time measurement is made from the natural resonance frequency of the test piece, which is detected after termination of the transmitting pulse. The received signal is fed into the transmitter and a new cycle starts. The measuring cycle begins by transmitting white noise. The plate acting as a filter, selects its own frequency and re-emits it. After a few round trips the signal level is sufficiently high for accurate measurements. With this technique accuracies of up to 0.1 per cent can be achieved(65). Another advantage of this technique is that the alignment of the probes is less critical than other techniques.

Szilard et al (64) used the principles of the pulsed resonant technique and developed a method for measuring the defects behind a metal plate (e.g. interface of rubber coatings on steel). By using the appropriate frequency acoustic transparency of the metal layer can be achieved, so that the incident energy can penetrate deeper into the sample. A block diagram of this system is shown in Fig 4.17 . Bursts of Ultrasound having step-wise characteristic frequencies are generated and transmitted into the sample via a delay line. An acoustic delay is essential between the transducer and the test piece in order to prevent interference of the reflected and

transmitted waves.

The received signals have amplitudes which correspond to the frequency response of the transducer. At the resonant frequency of the plate, a portion of one of the reflected bursts shows a dip Fig 4.17 . At this frequency the plate becomes effectively transparent to the incident acoustic wave. If a defect is present at the interface of the plate/coating, the resonant dip tends to fill in , because of the high reflection coefficient of the solid/gas interface, Fig 4.17 . This technique is more suitable for materials with small attenuations, where multiple reflection in the plate prevents the application of conventional pulse-echo method.

The techniques based on resonance methods are of little use for testing plasma sprayed coatings, because of their high attenuation of ultrasound, preventing proper resonance from taking place.

Rose and Mayer (79) have shown that there is much more information in ultrasonic signals than is normally extracted from amplitude versus time traces when the layer is thin relative to the pulse duration, although the echo resolution is lost, the layer thickness information is still present. Applying the Fourier transform to the reflection allows the extraction of the thickness data by looking at the reflection amplitudes of all the frequency components of the input pulse. Those frequency components of the incident pulse which correspond to the natural frequency of the layer or its harmonics, will be transmitted and therefore absent from the reflection. Although, this is a powerful technique , it would not be surprising if complicated frequency spectrums were produced for plasma sprayed coatings. Because plasma sprayed coatings inherently have large

numbers of cracks and voids of various thicknesses, each transmitting certain components in the frequency band.

4.6 Ultrasonic testing of plasma sprayed coatings

Frank and de Gee (80) have carried out tests using pulse echo, backwall echo and transmission pulse echo techniques. Their results suggest that the pulse echo and backwall echo are not very suitable for testing plasma sprayed coatings. The results of the transmission pulse echo gave a good correlation with metallographic observations and tensile tests. Steffens (8), used a backwall pulse echo technique and was able to detect artificial bond imperfections produced in 0.1% C steel arc sprayed coatings. The smallest diameter of these defects was 7 mm. Steffens et al (8) also suggested the use of pulse resonant techniques to detect bond imperfections in situations where the backwall echo due to geometric restrictions are lost.

Cox et al (81) also studied the acoustic properties of plasma sprayed coatings. Cox measuerd the attenuation of the ultrasound in the range 2.5 to 15 MHz in aluminium, nickel aluminide and molybdenum coatings. Fig 4.18 shows the attenuation of ultrasound in their materials at different thicknesses (0.2 mm to 0.6 mm). They have also reported that the large scatter for aluminium coatings was due to variation in the porosity of the coatings (Fig 4.19). Cox et al (82) also used transmission and backwall pulse echo techniques to study the bond integrity of plasma sprayed coatings. Fig 4.20 shows a line scan at various frequencies accross an aluminium sample with a line defect . The peaks on the attenuation trace correspond to the line defect.

Chapter 5

Acoustic emission

5 Introduction

This chapter attempts to identify the problems assosiated with and the significance attached to the signal processing of acoustic emission. A review of the literature on acoustic emission is presented to show that any development in this area, will enhance the possible use of acoustic emission techniques for non-destructive evaluation of materials.

5.1 What is acoustic emission ?

The noise emitted from tearing of paper or breaking a piece of wood is familiar to everybody. Metallurgists have been aware of audible clicks assosiated with martensitic transformations, whilst mine workers are well aware of creaking noises emitted prior to a cave-in, and the story of dogs sensing the impending earthquake is familiar.

The phenomenon of acoustic emission has been known for centuries. Geologists have been using stress waves for studying earthquakes (83). However it is only recently that material testing has made use of acoustic emission tehniques. The name acoustic emission is given to stress waves generated when a material reacts to decrease its internal energy. The specimen must suffer some degree of damage if emissions are to be produced. However this does not mean that acoustic emission is associated with all failure mechanisms.

If acoustic emission is to be used as a non-destructive testing technique, the first question to be answered is whether the acoustic emission may be generated prior to fracture? The fact that acoustic emission is the result of processes within a material has enormous practical significance, which

enables the study of micro-failure mechanisms and real-time monitoring of performance of components and structures. However the fundamental problem of source identification by acoustic emission in many applications is yet to be solved.

The recent rapid development of AE technique is partly due to the new developments in the field of electronics. Piezoelectric transducers are the most widely used sensors in AE testing of materials. With PZT5 transducers , theoretically, displacements of the order of femtometers $6X10^{-15}$ m can be detected (65), which enables microscopic phenomena to be studied. The work described here is intended to develop methods of signal and data analysis to extend the application of acoustic emission techniques.

5.2 Source of acoustic emission

The first systematic study of acoustic emission was carried out by J. Kaiser. Liptai et al(83) reported that Kaiser employed transducers, amplifiers and oscilloscopes to study the acoustic emission during tensile testing of polycrystalline zinc, steel, tin, brass, aluminium, copper and lead samples. His conclusions that the source of acoustic emission was grain sliding, has long been disproved (84). However his observation that acoustic emission appears to be irreversible, has been confirmed many times and has been named the 'Kaiser effect'. He also observed that the amplitude and frequency of the emissions were characteristic of the material and stress level. Kaiser reported that emissions were made up of two types, a low amplitude continuous sound with high amplitude bursts superimposed.

Schofield (84) discovered that grain boundaries were not the only source of

acoustic emission, because single crystals also give rise to acoustic emission under applied stress. Tatro and Liptai (85) made similar observations. They also reported that surface features (e.g. oxide layers or polished surfaces) changed the emission spectra.

Fisher and Lally (86) studied the acoustic emission caused by the plastic deformation of single crystals of copper, iron and magnesium. They found that the acoustic emission event rate increased with increase in the plastic strain rate . Fig 5.1 shows their result for magnesium single crystals. In Fig 5.1 only large amplitude signals are shown. James and Carpenter (87) have extended Fisher and Lally's work. They used sodium Chloride, lithium fluoride and zinc single crystals. Their results show that the rate of acoustic emission was proportional to the change in the mobile dislocation density ratio. James and Carpenter consider the breakaway of dislocations from pinning points as a model of an emission source. Kiesewetter and Schiller (88), using aluminium single crystals, observed that the mean square emission voltage was proportional to the strain rate, and proposed that the source of the emission was elastic radiation accompanying dislocaion acceleration and deceleration Fig 5.2 . Imanaka et al (89) simultaneously monitored the stress, strain, acoustic emission amplitude and the ultrasonic attenuation of 27 MHz longitudinal waves during compression testing of copper single crystals. They found that deformation started with dislocations detaching from pinning points at low stress levels. As the stress level increased, the free dislocation segment length increased towards a critical value of 10^{-6} m. Once the critical length was reached, rapid dislocation multiplication occured by the activation of Frank-Read sources. They suggested that the source of emission during this stage was the rapid increase in the mobile dislocation density associated with Frank-Read source operations.

The strain dependence of acoustic emission in single crystals suggests that AE activity depends upon crystal orientation, stacking fault energy, composition etc, because all of these effect the magnitude of slip events (90). The influence of some of these parameters on acoustic emission activity have been investigated by some workers (91, 92).

It would appear that the source of acoustic emission in both aluminium and copper single crystals is the sudden release and propagation of dislocations.

Other phenomena generating acoustic emission in single crystals have also been investigated. Mohamed et al (93) studied the acoustic emission generated in ferroelectric materials ($Pb_5Ge_3O_{11}$ and TGS) under an applied electric field. They found that AE occurs predominantly near the regions of saturation polarisation at the two extremes of the hysteresis loop. Mohamed et al attributed the source of AE in ferroelectric materials to domain wall movements. Zammit-Mangion (94) furthered Mohamed's work and studied AE of rochelle salt, lead germanate gadolinium molybdate and terbium molybdate. He found that there was a threshold electric field below which no AE was produced. Also by simultaneous monitoring of the AE and visual observation of the domains in gadolinium molybdate and lead germanate, he observed that domain nucleation and collapse were the source of AE in these materials.

In addition to the factors influencing plastic deformation of single crystals, grain size will impose restriction on the movements of dislocations in polycrystaline materials. Kiesewetter and Schiller (88) presented results for 99.99 % pure aluminium, which indicated a relationship between grain size and acoustic emission. Fig 5.3 shows

their result, where AE activity increases with grain size up to a maximum limit of single crystals. These results were interpreted by considering the changes in slip increment accompanying changes of grain size. They explained their result by pointing out that dislocations in one slip system can interact with dislocations in another and are stopped from moving, because increasing grain size reduces the possibility of this interaction. However Frederick's (95) results on 99.99% aluminium contradict their finding. Frederick found that as the grain size increased AE activity increased up to a maximum limit after which it started to decrease Fig 5.4 . Frederick pointed out that the decrease in AE activity is due to the reduced grain boundary area which results in reduced dislocation sources.

Kishi et al(96) presented results which somewhat contradict the above mentioned model. They used polycrystaline of 99.9% purity with grain size of 30,43,60 and 94 micrometer. The emission activity of the two specimens with largest grain size were similar, but reduction of grain size led to an increase in emission activity. The discrepancy between Kishi et al's results and the above mentioned model could be the result of the higher impurity concentration in their material. Also Kishi et al used a resonant transducer, which might have affected their result.

Fleischman et al (97) used 99.99% purity aluminium to study the frequency dependence of acoustic emission. They measured acoustic emission energy at three frequencies (.94 , 1.56 and 2.17 MHz). They found that at constant grain size, the position of the maximum emission was shifted to higher strains and the breadth of the peak widened as the observation frequency increased. Also they reported that when the grain size varied, the position of the peak moved to higher strains with increasing grain size.

Another important microstructural factor is the presence of alloying additions. This is especially the case because alloys are more important materials in engineering. The most frequently reported experiments have been performed with aluminium alloys.

Agarwal et al (98) studied the acoustic emission activity associated with the deformation of room-temperature aged 2024 (Al-Cu-Mg) aluminium alloys. They observed a rapid decrease in acoustic emission count as the aging time was increased, the count only returning when the material had been overaged at higher temperatures. Agarwal et al (98) attributed the emission to the operation of dislocation sources. During aging the average interparticle spacing decreased until peak hardness which was about 0.05 micrometer. The reduction of interparticle spacing restricts the slip distance thus reducing the acoustic emission. They also showed that in peak-hardened material the strains were below the sensitivity limit of the detection system. Hatano (92) has also reported similar effects in 2024 (Al-Cu-Mg) aluminium alloys.

Scruby et al (99) have carried out a systematic study on the origin of acoustic emission and its dependence on microstructural parameters. They assumed that the source of the acoustic emission was an expanding dislocation loop inclined at 45 degrees to the tensile axis Fig 5.5 . They have calculated the ramp of slope and peak amplitude for the displacement at the surface for such a dislocation loop due to the first longitudional pulse, which is given by

$$\frac{U}{T} = \frac{bV^2C_s^2}{DC_l^3} \qquad 5.1$$

$$U = \frac{baVC_s^2}{DC_l^3} \qquad 5.2$$

Where b is the burger's vector, a is the radius in which the loop expands, V is a constant velocity at which the loop expands, C_l is the longitudinal wave speed, C_s is the shear wave speed and D is the depth of the dislocation loop below the surface.

Equation 5.2 shows that the peak displacement amplitude U is proportional to the radius of a dislocation loop, and the velocity at which it expands. Signals from multiple loops expanding cooperatively would be additive, so that if they had a common velocity the radii must be added to give the effective strength. Using equation 5.2 Scruby et al(99) estimated the smallest detectable dislocation loop for their material and detection system. In practice a loop is more likely to expand at variable velocity. Assuming a mean velocity of 200 m/s gives a_{min} = 180 micrometer. This also gives an indication of the highest frequency components of the elastic wave. For the above example the lifetime of the smallest dislocation loop is 0.9 microseconds. This model also predicts that if the distance which individual dislocations propagate decreases, and if the dislocation velocity does not decrease, the lifetime of each source should decrease. Thus, the spectrum will be extended to higher frequencies.

The results obtained by Scruby et al (99) in 99.99% pure single crystals and polycrystalline aluminium are shown in Fig 5.6 . For the aluminium single crystal, the slow fall in emission power after reaching its maximum was due to a reduction in the average area to which dislocation loops expand due to forest interaction. For polycrystalline aluminium, dislocation movement was restricted by the grain boundaries as proposed by Kieswetter and Schiller (88). The expanding dislocation loop model given by Scruby et al (99), required that for a given strain rate the total acoustic emission energy released during a test should increase with

increasing grain size, and that the emission power should vary linearly with strain rate for a given grain size . Both of these requirements were experimentally observed by Scruby et al (99). Fig 5.7 shows the relationship between acoustic emission power and strain rate for both single and polycrystalline aluminium. The addition of 1.3 Wt.% Mg to otherwise pure aluminium to form a precipitation and segregation free solid solution, had a profound effect upon both the strain and grain size dependences of the acoustic emission activity, as shown in Fig 5.8 . The acoustic emission activity at first increased with increases in grain size up to a maximum occurring at grain size of 80 micrometer. After which it decreased, almost to zero for large grain size. One other important effect which the solid solution had on acoustic emission was the replacement of continuous emission with burst emission. Scruby et al (99) suggested that the rise in emission activity was due to increase in grain size and rapid disappearance of subgrain structure. The decrease in emission for large grain specimens (>80 micrometer), may be due to a decrease in flow stress associated with increase of grain size, which was sufficient to inhibit dislocation escape (99).

The effect of precipition on acoustic emission was investigated by Scruby et al (100) on a 4 Wt.% copper aluminium alloy. They found that there was a pronounced increase in emission activity after aging of material for a short period of time. However the detected emission reached a maximum after about two hours before decreasing again Fig 5.9 . Scruby et al (100) proposed a model to explain the aging peak, based on the changes in the deformation mechanism. The acoustic emission in quenched condition was low because of homogeneous and continuous deformation, as there were not many obstacles that could inhibit the motion of dislocations. As aging progressed (1.5 hours), fine precipitates form which initially inhibit the

motion of dislocations, and result in a pile-up of dislocations. As the stress increased, in the vicinity of yield the dislocations could break through some of the obstacles leading to a sudden strain increment, resulting in high energy burst emissions. With increasing aging time the precipitates grow stronger and dislocations were no longer able to break through, resulting in a decrease in acoustic emission ativity.

Scruby et al (101) studied the effect of changes in microstructure of A533B steel (Mn-Mo-Ni) upon the acoustic emission. Their experiments were designed to determine only the acoustic emission generated from the deformation process. The sulphur content was reduced to a minimum (0.0045 wt.%), to eliminate the possibility of acoustic emission generated from the fracture of MnS inclusions. Two types of heat treatment were used. One set of specimens were austenitized for 1 hour at 1000°C in an argon atmosphere and cooled at varying rates. The differing cooling rates were achieved by quenching specimens in either iced brine at -10°C, 10% NaOH solution at room temperature, water, oil or by air or furnace cooling. The second set of specimens were water quenched from 1000°C and tempered at 650°C in argon for 6 - 10020 minutes, and then water quenched. These treatments resulted in a wide range of microstructures and mechanical properties.

The four most rapid quenching rates resulted in no significant emission during the pre maximum stress deformation, Fig 5.10 . The few isolated and random emissions which were observed during this period were thought to be the decohesion-cracking of spheroidal inclusions. Scruby et al (101) explained that because of the high dislocation density and the small width of martensite lathes in the quenched material, dislocations can only propagate over very short distances. According to the dislocation model the acoustic emission associated with such dislocation motions are well below

the detection limit. Air and furnace cooled specimens gave increased levels of acoustic emission. This is in agreement with the dislocation model, because in the slow cooled specimens the distance over which dislocations could move freely increased due to the disappearance of the lath structure and a reduction in initial dislocation density. The tempering of water quenched specimens had a greater effect. Lightly tempered specimens generated little emission, which was consistant with dislocation pinning. Prolonged tempering resulted in a strong increase in emission as the free dislocation path increased Fig 5.11 .

In the post-maximum stress, the two fastest quenched specimens generated very large amplitude emissions as final facture approached. Scruby et al (101) attributed the soure of emission to the formation of subcritical cleavage micro cracks. When the cooling rate reduced the emission activity was both delayed and reduced in energy Fig 5.10 . Where the fracture mode was alternating shear with only isolated areas of cleavage. Neither the slow cooled nor tempered specimens generate any emission other than during the final fracture. The slow cooled specimens failed by ductile void coalescence. It is clear from the foregoing that not all deformation mechanisms generate acoustic emission and some generate more than the others.

5.2.1 Acoustic emission associated with fracture

One of the most important potential applications of acoustic emission in engineering is monitoring the integrity of the structures. However, as will be shown later, not all fracture modes produce detectable acoustic emissions, and this is a major drawback to the widespread application of

acoustic emission to engineering structures. Many workers have claimed that they were able to identify various fracture modes with acoustic emission. For example McCousland and Scale (102) have investigated the source of emission and the effect of precipitates in 7075 aluminium (Al, 6.2 Zn, 2.2 Mg, 2.3 Cu, 0.1 Zr wt.%) and 7050 aluminium (Al, 6.2 Zn, 2.2 Mg, 2.3 Cu, 0.1 Zr wt.%). Tests carried out in compression produced little or no acoustic emission, but copious emission was generated during tensile tests. McCousland and Scala (102) pointed out that deformation processes would be similar in tension and compression while particle fracture would only be expected during tensile testing and conclude that the source of emission was the fracture of brittle precipitates. Support for their argument came from the fact that the amount of acoustic emission was dependent upon the cross-section area of the particles normal to the applied load.

Byerlee and Peselnick (103) studied the acoustic emission associated with fracture of glass. When unslotted specimens were subjected to compressive load no acoustic emission was produced. However compressive testing of slotted specimens produced acoustic emission upon the appearance of a crack but no emission was produced during stable crack growth. This is in parallel with the acoustic emission generated by dislocation movement, in which only acceleration and deceleration of dislocations produced acoustic emission. Similarly, only the starting and stopping of the crack tip during fracture will create acoustic emission. In fact this is to be expected because vibrations are only associated with acceleration and deceleration of particles. Further support for these findings came from the work of Knehans et al (104). Who studied the acoustic emission associated with the fracture of porous sintered glass. Knehans et al (104) monitored the acoustic emission generated during controlled slow crack growth with five different mean grain sizes (17 - 530 micrometer). They observed that

the first acoustic emission was generated when the deviation from linearity of the load-deflection curve occurred, indicating the start of cracking, and that the total number of events was proportional to the fracture area. They also found that the number of partial steps (micro-cracks) was related to the number of acoustic emissions and the grain diameter. Smaller grains produced more acoustic emission events but their amplitude was generally smaller. This was explained by the incremental crack growth and the size of each micro-crack. The small grains fractured almost in one step, while the large grains fractured in several partial crack steps.

Metals however do not fracture in such a brittle manner as glass. Ingham et al (105) studied acoustic emission generated during crack propagation in a range of steels with yield strengths between 230 and 1620 MN/m^2. They found that the acoustic emission activity increased with decreasing ductility. In steels with low yield strength, the majority of the emission occurred during plastic deformation, and crack extension was quiet. When high strength steels were tested the majority of events occurred during the last 20 percent of the test. This was mainly associated with the formation of subcritical cracks. These results are consistent with the systematic study of Scruby et al (101) shown in Figs 5.10 and 5.11 .

McBride et al (106) studied the source of acoustic emission during slow crack growth caused by fatiguing 7075 aluminium containing different sizes of precipitat s produ by heat treatment. Their results show a direct dependence of the emission upon the size of the inclusions which fractured in the material. Also acoustic emission was not detected if the strength of the materials surrounding the inclusions was too low. McBride et al (106) concluded that the acoustic emission from 7075 aluminium alloys could be predicted from the cross-sectioned area of the inclusions. It was also

suggested that the discontinuous movement of the crack tip in the inclusions along the crack front was the source of acoustic emission .

Nozue and Kishi's work (107) provided further support for the discontinuous movement of crack being responsible for the generation of acoustic emission. They studied the tensile failure of 4340 steel (Fe, 1.8 Ni, 0.81 Cr, 0.78 Mn, 0.3 Si, 0.19 Mo wt.%) , tempered at various temperatures. Specimens with the highest tempering temperature produced no acoustic emission, and microscopic examination showed that the fractured surface consisted entirely of the characteristic dimpled ductile fracture. Specimens tempered at lower temperatures produced acoustic emissions which were inversely related to the tempering temperature, the fracture surface showing a varing amount of intergranular brittle fracture. Significantly they found that there was a linear relationship between the cumulative squared emission voltage (which is a measure of energy) and the cumulative area of intergranular cracking on the fracture surface.

5.3 Acoustic emission source model

In the early 60's acoustic emission was introduced as a powerful testing technique and many extravagent claims were made about its potential to detect and identify flaws in structures as well as for studying the dynamics of deformation and fracture processes. However, as was discussed in the previous section, some fracture and deformation mechanisms generate acoustic emissions while others do not. Therefore a clear understanding of the nature of the source mechanism is essential.

A number of attempts have been made to model the acoustic emission source.

Birchon's (108) illustration of the elastic strain energy released during a crack-growth event, showed that only, part of the energy released from a growing crack or moving dislocation may be emitted as acoustic emission Fig 5.12 . If the energy of the acoustic wave could be measured and the partition function determined, then it might be possible to estimate the energy of the source event.

In practice however this has proved to be difficult because, as will be discussed later, the fraction of the energy released as acoustic emission is not always a constant proportion of the released strain energy, and it depends on the nature of the source mechanism and the properties of the surrounding materials. For example the rate of energy release can have a large effect on the energy dissipative processes. If the rate of energy release is high, the material surrounding the emission source may not have enough time to absorb the energy, and a large fraction may be radiated as elastic waves. There might be additional problems due to inconsistent energy measurement for reasons such as bad coupling etc.

Stone and Dingwal (109) argued that since the movement of dislocations during deformation or crack propagation during fracture tends to lower the internal energy of the material, these processes can be considered as one of relaxation . They used the expression for the energy density given by Curtis (110), for a spherical wave accompanying such relaxation;

$$\varepsilon = \frac{P_0^2}{2\rho_0 C^2}\left(1 + \frac{C^2}{2\omega^2 r^2 2}\right) \qquad 5.3$$

Where P is the acoustic pressure, C is the wave speed, ρ is the density of the material, ω is the angular frequency and r is the distance from the source. The first term is the energy density of the plane wave. Curtis

pointed out that beyond one wave length the second term is negligible, therefore it is reasonable to treat all longitudinal waves as plane waves.

$$\varepsilon = \frac{P_o^2}{2\rho_o C^2} \qquad 5.4$$

The acoustic pressure is given by (67)

$$P_o = \frac{\rho_o C^2 \delta\sigma}{E} \qquad 5.5$$

where $\delta\sigma$ is the change in stress (stress drop) and E is the Young's modulus, hence

$$\varepsilon = \frac{\rho_o C^2 (\delta\sigma)^2}{2E^2} \qquad 5.6$$

The elastic energy in the material is given by

$$U = \sigma^2/2E \qquad 5.7$$

and

$$\delta U = \frac{\sigma}{E}\,\delta\sigma \qquad 5.8$$

Dividing 5.7 by 5.8 will give the relationship between the energy carried by acoustic emission and the elastic energy released.

$$\frac{\varepsilon}{\delta U} = \frac{\rho_o C^2 \delta\sigma}{2E} = K\frac{\delta\sigma}{\sigma} \qquad 5.9$$

where K is a constant. The equation 5.9 shows that the energy of the acoustic emission wave is not a constant proportion of the released stored energy, but depends on the magnitude of the stress at which the drop occurs. Pollock (111) developed a model for the energy carried by acoustic emissions based on a mass supported between two springs. When the spring

constant of one spring was instantaneously changed, the resulting shift to the new equilibrium was considered as the emission-generating process. Siginificantly the result of his crude model agrees with that of Stone and Dignwal (109) which provides further support for the suggestion that acoustic emission is generated by relaxation processes. Furthermore Pollock (111) presented experimental results which confirmed the stress dependence of acoustic emission Fig 5.13 .

Scruby et al (101) calculated the minimum detectable crack increment below the surface of a material. They assumed that the source of acoustic emission was a small horizontal microcrack buried at a distance h below the surface. Assuming a constant crack velocity V , the minimum detectable crack increment is given by:

$$a_{min} = \sqrt{\frac{3C_l E h X_{min}}{8(1-\nu^2) V \sigma}} \qquad 5.10$$

Where a_{min} is the minimum detectable crack increment, C_l is the longitudinal wave speed, E is Young's modulus, X_{min} is the minimum detectable displacement at the surface of the material, ν is the Poisson's ratio and σ is the applied stress.

From equation 5.10 it is clear that the smallest crack advances are most easily detected when they are close to the surface. Also smaller cracks with higher velocities (short duration) and surrounded by a high strength matrix are more easily detected. Scruby et al (101) also calculated the minimum radius of a detectable dislocation loop, which is given by

$$a_{min} = \frac{hC_l^3 X_{min}}{bhVC_s^2} \qquad 5.11$$

where b is the Burger vector and C_s is the shear wave velocity. Equation 5.11 means that a dislocation loop expanding near the surface of the material is more easily detected and also if their velocity increases or if n loops situated close to each other expand over the same time interval so that their combined radii exceed the detection limit. Dividing equation 5.11 by 5.10 leads to :

$$\frac{a_{min}\ (\text{dislocation})}{a_{min}\ (\text{crack})} \propto X_{min}^{1/2} \qquad 5.12$$

This means that according to the model presented by Scruby et al (101), it is expected that for detecting dislocation movements more sensitive instruments are required. Significantly all these theoretical predictions have been observed experimentally.

Apart from the importance of the factors influencing the source mechanism of acoustic emission it is of interest to consider the shape of the stress wave near the source. If the shape of the AE wave at the surface is known, by considering the wave propagation in the material, one might be able to determine the shape of the stress wave near the source.

Seismologists have made a considerable contribution to the understanding of elastic wave propagation in solids.

Breckenridge et al (112) were the first to utilize seismologists findings and apply them to acoustic emission. Their experiment and findings will be discussed later as they are more relevant to the calibration of transducers. Hsu et al (113) obtained results for a step displacement source at the epicentre of a large aluminium plate. They simulated a step function normal force by breaking a glass capillary of 0.5 mm diameter on

one side of a large aluminium plate. A capacitative transducer was used to detect the signal. Hsu et al's (113) experimental set up is shown in Fig 5.14 . Their experimental results for the vertical displacement at the epicentre agreed well with their numerical calculations as shown in Fig 5.15 . The agreement between theory and experiment convinced them that the breaking capillary was acting like a step displacement, since that was what had been assumed in theory. These calculations (displacement at the epicentre) are based on the theory of the generalized ray taken from Seismoligists. Following is a brief description of the generalized ray theory given by Hsu et al (113). The displacement $U(x,t)$ can be written as the convolution integral

$$U_i(x,t) = \int\int G_{ij}(x, x_0, t-\tau) S_j(x_0, \tau) d^3x_0 d\tau \qquad 5.13$$

Where $G(x, x_0, t-\tau)$ is the medium transfer function also called the Green's function, and represents the displacement in the structure at point x and time τ , $S_j(x , \tau)$ is the source function operating in direction j at position x . The equation 5.13 is in the form of an infinite series expansion called a generalized ray expansion. The initial source function is resolved into its characteristic components longitudinal, horizontal shear, and vertical shear and each of these components is followed through a series of reflections at the top and bottom faces of the plate until the receiver is reached, at which time they are recombined. One ray is the contribution of one such component followed through a particular series of reflections taking into account mode conversions. All rays arriving at the same time at the receiver are grouped together and classed by arrival time. The solution can be generalized for force monopoles, dipoles etc, located on the surface or within the plate.

The Green's function has been calculated for an infinite space, an infinite half space and an infinite plate(114) . Although these cases physically do not exist, the results of the calculation are valid in a finite plate from time zero to a time just before the arrival of any reflected waves. Hsu et al (113) deconvolved equation 5.13 to obtain the force-time function for breaking a glass capillary .

Since the validity of the overall system was established, Scruby et al (101) investigated the actual acoustic emission source by cracking in A533B steel. They developed a sample geometry that is a compromise between a large body for propagation purposes and a long slim sample for tensile testing and they called it a "Yobell" geometry Fig 5. 16. The sample can be tested in a conventional tensile testing machine and the upper large portion should allow 6 microseconds of undisturbed wave propagation in steel. The acoustic emission events were forced to occur in the 2 mm long gauge section immediately below the large portion. Their experimental set up is shown in Fig 5.17. Scruby et al (101) used a capacitance transducer because of its large bandwidth(20 KHz - 25 MHz.) and its flat response. But a large bandwidth always implies a lower sensitivity. They used a capacitive transducer only to monitor acoustic emission activity from ice brine and water quenched samples. These specimens produced high energy events prior to its fracture. Using equation 5.13 and assuming a step function for crack opening, they calculated the displacement time function at the epicentre. The area under the longitudinal wave pulse is given by Scruby et al (101)

$$S_c = \frac{V}{2\pi C_l h} \qquad 5.14$$

Where V is the crack volume. Scruby et al's experimental observation of

displacement waveforms at the surface from microcracking of A533B steel are shown in Fig 5.18. They then deconvolved these displacement wave and obtained results which showed how the crack volume varied as a function of time, also shown in Fig 5.18. The agreement with the theoretical calculation is not exact; Scruby et al (101) explained that the negative values of volume obtained were a result of low frequency filtering.

5.4 Acoustic emission signal processing and detection

An acoustic emission wave like any other wave is not immune from the effects of its surroundings. The affect of the propagation medium on the acoustic emission wave is similar to that on ultrasound discussed in chapter 4. However two mechanisms, namely geometric spreading and mode conversion, are more important in acoustic emission. The geometric spreading is an important part of attenuation for acoustic emission waves, because unlike ultrasound, it comes from a point source. Kinsler and Frey (67) give the equation of pressure and amplitude for a spherical wave as;

$$P = \frac{A}{r} \exp(j\omega t - Kr) \qquad 5.15$$

$$A = A_0 \exp(-\alpha r) \qquad 5.16$$

Where P is pressure and A is amplitude , r is distance from source, j is $\sqrt{-1}$, ω is the angular frequency, K is the wave number ω/C , A_0 is the original amplitude and α is the attenuation. The meaning of these equations is that the amplitude of a signal detected by a force sensitive transducer is inversely proportional to its distance from the source.

Mode conversion occurs at the boundaries where a longitudinal wave produces a shear component or vice versa. For example if a longitudinal wave arrives

at a boundary between a solid and air, it exerts a force F on that boundary Fig 5.19. Resolving F into components normal F_y and parallel F_x to the surface, it can be seen that the component normal to the surface is partly balanced by a compressional force in air and partly by the elastic force of the solid. However the shear component must be entirely balanced by a shear force in the solid since air cannot support a shear stress.

Other factors which influence the acoustic emission signals detected including the fact that the actual source may emit both longitudinal and shear waves both of which have a distribution of frequencies and amplitudes. Even in a specific direction these waves can propagate with different speeds, and the higher frequency components experience stronger attenuation than the lower frequency components. This may severely affect the acoustic emission wave forms. Green (115) has quoted Heisinger's theoretical calculation for the effect of geometry on the acoustic emission wave form and its frequency components. The schematic illustration of this problem is shown in Fig 5.20.

5.5 Acoustic emission transducers

The transducer used should be chosen for each specific application since, as will be discussed later, some are completely unsuitable for certain applications. The most widely used acoustic emission transducers are piezoelectric transducers coupled to the work piece through an acoustic impedance matching medium (grease). Acoustic emission transducers, in principal, should convert a component of an elastic wave into an electrical signal. The most desirable characteristics of an acoustic emission transducer are; broad bandwidth, high sensitivity, small element size, low

acoustic impedance and a wide dynamic range. Some of these requirements are in conflict, like high sensitivity and broad bandwidth. Thus a compromise is necessary in designing a transducer.

Acoustic emission transducers are usually designed to respond to displacements normal to the surface. Kino (116) has given the response of the transducer to the normal displacement caused by a longitudinal wave

$$V_1 = 2 \frac{J_1(K_1 a \sin\theta)}{K_1 a \sin\theta} \qquad 5.17$$

Where $K = 2\pi / \lambda_1$, a is the radius of the transducer and $J_1(x)$ is a Bessel function of the first kind. The dependence of the transducer response upon the ratio of the transducer diameter to the sound wavelength is termed the aperture effect. The power transmitted to the transducer depends upon the acoustic impedance of the material and the transducer.

For a longitudinal wave the power transmission coefficient for a normal incident is (67);

$$P_1 = \frac{4 \rho_1 C_1 \rho_2 C_2}{(\rho_1 C_1 + \rho_2 C_2)^2} \qquad 5.18$$

Where $\rho_1 C_1$ and $\rho_2 C_2$ are acoustic impedance of the first and second medium respectively. Assuming that medium one is steel and medium two PZT5 then;

$\rho_1 C_1 = 46.8 X 10^6$ Kg/m^2S

$\rho_2 C_2 = 28 X 10^6$ Kg/m^2S

$P_1 = 0.94$

This means that 94% of the acoustic power will be transmitted into the

transducer (assuming a perfect bond).

The output voltage of a transducer depends on the type of transducer and its construction. Air backed transducers are more sensitive than backed transducers, but this is at the expense of narrow bandwidth. Kino (116) has shown that the response of an air backed transducer falls off at low frequencies and at low frequencies there is no net applied strain.

Another transducer widely used in acoustic emission is the capacitative transducer. Although capacitative transducers have sensitivities of two orders of magnitude less than PZT transducers, they have a much wider bandwidth (up to 30 MHz). In principal capacitative transducers consist of a polished disc of area A suspended over the surface of a test piece Fig 5.21. Typically this distance is in the order of a few micrometers. The capacitance of such a transducer is :

$$C = \frac{Q}{V} = \frac{A \varepsilon_o}{l} \qquad 5.19$$

Where Q is the charge, V is the operating voltage and ε_0 is the permittivity of the free space. For this transducer the voltage change for a given displacement is given by

$$dV = \frac{dQ}{C} = - \frac{dl}{l} = - E\, dl \qquad 5.20$$

Where E is the electric field in the transducer. For example, for a potential of 50 volts and a separation of 5 micrometers, a displacement of the order of 1 picometers will produce an output voltage of 10 micro-volts. A PZT5 transducer produces the same output voltages for only a displacement of the order of 6 femtometers (chapter 4). However a

capacitative transducer has the advantage that its output is directly proportional to the displacement and is independent of frequency. Fig 5.22 shows the response of a capacitative transducer and a commercially available piezoelectric transducer to the same step function of force. The responses are completely different. Also optical systems for detection of acoustic emission signals have been developed (115). Fig 5.24 shows the waveforms from the fracture of a glass capillary detected by an optical and a piezoelectric transducer (115). From these results and those of Hsu et al (113) it is clear that piezoelectric transducers are unsuitable for AE source characterization. However capacitative and optical laser methods are capable of detecting surface displacements.

Although capacitative and optical transducers are more suitable for source characterization, piezoelectric trasnducers are the most widely used in AE testing. This is partly due to the fact that in acoustic emission it is important to maximize the signal to noise ratio. Therefore it is advantageous to use a piezoelectric transducer, since output voltage is much higher for the same surface displacement. Other factors in favour of PZT transducers include their relative cheapness and ease of operation. If capacitative transducers are employed, after a few tests the suspending element must be repolished and the adjustment of the air gap is very difficult.

5.6 Signal processing of acoustic emission

Signal processing of acoustic emission requires highly specialised equipment. One of the major problems in signal processing is the very wide dynamic range of AE signals, whose displacement amplitude may fall in the

range of 10^{-15} to 10^{-9} meters. Another important and difficult problem is the large variation in the rate of generation of acoustic emission signals. In some cases emissions are generated at such a high rate that they can overlap in time.

Several methods have been developed to analyise AE signals. The most common ways in which signals have been processed are ;

1- Frequency analysis

2- Energy analysis

3- Ring down and event counting

4- Amplitude analysis

5.6.1 Frequency analysis

Frequency analysis of acoustic emission signals may provide information about source rise time and fracture type . As has been discussed, for frequency analysis either capacitative or laser optical transducers must be used. Furthermore only high energy AE events may be detected and processed, and it might be necessary to use a special sample geometry like that of Scruby et al (101). Mullin and Mehan (117) applied frequency analysis to carbon and boron reinforced epoxy composite materials. They studied acoustic emission signals photographed from an oscilloscope screen and claimed that different frequencies were associated with different failure processes in the composite (e.g. fibre fracture). Their results must be viewed with scepticism because they did not carry out their test rigorously. For a rigorous frequency analysis it is essential to use a computerized pattern recognition technique. This would eliminate any biased judgement of the eye. This is especially important since acoustic emission

events are transient signals.

In a brief review of the signal processing of acoustic emission, Stone and Dingwall (109) have quoted Curtis, who suggested that in nearly all practical situations, the acoustic pulse loses its identity if it is of sufficient duration and bandwidth to stimulate some of the natural modes of vibration of the system. However Graham and Alers (118) claimed that for A533-B low alloy steel, they were able to detect different spectra at different stages of the test. Graham and Alers(118) related the low frequecy emission with crack extension and the high frequency emission with plastic deformation.

5.6.2 Energy analysis

The acoustic emission energy is assumed to be proportional to the integral of the output voltage of the transducer. Usually the signal is squared and then the area under the curve of voltage squared against time is measured. This area is proportional to the signal energy. However it is difficult to relate this energy to the actual acoustic wave energy. Curtis(119) pointed out that two of the most important problems associated with this relation are the uncertainty in the mode of transducer operation and partial detection of the acoustic wave due to its bandwidth limitation . The uncertainty in the mode of transducer operation is only relevant to the piezoelectric transducers where the response of the transducer may be velocity, displacement or accelaration sensitive.

Another method of energy measurement is the root mean square (RMS) voltage, which is related to the rate of energy emission. Scruby et al (101)

suggested that the use of RMS voltage is advantagous, because firstly it gives a continuous measurement and secondly it does not need any threshold level.

5.6.3 Ring-down and event counting

This is the simplest method for analysing acoustic emission signals. In this technique the signal amplitude is compared with a threshold voltage. Counting the number of times the signal amplitude exceeds the threshold level gives the cumulative ring down count. A more useful way of analysing the result of ring down counting is the rate mode (rate of ring-down counts). The rate mode can be more informative because the ring down counting does not give any information about the signal energy or amplitude. However the shape of an AE pulse is usually a damped sinusoid, whose more counts will be generated from pulses of higher amplitude and this is more evident in the rate mode (Fig 5.24). Because of the simplicity of this method, there is fast circuitry available for ring-down counting.

A more sophisticated method of analysing acoustic emission signals is event counting. This technique was developed with the hope of a one to one correspondence between microfailure events and each AE burst. One event is defined as a threshold crossing or a group of threshold crossings which are separated from the next threshold crossing or group of threshold crossings by a minimum fixed period called "dead time" Fig 5.24.. Pollock (111) has given an empirical relationship between the number of ring down counts and an event;

$$N = \frac{f_r}{\dot{\alpha}} \operatorname{Ln} \frac{V_0}{V_t} \qquad 5.21$$

Where f_r is the resonant frequency of the transducer, α the logarithmic decrement, V_0 the initial voltage and V_t the threshold voltage.

5.6.4 Amplitude distribution analysis

In this technique the amplitudes of the voltage of the signals from a piezoelectric transducer are plotted as distributions. Using currently available AE equipment with piezoelectric sensors, the most hopeful method for finding information about the specific character of source events is the amplitude sorting technique (120). Other techniques (e.g. frequency analysis) offer little hope of understanding the source mechanism (120). With the use of amplitude distribution analysis it is possible to examine individual emissions in more detail. Hill and Stephens (121) have shown that the output of a resonant transducer with a square band pass is dependent on the stress pulse width as well as on the amplitude of the stress pulse. Their model was based on an ideal situation where the input pulse was also a perfect square, but it still shows that the maximum output voltage is dependent on the maximum amplitude of the stress pulse.

Various amplitude models have been suggested to describe the distribution of peak amplitudes . Pollock (111) used a function $f(v)/f(v_t)$ which defines the fraction of the emission population whose peak amplitude exceeds a voltage level V. The relationship between f(v) and v is given by

$$\frac{f(V)}{f(V_t)} = \left(\frac{V}{V_t}\right)^{-b} \qquad 5.22$$

where V is the threshold voltage and b is an exponent. A plot of Log f(v)

versus Log v frequently approximates to a straight line, and is known as the power law model . Also the Log-cumulative presentation of amplitude distribution is sometimes called a "b plot".

A low value of b usually means that a higher proportion of AE events were of high amplitude and, conversely, a high value of b often corresponds with a large number of low amplitude signals. Because of some of the short comings of the power law model, other workers developed different models and methods for analysing amplitude distributions. Pollock (122) has reviewed some of these models.

5.7 Acoustic emission behaviour of more complex systems

Up to this point the discussion of acoustic emission behaviour has centred on relatively simple and well characterized materials. It has been shown that despite considerable progress, the mechanism of acoustic emission generation is still not fully understood. However this has not discouraged others from the study of the acoustic emission behaviour of complex systems and materials. These studies range from the monitoring of AE activity from a military bridge (123) and a GRP plant (124) to coupon tests on high performance composites (125). Significantly some of these attempts have been very successful, for example there is now commercially available AE equipment which can supervise spot welding (126) and (127) have produced a code of practice for the proof testing of large GRP pressure vessels. In the field of composite materials especially, acoustic emission has been extensively used to study the mechanism of damage accumulation (128, 129). Dickson et al (125) were able to detect the transverse ply cracking and longitudinal splitting in glass/epoxy (0/90) laminates. They also found

that environmental treatment of these composites had a significant effect on the acoustic emission behaviour .

Fuwa et al (130) found that the "Kaiser Effect" does not hold in composites. They observed that in composite, on reloading, the emission start before the previous maximum load was reached. This effect has become known as the "Felicity " effect. A more useful derivation of this effect is known as the Felicity ratio which is the ratio of the stress level at which the emissions starts on reloading, to the previous maximum stress level. This ratio has been used as an index of damage accumulation within the material.

5.8 Calibration of transducers

Acoustic emission experiments are usually performed using uncalibrated transducers. However it is beneficial to use calibrated transducers. If calibrated transducers are used, it is more probable that a direct comparison between the results of different experimenters can be made. Other benefits gained from using a calibrated transducer include; the potential ability to compare results with theoretical calculations, the ability to select a sensor appropriate for a specific application and the ability to detect any malfunction of the sensor. Even if calibrated transducers are used, care must be taken because in calibrating a transducer certain assumption have to be made, which may not hold in a specific situation. Sachse and Hsu (131) have described the assumptions commonly made. The first assumption is that the pressure of the sensor does not significantly change the mechanical field vector quantities (i.e. force per unit area, particle velocity) near the sensor. This assumption

can be fulfilled by using non-contacting transducers (e.g. a capacitative transducer). The second assumption is that the transducer is only sensitive to the stress wave of a single mode i.e. only longitudinal or shear waves. The third assumption is that the transduction process is linear. The forth assumption is that the excitation was fixed. The fifth assumption is that the calibration medium is fixed.

Between various methods devised for transducer calibration, the comparison method is more suitable for acoustic emission transducers. Other methods of transducer calibration are either difficult to perform (132) or they do not cover the whole range of signals encountered in AE testing. Moghisi and Squire (133) used a simple but direct method for calibrating PZT5 transducers. They were able to relate the output voltage to the force applied to the surface of the transducer. Their method may be suitable for the range where large amplitude signals are detected.

In the comparison method the output of the transducer under calibration is compared with the output of a standard sensor (e.g. 5 MHz quartz transducer).

Hsu and Breckenridge (132) used a step function source in their calibration method. They chose the condition of their experiment in such a way that they could compare their result with the theoretical calculation. Hsu and Breckenridge (132) used the experimental set up shown in Fig 5.25. A glass capillary of 0.2 mm diameter was placed on the test block, and was broken by tightening a screw. The step force released was measured by a load cell and was displayed on the storage oscilloscope. The surface displacement caused by the step force was measured at symmetrical points by two transducers with both the capacitive reference transducer and the transducer under calibration. The transducer outputs were digitized and stored in a computer for later analysis. Since the response of the

capacitative transducer is in good agreement with the theoretical calculation, it can be used as the standard and compared to the response of the transducer under calibration.

Another comparative method for calibrating AE transducers is by using a helium gas jet. McBride and Hutchison (134) were the first to use this technique. In this technique the frequency spectrum of a helium jet on a steel block is detected by a quartz crystal. The quartz crystal acts as the standard transducer. Next the quartz crystal is replaced by the transducer to be calibrated and similar measurement is made. The calibration of the transducer is then defined as the ratio of the output of the quartz crystal to that of the tra∩$ducer under calibration at all frequencies. Hsu and Berckenridge (132) argued that the capillary method has the following advantages:

1- It employs a known mechanical impulse as the source.

2- There is a theory for relating input force to displacement at the sensor.

3- It employs a true displacement sensor.

4- Both the magnitude spectrum and the phase spectrum of the sensor can be calculated.

5.9 System calibration

The transducer calibration alone can not guarantee that the result of an acoustic emission test can be produced by other experimenters. All transducer calibration guarantees is that the transducer for a known input AE pulse under specific conditions will produce a known output voltage. Perhaps system calibration is more useful for guaranteeing reproduceable

results, where any system mulfunction or change of conditions can be detected. For system calibration a similar approach to that of transducer calibration has been attempted. The simplest technique for creating a standard input is the breaking of a modified mechanical pencil lead as patented by Hsu (135). The modification consists of mounting the pencil on a stand to allow the generation of both vertical and horizontal components in the stress pulse. By restricting the lead used to a single manufacturer Hsu (135) was able to generate reproduceable signals. According to Hsu the advantages of the pencil acoustic emission simulators are: realistic stress wave generation, simplicity, ruggedness, portability, convenience of use and inexpensiveness. The main disadvantage of this technique is that the stress pulse amplitude is some three orders of magnitude above the minimum level of detectable displacement of most commercially available AE equipment.

Other workers have devised different methods of generating AE pulses. Scruby et al (136) used a short duration laser pulse which was applied to the surface of a test piece. The advantages of this technique are the fact that the stress pulse generated is the result of a dipole force, and is similar to the stresses around a crack tip or dislocation loop (136). Other benefits of this technique pointed out by Scruby et al (136) are that it is non contacting, and the energy transferred into the test piece can be quantitatively controlled.

Chapter 6

Experimental techniques

6. Introduction

This chapter covers the experimental details of sample preparation and the ultrasonic and acoustic emission testing of sprayed coatings. In this study the coating variables investigated were the lack of adhesion between coating and substrate, and the effect of process parameters during coating preparation. For these investigations three groups of samples were prepared. The first group of samples were prepared under optimum conditions (recommended practice), samples of the second group contained artificially introduced adhesion defects and the third group of samples were prepared with one of the process variables differing from that of the recommended practice.

6.1 Sample preparation

6.1.1 Plasma spraying equipment

Plasma spraying was performed using a Metco 3M system. Nitrogen and hydrogen were used as primary and secondary gases respectively. The substrates were held on an asbestos plate mounted on a trolley beneath the spray gun which was traversed by a pneumatic/hydraulic ram. The spray range was adjusted by raising and lowering the asbestos plate mounted on the trolley.

6.1.2 Materials

6.1.2.1 Powders

For plasma spraying, four different powders were used. These were aluminium (Metco 54), alumina (Metco 105), molybdenum (Metco 63) and self fusing molybdenum (Metco 505) powders. The chemical compositions and other relevant properties of these powders are given in table 6.1 .

6.1.2.2 Substrates

Two types of substrate materials were used: mild steel and heat treated high carbon steel (EN42). The materials used and the sample dimensions are given in table 6.2 . Mild steel substrates were used for the study of the adhesion defects. Heat treated spring steel (EN42) substrates were used to prepare samples with various process parameters. It was important to ensure that the substrates did not deform during the bending test, because it was desirable to study the resultant damage using ultrasonic C-scanning. Thus EN42 steel was selected since, after heat-treatment, it exhibits high strain levels in the elastic region during 4 point bending. The EN42 substrates were quenched in water from a temperature of 910^{0} C and then tempered at 350^{0} C for a period of half an hour.

6.1.3 Spraying procedure

All substrates were preheated to a temperature of 100^{0}C in a furnace prior to spraying, as it was previously found that optimum adhesion was obtained in this way.

The control samples were sprayed under the recommended condition given by Metco Ltd. It was only possible to introduce artificial adhesion defects in aluminium and alumina coatings. It was found that by masking part of the surface of the substrate prior to grit blasting, it was possible to introduce an adhesion defect in aluminium coatings. However introducing adhesion defects in alumina coatings was difficult and it was impossible to produce coatings of molybdenum or self-fusing molybdenum with a known artificial adhesion defect. Various methods of introducing adhesion defects into these materials were used. It was found that, for alumina coatings, by masking a region of the surface of the substrate prior to grit blasting and spraying in the absence of coolant air, it was possible to obtain coatings with adhesion defects.

It is believed that small deviations from the correct spraying parameters can produce coatings with significantly inferior properties(7,16,17,18,29). This situation may arise either due to equipment failure or lack of attention on the part of the operator. To study the effect of process variables on the acoustic properties of plasma sprayed coatings, four groups of samples of each coating material were produced. The details of the process variables for each of these groups is given in table 6.3 . After surface preparation, spraying was carried out using both good and bad practices. Examples of the latter are low plasma power, poor surface preparation or overheating of the sample during spraying. This should have produced coatings with a variety of bond integrities and microstructures. Plate 6.1 shows several of the sprayed samples.

6.2 Ultrasonic testing of plasma sprayed coatings

Ultrasonic studies of plasma sprayed coatings were carried out using the transmission pulse echo technique. This work was carried out with the intention of extending the preliminary findings of R.L.Cox (57) on ultrasonic testing of plasma sprayed coatings. Thus a computer controlled ultrasonic C-scan system was constructed. The block diagram of the apparatus used is shown in Fig 6.1 , and a detailed description of this system follows.

6.2.1 Coupling medium

High-frequency ultrasound is usually used in material testing (of the order of MHz). Sound waves with such high frequencies do not propagate well in air, so some means of coupling the ultrasound generated by the transducer to the sample is essential. The two most commonly used coupling techniques are the direct contact method and the immersion technique. In the direct contact method the transducer is attached to the surface of the sample using either glue or coupling grease. This technique is suitable for applications where smooth flat surface are in easy reach, and when scanning of the sample is not required. The immersion technique is perhaps not as efficient as the direct contact method, but it is very versatile and suitable for scanning more complex shapes and rough surfaces. Because of these advantages, the immersion technique was used. Of the many possible coupling liquids, water is the most practicable , due to its transparency, cheapness and ease of handling. To avoid corrosion of the test rig and samples, 0.1 wt% NaBTA was added as inhibiters.

6.2.2 Ultrasonic test rig

6.2.2.1 Signal generation and detection

A block diagram of the ultrasonic test rig is shown in Fig 6.1 . A Matec model 6600 pulsed oscillator and receiver unit, with a plug in unit No. 750 was used to generate and receive ultrasonic waves. The pulsed modulator unit of the Matec responds to a trigger pulse by activating the pulsed oscillator to produce a radio frequency electrical pulse of a preset frequency in the range of 1 - 20 MHz. The amplitude and pulse width are variable; typically a pulse width of 1 microsecond and a peak voltage of 100 volts was used. The electrical pulse was used to excite the transmitting transducer, a focussed PZT5 transducer, which converted the signal to ultrasonic waves. An identical transducer was used to receive the ultrasonic signal after it had passed through the sample. The received signal was amplified by 50 dB and displayed on the oscilloscope screen. An inhouse built pulse generator which produced 5 volt TTL pulses with a repetition frequency of up to 1000 Hz was used to trigger all the units in the system, so that they were synchronised. A linear gate, Brookdeal model 9415 was used to measure the height of the required peak on the output signal from the Matec unit. The output voltage of a linear gate was proportional to the amplitude of the gated signal. The gate was operated by a Brookdeal model 9425 scan delay generator. The maximum allowed input voltage to the linear gate was 1 volt. The amplitude of the drive pulse on the Matec unit was many times larger than this limit. To remove the drive pulse, the output from the Matec was passed through a signal gate unit . The gated signal was passed to the linear gate and also fed into one channel of a two channel oscilloscope (Gould model OS3300B). The signal from the scan delay generator to the linear gate was fed into the other channel to show the position of the gate. A schematic diagram of signals on

the oscilloscope screen is shown in Fig 6.2 .

6.2.2.2 Measurement system

Pairs of focussed lead zirconate titanate transducers, operating at 2.5, 5. or 10. MHz were used to generate and receive the ultrasonic beam. The transducers were mounted on an optical bench on specially designed transducer holders, enabling accurate and quick alignment of the transducers. The translational movements of transducers were attained by use of optical bench stands. The correct position and alignment of the transducers were assessed from the height of the required echo on the oscilloscope screen or from the output of the box-car monitored by the commodore 3032 microcomputer.

The detected signal contains a series of echoes decreasing in amplitude as a function of time or echo number Fig 6.2 . With the aid of box-car the relevant echo can be monitored. The output of the box-car is an analogue voltage (0 - 10 Volts) proportional to the amplitude of the echo. An 8-bit analogue to digital converter (RSZN427E) was used to convert the output of the box-car to a digital form. The output of the ADC was interfaced to the parallel user port of the commodore 3032 micro-computer. The ADC was interfaced to the parallel user port in the free-running mode. In this mode after each conversion, which takes about 1.25 miliseconds, the ADC starts a new conversion. However the new conversion cycle does not effect the previous result which was latched at the output port. The negative going edge of the busy line on the ADC output was used to strobe the CA1 line on the parallel user port which automatically latches the data on port B of the 6522 PIA. This would ensure that valid data is always collected by the

Commodore 3032. A more detailed description of the interfacing and the operation of the ADC is given elsewhere(137). The latched data on the 6522 PIA port was available to the programme for processing.

6.2.2.3 Scanning system

The samples were mounted on a suitable holder Fig 6.3 in the water-tank and their movement in the horizontal and vertical axes was controlled with two stepping motors. The main advantages of the stepping motors over servo systems are that the stepping motor can be used in an open loop system without the need for feedback, and the position of the object is always known from the number of pulses applied to its coils.

For small size samples it is advantageous to scan the sample and keep the transducer stationary. This simplifies the scanning system and reduces the problem of misalignment of the transducers. If large objects have to be scanned, then it is more practical to keep the object stationary and scan the transducers.

A schematic diagram of the scanning system used is shown if Fig 6.3 . Two Astrosyn stepping motors (20 PM - A001) were used to scan the sample in X and Y direction. The stepping motors were controlled by the Commodore 3032 micro-computer, via the IEEE488 port. The amount of power required to drive a stepping motor is usually much higher than a micro-computer can provide, so it is necessary to control a stepping motor via driver circuits. The Astrosyn 20 PM - A001 motor used in this work, is a three phase stepping motor with a 15^{0} step angle. The armatures were connected directly to the cross-slide lead screws which were machined with a pitch of about 1mm. A

full rotation of the lead screw was necessary to move the test piece from one scan position to the next. The one millimeter scan steps are of the order of the wave length of ultrasound used and the spot size at the focal point of the transducer. Therefore the resolution of the system was 1 mm.

6.2.2.4 Data collection and image processing

The data latched at the user port was transferred into a temporary array at suitable times. Five consecutive readings of the amplitude of the signal transmitted through the sample were made, after a small pause, following each movement of the test piece. The average of these five consecutive readings was assigned to a variable which was dependent on the sample position. For each test one thousand data points were collected, corresponding to one thousand scan positions (40 mm X 25 mm). It was advantageous to store the actual data for future processing. After completion of a scan, the data was transferred and stored on a commercial audio tape.

The acoustic images of the samples were produced in syncronism with the mechanical scan. Seven graphic characters were used to produce the C-scan image of the samples. Each of these characters represented a range of signal amplitude levels (attenuation) in the dB scale. Following each movement of the test piece, during a C-scan a graphics character was displayed at the corresponding point on the micro-computer screen. An example of a C-scan image produced from a typical sample is shown in chapter 7 .

One of the main advantages of a computerised C-scan system is its ability

to store, reprocess and redisplay the image in a relatively short time from the large amounts of data collected during scanning. In many cases the reprocessing and redisplaying of data can provide useful information. By altering the attenuation ranges that the various characters represent it is possible to emphasise a particular feature in the image (e.g. enhance an adhesion defect) and suppress the display of the other unwanted details (e.g. thickness variation).

6.2.2.5 Signal calibration

The amplitude of the signal transmitted through the sample was always compared to the signal level transmitted through the water. An Alan Industries Inc Model 50 TA42-10 attenuator was used to calibrate the signal attenuation. One of the options of the C-scan programme allowed the continuous monitoring of the amplitude of the signal and also displayed its value on the monitor screen. The calibration of the signal level in a dB scale was carried out by increasing the signal attenuation in steps of one dB and reading the ADC value from the monitor's screen.

Although the calibration of the signal level was in a dB scale, the data collected during a C-scan was always kept in the form of the ADC numbers and was only converted to the dB scale prior to image processing.

6.3 Acoustic emission testing of plasma sprayed coatings

In this section a detailed description of the techniques used for AE testing of plasma sprayed coatings is given, and to discuss the basic

principles of the operation of AE analysers.

All acoustic emission testing was carried out on spray coated steel strips 240 mm X 25 mm X 3 mm loaded in four-point bending such that the coating was in tension. An Instron-1195 testing machine was used for loading the specimens. Three different acoustic emission analysers were used: these AE sorters were an Acoustic Emission Technology Corporation Model 203 (AETC-203) amplitude distribution unit, an Acoustic Emission Technology Ltd Model 105 (AETL-105) stress wave analyser and a Physical Acoustic Corporation Model 3400 (PAC-3400) four channel acoustic emission analyser unit. A detailed description of these units will be given in the following sections.

In this work more attention has been paid to the analysis of the amplitude distribution and ring-down counting than other AE parameters (e.g. energy etc). However these other AE parameters were also studied to a lesser extent. These parameters include the energy, duration and frequency of AE events.

A block diagram of the acoustic emission system used is shown in Fig 6.4 . In each test the load applied to the specimen along with extension, time and acoustic emission data were collected. Although the AETC-203 and AETL-105 both have adequate data collection rates, they lack the storage capacity and analytical power. To overcome these shortcomings, the AETC-203 was interfaced with a Digital Equipment Corporation (MINC-11/03) mini-computer and the AETL-105 was interfaced to a Commodore 3032 micro-computer. The PAC-3400 has a built in dedicated micro-computer. In all these systems data was collected sequentially and in chronological order, written to a floppy disc or to an audio tape. The main features of these

acoustic emission systems are explained in more detail below.

6.3.1 The transducers

In acoustic emission testing transducers are normally attached to the surface of the structure under test. The acoustic coupling of the transducer to the surface of the test object is achieved with a thin layer of grease.

Most commercial AE transducers make use of a PZT sensitive element. In this work two types of transducers, broad band and resonant were used. A FAC-500 broad band transducer was used in conjunction with the AETC-203 amplitude sorter. The FAC-500 transducer has a reasonably flat response up tp 2 MHz, with a nominal resonant frequency of 500 KHz. Broad band transducers are particularly suitable for event counting because the ringing of the transducer dies down in a short time. Therefore with broad band transducers much higher data rates can be achieved.

A Dunegan/Endevco model D140B resonant transducer with a resonant frquency of about 200 KHz was used in conjunction with the AETL-105, while a PAC resonant transducer was used with the PAC-3400 system. The use of resonant transducers is particularly suitable for small signals and also if energy considerations are important.

6.3.2. The preamplifiers

Since the electrical signal generated by the crystal is very low in power, it is necessary to mount an amplifier very close to the sensor.

Preamplifiers allow the signal to be transmitted over long cables while maintaining a high signal to noise ratio. Because most instruments further amplify the signal during processing, this initial amplifier is called the preamplifier. Preamplifiers typically provide 40 - 60 dB gain.

The AETC-203 had a preamplifier with a fixed gain of 60 dB and a bandpass filter with a frequency band of 150 KHz to 1MHz. The AETL-105 had a preamplifier with a gain of 40 dB and a bandpass filter (100 KHz - 300 KHz). The preamplifier of the PAC-3400 had a selectable gain of 40 or 60 dB, with a 10 KHz - 300 KHz bandpass filter.

6.3.3 Signal processing of acoustic emission

Acoustic emission signal processing depends to a very large degree on the type of instrument used. The three AE analysers used in this study, each processes the AE signals somewhat differently.

6.3.3.1 Amplitude distribution using the AETC-203

The AETC model 203 is an AE event and amplitude sorter unit. An AE event in this unit is defined in terms of the instrument threshold, which is adjustable, and a fixed "dead time" of 100 microseconds. If the "dead time" has elapsed since the last threshold crossing, the next threshold crossing is the begining of a new event (Fig 5.24). Therefore in the AETC-203 one AE event is at least 100 microsecond apart from the next oncoming event.

The AETC-203 has a sorting range of 60 dB and 51 channels. Channels 0 - 49

have a width of about 1.2 dB. Table 6.4 gives the exact value of the width of each channel. Channel 0 has a threshold of 10 milli-volts and channel 50 a threshold of 10 volts. These voltage levels correspond to 10 micro-volt and 10 milli-volt at the transducer respectivly. It was observed that in most cases the first four channels were susceptible to background noise. These channels were excluded using the front panel 10-turn threshold adjust potentiometer, making the effective counting threshold 17.38 milli-volt.

The AETC-203 has an oscilloscope type display which can display the events in two modes; a histogram plot showing the number of events in each channel, or a cumulative plot summing all events with amplitudes above a given channel. The histogram display mode limits the count rate to around 300 events per second. This is due to 4 milliseconds needed for data transfer. In the cumulative mode the transfer time is less than 100 microseconds, so the cumulative mode in this work was used. The count rate achieved in this mode is derived from the events duration and the 100 microsecond dead time. In cumulative mode an event rate of about 2000 events per second was achieved. In some applications the limited rate of event counting an AE instrument may prove to be a handicap.

The data collection and storage capacity of the AETC-203 imposed serious limitations for post data analysis. A further limitation is that each channel resets to zero when its event count exceeds 1023. To overcome these limitations and also enhance the capacity of AE data analysis, the AETC-203 was interfaced to a Digital Equipment Corporation mini computer MINC-11/03.

The data for each event was transferred from the AETC-203 to the MINC-11 as a six bit digital word, designating the channel number. The data was intercepted before it entered the memory of the AETC-203 and the memory

ready signal was used to strobe the MINC-11 digital input module to read the data.

6.3.3.2 Real time data collection software on MINC-11

The MINC-11 is a Digital Equipment Corporation mini computer with an LSI-11/03 processor designed for experimentation. It is designed to allow for the addition of MINC modules for data processing. In this study three MINC modules were used. A clock module (MNCKW / M7953) was used to generate an accurate timing signal. A digital input module (MNCD / M5915) was used to interface the AETC unit through six data lines and one strobe line. The analogue data (load, extension etc) was fed into MINC-11 through the analogue input module (MNCAD / AD13). The analogue input module was set to accept 0 to 5 volt signals. The software which controls these modules and collects the data is called DCOL5 and was written in assembly language (Macro-11) to utilize the maximum capacity of the system.

After envoking the DCOL5 programme and after the initialisations are complete, data is collected and stored upon interrupts from either the analogue or digital input devices. The data is first stored in one of the two 7 K byte buffers. When a buffer fills a flag is set and the programme will write the data to a floppy disk. The process of transferring the data to disk is the slow step in the recording, but by using the double buffering technique this process is considerably improved. The data is stored in chronological order. The AE event is stored in one byte, and its value is the amplitude channel number, which is always less than 60. The analogue data is stored in three bytes. The first byte holds the analogue marker and the channel number. The value of this byte is the channel number

plus 128 (analogue marker). The second and third bytes of the analogue data are the low byte and high byte of the analogue data.

A supporting Fortran code called "calib" was always used to check the zero and full scale levels of the inputs to the analogue module prior to each test. It was found that the MINC-11 was not suitable for data analysis. Hence all data files were transferred through a modem to a main frame PRIME-750 computer at Rutherford Appleton Laboratories, using the PRIME's file transfer system (FTP).

6.3.3.3 Data analysis software

A block diagram of the software modules used and their interaction with the binary data file (***.BIA) is shown in Fig 6.5 . The aim of this software package was to present data such that it may assist in the interpretation of the acoustic emission results. A detailed description of these programmes and their operation along with a listing of the source code is given elsewhere (138). Also table 6.5 gives the various options available on this package.

The user first inputs all test parameters (e.g. Time interval, number of analogue input channels used, etc) and some analysis options (e.g. load levels for histogram plotting etc). Then these parameters and options are stored in six files, called ZERLEV.FIL, AXI.HIS, AXI.COT, AXI.STR, AXI.LOD and PEN.SET. The advantage of storing these items of information is that it avoids the laborious and time consuming task of inputting them all each time the programme is run. In this way it was only necessary to alter the file which was different for a particular test. The programme then proceeds

to produce plot module files and the required plots on a Watanabe (WX4636-UM-152) Plotter. The inhouse Watanabe plotter was interfaced to the PRIME-750 computer through a CIFER (1886) micro-computer. Examples of these plots will be given in chapter 7. However a brief description of these plots is given below.

6.3.3.4 Load vs time and stress vs strain graphs

The load versus time graph was generally plotted as the first stage of analysis, because comparison of this with the load-time trace recorded on the Instron-1195 showed up any major faults that may have occured in the data collection.

When an extensometer was used it was possible to produce plots of stress versus extension or strain. The load and stress were on the Y axis and the user has three choices for the type of axis required. These were default, maximum or a pre set level. If the default option was selected, the nearest round number to the maximum was selected as the highest value of that axis.

6.3.3.5 Histogram plotting

Histograms showing the number of events in each channel at any load level could be drawn. For each test up to twelve histograms at different load levels could be produced. Also it was possible to produce histograms for any portion of the test. Using a separate histogram plotting routine, it was possible to produce all the above mentioned information in a three dimensional histogram.

6.3.3.6 b-plots

Although histogram distribution plots are informative, for mathematical analysis, it is preferable to have the cumulative distribution plot. It is found that the cumulative distribution plots in a log-log axis often approximate to a straight line(111). In this way the distribution can be represented by a single parameter (the slope of the line). This is known as the power law model or "b" plot.

one of the options of this software package produces the "b" plots for each histogram distribution.

6.3.3.7 Event counting

A representation of the evolution of the AE events versus time, load or stress can be produced by using this option. This option produces two graphs of cumulative events and the event rate plus five curves for groups of pre determined channels. The abscissa for these graphs can be time, load, stress, extension or strain. The same three options for axis scaling are avialable for these plots.

6.3.3.8 Percentage share graphs

This option was found to be a very useful method of normalizing the event counting graphs. Here the same type of graphs as the event counting could be produced, but with the events at any time normalized as a percentage of

the total number of events at that time.

6.3.3.9 Statistical treatments of the amplitude distribution

For acoustic emission applications it would be useful to be able to group similar samples by one or more parameters and distinguish them from samples not belonging to that group. This is especially the case for the amplitude distributions due to the large amount of information present in each histogram. Various methods for presenting each histogram with a specific parameter have been used. The power law model ("b" plots) as mentioned in the previous section is one of these techniques. However, as will be shown later (chapter 8) these methods are insensitive to small changes in the materials characteristics and their AE amplitude distribution.

A chi-squared programme for the analysis of the amplitude distributions has been developed by the composite group in the School of Materials Science at Bath University. This programme allows analysis of up to eight samples, either at a specific load level or up to twelve load levels. The final result of each test was produced in a tabular form and in their ranking order.

The chi-squared test is particularly suitable for analysing the AE amplitude distribution. It allows for the examination of a number of distributions and determines whether or not they belong to the same group. The development of chi-squared analysis and part of its programming is given by Phillips et al(139). The value of chi-squared is a measure of the deviation between observed and expected frequencies. Large values of chi-squared indicate a greater difference between the samples. A detailed

description of the software used and the basics of the chi-squared test method is given (138).

6.3.4 Ring-down counting

Ring-down counting is the simplest form of acoustic emission signal processing. In this method the amplitude of the signal is compared with a preset threshold level and each time the threshold is crossed the comparator outputs a pulse. These pulses are counted by a conventional counter which can give either the cumulative or the rate of ring-down counts (Fig 5.24). Because of the relative simplicity of the circuits required for this task, very fast circuitry is available for this purpose.

Ring-down counting was carried out using an AETL-105 stress wave emission processor. The AETL-105 is a single channel analyser. The output of this unit is displayed on a 3-digit display and an analogue signal proportional to the number of ring-down counts is provided. The analogue output of the AETL-105 was fed to an ADC (analogue to digital converter) which was interfaced to a commodore 3032 micro-computer. The acoustic emission signal along with the output of the Instron-1195 (usually load) were monitored by a Commodore 3032 micro-computer. The recorded data was stored in a commercially available audio tape for post analysis. The post analysis of the data was also carried out using the Commodore 3032 micro-computer.

The software on the Commodore 3032 allowed for the production of graphs of cumulative ringdown counting versus time, load or strain. Also it was possible to produce graphs of the rate of ringdown counts versus the above mentioned parameters. A source listing of the software used and the details

of the interfacing is given elsewhere (140).

6.3.5 PAC-3400 four channel analyser

The PAC-3400 is a four channel acoustic emission analyser. It is a self-contained unit with a dedicated Z80 based micro-computer, which is used for data collection and post analysis of the data. This unit has four independent channels, which can be used to monitor four tests simultaneously. In location mode all four channels are used to locate the source of an event. In this work the PAC-3400 was only used in single channel mode.

For each AE pulse the PAC-3400 provides the following information:

1- Peak amplitude

2- Event count

3- Ring-down count

4- Energy

5- Rise time

6- Duration

In this work the PAC-3400 was used to study some of these parameters which the AETC or AETL did not process. The PAC-3400 was used in conjunction with a PAC pre-amplifier and a PAC resonant transducer.

6.4 Metallographic observation

For metallographic obsevation the samples were cut using a diamond saw. To minimize the risk of inducing damage , the samples were embedded in a plasticised resin prior to cutting. The polishing and etching of the

samples were carried out using conventional techniques. The structure and integrity of the coatings were examined using optical and electron microscopes.

Chapter 7

Results and discussion

7 Results and discussion

7.1 Resolution of the ultrasonic C-scan system

Acoustic images of a 1 mm wide rubber strip and a metal gauze were produced to investigate the resolution of the ultrasonic C-scan system. Fig 7.1 shows the acoustic image of the one millimeter wide rubber band. The rubberband was held in the vertical position. Fig 7.1 was produced using a pair of 2.5 MHz transducers. As can be seen the over-all picture of the rubber band is clear. However the edge definition is not exact, due mainly to the vibration in the scanning system and the edge effect. The ultrasonic picture was produced by scanning the sample in a raster fashion. The scanning system was described earlier in chapter 6. The movement of the sample was usually accompanied by vibration. To reduce the amount of vibration during scanning the horizontal lead screw was partially clamped. Although this considerably reduced the vibration, it did not stop it completely. The final vibration of the sample was quite small and only affected the acoustic image at the edges of the sample where any small changes in the position could significantly alter the acoustic image. This edge effect is mainly due to the fact that part of the sample is out of the path of the ultrasonic beam and the vibration of the sample exaggerates this effect.

Fig 7.2 shows the acoustic image of a metal gauze made of 1 mm diameter wire. The image was produced using a pair of 10 MHz transducers. As can be seen the image is not exact and some of the wires are not clearly defined. This is especially the case for the horizontal wires. The reason for this is as follows; the diameter of the wires was about 1 mm which is

approximately equal to the ultrasonic wave length used in steel at 10 MHz , and also the focal spot size of the transducers. The focal point of the transducers was adjusted to be at the centre of the vertical wires, but because of the woven structure of the gauze the horizontal wires were not exactly at the focal point. This meant that the ultrasonic beam was wider than 1 mm and as a result some of the ultrasound could have travelled through water without being intercepted by the wires. The ultrasound travelling through the water arrived approximately 0.4 microseconds later than that which had passed through the 1 mm wire. This 0.4 microsecond delay was less than half of the gate width usually used in this work, therefore the two echoes were not properly resolved in time. Fig 7.3 shows a schematic representation of the echoes. Where part of the echo travelled straight through the water, it would have arrived at the transducer at approximately the same time as the signal through the sample. Therefore the output of the box-car integrator was proportional to the summation of the two echoes, resulting in a modified acoustic image. The amount of attenuation through the metal gauze was small, in Fig 7.2 the total attenuation is less than 0.2 dB. The values shown in Fig 7.2 are the actual ADC numbers which are proportional to the signal level.

Although the acoustic images shown in Figs 7.1 and 7.2 are not exact, it is clear that the resolution of the ultrasonic C-scan system was about 1 mm, even at 2.5 MHz. Also it is fair to conclude that if the thickness of the samples was large enough to produce the necessary time delay to separate the echo which travelled through the sample from that through water, it would be possible to produce an exact image of the sample. Another conclusion which can be drawn from these results is that it is much easier to produce an acoustic image of an object with high attenuation (e.g. a rubber band in comparison with a metal gauze).

7.2 Ultrasonic studies of plasma sprayed coatings

7.2.1 Thickness measurements

Fig 7.4a shows an acoustic image of a molybdenum coating (Mo63) on a mild steel substrate. The coating thickness variation was between 0.36 mm to 0.44 mm, as shown in Fig 7.4a. It is quite clear that the attenuation through the coating corresponds well with the thickness variation. This conclusion was confirmed by subsquent grinding of the coating to obtain a uniform thickness of about 0.3 mm. The acoustic image of this sample after grinding showed a uniform attenuation across the sample as shown in Fig 7.4b.

The images, Fig 7.4a&b , were produced using a 10 MHz ultrasound. The ultrasonic attenuation per unit thickness for the coating shown in Fig 7.4a is given in table 7.1 . In these calculations a 10 dB attenuation due to the mismatch between the water and molybdenum is taken into account. As can be seen from table 7.1 the attenuation per unit thickness of this coating is about 1200 dB/cm. This value is of the same order as those of Cox et al(81). A better estimate of the attenuation can be made from differential thickness and attenuation measurements. As can be seen from Fig 7.4a a thickness variation of the order of 0.02 mm corresponds to a 2 dB loss. Therefore the attenuation per unit thickness is about 1000 dB/cm. This is a better estimate of the attenuation per unit thickness, because the absolute thickness measurements of the coating is less accurate than the differential one. This is mainly due to the fact that in these calculations it was assumed that the substrate thickness was 3 mm (as received thickness), while after surface preparation the substrate thickness is usually reduced. For the same reason the attenuation per unit thickness

calculated from Fig 7.4b is also higher (1233 dB/cm). This value is of the same order as those calculated from Fig 7.4a, which confirm the suggestion about the inaccuracy of the absolute thickness measurements. It is noteworthy that in these calculations it was assumed that the attenuation through the coating substrate interface and also the steel substrate was negligible.

Fig 7.5 shows an acoustic image of a Mo63 coating produced at 5 MHz. The Thickness variation of this coating was between 0.29 and 0.35 mm as shown in Fig 7.5. The calculated results for the attenuation per unit thickness at 5 MHz for this coating is given in table 7.1 . These values are somewhat less than those reported by Cox et al(81). Their result for the attenuation per unit thickness at 5 MHz was about 700 - 1000 dB/cm. However, the attenuation per unit thickness calculated from the differential thickness and attenuation is closer to their results (670 dB/cm). As can be seen in Fig 7.5 a thickness variation of about 0.03 mm corresponds to a 2 dB loss.

Fig 7.6 shows an acoustic image of a Mo63 coating using 2.5 MHz transducers. The thickness variation of this coating was between 0.26 mm and 0.3 mm. The calculated attenuation per unit thickness of this coating is given in table 7.1 . In comparison with Cox et al's(81) results these values are somewhat higher. Here a 2 dB attenuation corresponds with 0.04 mm thickness change.

It is quite clear from these results that the attenuation through molybdenum coatings (Mo63) is frequency dependent and the 10 MHz ultrasound is more sensitive to thickness variation. Another important point is that the sound energy loss through these coatings is of the order of several hundred dB/cm, which has no resemblence to the acoustic properties of

wrought metals. Therefore it is of considerable interest to understand the mechanism(s) of sound transmision through plasma sprayed coatings.

7.2.2 Possible mechanisms of sound transmission through plasma sprayed coatings

The sensitivity of the ultrasonic attenuation to coating thickness variations is a direct consequence of the microstructure of the plasma sprayed coatings. Inclusions, oxides, cracks and voids are the inherent part of such microstructures (23).

Between various attenuation mechanisms, the most important and dominant in plasma sprayed coatings appear to be losses due to the presence of cracks and voids. Other attenuation mechanisms are of less importance. For example the attenuation loss due to the grain scattering for the case where the mean grain size (D) is much smaller than the ultrasonic wave length ($D<<\lambda$) is proportional to D^3f^4. A smaller grain size will result in less attenuation. This has been shown by many experimenters (141). The grain size in plasma sprayed coatings is in the sub-micron region (23). Plate 7.1 shows the microstructure of a molybdenum coating and it is possible to see the very fine columnar grain structure in each sprayed layer. The attenuation due to grain size at around 10 MHz frequency range for most metals is less than 10 dB/cm (141). Comparison of this figure and those of sprayed coatings clearly shows that the grain scattering can not account for the losses in sprayed coatings. Other loss mechanisms such as attenuation due to inclusions can not be very significant either, because inclusions in sprayed coatings have similar dimensions to the grain size.

In an attempt to investigate the thermal and ultrasonic wave attenuation in

plasma sprayed coatings, Patel and Almond (63) modelled plasma sprayed coatings using the three layer system shown in Fig 7.7 . In this model the sprayed layers (lamellae) are separated by an air gap of about 0.1 micrometers. Patel and Almond (63) calculation from this model showed an ultrasonic attenuation in excess of 10000 dB/cm. The results of their calculation is at least one order of magnitude larger than the actual experimental values. Patel and Almond (63) attributed the difference between the experimental results and their calculation to the simplified model of the sprayed coatings used, where the effect of contact points was ignored.

Plasma sprayed coatings have a layered structure and elongated pores and cracks running between layers are a feature of their structure. In reasonably good quality coatings these cracks are usually less than 50 micrometers long. Plate 7.2 shows a typical shrinkage crack in an alumina coating, which is about 30 micrometers long. Plates 7.1 and 7.3 show the interlamella cracks in Mo63 and Mo505 coatings. The cracks shown in these two plates are amongst the longest and worst kind observed in these coatings. Plate 7.4 shows a lower magnification of the microstructure of the Mo505 coating, confirming that the cracks shown in Plates 7.1 and 7.3 were of the worst kind (longest). The majority of these cracks are less than 50 micrometers long. Therefore a more realistic model of plasma sprayed coatings should have contact points between lamellae with parallel cracks of no more than 50 micrometers. This would mean that a 1 mm ultrasound beam is about 20 times larger than these cracks, and the presence of these cracks would only partially effect the ultrasonic beam. However the wave propagation and attenuation model given by Patel and Almond (63) is useful, because it shows that the sound transmitted through a 0.1 micrometers crack is very small (60 dB loss), which is the direct

result of the large reflection coefficient of the solid/air interface.

A general review of the mechanisms of sound propagation through a thin gap has been presented in chapter 4. Szilard (75) suggested that the sound propagation was due to the non linear behaviour of the air trapped in the thin gap. In very thin gaps (sub-micron) where the mean free path of the air molecules is about the width of the gap, the trapped gas behaves like a two-dimensional gas. Therefore the number of collisions of the air molecules with the gap walls are much more than with each other. Szilard (75) argued that during compression the density of the gas will rise and so will its temperature. As a result sound velocity in the gas will increase along with its the wavelength. In the compression half period the increasing , c and ρ will improve the Rayleigh transmission. Szilard's postulated mechanism for ultrasonic wave propagation through a thin gap was based on Tarnoczy (77) and his own experimental results for the attenuation of sound wave through a small gap. However, there is no evidence to support his claims, especially as far as the non-linear effect is concerned. In fact Gustafson (76) unsuccessfully attempted to measure the harmonics of the sound wave which is expected to be associated with such non-linear effect. Clark and Chaskelis (142) calculated the energy transmitted across an air gap whose thickness is of the order of the mean free path of the gas molecules in the gap. The maximum energy transmitted corresponds to a monoatomic gas is given by

$$\frac{I_t}{I_i} \ll \frac{\rho_g C_g}{\rho C} \left(\frac{m}{m_g}\right) \qquad 7.1$$

where I_t is the transmitted acoustic intensity and I_i is the incident

acoustic intensity. $\rho_g C_g$ and ρ C are the density and acoustic wave velocity in the gas and the solid respectively, m is the mass of a solid molecule and m_g is the mass of a gas molecule. The value of the right hand side of the equation 7.1 for a glass walled gap, filled with air, is about 10^{-3}. This shows that effectively no sound is transmitted through a thin gap. Another important point about Szilard's suggestion is that even if his postulated mechanism was correct, it would not have been of any practical use in material testing, using methods such as pulse echo technique, where the receiver transducer and the electronics (e.g. amplifiers, filters etc) are tuned to a specific frequency.

In sprayed coatings there are two mechanisms by which ultrasound can travel through the coatings. As has been pointed out in chapter 4, the most likely mechanism of sound propagation in plasma sprayed coatings is through contact points. The second mechanism is due to the resonance vibration of the lamellae in the coatings.

Clark and Chackelis's (142) experimental results are good evidence for the suggestion that the contact points between lamellae are the major factor in the transmission of sound waves through sprayed coatings. Clark and Chaskelis (142) showed that even the residue from cleaning agents (which they used to clean The glass discs) can form microbridges between the gap walls. They have also shown that the number and the area covered by these microbridges depends on the width of the gap. Decreasing the gap thickness resulted in increasing the number of the microbridges. The presence of these microbridges alters the transmission and reflection of sound through the thin gap. Although Tarnoczy (77) and Szilard (75) were not able to detect gap separation of less than 100 nm, Clark and Chaskelis (142) were able to detect a gap separation of about 20 nm for very clean discs. From

this discussion it is clear that the presence of contact points in a thin gap significantly alters its acoustic properties.

It is possible to show that the presence of contact points alone can not account for all of the sound energy transmission through the sprayed coatings. A simple calculation from the experimental results shows that for a three layer coating (similar to that of Patel and Almond (63) model), the actual attenuation is about 0.5 to 1 dB. Assuming an attenuation of 500 dB/cm for the coating model shown in Fig 7.7, the attenuation for the three layer model will be 0.5 dB.

Fig 7.8 shows a schematic diagram of two layers of a plasma sprayed coating. The thickness of each lamella is 5 micrometers with areas where there is no contact between the two lamellae. Clark and Chaskelis (142) have suggested that the reflection coefficient for a gap with some contact point, to a first approximation is;

$$\alpha_t = (A/A_0)^2 \qquad 7.2$$

where A_0 is the total insonified area and A is the portion of the insonified area which is acoustically opaque. Based on Clark and Chaskelis's suggestion, the transmission coefficient to a first approximation would be;

$$\alpha_t = \left(\frac{A_0 - A}{A_0} \right)^2 \qquad 7.3$$

For the purpose of the model under discussion here the transmission coefficient calculated from equation 7.3 is satisfactory. For example equation 7.3 gives good values for the boundary conditions. For the case of no contact between the two lamellae, $A=A_0$ the transmission coefficient is zero and total reflection occurs. When the two lamellae are in good contact

A=0 and α_t=1 and total transmission occurs. In the dB scale, the attenuation in terms of the transmission coefficient is given by(67).

$$dB = 10 \text{ LOG } (I_t/I_i) = 10 \text{ Log } (1/\alpha_t) \qquad 7.4$$

Table 7.2 gives the calculated ultrasonic attenuation for the model shown in Fig 7.8, using five different contact ratios (90%, 80%, 75%, 50%, 25% good contact). Even for the case of $A=0.2A_0$, the attenuation is about 2 to 4 times more than the experimental values. From the micrographs of the sprayed coatings it is possible to conclude that the total area of good contact is generally less than 80% . McPherson (143) in his model of the thermal conductivity of the plasma sprayed ceramic coatings, assumed that the total area of no contact was about 20 percent. Therefore it is possible to conclude that the presence of the contact points alone can not account for the total sound transmitted through the coatings.

In the ultrasonic pulse echo technique a pulse width of a few microseconds is usually used. In this work a pulse width of about 1 microsecond was used. A simple calculation shows that an ultrasonic pulse of about 1 microsecond in a solid with a sound velocity of 5000 m/s , covers a distance of 5 mm . The time taken for the sound wave to travel through a lamella of 10 micrometer thick is about 2 X 10^{-9} seconds. Therefore during the transmission of a 1 microsecond wide pulse through a sprayed coating, a part of the acoustic wave can bounce back and forward in a lamella approximately 500 times. This means that for a lamella , a 1 microsecond acoustic pulse looks like a continuous wave, so the condition in a lamella is such that resonance can easily occur. A lamella can behave like a highly reverberating medium. Because the thickness of a lamella is very small (e.g. 10 micrometer) therefore the attenuation within a lamella is negligible, also the solid air boundary reflects a large part of the acoustic energy

back inside the lamella. The result is a forced vibration of the lamella. The actual displacement of the vibrating lamellae can be comparable with the gap thickness, which enables the direct energy transfer from one lamella to the next. Although there is no evidence (apart from the fact that sound travels in sprayed coatings) to support this claim. It is possible to show that;

1) the vibration of a lamella in sprayed coating is very similar to a vibrating thin flat plate fixed round the edges.

2) the fundamental frequency of many of these lamellae are around 2 to 10 MHz (test frequencies used).

3) The maximum deflection of some of the vibrating lamellae are comparable to the gaps present in sprayed coatings.

A detailed description of the mechanism of formation of plasma sprayed coatings was presented in chapter 2. It was pointed out that as the molten droplets impinging on the substrate surface or the previously solidified material, they flatten to form lenticular shape lamellae as shown in Fig 2.5 . Also it is fair to assume that the lamellae which have no contact with their immediate neighbours, have a good degree of adhesion near their edges. Although it is not possible to generalize the exact shape of these lamellae or the position of the interlamella separation, the assumptions made here are reasonable. At least for the case of the model presented here these assumptions are satisfactory, since the actual mechanism of ultrasonic wave propagation is in question, and the exact calculation of the sound attenuation is not of paramount interest.

The study of the vibration of a circular plate fixed round the edges in simple harmonic motion is a classical problem in acoustics. Stumpf (144) has shown that the allowed values of the frequency is given by the equation

$$f_{p,q} = 0.9342 \left(\frac{h}{2R^2}\right)\sqrt{\frac{E}{\rho(1-\nu^2)}} \qquad p=0,\ q=1 \qquad 7.5$$

where f is the frequency, h is the plate thickness, R is the radius of the plate, E is the Young's modulus, ρ is the density, ν is the Poission's ratio, p and q are subscripts indicating the nodal patterns. Fig 7.9 shows the shape of the normal modes of vibration of the circular plate. The relationship between the frequency of these nodes and the fundamental frequency of the plate is given below.

$$f_{11}=2.091f_{01} \quad , \quad f_{21}=3.426f_{01} \quad , \quad f_{02}=3.909f_{01}$$

Equation 7.5 was used to calculate the fundamental frequency of the vibrating lamellae. The results of these calculations for three lamella sizes of 125, 100 and 50 micrometer of aluminium, alumina, molybdenum and steel is given in table 7.3 . In table 7.3 the calculated results for the frequency of the other three modes of vibration shown in Fig 7.9 are also included. In all these calculations it was assumed that the thickness of the lamellae was 10 micrometer. As can be seen from table 7.3 the frequencies obtained for lamellae of Al, Mo and steel are very similar. The relatively large differences of the vibrating frequencies between the alumina lamellae and the other three metal lamellae is due to the difference between their Poission's ratios. From the equation 7.5 it is possible to see that the lamellae with a radius of 25 micrometer or less can vibrate in the frequency range of 2.5 to 10 MHz provided that their thickness is less than 10 micrometers.

An estimate of the magnitude of the deflection of a vibrating lamella can be made from the condition of resonance. The maximum deflection of a lamella depends on its Q factor, which is a measure of the sharpness of the resonance. The Q factor depends on the amount of energy trapped in a

lamella. To calculate the Q factor of a lamella it is necessary to know the energy transmitted into the lamella and the amount of energy reflected back and forward in the lamella. The acoustic wave generated by the transducer must pass through two boundaries (PZT & water, water & coating) before entering into the lamella. The acoustic intensity produced by the transducer is given by (67);

$$I = \frac{1}{2} \rho C \omega^2 A^2 \qquad 7.6$$

Where I is the sound intensity, ρ and C are the density and sound speed in PZT5, ω is the angular frequency ($2\pi f$) and A is the vibration amplitude (displacement at the transducer surface). The displacement at the surface of the transducer is given by (64);

$$A = d_{33} V \qquad 7.7$$

Where d_{33} is the piezoelectric modulus for thickness oscillation and V is the applied voltage. The d_{33} for PZT5 is about 150×10^{-12} m/V (64) and the applied voltage to the transducer was around 100 volts. The displacement produced at the surface of the PZT5 transducer for this voltage is 1.5×10^{-8} meters. The acoustic intensity I associated with such a displacement for PZT5 transducer at 10 MHz is 13.3×10^{6} W/m^2. The acoustic intensity I_{water} transmitted to water from the PZT5 transducer is 2.4×10^{6} W/m^2. Similarly the acoustic intensity transmitted from water to coating I_{steel} is 2.9×10^{5} W/m^2. The displacement associated with this sound intensity in steel is 1.77×10^{-9} m. The sound beam reflects back and forward in the lamella and the displacement associated with the second reflection in this lamella is 1.66×10^{-9} m. The Q factor is given by (64);

$$Q = \frac{\pi}{\delta}$$

Where

$$\delta = \mathrm{Ln}\,(A_0/A_1)$$

A_0 and A_1 are two consecutive displacement amplitudes. The Q factor for the above lamella is about 49. The deflection of the lamella at resonance is Q times the static displacement and this is calculated to be 0.09 micrometers. This is comparable with the interlamella separations present in sprayed coatings. Therefore it is quite possible for the vibrating lamellae to transmit acoustic energy to their neighbours. Table 7.4 gives the deflections of the lamellae for four different materials at three frequencies 2.5, 5 and 10 MHz. As can be seen the deflection of the lamellae at all these frequencies and for different materials are similar (about 0.09 micrometers).

The mechanism of sound transmission described here does not explain the frequency dependent of the attenuation. The frequency dependence of the attenuation can be clearly seen from Figs 7.4, 7.5 and 7.6 and table 7.1 .

The frequency dependence of the ultrasonic attenuation of plasma sprayed coatings can also be explained using the sound transmission model through a thin gap. Using Patel and Almond (63) model it is possible to calculate the attenuation for various gap separations at different frequencies, and it can be shown that the sound attenuation through a thin gap increases with frequency. This is similar to the sound transmission through a gap shown in Figs 4.7 & 4.8 . It can be seen that for very large gaps the sound transmission is virtually zero (total reflection) and is independent of frequency. Also when the gap separation tends to zero total sound transmission occurs, which is also independent of frequency. However, between these two extremes there is a region where strong frequency dependence can be seen.

7.2.3 Ultrasonic detection of the adhesion defects

It was noted in chapter 6 that Mo63 and Mo505 coatings with artificially introduced adhesion defects could not readily be produced. However, aluminium coatings with adhesion defects could be produced relatively easily. In this case it was only necessary to mask a part of the substrate surface during grit blasting. The masked area was sufficiently smooth to prevent the mechanical interlocking of the sprayed aluminium with the substrate surface. For alumina coating, the masking of the substrate alone was not sufficient to introduce adhesion defects, and it was found to be necessary to induce thermal stresses in the coating also.

Fig 7.10 shows an acoustic image of an aluminium coating which had an artificially introduced line defect. The defect was 3 mm wide strip across the substrate surface. The position and the extent of the line defect is quite clear from the acoustic image. The image also exhibits other features of the coating. The variation of the attenuation is mainly due to the porosity and the thickness variation of the coating.

The effect of porosity and other features of the coating (e.g. thickness variation) may be eliminated by image enhancement facilities which a micro-computer can provide. Using a micro computer it is possible to store the actual data either as attenuation or as representative ADC numbers. The data can be subsequently reprocessed and redisplayed using alternative character designations. An example of the way selective redisplay can be used to enhance an image is shown in Fig 7.11 . The images were generated using the data obtained from the defect sample which was shown in Fig 7.10.

By altering the attenuation ranges that the various characters represent it can be seen that the displayed sensitivity to small local variations can be reduced and the image of the defect emphasised.

Fig 7.12 shows an acoustic image of an alumina coating. The image was produced using 10 MHz ultrasound. The masked area during grit blasting was a square shape of 2 cm X 1.5 cm . The position and the extent of the debonded area is quite clear. Significantly no bonding between the substrate and coating exists at the masked region, and there is a one to one correspondance between the intended defective region and the acoustic image. As can be seen from the Fig 7.12a the attenuation corresponds well with the thickness changes across the coating. An enhanced image of this picture is shown in Fig 7.12b, where the effect of thickness variation is suppressed. At the bottom left corner of Fig 7.12b a cluster of higher attenuation points can be seen. This region most probably had exess porosity, since no thickness changes could be measured.

In order to produce a control sample with some delamination and adhesion defects, a steel strip coated with alumina was deformed in four point bending. The subsequent ultrasonic C-scan image revealed some damage in the area just under the inner rollers. Fig 7.13a shows the acoustic image of this sample before the bend test, produced by 2.5 MHz ultrasound. As can be seen the coating is fairly uniform and the small thickness variation of the coating is clearly visible. Fig 7.13b shows the acoustic image of the coating after bend test. This image was produced using 2.5 MHz ultrasound. As can be seen the extent of the damage is clealy shown. From these results it can be concluded that the ultrasonic pulse echo technique can be used to detect adhesion defects in sprayed coatings. This is made possible by the high reflection coefficient for the solid air boundary. It is also clear

that the gaps present in defective regions are much larger than the interlamella cracks in the coating.

7.2.4 Effect of process parameters on acoustic properties of plasma sprayed coatings

The aim of this part of the work was to investigate the effect of process parameters on the ultrasonic attenuation of plasma sprayed coatings . The coatings were applied to steel strips , 240 mm X 25 mm X 3 mm. As indicated in plate 6.1 which shows several of the samples, only the central sections (about 80 mm long) were actually coated. Four groups of coatings were prepared. These were standard, low power, poor surface preparation and also without cooling. Also ultrasonic C-scans were carried out on 40 samples supplied by Phillips of Eindhoven. These tests will also be discussed.

7.2.4.1 Ultrasonic C-scan results of alumina control coatings

Fig 7.14 shows a typical C-scan image of an alumina coating. This sample was prepared according to Metco's recommended procedures and process parameters. The details of the process variables are given in table 6.3.

The thickness variation across the coating was about 0.1 mm. The effect of thickness variation on ultrasonic attenuation is clearly shown in the Fig 7.14 . The coating thickness near the bottom edge was 0.5 mm and the attenuation was between 39 - 40 dB. At the top edge where the coating thickness was around 0.4 mm the attenuation was less than 33 dB. Thus the attenuation per unit thickness of this coating calculated from the C-scan image is about 630 to 720 dB/cm. However, the attenuation per unit

thickness calculated from the difference in attenuation and thickness across the coating gives a value of about 640 ± 100 dB/cm. The calculated results of the attenuation per unit thickness for all of the control alumina coatings studied are given in table 7.5. The mean attenuation per unit thickness as shown in table 7.5 is about 610 dB/cm and the scatter of the results within two standard deviation is about 100 dB/cm.

7.2.4.2 Effect of poor surface preparation on ultrasonic attenuation of alumina coatings

Fig 7.15 shows a typical C-scan image of an alumina coating sprayed on a steel substrate. The surface of the substrate was grit blasted using worn grit. Other process parameters used were those shown in table 6.3. The attenuation per unit thickness of this coating calculated from the difference in thickness and attenuation was 720 ± 130 dB/cm. The calculated results of the attenuation per unit thickness for the alumina samples with poor surface preparation is given in table 7.5. It is possible to see from these results that ultrasonic C-scanning can not reliably differentiate between these samples and the control ones.

7.2.4.3 Effect of low input power on the ultrasonic attenuation of alumina coatings

Fig 7.16 shows a typical C-scan image of an alumina coating prepared with 20 percent less input power than the recommended practice. The process parameters used for the preparation of these coatings are given in table 6.3. This sample had a fairly uniform coating. The thickness of the coating

was generally 0.55 mm although near one edge it fell to 0.475 mm. The ultrasonic attenuation in most part of the coating was about 620 dB/cm. The attenuation per unit thickness calculated from the difference in thickness and attenuation across the coating was about 620 ± 80 dB/cm. The calculated results of the attenuation per unit thickness of these coatings are also given in table 7.5. The average values of the attenuation per unit thickness of these coatings were generally lower than the control samples, but the difference was well within the scatter band of two standard deviation.

7.2.4.4 Effect of absence of cooling during spraying on the ultrasonic attenuation of alumina coatings

Fig 7.17 shows a typical C-scan image of a thermally stressed alumina coating . The attenuation per unit thickness of this coating was about 710 ± 120 dB/cm. The values of the attenuation per unit thickness for these coatings are also shown in table 7.5. Although the mean attenuation per unit thickness of these coatings was somewhat larger than that of the control samples, the difference is less than the scatter in the results (two standard deviation).

A graphical presentation of the attenuation per unit thickness of an alumina coating (poor surface preparation) is shown in Fig 7.18 . The abcsissa of this graph shows the thickness of the coating from which the attenuation has been calculated. The mean attenuation per unit thickness is 660 dB/cm and the scatter band (one standard deviation) is about 45 dB/cm.

Each point on this graph is an average attenuation calculated from an area of 16 mm X 6 mm.

From these results it is possible to conclude that ultrasonic C-scanning is not sensitive to the effect of the process variables reported here. This conclusion is also true for the other three materials studied, thus only a few of the typical C-scans of these materials will be discussed.

7.2.4.5 Ultrasonic C-scan results of Mo63 coatings

Fig 7.19 shows a typical C-scan image of a Mo63 coating. This sample was prepared according to Metco's recommended procedures. The coating thickness near the top edge was 0.15 mm and near the bottom edge was 0.125 mm. The attenuation per unit thickness of this coating calculated from the difference of the thickness and attenuation was 1000 $\pm$ 80 dB/cm. The calculated attenuation for the Mo63 coatings studied are given in table 7.6.

Fig 7.20 shows a typical C-scan image of a molybdenum coating prepared using 20 percent less input power than the recommended practice. The attenuation per unit thickness of this coating is 920 $\pm$ 50 dB/cm. As can be seen from these figures and the attenuation results given in table 7.6, in general the average attenuation per unit thickness of low power coatings is somewhat less than that of the control samples, however the difference is not significantly higher than the scatter in the results. Also the thermally stressed coatings showed somewhat higher attenuation than the control samples, while it appears that surface preparation did not have any effect on the attenuation per unit thickness of Mo63 coatings. As can be seen because of the relatively large scatter in attenuation per unit

thickness, ultrasonic C-scanning technique is not readily capable of differentiating between these coatings.

7.2.4.6 Ultrasonic C-scan results of Mo505 coatings

Fig 7.21 shows a typical C-scan image of a Mo505 coating (control sample). The coating thickness of this sample in most areas was 0.225 mm. The attenuation per unit thickness of this coating was 820 ± 50 dB/cm. The calculated results of the attenuation per unit thickness of Mo505 coatings are given in table 7.7 . As can be seen the attenuation per unit thickness of Mo505 coatings are considerably lower than that of Mo63 .

Effect of the other process parameters studied were similar to those observed from Mo63 coatings. However, as can be seen from tables 7.6 and 7.7, Mo505 coatings showed less attenuation than the Mo63 coatings. The most likely reason for this is the presence of low melting point matrix in Mo505 coatings, as this is the main difference between these two coating materials. The effect of the low melting point matrix is the reduction in porosity, cracks and residual stresses in these coatings. This has been shown by many experimenters (147,148).

7.2.4.7 Ultrasonic C-scan results of aluminium coatings

Fig 7.22a shows a C-scan image of an aluminium control sample. The thickness of this coating at the central region was 0.425 mm and 0.375 mm near the edges . The attenuation per unit thickness of this sample was 810 ± 250 dB/cm. As can be seen the scatter in attenuation per unit

thickness of this coating is much larger than those observed for the other three materials. This is believed to be due to the high porosity of aluminium coatings (57). As it has been shown that ultrasonic attenuation is sensitive to the porosity of the coatings (57,82).

The variability of the aluminium coatings were quite large. For example Fig 7.22b is an acoustic image of another aluminium control sample. As can be seen, although the thickness of this coating was between 0.475 mm and 0.525 mm, the attenuation through this sample was much less than that shown in Fig 7.22a . In fact the attenuation per unit thickness of this coating was 640 ± 180 dB/cm. From the comparison of Figs 7.22a and 7.22b it is quite clear that the former had much higher porosity.

The aluminium coatings prepared with other process parameters also showed similar results. Although the thickness variation and porosity in the coatings were easily detectable, it was not possible to differentiate between coatings prepared with different process variables.

7.2.4.8 Effect of embedded grit particles

The samples used in this part of the work were provided by Phillips of Eindhoven. The coatings were applied on aluminium substrates grit blasted using alumina grit. Different surface conditions were achieved by 1,2,3,4,6,8,10,12,14,16 passes of the grit blasting gun over the surface. For each of these conditions four identical samples were provided. The thickness of the coatings were 0.2 ± 0.025 mm. The C-scan images of these samples were produced using 2.5, 5 and 10 MHz ultrasound.

Fig 7.23 shows four typical C-scan images of the coatings. They were produced using 2.5 MHz ultrasound. The low attenuation bands on the left hand side of the C-scan images corresponds to part of the uncoated aluminium substrates. The total attenuation in most parts of the coatings was;

Fig 7.23a	sample 4X/1	15 to 16 dB
Fig 7.23b	sample 6X/3	16 to 17 dB
Fig 7.23c	sample 10X/4	16 to 17 dB
Fig 7.23d	sample 16X/3	15 to 16 dB

The sample identification number denotes the number of passes of the grit blasting gun over the substrate followed by the sample replicate number. The attenuation per unit thickness of the coating calculated from the differences in thickness and attenuation was about 400 dB/cm. The calculated values of the attenuation for these samples are given in table 7.8 . From these results it is clear that at 2.5 MHz there is no significant difference in the ultrasonic attenuation of these coatings.

The attenuation results at 5 and 10 MHz were somewhat similar to those at 2.5 MHz. Thus only two typical C-scan images at these frequencies will be discussed.

Fig 7.24 shows two typical C-scan images at 5 MHz. The attenuation at this frequency was between 19 to 21 dB. Also as is expected, the effects of thickness changes are more evident at 5 MHz. The attenuation results of these coatings at 5 MHz is given in table 7.9 . These results clearly show that the attenuation level at 5 MHz is insensitive to the level of grit blasting.

It was shown that 10 MHz ultrasound is more sensitive to the small features of the plasma sprayed coatings (section 7.2.1). However, even when 10 MHz

ultrasound was used, the effect of different levels of grit blasting on ultrasonic attenuation was below the detection limit. Fig 7.25 shows two typical C-scan images of these coatings using 10 MHz ultrasound. The attenuation through these samples varies between 26 and 32 dB, which is higher and the spread greater than at 2.5 and 5 MHz. Table 7.10 gives the measured attenuation of these coatings at 10 MHz.

7.3 Factors influencing the scatter in attenuation per unit thickness of plasma sprayed coatings

The large scatter in attenuation per unit thickness is mainly due to the microstructure of plasma sprayed coatings and also, to some extent, is influenced by the inaccuracy in the measurements. There are two possible sources of measurement inaccuracy, namely system stability and the errors associated with the thickness measurements. An estimation of the system stability (which is a measure of the accuracy of the attenuation measurements) was made by continuously monitoring the signal level through water for a period of four hours. The maximum signal fluctuation during this time period was less than 0.5 dB. At 10 MHz, this would account for a variation of about 1 to 2 percent of the total attenuation, for a typical sample in this study. The thickness measurements were made using a pin-micrometer at 16 mm intervals along the specimen length and 6 mm intervals along the width. It was assumed that the thickness variation between these points were linear. The attenuation per unit thickness of the coating at each new scan position (1 mm intervals) was calculated from the following relationship.

$$\text{Att.}_{\text{per unit thickness}} = \frac{\text{Att.}_{\text{measured}} - \text{Acouctic mismatch}}{\text{Thickness}}$$

The acoustic mismatch between water - coating, coating - substrate and substrate - water was calculated from their respective acoustic impedances as explained in section 4.3. The attenuation was measured at 1 mm intervals, however, the thickness of the coating at each point was calculated from a linear grid which was fitted on each of the squares (6 X 16 mm). In this way it was possible to make much better estimate of the coating thickness. The inaccuracies in thickness measurements can have profound effects on the calculated attenuation values. For example for a typical thin coating a 20 percent inaccuracy in thickness measurement, at 10 MHz can produce a scatter of up to ± 150 dB/cm.

Another major source of scatter in the attenuation results, is a direct consequence of the coating's microstructure. The wave propagation model discussed in section 7.2.2 showed that the discontinuities (e.g. interlamella cracks) are the main source of the high attenuation in plasma sprayed coatings. It is also well known and can be easily seen from the microstructure of the coatings that these interlamella cracks are randomly distributed in the coatings. Thus at each scan position different numbers of cracks, delaminations and pores are in the path of the acoustic wave, so an inherently large scatter in attenuation per unit thickness is to be expected.

7.4 Effect of the substrate's surface preparation on the adhesion and ultrasonic wave propagation

Probably the most important adverse result of poor surface preparation is the lack of bond integrity between substrate and coating. Since if good

adhesion between the coating and the substrate is to be obtained, then surface cleanliness is of the outmost importance followed closely by surface roughness. The degrees of cleanliness and surface roughness required, depends to a large extent on the coating material. For example, it was shown that surface roughness plays an important role in the adhesion of the aluminium coatings, and when part of the substrate's surface was masked during grit blasting, a region of poor bonding resulted (e.g. Fig 7.10). However, when alumina powders were sprayed, the degree of substrate surface roughness alone did not influence the adhesion of the coating and it was neccessary to introduce thermal stresses in the coating, (section 6.1.3), in order to produce defective adhesion. In fact the thermal stresses were sufficiently high to lift off the alumina coating from those regions of the substrate where the surface roughness was inadequate. Thus it is clear that for alumina coatings apart from the mechanical interlocking other bonding mechanisms are also present, while for aluminium coatings, it appears that mechanical interlocking is the dominant adhesion mechanism.

In section 6.1.3 it was pointed out that when Mo63 or Mo505 powders were sprayed, no coatings with any detectable adhesion defects could be produced. Various techniques thought to affect adhesion properties were tried unsuccessfully, and even when a trace of oil was left on the substrate surface, the adhesion between the substrate and the coating turned out to be satisfactory, and the only effect of the treatment was a reduction in coating thickness on the oil contaminated areas. This was also confirmed from the C-scan images produced. Thus, it is quite clear that in the case of Mo63 and Mo505 coatings, even surface cleanliness is not critical factor in obtaining good adhesion. This may be attributed to the nature of the bond between the molybdenum coatings and the steel substrate,

which has been shown to be of a metallurgical nature(52).

For adhesion defects larger than 2 mm X 2 mm, the wave propagation followed the geometric ultrasonic laws. As far as the ultrasound is concerned the debonded area acts like a large interlamella crack and a simplified model of the interface is similar to the model discussed for a three layer medium (section 7.2.2). Here the three mediums are the coating, air and the substrate. The sound energy transmitted through a thin gap is a function of the gap separation and the ultrasonic frequency used (see Figs 4.7 and 4.8). For a particular frequency the sound energy transmitted decreases as the gap separation increases. This clearly demonstrates that if the ultrasonic C-scan is to be able to distinguish between the bond imperfections and the interlamella cracks or other small features of the coatings, the gap separation has to be considerably larger than that of the interlamella cracks. Interlamella cracks are randomly distributed in the coating. In a 0.5 mm thick Mo63 coating, there may be as many as 100 lamellae, with a random number of cracks, and each of these cracks contribute to the over all attenuation. Therefore it is important to note that the ultrasonic C-scan technique cannot detect bond imperfections when the separation between the coating and substrate is of the order of the interlamella cracks. This means that ultrasonic pulse echo technique cannot reliably give any information about the actual bond strength of plasma sprayed coatings, however it can detect the tightness of the coating substrate interface.

7.5 Effect of surface roughness and embedded grit particles on ultrasonic attenuation

Excessive grit blasting is not necessary for good surface preparation, since there is a limit to the amount of grit blasting required to give maximum values in the surface roughness and the density of anchoring points on the surface. However, another more obvious consequence of excessive grit blasting is that there is an increasing likelihood of grit particles becoming embedded in the substrate surface, which may cause local losses of bond integrity.

The results given in section 7.2.4.2 showed that the ultrasonic C-scan imaging technique could not distinguish between coatings sprayed on aluminium substrates that had different surface roughnesses nor could it detect the presence of the embedded grit particles. This was the case even when 10 MHz ultrasound was used. Further evidence of the lack of sensitivity of the ultrasonic C-scan technique to the surface roughness of the substrate was given in sections 7.2.4.5 and 7.2.4.6 . Where it was shown that at 10 MHz, no significant difference in attenuation levels of the control Mo63 and Mo505 coatings and those sprayed on the substrates with no surface preparation could be detected. The difference in the surface roughnesses of these substrates can be seen from plates 7.5 & 7.6.

The sound scattering from the surface roughness to a first approximation can be assumed to be similar to the grain scattering, and it was shown (section 4.3) that for most metals the attenuation due to the grain scattering is generally less than 10 dB/cm. Clearly this range of values is much smaller than even the scatter in attenuation per unit thickness found for sprayed coatings.

Further evidence of the lack of sensitivity of the ultrasonic C-scan technique in detecting embedded grit particles and debris on the surface of

the substrate was given in section 7.2.4.2 , where it was shown that there was no significant difference in the attenuation levels of the control alumina coatings and those whose substrates had been grit blasted using worn grit.

To explain these results it was necessary to examine the microstructure of the coatings, especially in the context of surface preparation and its effect on the interface.

Plate 7.5 shows the surface topography of a steel substrate (EN42) after grit blasting, which was carried out according to the recommended practice, using alumina grit. It can be seen in this plate that the surface of the substrate is clean and adequately roughened, and when viewed at higher magnification (as shown in plate 7.5b) there is still no sign of any debris or any particles embedded in the surface. However, when worn grit was used, the surface roughness remained relatively good, but the surface cleanliness was of a very poor standard, large numbers of embedded dirt particles could be seen on the surface as shown in plate 7.6 . When this specimen was viewed under a higher magnification (plate 7.6b), even more small size grit particles embedded in the surface could be seen. Most of these particles were in the order of one micrometer or less, however some were as large as 10 micrometers (plate 7.6a).

Although differences in surface preparation are very clear from the micrographs of the surface of the substrates, no appreciable differences between the coating-substrate interfaces could be detected. This is partly a result of the small size of these particles and may be partly a result of the grinding and polishing undergone by the specimens, which may have separated the embedded particles from the substrate leaving behind defects

which are indistinguishable from the porosity at the interface. Plate 7.7a shows a micrograph of an alumina coating prepared according to the recommended practice. The coating-substrate interface showed regions of both good and poor adhesion, with pores at the interface of typical length about 20 micrometers. Micrographs of the coatings with poor surface preparation had similar coating-substrate interfaces (e.g. plate 7.7b).

Although the embedded grit particles may cause a local loss of bond integrity, they do not significantly alter the acoustic properties of the interface because of their small size.

7.6 Effect of low power input on ultrasonic attenuation

The results presented in section 7.2.4 clearly show that ultrasonic C-scan imaging cannot detect any significant differences between the attenuation levels for the coatings sprayed using 20 percent less power and the control samples.

The optimum arc power will vary from powder to powder because the amount of heat required to melt a particle depends upon the properties of the material. It was also pointed out that the arc power will control the heat available in the arc such that, if the arc power is too low, particle melting will be incomplete, whereas if it is too high the particles will vaporize. The optimum arc power is usually based on the spraying efficiency rather than coating characteristics (39), since normally optimum spraying efficiencies produce the required coating characteristics. However, optimum spraying efficiency does not necessarily mean the best coating quality. Plate 7.4b shows a micrograph of a Mo505 coating, in which unmelted

molybdenum particles can be clearly seen (spherodized particles), and in which the bonding between these particles and their neighbouring lamellae is good. Comparing this sample (plate 7.4b) with control samples (e.g plate 7.1), it is clear that apart from the presence of a few unmelted molybdenum particles there is no appreciable difference between their microstructures. Similar results to these were found for the other materials.

Therefore although the C-scan imaging technique is sufficiently sensitive to be able to detect defects such as delaminations porosity etc, it was only to be expected that there was no change in attenuation levels in the case of these low power specimens, as there was no appreciable differences in their structures compared to those of controls.

7.7 Effect of no coolant dir during spraying on ultrasonic attenuation

It was shown in section 7.2.4 that ultrasonic C-scan imaging cannot detect any significant change in attenuation levels for the coatings sprayed in the absence of cooling air compared with those for the control coatings. When plasma spraying in the absence of cooling air the heat content of the droplets increase and consequently the amount of heat absorbed by the substrate also increases, leading to an increase in substrate temperature. Harris et al (145) have shown that higher heat contents of the molten droplets result in larger stress levels in the coatings, and in support of this, micrographic examination of the coatings in this study revealed that they were subjected to high tensile stresses especially near the coating-substrate interface, where a large number of cracks were present. Plate 7.8 is a typical micrograph of an alumina coating sprayed in the absence of cooling air which shows that most of the cracks are normal to the surface

of the substrate, suggesting the presence of high tensile stresses at the interface. However because most of these cracks, run almost parallel to the sound beam, they do not produce a significant alteration in the sound attenuation level through the coating.

Mo63 and Mo505 coatings sprayed in the absence of cooling air showed similar results. For example plate 7.9 shows a typical Mo63 coating micrograph in which the cracks resulting from the thermal stresses can be easily seen, especially near the interface.

7.8 Acoustic emission results and discussion

7.8.1 System calibration

System calibration was carried out using the lead pencil breaking technique (135). Prior to any AE test a three millimeter lead was broken on the top surface of the test piece at the mid point of the AE sensors and the AE activities were monitored. This was a useful way to check that the AE analyzers were operational and also gave some indication of the coupling between the transducers and the test piece.

Significantly, the AE activities generated from the lead pencil breaking were reproducable. Plate 7.10 shows a typical amplitude distribution (b-plot) of the AE activities recorded by the AETC-203. This picture was taken from the oscilloscope screen of the AETC-203. The low amplitude events were, most probably, due to the reflection of the sound wave from the boundary of the test piece. Plate 7.11 shows the AE signals recorded by the AETC-203 and AECL-105. A broad band transducer (FAC-500) was used in conjunction with the AETC-203 and a resonance transducer (Dunegan/Endevco D140B) was connected to the AECL-105 . As was expected the output of the broad band transducer was less influenced by the resonance frequency of the PZT element than that of the resonant sensor . The frequency analysis of these two signals show this clearly, plate 7.11 . The bottom trace is the frequency component of the signal from the resonant sensor and the top trace is that of the broad band transducer. Both these traces show a nominal resonance frequency of about 200 KHz.

Plate 7.12 shows the frequency response of the broad band and the resonant transducers. Although the broad band transducer displays a fairly flat

response up to frequencies about 2 MHz, there is a resonance peak about 250 KHz. The fundamental resonance frequency of the D140B transducer is also about 250 KHz. From these results it is clear that the prime frequency components of the AE signal are the resonance frequencies of the sensors and also that the broad band transducers are more suitable for event counting.

7.8.2 Acoustic emission activities of the steel substrates

All acoustic emission records were made while carring out 4 point bend tests on the specimens, such that the coatings were in tension. To establish the contribution of the noise generated by the substrate to the overall AE activities observed, some steel strips were tested in four point bending and the AE activities monitored. Fig 7.26a shows a load deflection curve obtained from a typical steel strip. The corresponding AE activities observed (ring-down counts) versus strain is shown in Fig 7.26b. The total number of ring-down counts monitored from this sample were five. As can be seen from Fig 7.26 all these AE activities were observed at very low load levels, and are believed to be due to the friction between the test piece and the rollers of the four point bend testing jig. This was typical of all the test pieces studied. Event counting also showed similar results and in all the cases studied, the total number of events was invariably less than 5.

7.8.3 Acoustic emission studies of alumina coatings

7.8.3.1 Ring-down counting

Fig 7.27 shows two typical curves of ring-down counts versus strain for alumina coatings (control samples). Generally these samples showed very few AE activities up to the .03 percent strain level (less than 200 counts). Between strain level of 0.03 and 0.06 the AE activities occured in short bursts and above 0.06 percent strain generally the AE rate increased in a steady manner. Although this behaviour was observed for most alumina control samples, in some cases these features were not very clear. Also there was a considerable variation in the total number of ring-down counts observed at any particular strain level, as illustrated in Fig 7.27. At a strain level of 0.06 percent Fig 7.27a shows 800 counts while Fig 7.27b shows 1500. This was mainly due to the thickness of the coatings. Thicker alumina coatings generally produced more AE events.

Fig 7.28 show two typical curves of ringdown counts versus strain for alumina coatings sprayed with 20 percent less input power than the recommended practice. These coatings generally produced very few AE events until about 0.04 percent strain levels. Above this strain level AE activities increased in short bursts. The AE activities of these coatings at any given strain level also showed large variations and were found to be sensitive to the coatings thickness. The total number of ring-down counts recorded was, again larger for thicker coatings.

Fig 7.29 shows two typical curves of ring-down counts against strain for alumina coatings sprayed with no coolant air. The AE activities from these coatings at strain levels up to about 0.02 percent were similar to those of the control samples. However, above this strain level the acoustic activities were much higher than those observed for the control samples.

For example at 0.06 percent strain level the total number of ring-down counts shown in Fig 7.29 is about 150000 while at the same strain level control samples produced no more than 7000 ring-down counts (see Figs 7.27 & 7.29). Although generally thicker coatings produced more acoustic emission, the variations in the total number of ring-down counts recorded was much higher than in the case of the control samples (Fig 7.29).

Fig 7.30 shows two typical curves of the ringdown counts versus strain for alumina coatings sprayed on substrates with poor surface preparation. Even at very low strain levels (e.g. 0.02 percent strain), some of these coatings produced many more counts than a typical control sample during the whole test. The variation in the AE activities of these coatings was much greater than that observed for the other three preparation methods studied.

Fig 7.31 gives a graphical representation of the total number of counts recorded up to 0.06 percent strain from all of the alumina coatings studied. Again it can be seen that in general thicker coatings produced more acoustic emissions and also that the low power coatings produced the smallest number of AE events. Whereas specimens with bad surface preparations and those which had been overheated produced a high AE count.

7.8.3.2 Event counting and amplitude distribution results

Fig 7.32a shows a load vs time graph obtained for 9 control alumina samples where, as can be seen, the maximum load applied was within the elastic limit of the substrate. The samples with the thicker coatings showed the smallest deflections at any particular load level. Dark areas between the curves in this figure represent the degree of scatter in the results. The

cumulative AE events versus time graph for these samples are shown in Fig 7.32b. The total number of events recorded during the tests varied between about 500 to 1000 events. As can be seen in Figs 7.32b & 7.27 the general evolution of the AE event curves were similar to that of the ring-down counts.

A typical plot of the event count and count rate in selected amplitude ranges for a control alumina sample is shown in Figs 7.32c and 7.32d. The amplitude ranges for each group were;

Group	Channels inclusive	Amplitude range (dB above 10 mV)
1	4 - 8	4.8 - 10.8
2	9 - 12	10.8 - 15.6
3	13 - 16	15.6 - 20.4
4	17 - 20	20.4 - 24
5	20 - 50	24 - 60

Fig 7.32c shows that the majority of events had amplitudes of between 4.8 to 10.8 dB above 10 milli-volt (channels 4 to 8). Also there were a small number of events with amplitudes above 24 dB (group 5). The high amplitude events were detected mainly at strain levels of above 0.05 percent. The event rate plot shows a gradual increase in the event rate with increasing strain level. It is also clear that the AE activities occured in short bursts. The maximum event rates were generally less than 20 events per second.

It was possible to produce histograms showing the amplitude distribution at any load level during the test. Usually for each test six histograms at load levels of 200, 400, 600, 800, 1000, 1200 Newtons were produced. Also, an additional histogram showing the amplitude distribution at the end of

each test was produced. Fig 7.33 shows seven amplitude distribution for 9 alumina control samples. It can be seen that up to a load level of 400 Newtons very few events were recorded and there are no events above channel 20. Fig 7.33 shows that the extent of scatter is much larger for low amplitude events.

A useful method of analysing the AE events and their amplitudes is illustrated in Fig 7.33h, showing the percentage share of events in the specified amplitude ranges (groups) during the test. At low strain levels (e.g. 0.02 percent strain) between 60 to 80 percent of the events had amplitudes of around 4.8 to 10.8 dB, and about 20 to 30 percent of the events were in the second group (10.8 to 15.6dB). The other three groups had less than 10 percent of the events. At high strain levels the scatter in the percentage share of events is much smaller and it can be seen that it tends to a single value. This effect is partly due to the method of analysis. The main limitation of this method is that at the low strain levels it is over sensitive, but the sensitivity decreases as the total number of events increases. For example in Fig 7.33h about 30 seconds after the start of the test, group 1 and 2 both have 50 percent of the events. The actual number of events recorded up to that point was four, two in each group. However, at higher strain levels, when there is a much greater number of events these values become more meaningful. From this figure it is clear that the percentage share of low amplitude events (group 1) decreases as the strain level increases, while percentage share of higher amplitude events increases with increasing strain. The relatively large scatter in acoustic emission response of the alumina control samples shown in Fig 7.33 is mainly due to the variation in thickness of the coatings . The coating thicknesses of these samples varied between 0.3 to 0.5 mm. Fig 7.34 shows a set of acoustic emission curves obtained from three replicate

alumina control samples (0.5 mm thick). Clearly the load deflection curves for all three samples are virtually identical. The cumulative AE events versus time curve shows a relatively small scatter in the total number of events. This can also be seen in the cumulative AE events plot in selected amplitude channels, the histograms of amplitude distributions and from the percentage share graph. Below the 600 Newton load level the amplitude distributions (Figs 7.33 & 7.35) have not any specific shape, and comparison of the two percentage share graphs shows that at low strain levels the percentage of low amplitude events is greater for thicker coatings.

A set of AE event curves for alumina coatings (10 samples) prepared with low input power is shown in Fig 7.36 . Comparing these load deflection curves with those of the control samples, it can be seen that the load deflection characteristics of these samples are similar to the control samples. The cumulative AE events plot shows that the acoustic activities of these coatings started at higher strain levels and the total number of events was less than for the control samples. The cumulative AE events plot in selected amplitude ranges (Figs 7.36c & d) showed that the majority of the events were in group 1 and there were very few events in groups 3, 4 and 5. A typical event rate curve of these coatings is shown in Fig 7.36d. As can be seen the maximum event rate was less than 10 events per second. The amplitude distribution histograms had few events even at relatively high strain levels, and clearly the scatter in the results is relatively large and there are few events above channel 20. The percentage share graph either shows that the AE activities start at high strain levels or that they were of the low amplitude type (group 1). In comparison with the control samples Figs (7.33 & 7.35), this graph shows that even at high strain levels the percentage share of the low amplitude events is higher

than that of the control coatings.

A set of AE curves from alumina coatings, (10 samples), sprayed on steel substrate that had poor surface preparation are shown in Fig 7.38 . The cumulative AE events plot shows that these coatings produced many more events than the control samples. The scatter in the number of events produced up to a given strain level for these coatings is greater than that of the control samples. As can be seen, there is a knee in this curve at a strain level of 0.06 percent, where the acoustic activities increase rapidly. The cumulative events plot in selected amplitude ranges shows that the majority of events fall in group 1. It is noteworthy that the ordinate of this graph has a maximum of 10000 events, where as in Figs 7.32 & 7.34 it was only 1000. A typical rate plot of these coatings is given in 7.38d, showing the event rate increasing with increasing strain, and also showing that the events are occurring in bursts. The maximum event rate in this graph is about 120 events per second, however in some cases event rates in excess of 500 events per second have been observed.

The amplitude distribution histograms are shown in Fig 7.39 . Even at low strain levels there are some differences between these histograms and those of the control samples. It was shown that (Fig 7.33) control alumina coatings up to 800 Newtons load level did not produce any event with amplitudes of greater than 24 dB. Fig 7.39 shows these coatings have produced some high amplitude events at relatively low load levels. At higher strain levels the difference between the amplitude distributions of these coatings and the control samples is even more significant.

The percentage share graphs for these coatings are shown in Fig 7.39h . The most significant difference between this graph and that of the control

samples is that at low strain levels the percentage share of high amplitude events is greater than that of the control samples.

A set of AE event curves for thermally stressed alumina coatings, (10 samples), are shown in Fig 7.40 . The load deflection curves are similar to those of control samples. The cumulative AE events plot shows that the total number of events recorded from these coatings was much higher than for the control samples. Even at relatively low strain levels (e.g. 0.04 percent strain) there was a significant difference between the total number of events recorded (more than 1000 events). This graph also displays a knee at around 0.06 percent strain. The cumulative events plot in selected amplitude ranges shows that although the majority of the events were in the group 1 amplitude range, there were also relatively large numbers of events in high amplitude channels. A typical rate plot for these coatings is shown in Fig 7.40d. The maximum event rate in this graph is in excess of 200 events per second.

The amplitude distribution histograms for these coatings are shown in Fig 7.41, and up to 400 Newtons load level there is no significant difference between these distributions and those of the control samples. However, above this strain level the difference is quite marked. The percentage share graph for these coatings is shown in Fig 7.41h, and here again the percentage share of high amplitude events is larger than that for the control samples.

In Fig 7.31 it was shown that one of the alumina control samples, showed more acoustic activities than the rest. At a strain level of 0.06 percent this sample produced 9000 ring-down counts. Fig 7.42 shows a set of event curves for this sample. The cumulative event plot shows that this coating

produced more events than any other control sample, however there were fewer AE events than was observed from the poor surface preparation or the thermally stressed coatings. The cumulative event plot in selected amplitude ranges of this sample was significantly different from that of the other coatings (Fig 7.32), with the majority of the events falling into group 2, and a relatively large number of events falling into group 3. This is also clear from the event rate plot Fig 7.42d. The maximum event rate was about 30 events per second.

The amplitude distribution histograms of this coating are shown in Fig 7.43.

Up to a load level of 400 Newtons no obvious difference between the amplitude distributions of this specimen and the rest of control sample (e.g Fig 7.33) could be observed. However, above this load level there was a significant difference between their histograms. As can be seen it appears that the amplitude distributions of this sample have been shifted to the right (higher amplitudes), and the peak of the amplitude distribution has moved from its usual channel 4 or 5 to 10. The percentage share graph of this sample is shown in Fig 7.43h. As can be seen even at low strain levels, about 70 percent of the events fall in the group 2 amplitude range, and also about 10 percent of the events were in group 3 which is about twice the percentage share observed for the rest of the control samples.

Subsequent examination of this coating showed that an area of the coating was broken off. Dye penetrant test showed traces of delamination around this region which are shown in plate 7.13 . This damage was additional to the more usually observed cracking occurring in the coatings of the other samples.

7.8.4 AE results of Mo63 coatings

7.8.4.1 Ring-down counting

Fig 7.44 shows two typical plots of ring-down count versus strain for the control molybdenum coatings. These plots were obtained from two replicate samples having 0.25 mm thick coating. The acoustic emission responses (cumulative ring-down counts) show some scatter. In general the over all AE activities of these coatings were similar. Usually, at about 0.03 percent strain level, the AE activities rapidly start to increase in an effectively linear fashion with increasing strain level. It is noteworthy that the plasma sprayed coatings do not show the Kaiser effect. Fig 7.45 shows a plot of ring-down count versus strain for the reloading of the sample shown in Fig 7.44a. As can be seen the AE activities start at a strain level of about 0.06 percent which is well below its previous limit. The Felicity ratio shown by this sample is about 0.8 which is typical for plasma sprayed coatings.

The effect of coating thickness on cumulative ring-down count was not as clear in the case of the Mo63 coatings as it was for alumina coatings. In fact ring-down counting showed some confusing results, whereby some samples with thin coatings produced more ring-down counts . Also, variation of other process parameters such as, quality of the surface preparation etc appeared to have little effect on the acoustic activities of the Mo63 coated specimens. For example, Fig 7.46 shows a typical ring-down count plot for a molybdenum coating sprayed on a substrate with no surface preparation, and clearly there is no significant difference between this

graph and those shown in Fig 7.44 .

7.8.4.2 Event counting and amplitude distribution results

Fig 7.47 shows a set of AE event plots for seven replicate control Mo63 coatings, with a coating thickness of 0.25 mm. The cumulative event versus time graphs for these coatings in Fig 7.47b, show that the AE activities at low strain levels are similar, but the scatter in the total number of events increases at higher strain levels. The cumulative AE event plot in selected amplitude channels of these coatings shows that the majority of events fall in the amplitude range of group 1, with a reasonable number falling into groups 2 and 3, whilst groups 4 and 5 had very few events. The event rate plot shows that at a strain level of 0.045 percent the event rate increased rapidly and after this initial increase it almost levels off, but still displays occasional bursts of activity.

The percentage share graph shows that above 0.04 percent strain level, group 1 has about 70 percent of the events, group 2 with 20 percent and group 3 has just 10 percent of the total number of events. The relatively flat shape of this graph suggests that the dominant source mechanism by which the acoustic emission was generated remained the same.

Fig 7.48 shows the amplitude distributions obtained from these coatings (Fig 7.47). It can be seen that even at low strain levels (e.g 0.02 percent strain) there are relatively large number of events recorded, especially in comparison to the alumina coatings. It is also clear that even at high strain levels there are very few events above channel 20 and that there are no events above channel 30. The general shape of the histograms even at low

load levels is exponential like and is skewed to the left.

It was pointed out that the cumulative ringdown counting showed no clear relationship between the coating thickness and the number of acoustic emissions recorded. However, variation in coating thickness had a profound effect on the amplitude distributions. Figs 7.49, 7.50, 7.51 and 7.52 show two sets of AE event curves for two Mo63 control samples. The coating thickness of these samples was about 0.18 mm . The cumulative event graphs show that the AE activities of these coatings were reduced in comparison to those shown in Fig 7.47 . The most striking difference between the AE response of these coatings and those in Fig 7.47 is their AE amplitude analysis curves. Fig 7.49c and 7.51c show the cumulative events in selected amplitude ranges, and in fact the majority of events are in group 2 amplitude range. This is also clear from their event rate graphs.

The amplitude distributions for these two samples are shown in Figs 7.50 and 7.52 , and clearly these have fewer events than those shown in Fig 7.48, and they are shifted to the right. The peak amplitude of these histograms corresponds to channels 8 and 9. In order to prove that this was a genuine effect, the threshold voltage of the AETC-203 was slightly reduced to below its usual level of 17 mV, and hence some noise was able to feed into the AETC-203 . This is clearly shown in Figs 7.50a and 7.52a, where a few events were recorded at channel 4. The percentage share graphs show that about 50 percent of the events had amplitudes in the range of group 2 while group 3, 4 and 5 were similar to those shown in Fig 7.48h.

As previously mentioned the ring-down counting could not distinguish between samples produced with different process parameters, and likewise event counting did not differentiate between coatings prepared with

different process parameters. However, all samples showed the above mentioned thickness effect. Fig 7.53 shows a set of AE event curves for a Mo63 sample which was sprayed to a thickness of 0.18mm on a substrate with no surface preparation. The cumulative event graph and also other amplitude curves of this sample are similar to those shown in Figs 7.51 and 7.52 .

The reduction in coating thickness had an even more pronounced effect on the AE amplitude distributions. Fig 7.55 shows a set of AE event curves for 4 replicate Mo63 coatings sprayed on to substrates with no surface preparation, to give a coating thickness of about 0.14 mm. As can be seen the load deflection curves are very similar, however there is some scatter in the cumulative event plot. The total number of events recorded for these samples at any strain level was smaller than that shown in Fig 7.51 (thickness effect). The cumulative events in selected amplitude ranges show that the majority of the events were in group 2, while group 1 had hardly any events. The event rate plot shows that the event rate was smaller than for the thicker coatings. The percentage share graph shows that more than 80 percent of the events had amplitudes in the range of group 2, and groups 3, 4 and 5 had similar shares of events as the thicker coatings. The general shift of the events to higher amplitudes is also clear from the amplitude distribution histograms (Fig 7.56). The peak amplitude of these histograms corresponds to channel 11.

7.8.5 Acoustic emission results of Mo505 coatings

7.8.5.1 Ring-down counting

Fig 7.57 shows two typical ring-down plots for the Mo505 coatings. The AE activities start to increase rapidly at strain levels of about 0.025 percent and then at around 0.05 percent strain it tends to level off. In comparison to Mo63 coatings, the Mo505 show much more vigorous AE activity. Also the AE activities start at lower strain levels and unlike Mo63 coatings do not increase linearly with increasing strain. Although there is a considerable scatter in the total number of ring-down counts from replicate samples, it was found that samples with thicker coatings produced more ring-down counts.

The AE response (ring-down counts) of the Mo505 coatings prepared with different spraying parameters were similar to those of control samples.

7.8.5.2 Event counting and amplitude distribution

A set of event curves for 6 replicate Mo505 control samples are shown in Fig 7.58. The coating thickness of these samples was about 0.11 mm. The cumulative event plot shows that vigorous AE activity started at around 0.025 percent strain level, and that above 0.05 percent strain level the event rate started to decrease. Similar behaviour was also observed in the ring-down count graphs. From these graphs it can also be seen that there is a large degree of scatter in the total number of events recorded at any particular strain level. The cumulative AE events plot in selected amplitude ranges show that majority of the events were in group 1. Comparing this graph with that of the Mo63 coatings,Fig 7.55, it can be seen that not only is the total number of events larger, but also that unlike Fig 7.55 the majority of events have amplitudes in the range of group 1. The event rate plot of these samples are also very different to

those of Mo63 coatings. Firstly, the maximum event rate shown in this graph is about 200 events per second, which is much higher than that of Fig 7.55, and secondly this graph has a maximum at around 0.05 percent strain.

The percentage share graph shows that above 0.05 percent strain, 60 to 70 percent of events fall in group 1, 18 to 20 percent in group 2, 8 to 10 percent in group 3 and 4 to 5 percent of the events fall in group 4 and 5. These figures for the similar Mo63 coatings are; group 1 less than 5 percent, group 2, 80 to 95 percent, group 3, 6 to 20 percent and groups 4, and 5 had less than 5 percent of the events.

The amplitude distribution histograms are shown in Fig 7.59, and clearly there are many more AE events even at low strain levels than those of Mo63, and also these histograms are much flatter than the Mo63 histograms (Fig 7.56).

On reloading the Mo505 coatings also did not show the Kaiser effect. Fig 7.60 shows some of the AE event curves for a repeated loading of a control sample. The first loading was up to 500 Newton load level (0.033 percent strain). On reloading the AE activities started at a strain level of about 0.027 percent. The Filicity ratio shown by this sample is about 0.8 .

Fig 7.61 shows a set of AE event curves for a contol Mo505 sample, with a coating thickness of 0.2 mm. As can be seen the total number of AE events recorded at any given strain level was higher than those specimens shown in Fig 7.58. Another interesting difference between these AE curves and those shown in Fig 7.58 is that the peak of the event rate plot has been shifted to a lower strain level (Fig 7.61d). This obviously means that thicker coatings fracture at lower strain level. The percentage share graph and the

amplitude distribution histograms are similar to those shown in Fig 7.59, except that the histograms show many more events. When samples with thicker coatings were tested, the AE activities were even more vigorous. Fig 7.63 shows a set of AE event curves obtained from a relatively thick coating (0.25 mm). The cumulative events plot shows that the number of events recorded from this sample at any given strain level is higher than those shown in Fig 7.58 or 7.61 . The most significant difference between these curves and those of the thinner coatings are the amplitude related curves. The cumulative events in selected amplitude ranges show that although there were a large number of events in the group 1 amplitude range, group 2 equally contained a large number of events. Also the Event rate graphs show that in the group 2 amplitude range, there were a few large bursts of AE activity which is believed to be due to the sudden fracture of the coating. The percentage share graph shows that group 1 and 2 each have around 40 percent of the events, group 3, 10 percent, while groups 4 and 5 had similar percentage shares to those of the thinner coatings. The amplitude distribution show that these histograms contained many more events, which were of higher amplitude.

Although in general it was not possible to differentiate between coatings produced using different spraying parameters, those coatings sprayed on rusty surfaces or using low power showed less AE activities of lower amplitude than their replicate control sample. This is shown in Fig 7.65 for a low power Mo505 coating (0.3 mm thick), and clearly the total events recorded at any given strain level is much lower than those shown in Fig 7.63 . The cumulative event plot in selected amplitude ranges did not show the same features as those in Fig 7.63c . In fact most of these curves are similar to those of thinner control samples, except that these coatings showed less high amplitude events. This is quite clear from the percentage

share graph, where group 5 in particular has a lower percentage share of events than observed for the control samples.

7.8.6 Acoustic emission results of aluminium coatings

Aluminium coatings showed very little AE activity, even at high strain levels. Fig 7.67 is a typical set of AE event curves for an aluminium control coating, showing that the total number of events emitted from this sample is less than 60. It is possible that most of these events were just background noise, particularly since nearly all of these events were in group 1. Also, it can be seen that the event rate was always less than 5 events per seconds. The amplitude distribution histograms show that nearly all of these events were in channels 4 and 5, and only a few events were recorded in channel 11 at relatively high strain levels. Other aluminium coatings of various thickness and those produced using different spraying parameters also showed similar results.

7.8.7 Further amplitude distribution analysis

In chapter 5 it was pointed out that if the acoustic emission technique is to be used as a practical NDE tool, it ought to be able to differentiate between good and low quality coatings at relatively low strain levels. The results presented in this chapter showed that only in some cases was it possible to distinguish between different quality coatings and also that the amount of scatter in the AE activities from replicate samples can be large. Thus it would be helpful to be able to eliminate the scatter or apply some statistical method to identify a poor quality coating. It is

also necessary to recognise the fact that the most hopeful method of analysing AE data for practical applications should be based on some form of amplitude sorting. As the event or ring-down counting alone can lead to false conclusions and also it is more susceptible to experimental errors.

7.8.7.1 b-plots

The amplitude distribution histograms are difficult to interpret owing to the large quantity of information which they contain. Thus it would be useful to be able to characterize each histogram with a single parameter, to make it possible to identify an amplitude distribution which does not belong to a group. One such method, as was discussed in chapter 5, is the b-plot technique.

The slopes of the log cumulative events versus log amplitude plot were determined for all the samples at each of the load levels. The slope of the b-plot for the standard Mo63 coatings and the Mo505 were remarkably consistent, lying in the ranges 1.0 - 0.9 and 0.31 - 0.27 respectively. However, the Mo63 coating sprayed onto a rusty surface changed in slope from approximately 1.2 to 0.6 with increasing load. A comparison of a typical set of b-plots is shown in Fig 7.69 where the shift in the amplitude distribution to higher signal values for the rusty test piece is quite evident as the bending load increases. The lower values of b obtained from this test piece suggests that interfacial failure is characterized by higher amplitude signals as it is generally accepted that good surface preparation results in better adhesion. It is noteworty that this coating was detached from the substrate at the end of the test. For Mo505 coatings the lower values of b (0.31 - 0.27) indicate a greater emphasis on source

events at high amplitudes as has been shown in section 7.8.5 , where channels above 40 were activated. However, the Mo505 samples prepared under non-standard conditions did not show significant differences in their b-plots during the early stages of the loading, where the detection of such differences is highly desirable.

The alumina coated samples were less noisy in the early stages of loading and gave no significant emission until a load level of 600 Newtons was reached (0.06 percent strain). The b-plot gave slightly flatter slopes with values varying from 0.39 to 0.32, suggesting slightly more energetic events.

These results suggest that the power law model is not sensitive enough to differentiate anything other than obvious differences in the amplitude distributions.

7.8.7.2 Chi-squared test applied to AE amplitude distributions

The chi squared method enables the scatter inherent in a group of samples to be determined and tests whether the AE amplitude distribution of any other sample lies within or outside that scatter band. Higher values of chi-square are obtained where there is a large degree of scatter between the samples.

The computer program allows an analysis of up to 8 samples tested up to twelve load levels over a range of 50 channels. One such analysis is shown in table 7.11 for 8 specimens of steel coated with Mo63 . Samples 1 - 7

were sprayed under standard conditions, whereas in sample 8 the surface preparation was omitted (slightly rusty). The load levels range from 200 to 1200 Newtons in equal increments. The eight samples are ranked in order of chi-squre. At each load level as well as across the complete range of load, sample 8, (in which grit blasting had been omitted), always had the highest value of chi-squred by approximately a factor of 2. An analysis of the Mo505 coating failed to differentiate between samples with and without grit-blasted substrates. However, when samples prepared with low input power were introduced, they always had the highest value of chi-squared.

A similar chi-squared analysis for alumina is shown in table 7.12 . This set of ranks is interesting in that sample 2, which was prepared as a standard, appeared to be from a different population and was the one already referred to as being cracked on unloading (Figs 7.42 and 7.43). Sample 1 prepared to simulate poor surface preparation by using dusty grit blasting material has a chi-squared value which places it outside the standard group, although it distances itself less than the sample found to have been cracked (plate 7.13).

7.8.8 Frequency analysis results

For the frequency analysis, the AE signals were captured by a transient recorder and were analysed using a Marconi (TF2370) spectrum analyser. Two typical AE signals and their corresponding frequency components are given in plate 7.14 . It can be seen that the main frequency components of these signals was the resonance frequency of the transducer (see plate 7.12). In some cases there were also other frequency components. These components are

believed to be due to the reflections of the acoustic wave and their resultant constructive or destructive interference.

7.8.9 Energy analysis of AE events

Energy analysis of AE signals was carried out using a PAC-3400 four channel analyser. In these tests the PAC-3400 was used in one channel mode, enabling the fastest possible data collection rate to be utilised. Fig 7.70 shows a typical trace of events versus energy. Most of the events were of low energy, which is consistent with the AE amplitude results. It was found that the energy graphs and similarly the other parameters provided by the PAC-3400 (e.g. rise time, duration etc) did not provide any more information than did the AE amplitude. Especially where the PAC-3400 has severe limitations compared with the AETC-203 system (146).

7.8.10 Damage accumulation in plasma sprayed coatings

Visual examination of the surface of the coatings after AE tests, usually did not detect any significant amount of damage (e.g delamination, cracks at the s ace etc). However, after using a dye penetrant, a number of cracks were visible (plate 7.15). Closer examination (using SEM) revealed that the cracks were mainly interparticle separation, although some particle fracture was also observed (plate 7.16).

The microstructure of all coatings after four point bending contained a number of translamellar cracks as well as interlamellar separations. When the microstructures of the alumina coatings were examined, after AE

testing, it was found that the translamellar cracks were changed to interlamellar separation as shown in plate 7.17. The interlamellar separation always occured between two layers of the coating deposited by two passes of the gun. This mode of fracture was common to all four types of alumina coatings. However the over heated coatings and the poor surface preparation samples showed relatively large delaminations at or near the interface (plate 7.18). In the case of poor surface preparation coatings this was to be expected as the adhesion between the substrates and coatings was far from perfect. It was also shown that the over heated coatings had a large number of cracks near the interface region (plate 7.8), and in fact one of these coatings had a catastrophic failure near the interface (plate 7.19). Clearly the mode of failure is predominantly cohesive.

The C-scans carried out on these samples confirmed the micrographic observations. C-scan imaging is not sensitive to cracks parallel to the ultrasonic beam, but cracks parallel to the substrate surface can be easily detected. Fig 7.71 shows a typical C-scan of an alumina coating after AE testing. The interlamellar cracks are quite clear, and knowing the history of the samples, it is possible to see that the delaminations result from the translamellar cracks.

The C-scan images of some of the poor surface preparation coatings after AE testing showed large areas of delamination, as can be seen from Fig 7.72. In general the total attenuation through the coatings after AE testings was about 10 dB more than before.

Aluminium coatings, after AE testing did not show any sign of damage from 4 point bending . Fig 7.73 shows a C-scan image of a typical aluminium coating after AE testing. The C-scan image of this sample before AE testing

is shown in Fig 7.23. It is clear that there is no detectable damage in this sample.

The micrographs of the control molybdenum coatings showed some translamellar and interlamellar cracks even before AE testing, as shown in Plate 7.1 . The micrographs of the low power and the "no surface preparation" samples were similar to those of the control samples, except the low power specimens showed some semi-molten spherodized molybdenum particles. The over heated samples showed many more cracks than the control samples (plate 7.9). The micrographs of the Mo63 coatings after AE test also showed large numbers of translamellar and interlamellar separations, and generally it appeared that cracks prefered to run between the lamellae as shown in plate 7.20 .

The Mo505 coatings did not have as many cracks as the Mo63 coating, before AE testing, (plate 7.3). Micrographs of the Mo505 coatings after the AE test showed large numbers of interlamellar and translamellar cracks and phase separations (plate 7.21). The micrographs of the poor surface preparation samples were similar to those of the control samples (plate 7.22) and it appeared that the over-heated coatings had more cracks.

When surfaces of the plasma sprayed coatings were examined it was found that in the case of control, over-heated and poor surface preparation specimens, a large number of the particles had disintegrated on impact (plate 7.23). However the low power samples showed far fewer defects (plate 7.24). Also it appeared that the adhesion between particles in low power coatings was good (plate 7.24). The particle fracture, was similar in both cases (plate 7.25) and it appeared that most of the cracks were initiated from a defect.

7.8.11 Damage accumulation mechanisms and AE response of plasma sprayed coatings

One of the objectives of this study was to gain an understanding of the relationship between the AE phenomena and the physical processes occuring within the coating. It is obvious that the extent of cracking and the presence of other defects in the coatings, is directly related to the coating durability, and that the cracking mechanism can identify the failure mode of the coating (e.g. cohesive or adhesive failure). But using the present AE analysis it is not readily possible to identify the cracking mechanisms. Although in some circumstances the technique can be used to identify a poor quality coating at relatively low strain levels.

The AE results of alumina control samples (ring-down and event counting) showed that in general thicker coatings produced more acoustic emission, and that the scatter in the results, especially total number of events or ring-down counts was relatively large. It is well known that thicker coatings are much more susceptible to fracture. This is mainly due to the residual stresses in the coating, which depends on the coating thickness (147). The scatter of the AE results is partly due to the nature of plasma sprayed coatings, and partly due to the AE testing. It was shown that the acoustic wave will suffer large attenuation in plasma sprayed coatings, therefore it is clear that the position of the transducer is critical. Also the coupling of the transducer to the specimens can have a large influence on the AE response, since poor coupling will affect the amplitude and total number of events recorded during the test. To minimize these effects system calibration (lead pencil breaking) was carried out prior to each

test, but because mainly high amplitude signals were generated, this test is not very sensitive to parameters such as coupling. Thus some variation in AE response of the replicate samples is to be expected.

The cracking mechanism of alumina control samples (due to the normal stresses in four point bending) was predominantly particle separation and fracture (translamellar cracks). However, as previously mentioned the mode of cracking usually changed to interlamellar fracture (plate 7.8). These mode changes only occured where different layers of coatings were deposited. The degree of porosity between these layers was much greater than the rest of the coating. In fact in some cases, from these lines of pores it was possible to see the number of passes of the gun used to deposit the coating (plate 7.17). Thus it is clear that the source of AE events was these traslamellar and interlamellar fractures in the alumina control coatings.

The poor surface preparation had a significant effect on the AE response of alumina coatings. In comparison to the control samples, these specimens had a larger total number of events and more high amplitude events. Since the only difference between these coatings and the control samples was the surface preparation, it is resonable to believe that the source of AE events was adhesion failure of the coatings. Although none of these samples failed catastrophically, the subsequent C-scan and also the micrographs (Fig 7.72 and plate 7.18) quite clearly support this view. The poor surface preparation samples showed a somewhat more variable initial take off point for the AE events (Fig 7.38). This is thought to be due to the more variable quality (adhesion) of these coatings.

Inspite of the overheated samples producing huge numbers of events, it was

found that the AE response started at relatively higher strain levels (in comparison to the poor surface preparation samples), suggesting that cracking or the extension of the cracks did not take place until such strain levels were reached. This is thought to be due to the lower residual stresses in these coatings, since during spraying the overheated samples were subjected to high thermal stresses which caused extensive cracking in the coating (e.g. plate 7.8). However, at room temperature the residual stresses in the coatings were smaller than those of the poor surface preparation specimens. Also, comparison of the percentage share graphs of the overheated and poor surface preparation sample show that the percentage of higher amplitude events (groups 4 and 5) is lower in the case of thermally stressed coatings (Figs 7.38 and 7.40). This is thought to be due to the larger proportion of particle fracture in poor surface preparation coatings, since the thermally stressed coatings contain relatively large number of translamellar cracks.

The low power samples contained far fewer defects than the control samples. Although the micrographs prepared from the cross sections of these coatings were similar to the control samples, closer examination of the surface using a SEM revealed that these coatings had fewer defects (plate 7.24). This may be the reason why these coatings were less noisy, and it may be that low input power results in better quality coatings. Because of the nature of the plasma sprayed coatings, it was difficult to decide, from the micrographs or the C-scans of these coatings, that after AE test the degree of damage was less than the control samples.

The AE response of the Mo63 coatings was much more complex than that for the alumina coatings. Although the effect of different process parameters is not as clearly defined as in the case of the alumina coatings, other

interesting information can be obtained from the Mo63 results. For example, it was found that the AE response of these coatings was closely related to the coating thickness, such that thin Mo63 coatings generally produced fewer AE events which were of higher amplitudes (e.g. Fig 7.49). As a result of these higher amplitude events ring-down counting showed some confusing results, where in some cases thin coatings produced more counts than a thicker coatings. The effect of thickness on the AE of the Mo63 is thought to be due, mainly, to the residual stresses in the coating and partly because of the Mo63 coating's microstructure.

It has been shown that the molybdenum coatings have high residual stresses (147), and that the as sprayed coatings contain microcracks where the residual stresses exceeded the fracture stresses of the coating. The pattern of these stresses appears to be very complex especially near the interface (145). It has been shown that the surface of the thin Mo63 coatings are under compresive residual stress. However, in the case of the thick Mo63 coatings,the surface is under tensile residual stresses (147). Thus a sample with a thin coating starts to fracture at higher stress levels, producing more energetic events, while thicker coatings fracture at lower stress levels producing lower amplitude AE events.

The cracking mechanism of Mo63 coatings was similar to that of the alumina coatings, except that the translamellar cracks tended to be smaller and the mode change occurred between most lamellae (mode change from translamellar cracks to interlamellar separation. e.g. plate 7.20). Also as the Mo63 coatings contained a large number of translamellar cracks, it appeared that, in 4 point bending, the crack paths run chiefly through these existing cracks. However, new interlamellar separations did occur. This cracking mechanism can explain the narrow band-width of AE amplitudes

recorded, since the cohesive bonds being separated between the lamellae are of a similar nature. This can also explain the behaviour of the event rate graph, where the event rate after initial increase, remained constant.

As expected, the AE response of the Mo63 samples that had no surface preparation was similar to that of the control samples. As it was shown in section 7.4 that surface preparation was not critical for the adhesion of Mo63 coatings to the steel substrates. However, the AE response of the Mo63 coating sprayed on a rusty surface was different from the control samples (see section 7.8.7). The amplitude ditributions of this sample covered a wider range, suggesting a greater range of AE sources, and the mode of failure of this coating was predominantly adhesive.

It was found that the AE response of the low power and the overheated samples was not greatly different to that of the control samples, although some differences between their microstructures were observed. The micrographs of the low power samples showed that there were some semi-molten particles trapped in the coatings, however, adhesion between these and the other particles was good. In fact, Shankar et al (13) suggested that the semi molten particles act like an anchoring point for the other semi molten particles which leads to an overall improvement in the cohesive strength of the coatings. It appeared that the damage accumulation mechanism was similar to that explained for the control samples. Thus it is not surprising that their AE responses were not very different.

The AE response of the Mo505 coatings differed significantly from that of Mo63 coatings. Since the Mo505 coatings produced about 10 times more AE events, and since the amplitude distributions were of a wider range with channels above 40 being activated. It was shown (section 7.8.5) that the

most significant difference between their AE responses was in their event rate graphs, where the event rate of Mo505 coatings rapidly increased to a maximum then started to decrease. This obviously indicates that most of the damage has occured when the maximum event rate is reached, after which the extent of cracking decreases. This behaviour is thought to be partly due to the residual stresses in the coatings and partly due to their microstructure. Keshtvarzi (147) and Munn (148) have shown that Metco 505 coatings have much less residual compresive stress in comparison to the Mo63, because of the lower solidification temperature of the Mo505. Thus cracking of the coatings starts at lower stress levels. Also because of the lower freezing temperature, Mo505 coatings are subjected to much lower thermal stresses during their formation, and have fewer translamellar cracks in comparison to the Mo63 coatings (147). Thus during 4 point bending, the fracture of the lamellae occurs, resulting in huge numbers of high amplitude AE events. In addition separation between phases and also matrix cracking will occur (plates 7.21 & 7.22).

It was shown that aluminium coatings produced very few AE events (section 7.8.6). The subsequent C-scans and also the micrographs of them did not show any significant damage which may have resulted from the bending test. This is expected since the strain levels reached were below the plastic strain level of the aluminum coatings, and as it was pointed out (Chapter 5) even plastic deformation of aluminium is not associated with large numbers of AE events. Thus the AE technique cannot give any useful information about aluminium coatings at low strain levels.

7.8.12 Frequency and energy analysis of AE events

The preliminary results of the frequency components of the AE signals did not show any clear difference between the various coatings (plate 7.14). In general all AE signals were similar and the dominant frequency was the resonant frequency of the transducer. This is because PZT transducers tend to ring at their fundamental resonant frequencies, making the task of frequency analysis very difficult. Also frequency analysis has other complications, such as the effect of sample geometry as described in Chapter 5. The frequency analysis results reported here had another important short-coming, that is, because the AE events are transient in these tests the AE signals were captured randomly by a transient recorder and were displayed on an oscilloscope. The first judgment on the signal had to made by eye which can be very biased. For a more exact study of the frequency components of the AE signals it is neccessary to be able to record the whole test using a fast wide-band tape recorder, to analyse the data, preferably using a computer.

It was shown that the energy analysis of the AE events did not give any new information (section 7.8.9). This is partly due to the close relationship between the amplitude and energy of the AE signals and partly due to the severe limitations of the AE analyser used (146). It was shown that majority of the AE events were of low amplitudes (low energy). The accuracy of the energy processor unit of the PAC3400 for small signals was poor (146).

7.8.13 Discussion of b-plots and chi-squared results

The shape of an observed amplitude distribution may be quite arbitrary and there is no way of predicting from the height of one histogram bar what the

height of any other will be. In search of rules governing AE behaviour various distributions have been suggested (111). The most frequently used distribution is the power law model. The distribution of this model was explained in section 5.4.4 . The main attraction of this analysis method is its ability to represent the whole of the distribution by a single parameter called b . A low value of b indicates a large number of high amplitude events, whilst a higher value indicates a large number of low amplitude events.

The range of b values observed were quite small (section 7.8.7.1), which indicates the insensitivity of the b values to the changes in the AE distributions. This is mainly due to the log-log scale used in this distribution. Another problem associated with this distribution is that the scatter in b values is still relatively large. This is mainly because in this distribution the scatter in the number of events at low amplitudes are heavily suppressed while the scatter in high amplitude ranges are enhanced. Thus retaining the scatter band.

It was shown that the chi-squared test in some circumstances differentiates between coatings prepared under differing conditions (section 7.8.7.2). It was also shown that in these cases the values of the chi-squared at each load level as well as across the complete range of load for the poor quality samples were the highest. However, in all these cases the actual values of chi-squared seem unusually high and well outside normal statistical tables. This means that the chi-squared test is too sensitive to the changes in the amplitude distributions. In principal the chi-squared test method seeks to test whether samples are identical . As there are fifty channels with up to 10000 events per channel and eight samples each produced by a processes in which control of variables is difficult, it

would be surprising if the samples were found to have identical AE patterns.

There are two other sources which have contributed toward the large values of chi-squared. These were 1)- Calculation method 2)- Experimental errors.

Because of the inherent variabilities of the properties of plasma sprayed coatings (including acoustic properties), it was difficult to select a set of AE histograms of the control samples as the expected distributions. Thus a method of estimating the expected distribution was used (weighted means). A detailed description of this method is given by Phillips et al (149). Although this technique is very powerful for estimating the expected distributions, in situations where the variability is large (e.g. AE amplitude distributions) this technique may not be suitable. To illustrate this effect and also demonstrate the ability of the chi-squared technique used, two examples for a simplified version of the programme used are shown in table 7.13 . As can be seen (table 7.13a) the values of chi-squared for all four distributions are zero and the calculated expected values are exact. This clearly demonstrates the ability of the technique used. In the second group of distributions (table 7.14b) , the (2,2) element was 52, which should have ideally been 82. As can be seen this single value has affected the expectation for each cell, forcing the expected distributions to have a dip at channel 2. Therefore it may be better, first, to establish a reasonable group of standard distributions, then compare each distribution with this group.

Another important factor which can result in large chi-squared values, is the shift of the amplitude distributions (to higher or lower amplitudes). This may be a genuine effect such as those shown in Fig 7.52 where the

histograms were moved to the right due to the compressive residual stresses in Mo63 coatings. Such effects can also occur due to the poor coupling of the transducer to the sample. The chi-squared test is very sensitive to such changes.

7.8.14 AE amplitude distribution from an infinitly large layered medium

In this section the expected amplitude distribution from a simplified model of sprayed coatings will be discussed. In this model it is assumed that the body is infinitly large and consists of isotropic layers. It is also assumed that the AE source mechanism is unique (specific amplitude) and is uniformly distributed in the sample. In this model the main parameter effecting the shape of the histogram is the sound attenuation, which is given by (67);

$$A = A_0 \exp(-2 \alpha x) \qquad 7.6$$

where A is the AE amplitude at the sensor, A_0 is the amplitude at the source, α is the attenuation coefficient and X is the distance of the source from the sensor. The amplitude distribution obtained from this body will have a highly skewed exponentially decaying shape. An example of this for a six layer medium is shown in Fig 7.74 .

As shown previously, the AE amplitude distributions of plasma sprayed coatings have a highly skewed exponential like decaying shape. This is generally due to the fact that there are only few damage mechanisms (AE sources) which are relatively uniformly distributed in the samples. For example in the 4 point bending test of plasma sprayed coatings the dominant damage mechanism was the formation of cracks across the coating, similar to

that shown in plate 7.15, where particle separation and fracture occured.

The presence of the other AE sources, depending on their strength and position may modify the shape of the amplitude distribution. It is to be expected that a localized AE source will have a greater effect on the shape of the amplitude distribution. Thus defects or localized adhesion failures may cause sufficient change in the shape of amplitude distributions to be identified.

There are two more factors which they may influence the shape of the amplitude distributions. Firstly, as the test progresses and more damage is introduced in the sample (more cracks), the attenuation of the material increases, thus, a particular event will be recorded with lower amplitude as the test progresses. The second factor has an opposite effect. In a constant displacement test, a crack extension of δa is associated with a stress drop of $\delta\sigma$. However, the energy released from this crack extension depends on the magnitude of the stress at which the crack extension occures, as shown in Fig 7.75 . It was also shown that (section 5.3) the energy carried by the AE wave is not a constant fraction of the released energy and depends on the magnitude of the stress drop. This suggests that the energy of the AE wave will be higher as the stresses increases. Thus the AE events released at higher stress levels will have higher amplitudes.

It is possible to estimate the furthest point away from the transducer from which acoustic emission activity can be detected. Assuming a 60 dB amplitude for the most energetic events, the detection limit for the three attenuation levels are;

$$\text{LOG}\,(A/A_o) = 60\ \text{dB} = -2\,\alpha\,X$$

For $\alpha = 20$ dB/cm $\qquad X = 1.2$ mm

For α = 10 dB/cm X = 3 mm

For α = 1 dB/cm X = 30 mm.

From these figures it is possible to see that practically all recorded AE events must have been generated from the coating just under the transducer, when the transducer mounted on the coated surface, or from those events which have travelled through the substrate.

Chapter 8

Conclusions

8. Conclusions

The mechanisms of ultrasonic attenuation in plasma sprayed coatings are very different from those in wrought metals. The ultrasonic attenuations in plasma sprayed coatings are hundreds of dB/cm, which is much higher than the attenuation levels observed in wrought metals. The large ultrasonic attenuation is due to the presence of interlamellar cracks and pores present in the coatings. As a results of the large attenuation, ultrasonic C-scanning can be employed for the thickness measurement of plasma sprayed coatings, and when 10 MHz ultrasound was used, thickness variations of 0.05 mm were readily detectable.

The mechanisms of sound transmission through plasma sprayed materials is largely via the contact points present between the lamellar and to a less extent due to the resonance vibration of the lamellae.

The ultrasonic C-scan technique was successful in the detection of delamination and the lack of bond integrity between the coating and the substrate, provided that the gap separation was larger than the interlamellar cracks. This means that the ultrasonic C-scan technique can detect the presence of adhesion defects in sprayed materials, but can not give a reliable indication of the bond strength. Also, by using a micro computer, it was possible to enhance the ultrasonic image to emphasise some specific feature of the coating (e.g. adhesion defect). It was also established that ultrasonic C-scan imaging was unable to differentiate between coatings produced with various process parameters. Another limitation of the ultrasonic C-scan technique is the geometrical restriction of the test piece, where in practice only relatively simple shaped components can be tested (e.g. flat plates, spheres or cylinders).

The acoustic emission responses of all four types of coating materials studied were different, e.g. aluminium coatings produced little acoustic activity, all of which was of low amplitude, while Mo505 coatings produced large numbers of AE events even at relatively low strain levels.

The AE activities of alumina (Metco 105) coatings were related to the coating thickness, in that thicker coatings generally produced more AE events. This effect was clear from both ring-down and event counting. It was also found that alumina coatings sprayed on the substrates with poor surface preparation and those sprayed with no coolant air showed more AE activities than the control coatings, while specimens produced with 20% less input power showed fewer AE activities. At lower strain levels these effects were more clearly defined in the AE event amplitude distribution results than they were in the ring-down and event counting results.

The AE activities of alumina coatings consisted of mainly low amplitude events, which were attributed to interlamellar fracture. Localised damage produced completely different AE amplitude distributions and this was clear even at low strain levels, however this effect was not clear from the ring-down and event counting results.

The AE response of Mo63 coatings were complex. Ring-down and event counting showed some relationship with coating properties and structure, however, this relationship was not as clear as that of the alumina coatings. It was found that the residual stresses in Mo63 coatings had a profound effect on the AE activities, such that thin coatings with compressive residual stresses produced a greater percentage of high amplitude events than thicker coatings which probably had tensile residual stresses. Mo63

coatings produced amplitude distributions which were spread over a relatively narrow band of amplitudes implying that there was predominantly one fracture mechanism in operation, which was thought to be due to cracks following the paths of the interlamellar separations. The majority of the translamellar cracks were caused during the formation of the coating.

The AE response of the Mo505 coatings were very different from those of Mo63 coatings. This is mainly due to the reduced residual stresses in these coatings. The amplitude distribution of Mo505 coatings were much broader and there were also high amplitude events present. It was established that this was due to the translamellar cracks produced during the 4 point bending. The AE technique could not differentiate between Mo63 and Mo505 coatings produced with different process parameters at low strain levels, (except in extreme cases e.g. substrates with rusty surfaces)

Aluminum coatings, as expected, showed very little AE activity and the AE technique can not be used for evaluating these coatings.

The b_plot analysis whilst able to differentiate between different coatings materials, was not sensitive to the changes in the plasma spraying process parameters.

The statistical analysis of the amplitude distribution, using chi-squared test showed more promise, since it was possible to detect at relatively low strain levels which of the alumina coatings were of a poor quality. However it is clear from the large values of the chi-squared obtained that this technique requires further refinement.

Some preliminary work on frequency and energy analysis of the AE signals

suggests that these analyses can not give any more information about the coatings than the amplitude distribution analysis.

Chapter 9

Suggestions for further work

9 Recommendations for further work

This work has shown that ultrasonic testing can successfully locate a region of bond failure, provided that the gap separation is larger than the interlamellar cracks. Further work is necessary to relate ultrasonic attenuation results with bond integrity. This work has made use of the immersion technique, however, for commercial applications the use of a contact method would be advantageous, and work should be done to demonstrate whether such a method is possible.

The AE results presented in this thesis suggest that AE techniques can be used to evaluate the quality of some plasma sprayed coatings. It was shown that different fracture mechanisms will produce events in different amplitude ranges, however, further work is required to clarify exactly which fracture processes correspond to a particular amplitude range.

Further refinement of some of the AE analysis techniques presented here are necessary. In particular, the chi-squared method could be refined by using a wider range of experimental data to provide the distributions needed for the analysis. It may also be useful to limit the number of channels to a specific range of amplitudes, since it may decrease the actual values obtained for the chi-squared.

This work has shown that the AE technique can detect which coatings were of extremely low quality (e.g. those sprayed on rusty surfaces), it is necessary to investigate the level at which changes in the plasma spraying process variables can be detected by the AE technique.

List of references

1 Thorpe M. L. ChemTech 1982, 364.

2 Hedge R. H. and Evens A. V. 9th Int. Thermal Spraying Conf., 1980, 73.

3 Putzier U. , Zickler H. and Koch F. 9th Int. Thermal Spraying Conf., 1980, 103.

4 Thieman K. and Malik M. 9th Int. Thermal Spraying Conf., 1980.

5 Almond D. P. Surfacing J., 13, 3, 1982, 50.

6 Almond D. P., Cox R. L., Moghisi M. and Reiter H. Int. Conf. on Metallurgical coatings, San Francisco, 1981.

7 Bucklow I. A. Proc. Int. Conf. on the Advances in Surface Coatings Technology, London, 1978, 7.

8 Steffens H. D. AGARD, 1980, 5.1 .

9 Safai S. and Herman H. Ceramic Bulletin, 1979, 24.

10 Esmail E , Grabec I and Krasevec V. J. Phys. D., 12, 1979, 265.

11 Gerberich W. W. and Hartbower C. E. Int. J. of Frac. Mech., 3, 1967, 185.

12 Wadley H. N. G., Furze D. C., Scruby C. B. and Wyre B. L., Metal Sci., 13, 1979, 451.

13 Shankar N. R., Berndt C. C. and Herman H. Proc. 6th Annual Conf. on Composites and Advanced Ceramic Materials, Coca Beach, 1982, 473.

14 Ravishankar N. and Herman H. Thin Solid Films, 83, 1981, 343.

15 Berndt C. C and Herman H. Thin Solid Films, 108, 1983, 447.

16 James H. C. and Daryl E. C. Metal Handbook 9th edition, 5, 361.

17 James D. H. Anti-Corrosion, 30, 7, 1983, 66.

18 Mayer C. A. Welding Design and Fabrication 1982, 66.

19 Boeing H. V. Plasma Science and Technology, Cornell University Press, 1982.

20 Edels H. Proc. Inst. of Elec. Eng., 108, 8, 1961, 55.

21 Ingham H. S. and Shepared A. P. Flame Spray Handbook, Metco INC, 1&2, 1967.

22 McPherson R. Thin Solid Films, 83, 1981, 297.

23 Safai S. and Herman H. Thin Solid Films, 45, 1977, 295.

24 Scott B. F. and Cannell J. K. Int. J. Mach. Tool. Des. Res., 7, 1967, 243.

25 Fizdon K. Int. J. Heat Mass Transfer, 22, 1979, 749.

26 Pawlowski L. Surfacing J., 11, 3, 1980, 8.

27 Vardel M. , Vardel A. and Fauchais P., 10th Int. Thermal Spraying Conf., 1983, 88.

28 Jagoda I. J. and Heinberg F. J. Proc. 3rd Int. Symp. on Plasma Chemistry, IUPAC University of Limoges, paper S. 3. 5, 1977.

29 Fisher I. A. Int. Met. Rev., 17, 1972, 117.

30 Atkins F. J. Second Conf. Inst. Welding, Metal Spraying and Plastic Coating Division, London, 1967, Paper 11.

31 Engelke J. L. American Ins. of Chem. Eng., Los Angeles, 1962.

32 Marynowski C. W., Halden F. A. and Farley E. P. Electrochemical Technology, 13, 1965, 109.

33 Ford R. F. and Furmidge C. G. L. Sci. Monogr., 25, 1967, 417.

34 Akao F. and Araki K. Trans. ISIJ, 20, 1980, 737.

35 Madejski J. Int. J. Heat Mass Transfer, 19, 1976, 1009.

36 McPherson R. J. Mater. Sci., 15, 1980, 1915.

37 Ruhl R. C. Mater. Sci. and Eng., 1, 1967, 313.

38 Pawlowski L. Thin Solid Films, 81, 1981, 79.

39 Gerdeman D. A. and Hecht N. L. Arc Plasma Technology in Mater. Sci., Spring-Verlag Wien(New York), 1972.

40 Mash D. R., Weare N. E. and Walker D. L. J. of Metals, 1961, 473.

41 Andrews C. W. D. and Fuller B. A. Surfacing J., 6, 2, 1975, 5.

42 Atkins F. J. Surfacing J., 7, 17, 1976, 2.

43 Baxter C. F. G. and Reiter H. Int. Conf. Advances in Surface Coating Technology, London, 1978, 23.

44 Baxter C. F. G. Ph. D. Thesis, Bath University, 1977.

45 Berndt C. C. and Mcpherson R. AWRA report p11-1-78. Australian Welding Research, 1979, 11.

46 Apps R. L. J. Vac. Sci. Technol. , 11, 4, 1974, .

47 Walker G. H. and Lewis B. W. Metall. Trans., 2, 1971, 2189.

48 British standard 4950, 1973, British Standard Institute.

49 Hasui A., Kitahara S. and Fukushima T. Tran. Nat. Res. Inst. Met., 12, 1, 1970, 9.

50 Baxter C. F. G. and Reiter H. 8th Int. Thermal Spraying Conf., Miami Beach, 1976, 271.

51 Nicholas M. G. and Scott K. T. Surfacing J., 12, 1, 1981, 5.

52 Steffens H. D. 3rd Int. Metal Spraying Conf., Madrid, 1962.

53 Endoh M., Shinmen S. and Shinmen S. 8th Int. Thermal Spraying Conf., Miami Beach, 1976, 492.

54 Kitahara S. and Hasui A. J. Vac. Sci. Technol., 11, 4, 1974, 747.

55 Smart R. F. 8th Int. Conf. on Thermal Spraying, Miami Beach, 1976, 195.

56 Kretzschmar E. Surfacing J., 8, 1, 1977, 2.

57 Cox R. L. M. Sc. Thesis, Bath University, 1979.

58 Boehme D. Int. Conf. on Advances in Surface Coating Technology 1978 .

59 Sharp R. S., Non-Destructive Testing, Oxford University Press, 1969.

60 Van Drunen G. and Cecco V. S. NDT Int., 17, 1, 1984.

61 Sayers C. M. British J. of NDT, 26, 1, 1984, 28.

62 Almond D. P., Patel P. M. and Reiter H. J. de Physique, 1983.

63 Patel P. M. and Almond D. P. J. of Mater. Sci., 20, 1985, 955.

64 Szilard J. Ultrasonic testing, Wiley - Interscience Publication, 1982.

65 Krautkramer J. and Krautkramer H. Ultrasonic Testing of Materials 3rd edition, Springer-Verlag, 1983.

66 Mason W.P. Piezoelectric Crystals and Their Application to Ultrasonics, Van Nostrand, New York, 1950.

67 Kinsler L.E. and Fry A.R. Fundamentals of Acoustics, 2nd edition, Wiley, New York, 1962.

68 Truell R., Charless E. and Chick B.B. Ultrasonic Methods in Solid State Physics, Academic press, 1969.

69 Goebbels K., National Bureau of Standards Special Publications 596, Proc. of the First Int. Symp. on Ultrasonic Materials Characterization, NBS, Gaithersburg, Md., 1978.

70 Blitz J. Fundamentals of Ultrasonics, London, Butterworths, 1963.

71 Mason W.P. and McSkimin H.J. J. Acoust. Soc. Am., 19, 1947, 464.

72 Smith R.T. and Stephens R.W.B. Prog. in Appl. Mater. and Research, 4, 1964, 39.

73 Attenborough K. Phys. Reports, 82, 3, 1982, 179.

74 Crouther M. Project report, Bath University 1981.

75 Szilard J. Proc. 4th Int. Conf. NDT, Butterworth, 1963.

76 Gustafson S. Proc. Mat. Eval. Conf., Nat. Bur. Standards, Gaithersburg, Md. 1978.

77 Tarnoczy H. Proc. 2nd Conf. Ultrasonics, Warsaw, 1956, 91.

78 Clark A.V. and Chaskelis H.H. Ultrasonics, 19, 1981, 201.

79 Rose J.L. and Meyer P.A. Mater. Eval., 1974.

80 Frank W. and deGee A.W. Int. Conf. Advances in Surface Coatings Technology, 1978, 99.

81 Cox R.L., Almond D.P. and Reiter H. Ultrasonics, 19, 1981, 17.

82 Cox R.L., Almond D.P. and Reiter H. NDT Int., 13, 1980, 241.

83 Liptai R.G., Harris D.O. and Tatro C.A. ASTM Special Technical Publication 505, 1971.

84 Schofield B. H. ASD-TDR-63-509, Wright-Patterson Air Force Base, Dayton, part 1, 1963 - part 2, 1964.

85 Tatro C. A. and Liptai R. G. Proc. of the Symp. on Phys. and NDT, South West Research Institute, San Antonio, 1962.

86 Fisher R. M. and Lally J. S. Canadian J. of Phys., 45, 1967, 1147.

87 James D. R. and Carpenter S. H. J. of Appl. Phys., 42, 12, 1971, 4685.

88 Kiesewetter N. and Schiller P. Phys. Stat. Sol. (A), 38, 1976, 569.

89 Imanaka T., Samo K. and Shimizu M. Cryst. Lattice Defects, 4, 1973, 57.

90 Read-Hill R. E. Physical Metallurgy Principles, 2nd edition, D. Van. Nostrand Company, 1973.

91 Kuribayashi K., Tanaka H., Kishi T., Horiuchi R. and Kato A. Proc. 3rd Acoustic Emission Symp., Tokyo, 1976.

92 Hatano H. J. Appl. Phys. , 48, 10, 1977, 4397.

93 Mohamed I. J., Lambson E. F., Miller A. J. and Saunders G. A., Phys. Letters, 71A, 1, 1979, 115.

94 Zammit-Mangion L. Ph. D. Thesis, Bath University, 1983.

95 Fredreick J. R. AFML-TR-72-114 Air Force Materials Laboratory, Wright-Patterson Air Force Base, Ohio, 1972.

96 Kishi T., Tanaka H. and Obata Y. Proc. Conf. Physical and Metallurgical Aspects of Acoustic Emission, Chelsea College, 1977.

97 Fleishman P., Rouby D., Lakestani F. and Boboux I. C. Non-Destr. Test. , 8, 1975, 241.

98 Agarwal A. B. L., Fredrick J. R. and Felback D. L. Metall. Trans., 1, 1970, 1069.

99 Scruby C. B., Wadley H. and Sinclair J. E. AERE Harwell, HL80/1787 (C14), 1980.

100 Scruby C. B., Wadley H. N. G., Rusbridge K. and Stockham-James D. AERE Harwell HL81/2967 (C14), 1981.

101 Scruby C.B. , Jones C. , Titchmarsh J.M. and Hadley H.N.G. Metal Science , 15, 1981, 241.

102 Mck Cousland S. and Scala C.M. Metal Science , 15, 1981, 609.

103 Byerlee J.D. and Peselnick L. "Elastic Shocks and Earthquaks", Naturwissenschaften, 57, ,2, 1970, 82.

104 Kneham R. , Steinbrech R. and Schaarwachter W. Mater. Sci. and Eng., 61, 1983, 17.

105 Ingham T. , Stott A.L. and Cowan A. Inst. J. Pressure Vessels Piping, 2, 1, 1974, 31.

106 Mc Bride S.L. , Mc Lachlan J.W. and Paradis B.P. Journal of Non-Destr. Eval., 2, 1, 1981, 35.

107 Nozue A. and Kishi T. J. of Acoustic Emission , 1, 1, 1982, 1.

108 Birchon D. Br. J. Non-Destr. Test. 18, 3, 1976, 66.

109 Stone D.E.W. and Dingwall P.F. NDT Int., 10, 2, 1977, 51.

110 Curtis G.I. AERE Harwell Report AERE - R 7686, 1974.

111 Pollock A.A. Non-Destr. Test., 6, 5, 1973, 264.

112 Breckenridge F.R. , Tschiegg C.E. and Greenspan M. J. of Acoustic Society of America, 57, 3, 1975, 626.

113 Hsu N.N. , Simmons J.A. and Hardy S.C. Mater. Eval. ,35 ,1977, 100.

114 Shibata M. Mater. Eval. ,42 , 1984, 107.

115 Green (Jr) R.E. Mechanics of Non-Destructive Testing, editor W.W. Stinchcomb, Plenum Press, 1980.

116 Kino G.S. D.K. Lenon report NADC-81087-60 , Naval Air Development Center, Warminster, Pennsylvania, 1981.

117 Mullin J.V. and Mehan R.L. J. Test. Eval., 1, 3, 1973, 215.

118 Graham L.J. and Alers G.A. STP 571, ASTM 1975, 11.

119 Curtis C.J. Non-Destr. Test. 8, 1975, 249.

120 Phillips M.G. Private comunications.

121 Hill R. and Stephens R.W.B. Acoustica 31, 1974, 224.

122 Pollock A. A. Int. Advances in Non-Destructive Testing , 7, edited by McGonnagle W. J.

123 Pollock A. A. and Smith B. Non-Destr. Test., 5, 6, 1972, 348.

124 Phillips M. G. and Harris B. Proc. Conf. of Institute of Chemical Engineers, 1980.

125 Dickson R. F. , Jones C. J. , Harris B. , Reiter H. and Adam T. 1st Int. Symp. on Acoustic Emission from Reinforced Composites, The Society of the Plastic Industry , Inc., 1983.

126 Physical Acoustics Corporation Litrature.

127 Adams H. 37 Annual Conf., Reinforced Plastics/Composite Institute, 1982.

128 Phillips M. G. , Guild F. J. , Ackerman F. J. and Harris B. 37th Annual Conf., Reinforced Plastics/Composites Institute, the Society of Plastic Industry, Inc., 1982.

129 Phillips M. G., Guild F. J, Moghisi M. and Harris B. Polymer Engineering Directorate Review Meeting, 1985, 1.

130 Fuwa et all Composites - Standards Testing and Design, Proceding Conference, NPL 8/9, 1974, 77.

131 Sachse W. and Hsu N. Physical Acoustics, Mason W. P. (editor), 14, Academic Press, New York 1979.

132 Hsu N. and Breckenridge F. R. Mater. Eval., 39, 1, 1981, 60.

133 Moghisi M. and Squire P. T. J. Phys., E: Sci. Instrum. , 13, 1980, 1090.

134 McBride S. L. and Hutchison T. S. Canadian J. of Phys., 57, 17, 1976, 1824.

135 Hsu N. United State Patent 4,018,084, 1977.

136 Scruby C. B. , Wadley H. N. G. , Dewhurst R. J. , Hutchins D. A. and Palmer S. B. AERE-R-10003 , Harwell, 1981.

137 Moghisi M. and Almond D. P. NDT Int., 16, 1983, 9.

138 Moghisi M. and Phillips M.G. Internal Report Bath University, 1985.

139 Phillips M.G., Ackerman F.J. and Harris B., Con. Proc. Ultrasonic International 1981, IPC, Science and Technology Press.

140 Moghisi M., Internal Report, Bath University, 1985.

141 Papadakis E.P. Physical Acoustics Mason vol iv - part B, 1968.

142 Clark A.V. and Chaskelis H.H. Ultrasonics 20, 1982, 173.

143 McPherson R., Thin Solid Films, 112, 1984, 89.

144 Stumpf F.B. Analytical Acoustics, Ann Arbor Science Publishers INC/The Butterworth group, 1980.

145 Harris S.J., Cobb R.C. and James H., 10th Int. Thermal Spraying Conf., 1983, 245.

146 Moghisi M., Bowman S.H., and Phillips M.G. Internal Report, School of Materials Science, Bath University, 1983.

147 Keshtvarzi A., Ph.D. Thesis, Bath University, 1977.

148 Munn S., Project Report, Bath University, 1978.

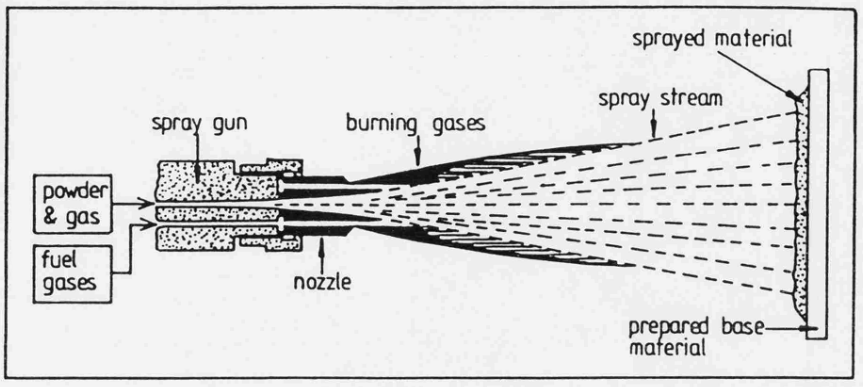

Fig 2.1 Cross section of a typical powder flame gun.
(After James and Daryl Ref. 16)

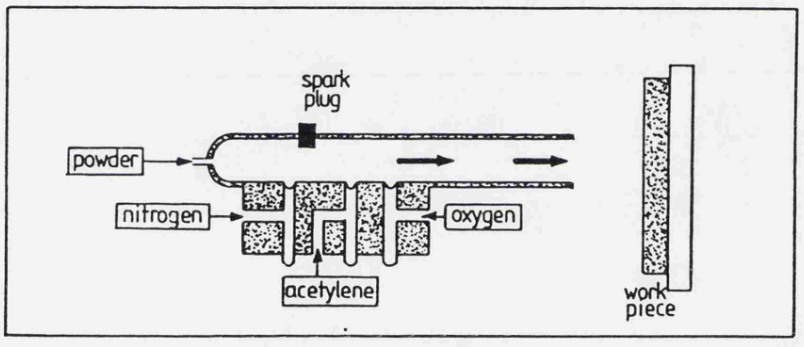

Fig 2.2 Schematic diagram of a detonation gun.
(After Mayer Ref. 18)

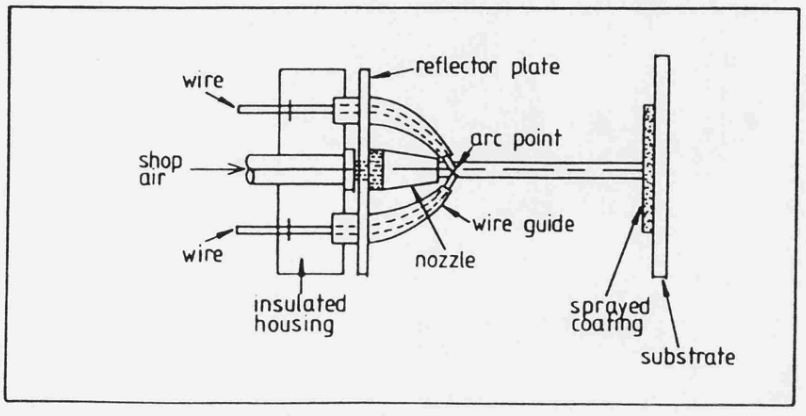

Fig 2.3 Typical electric-arc spray device.
(After James and Daryl Ref. 16)

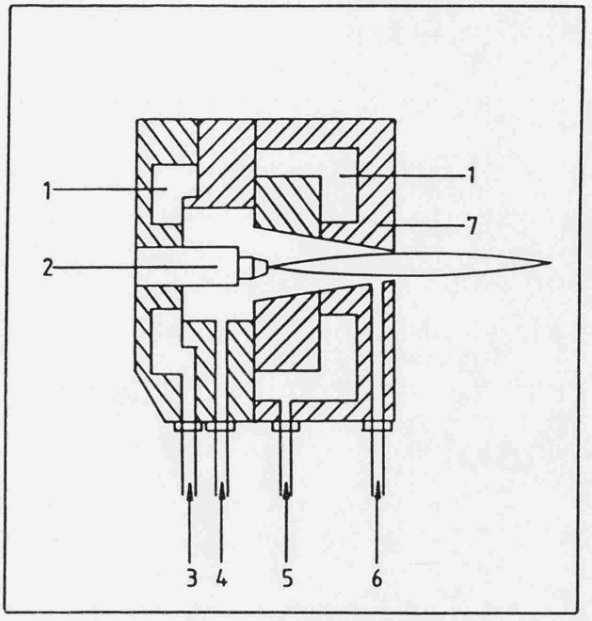

(1) Cooling chamber
(2) Cathode
(3) Power and water outlet
(4) Arc gas inlet
(5) Power and water inlet
(6) Powder feed inlet
(7) Anode

Fig 2.4 Schematic diagram of a plasma spray gun.

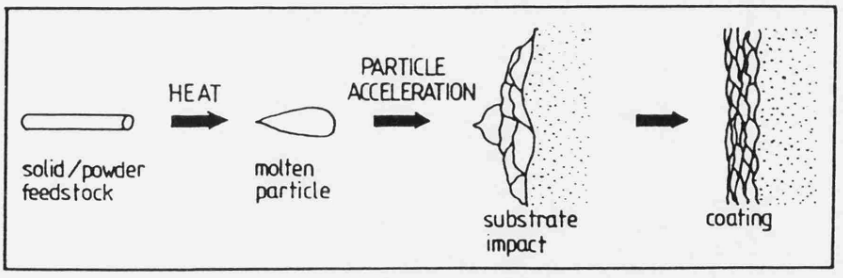

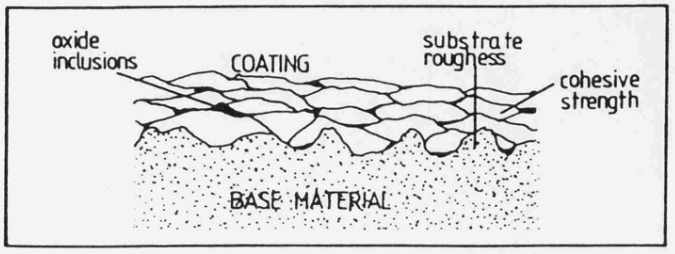

Fig 2.5 Schematic diagram of the formation of thermal sprayed coatings. (After Mayer Ref. 18)

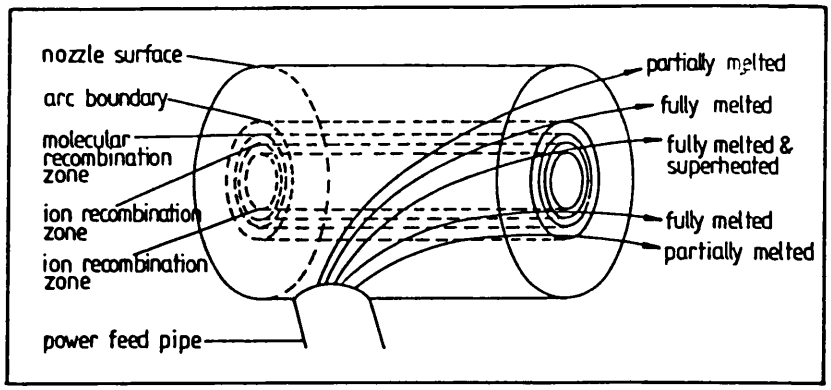

Fig 2.6 Schematic diagram of a section through a plasma jet, showing recombination zones and possible particle trajectories. (After Atkins Ref. 30)

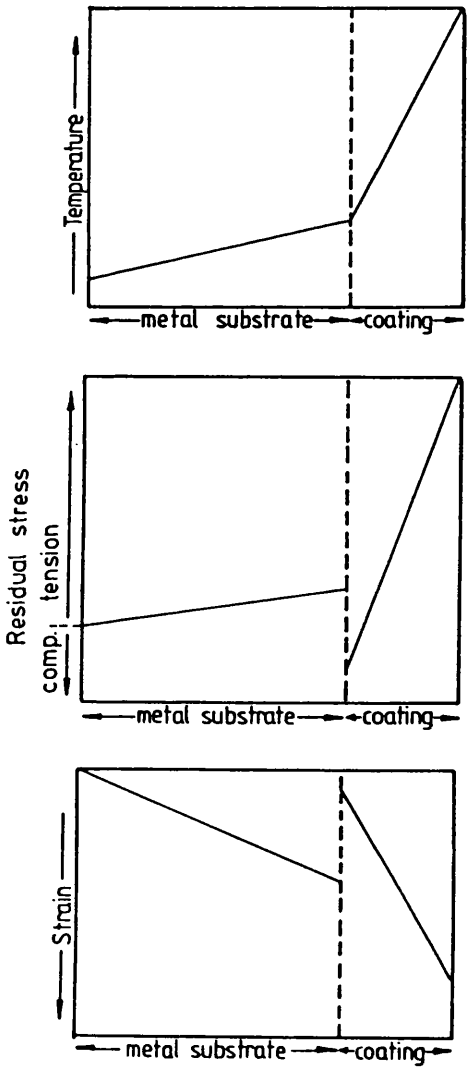

Fig 2.7 Temperature and stress profile in plasma sprayed coatings. (After Marynowski Ref. 32)

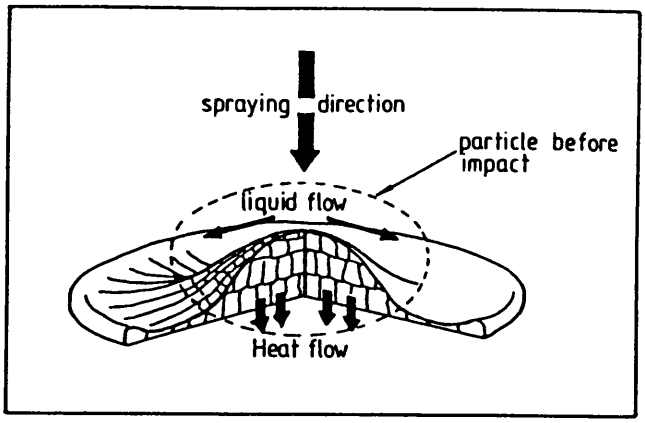

Fig 3.1 A schematic diagram of a particle after impinging onto a flat surface. (After Safai and Herman Ref. 23)

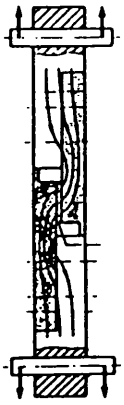

Fig 3.2 Shear testing of plasma sprayed coatings to determine shear strength of sprayed coatings. (After Boehne Ref. 58)

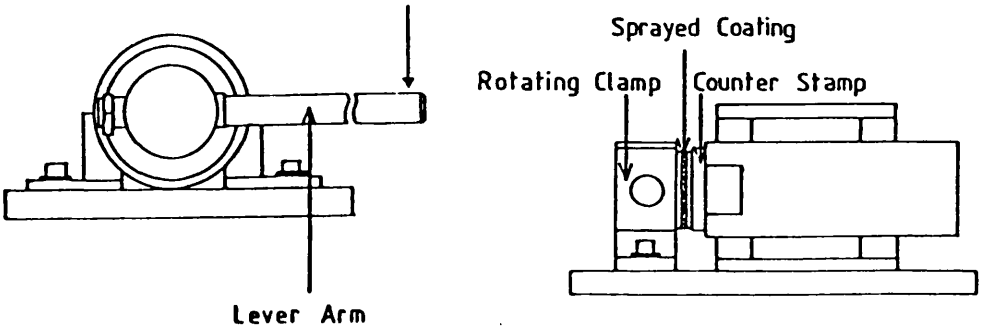

Fig 3.3 Torsion testing fixture to determine shearing strength of sprayed coatings. (After Boehne Ref. 58)

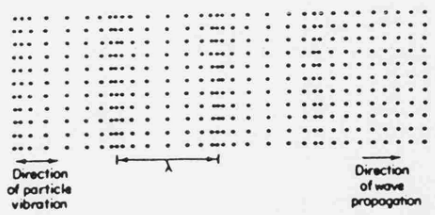

Fig 4.1 Schematic diagram of a pressure wave. (After Krautkramer Ref. 65)

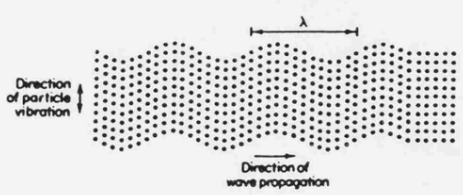

Fig 4.2 Schematic diagram of a transverse wave. (After Krautkramer Ref. 65)

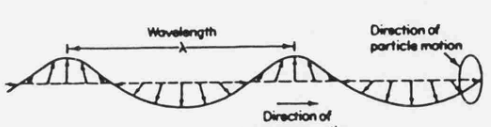

Fig 4.3 Schematic diagram of a surface wave in steel. (After Krautkramer Ref. 65)

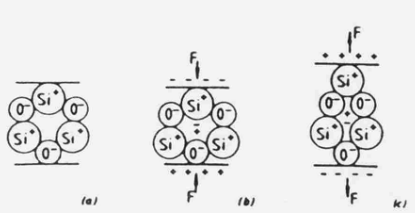

Fig 4.4 Piezoelectric behaviour of an elementary cell in a quartz crystal. (a) Cell unstressed (b) Cell compressed (c) Cell extended. (After Szilard Ref. 64)

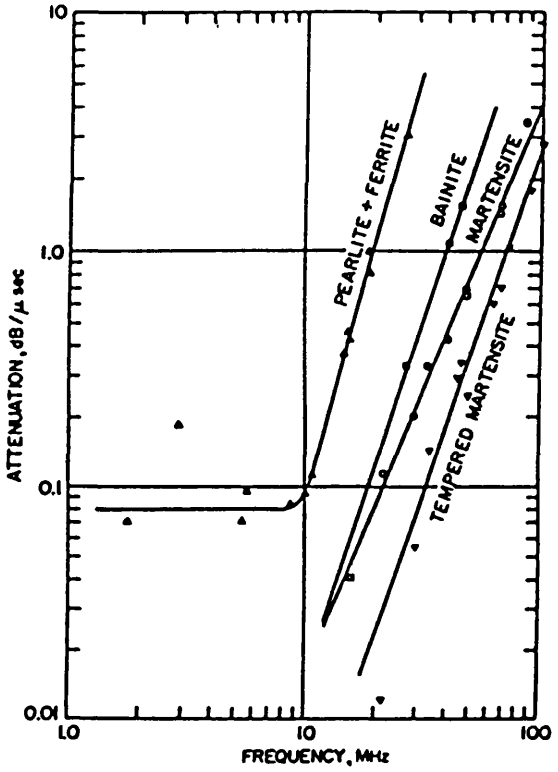

Fig 4.5 Attenuation of longitudinal ultrasonic waves versus frequency in SAE 4150 steel with microstructure as a parameter. All specimens were austenitized under the same conditions. (After Papadakis Ref. 141)

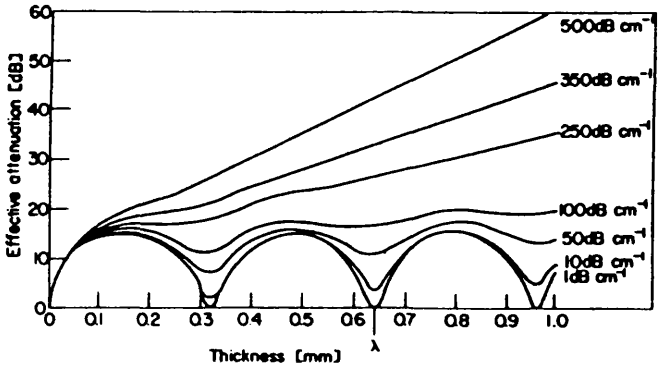

Fig 4.6 Theoretical relationship between attenuation of 10 MHz ultrasound and thickness of aluminium of specific attenuation. (After Cox Ref. 57)

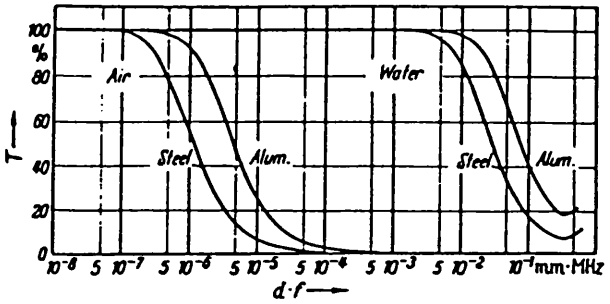

Fig 4.7 Transmittance through a gap in steel and aluminium when filled with air and water, plotted against the product of gap thickness and frequency. (After Krautkramer Ref. 65)

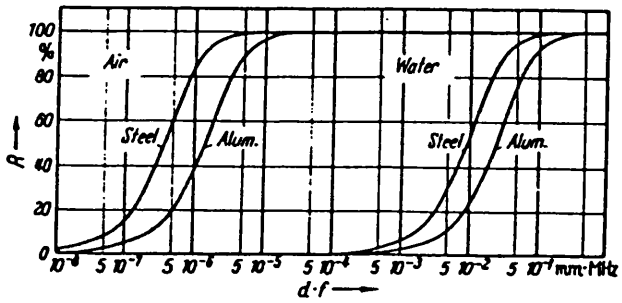

Fig 4.8 Reflection through a gap in steel and aluminium when filled with air and water, plotted against the product of gap thickness and frequency. (aAfter Krautkramer Ref. 65)

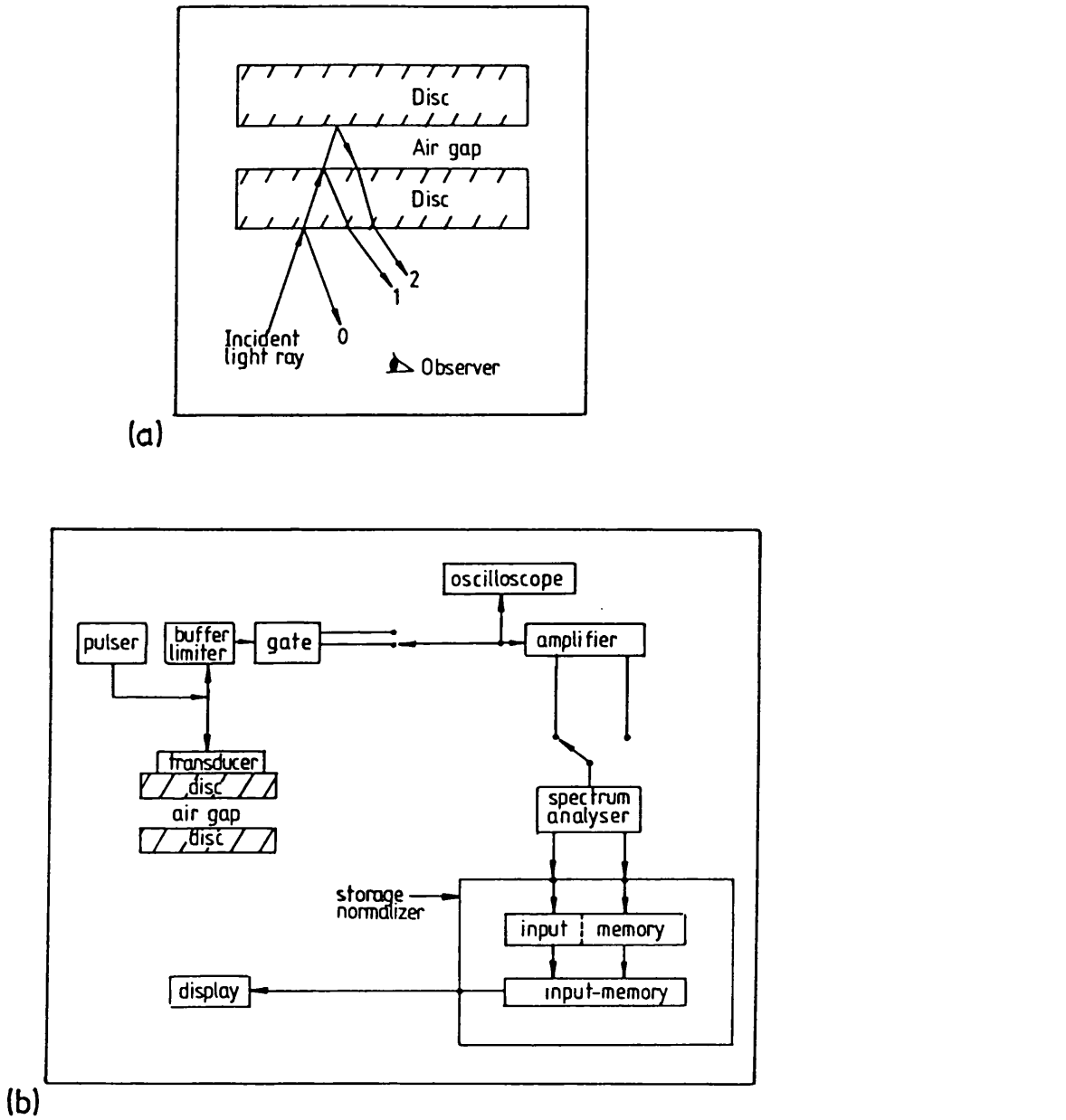

Fig 4.9 a) Method of using light to measure gap thickness. b) Block diagram of the system used to measure reflection coefficient. (After Clark Ref. 78)

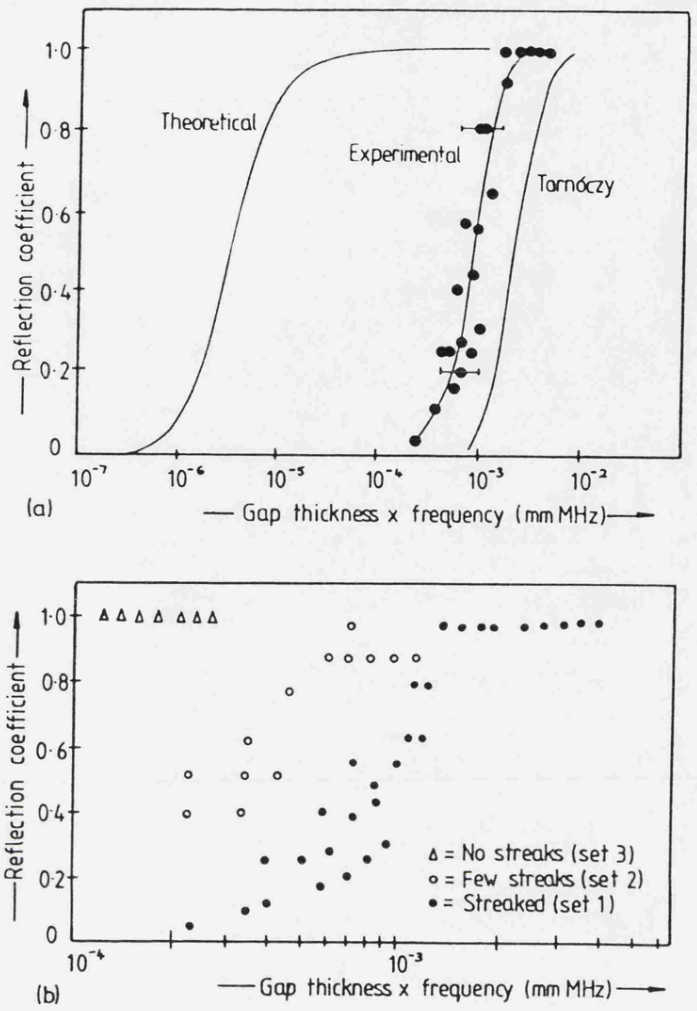

Fig 4.10 Comparison of the theoretical and experimental results of Clark. a) Reflection coefficient as predicted from acoustic theory and as measured at a frequency of 2.5 MHz, b) results of measurements of the reflection coafficient made with discs of varying cleanness. (After Clark and Chaskelis Ref. 142)

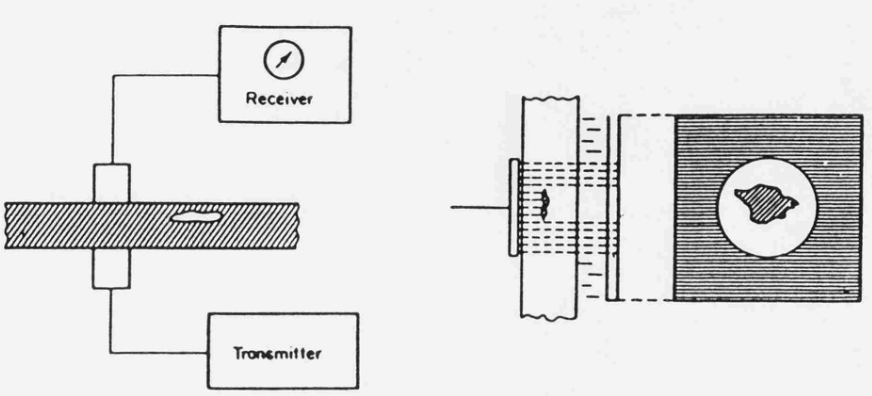

Fig 4.11 Schematic diagram of the intensity method for detecting flaws in through transmission. (After Szilard Ref. 64)

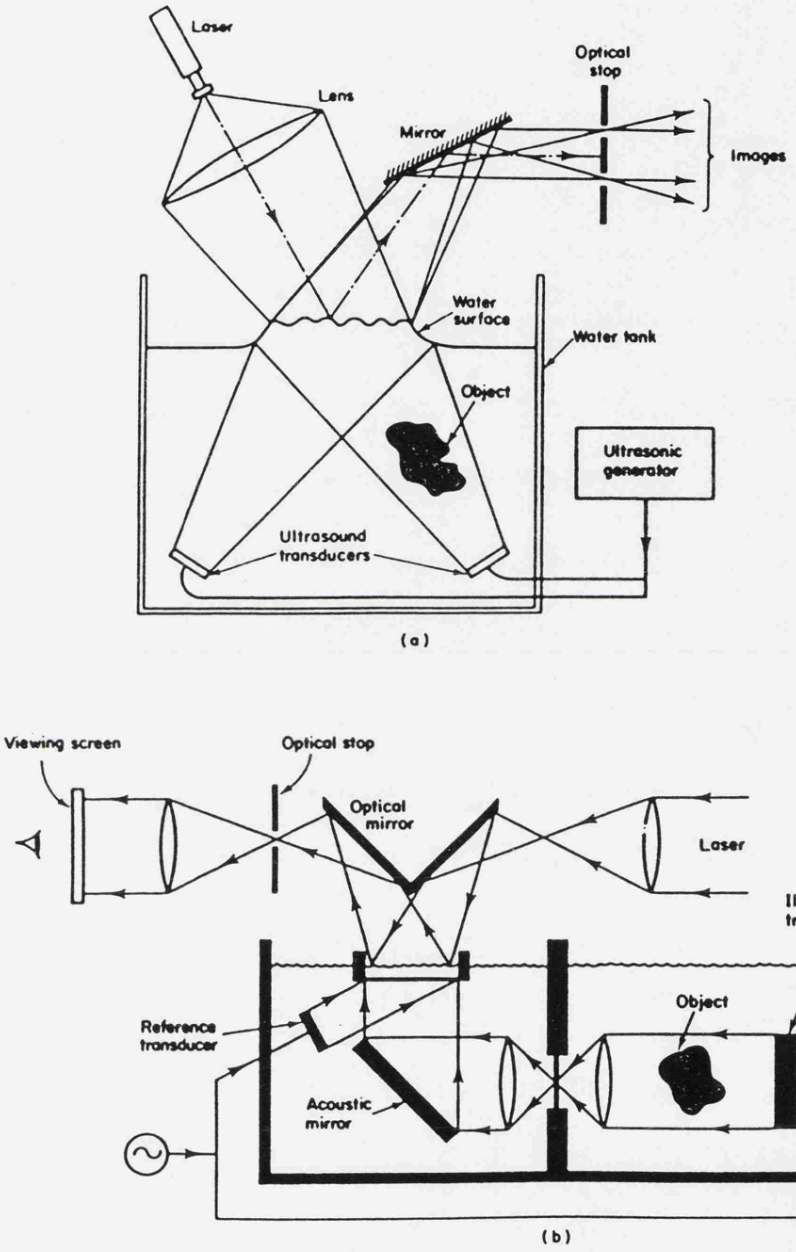

Fig 4.12 a) Elementary liquid surface levitation system. b) Commercial version of liquid surface levitation system (After Szilard Ref. 64)

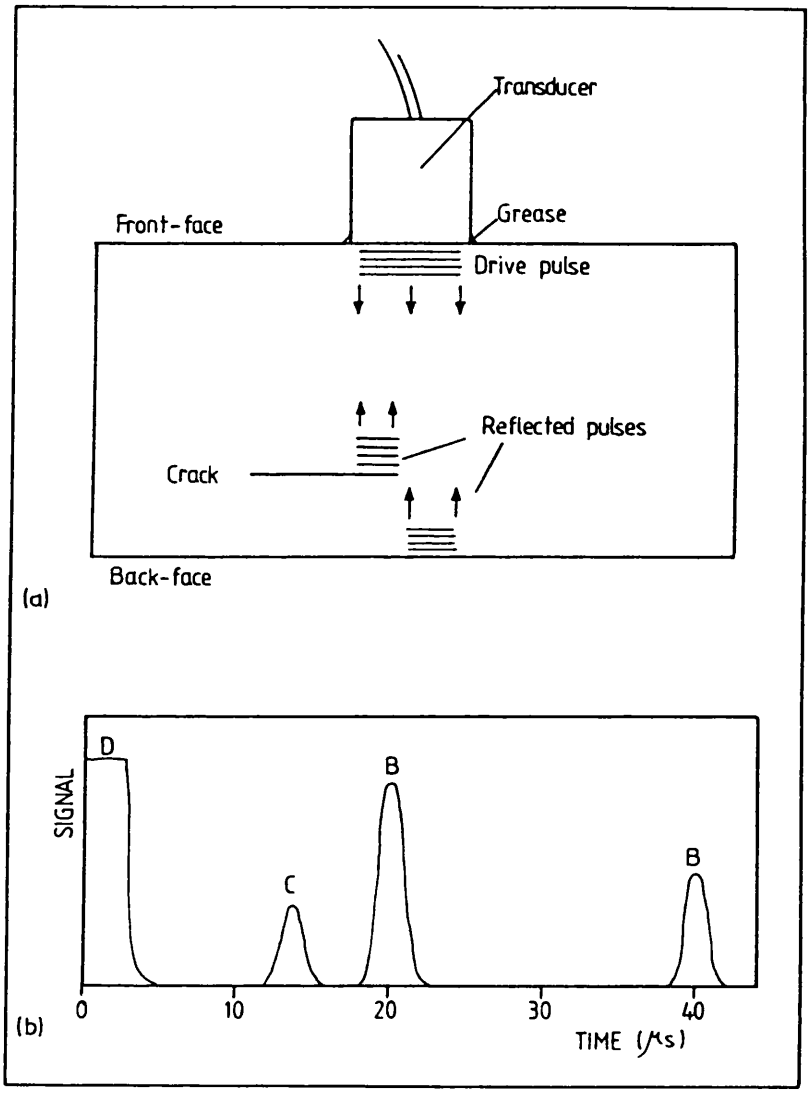

Fig 4.13 a) Schematic diagram illustrating the use of the reflection pulse-echo technique for the detection of a crack. A corresponding oscilloscope trace of signal vs time, is shown as Fig 4.13b . The crack is revealed as an echo C appearing between the drive pulse D and first back-face reflection echo B . (After Almond Ref. 5)

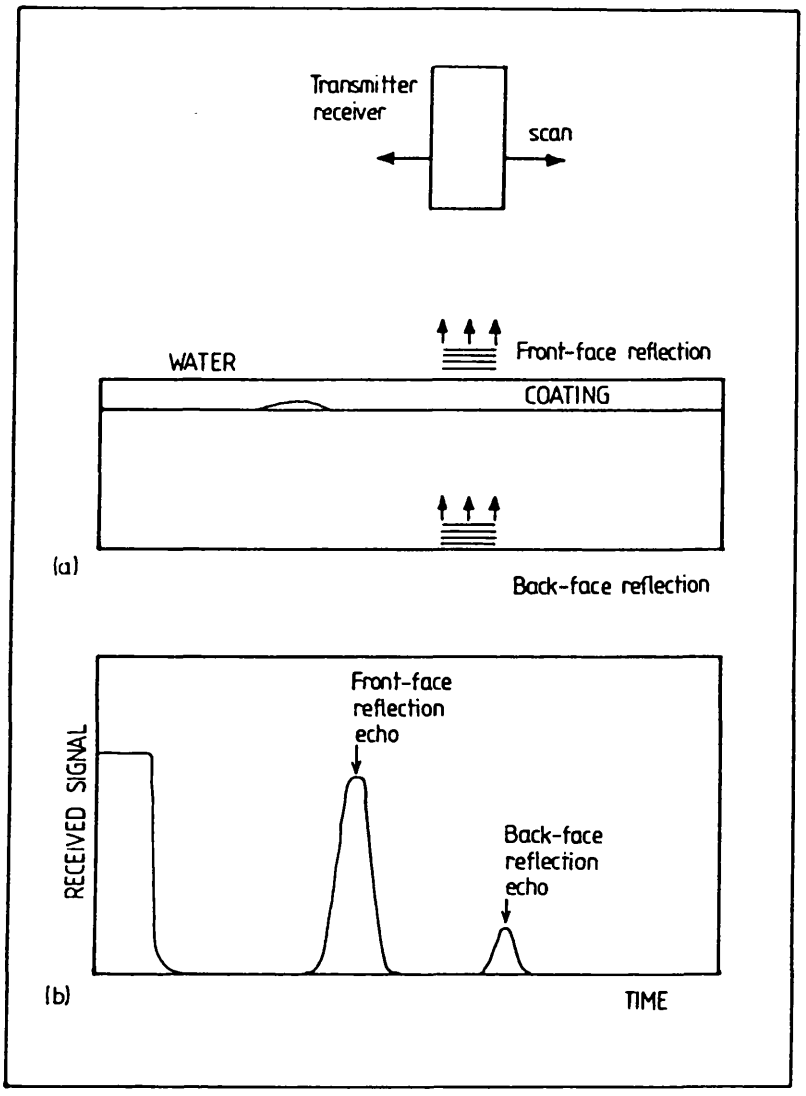

Fig 4.14 A schematic diagram of a back-face reflection system. A corresponding oscilloscope trace showing front and back-face reflectionechoes are also shown. (After Almond Ref. 5)

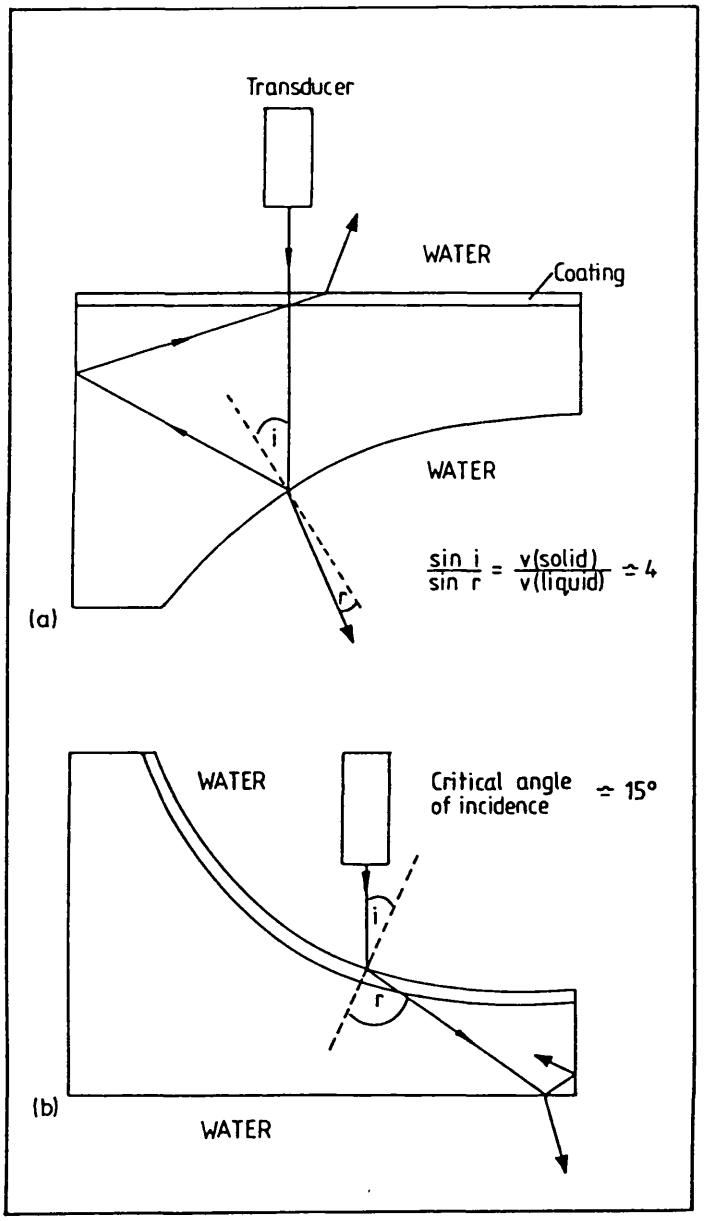

Fig 4.15 Acoustic beam paths in components of irregular geometry immersed in water. a) Incident beam normal to a coated surface. b) Incident beam at an angle to a coated surface. (after Almond Ref. 5)

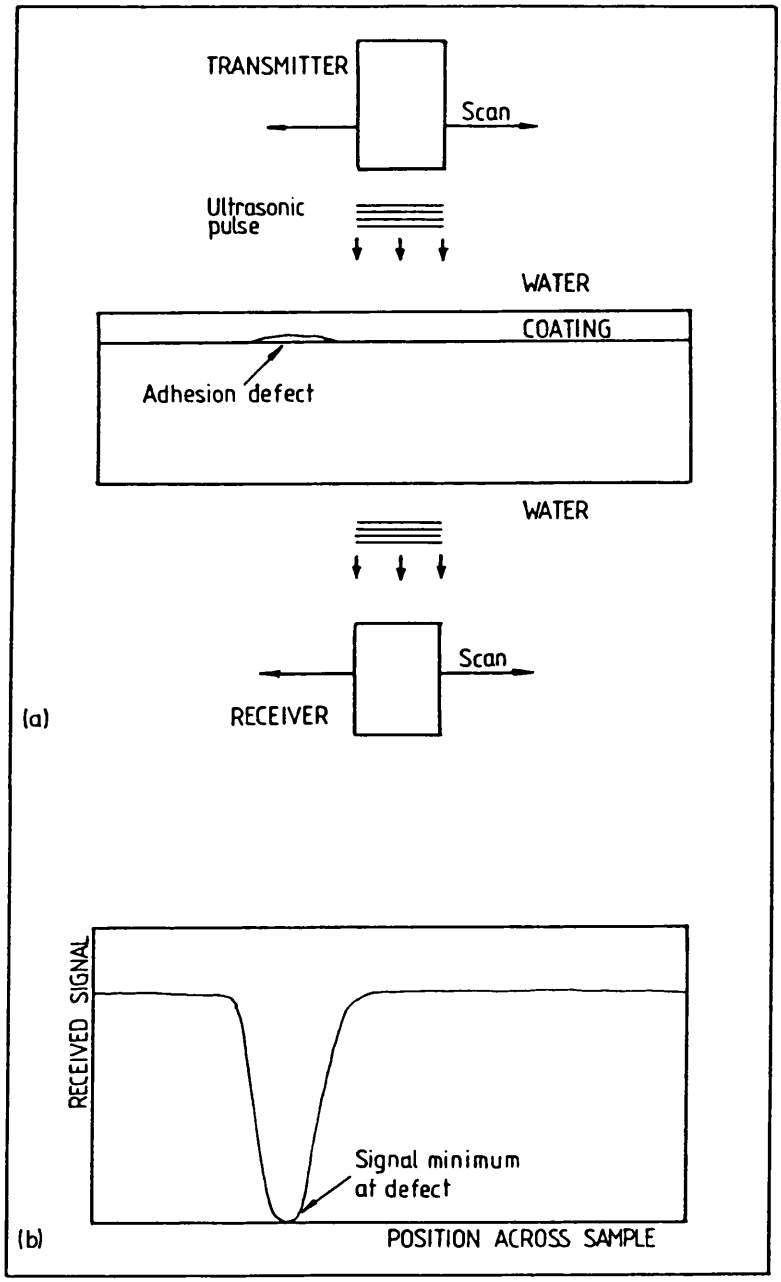

Fig 4.16 A schematic diagram of a transmission ultrasonic pulse-echo system. The variation of the ultrasonic signal transmitted through the sample to thr receiver is shown in Fig 4.16b. (After Almond Ref. 5)

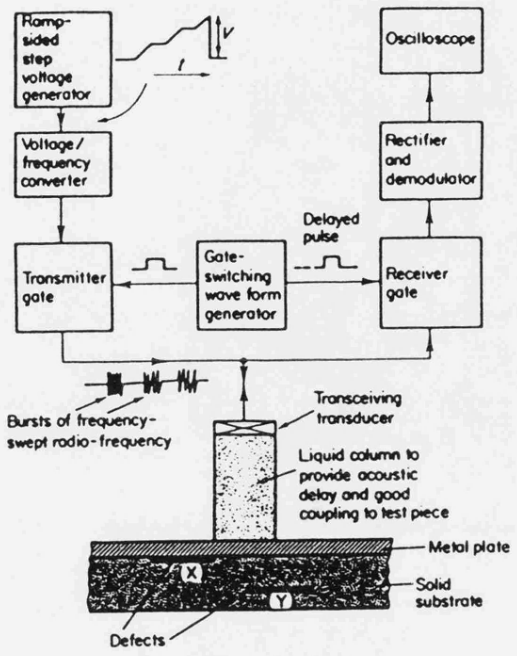

FIG 4.17a Basic system design for the resonance through-transmission technique

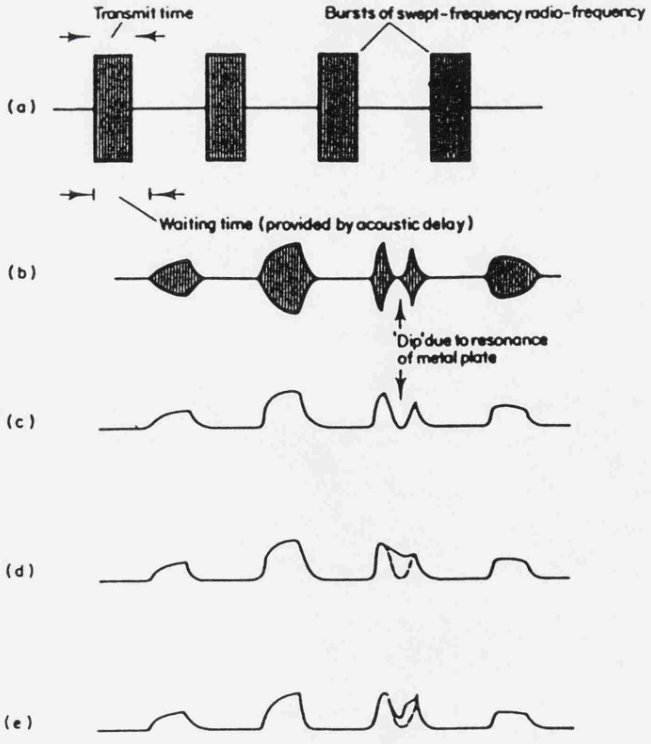

Fig 4.17b Typical wave forms for the resonance through-transmission system. a) Transmitted wave form; b) reflected wave form; c) rectified and demodulated reflected signal; d) effect on the resonance dip due to a defect close behind metal plate; e) defect a further depth behind plate. (After Szilard Ref. 64)

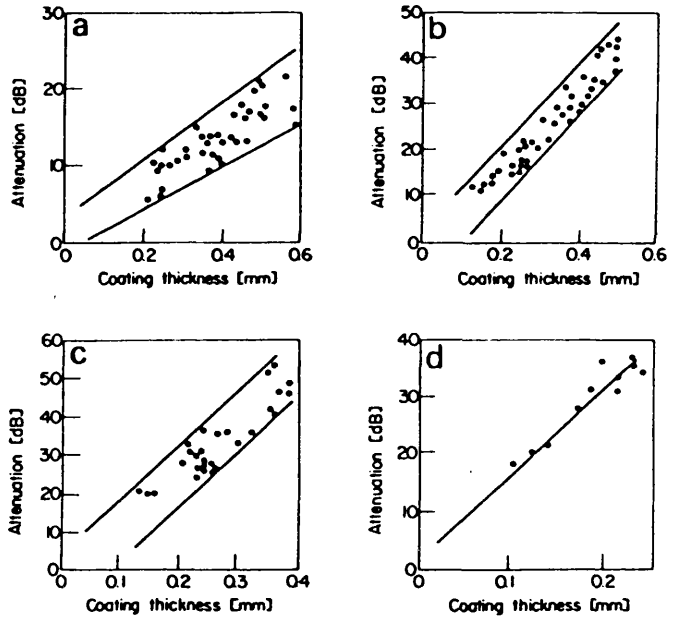

Fig 4.18a Attenuation of ultrasound at a) 2.5, b) 5, c) 10 and d) 15 MHz in samples of sprayed molybdenum of different thickness. (After Cox et al Ref. 81)

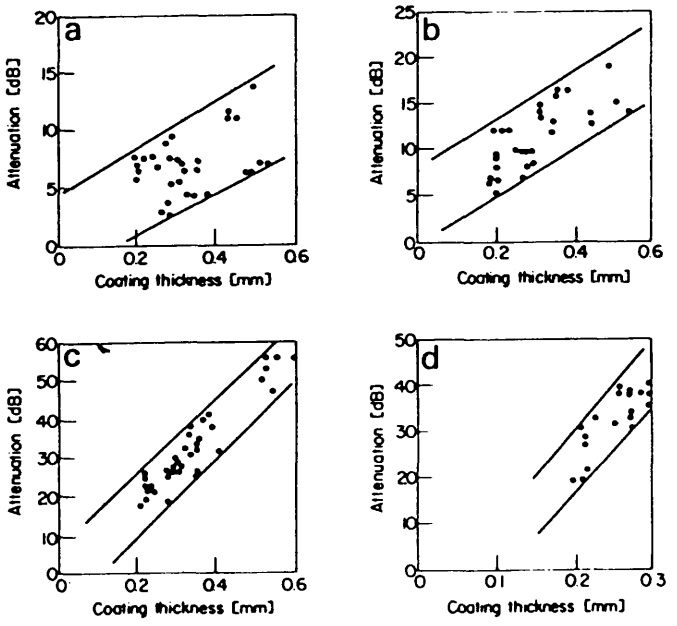

Fig 4.18b Attenuation of ultrasound at a) 2.5, b) 5, c) 10 and d) 15 MHz in samples of sprayed nickel aluminide of different thicknesses. (After Cox et al Ref. 81)

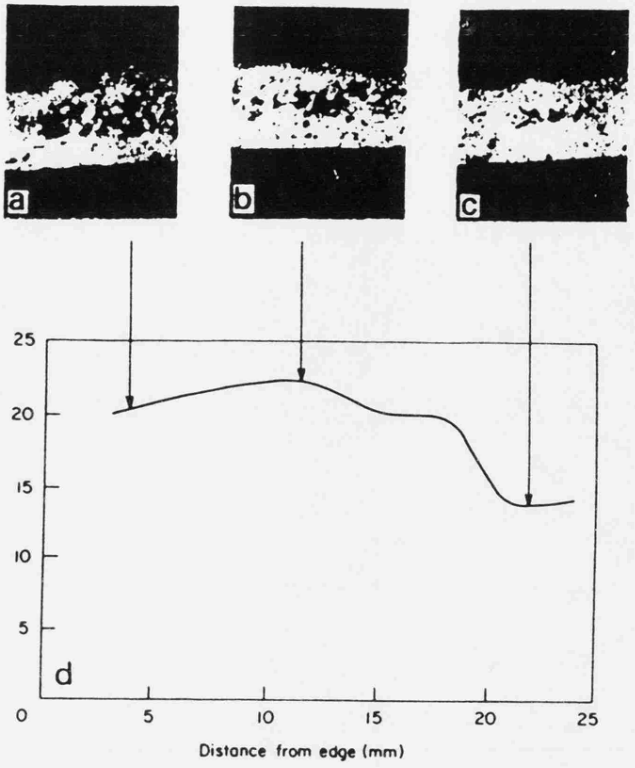

Fig 4.19 Microstructure of sprayed aluminium (X 30) and corresponding attenuation values at 5 MHz. (After Cox et al Ref. 81)

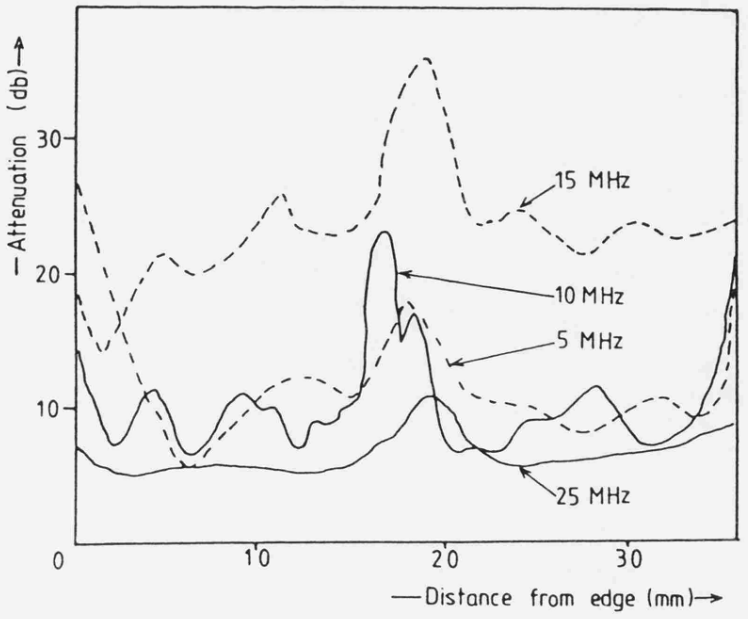

Fig 4.20 Attenuation traces of transmitted ultrasound through an aluminium coated sample with a bonding defect. (After Cox et al Ref. 82)

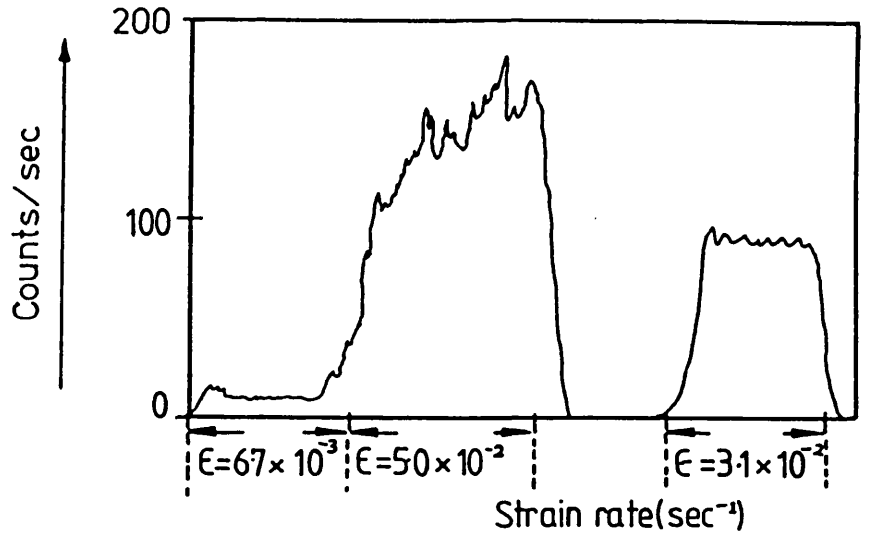

Fig 5.1 The rate of emission of the largest acoustic pulses from Mg single crystal as a function of strain rate. (After Fisher and Lally Ref. 86)

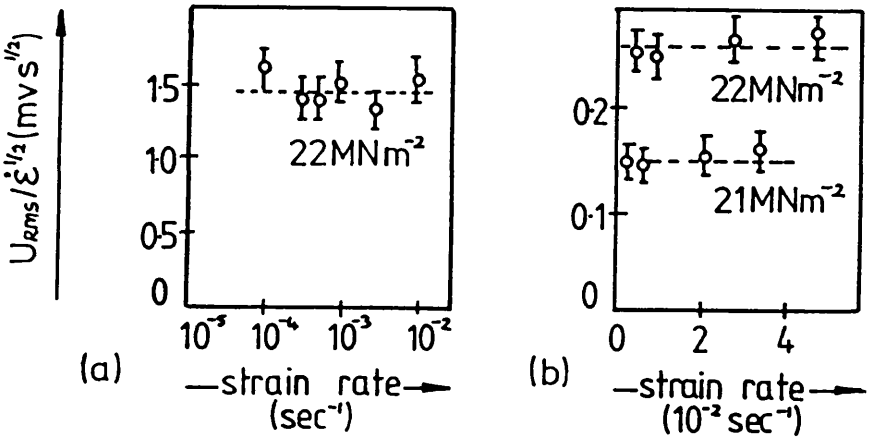

Fig 5.2 Strain rate dependence of the acoustic emission of AL 99.99% (a) 140 KHz transducer (b) transducer 500 KHz. (After Kieswetter and Shiller Ref. 86)

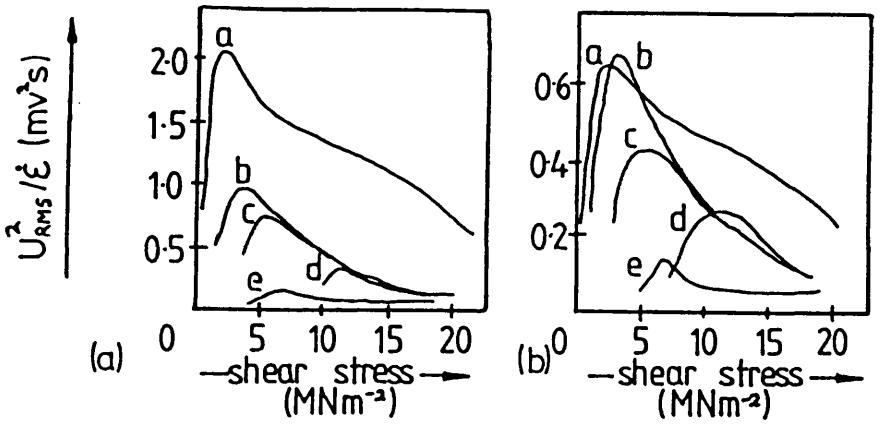

Fig 5.3 Dependence of acoustic emission on the resolved stress for 99.99% Al, (a) single crystal, (b) polycrystal (grain size 2mm), (c) polycrystal (grain size 0.2 mm), (d) polycrystal (without anealing), (e) AL 99.5% polycrystal (grain size 0.05 mm). (a) 140 KHz transducer, (b) 900 KHz transducer. (After Kieswetter and Schiller Ref. 88)

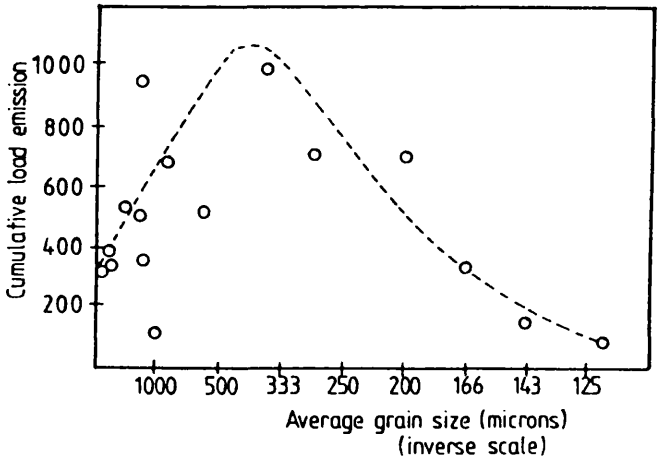

Fig 5.4 Cumulative AE emission vs grain size for 99.99% Al. (After Fredreick Ref. 95)

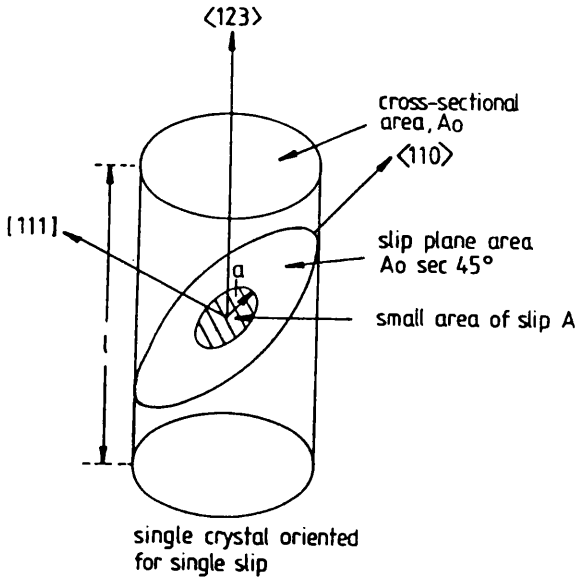

Fig 5.5 Schematic diagram showing the expansion of a small dislocation loop on a <110> [111] slip system in a single crystal. (After Scruby et al Ref. 99)

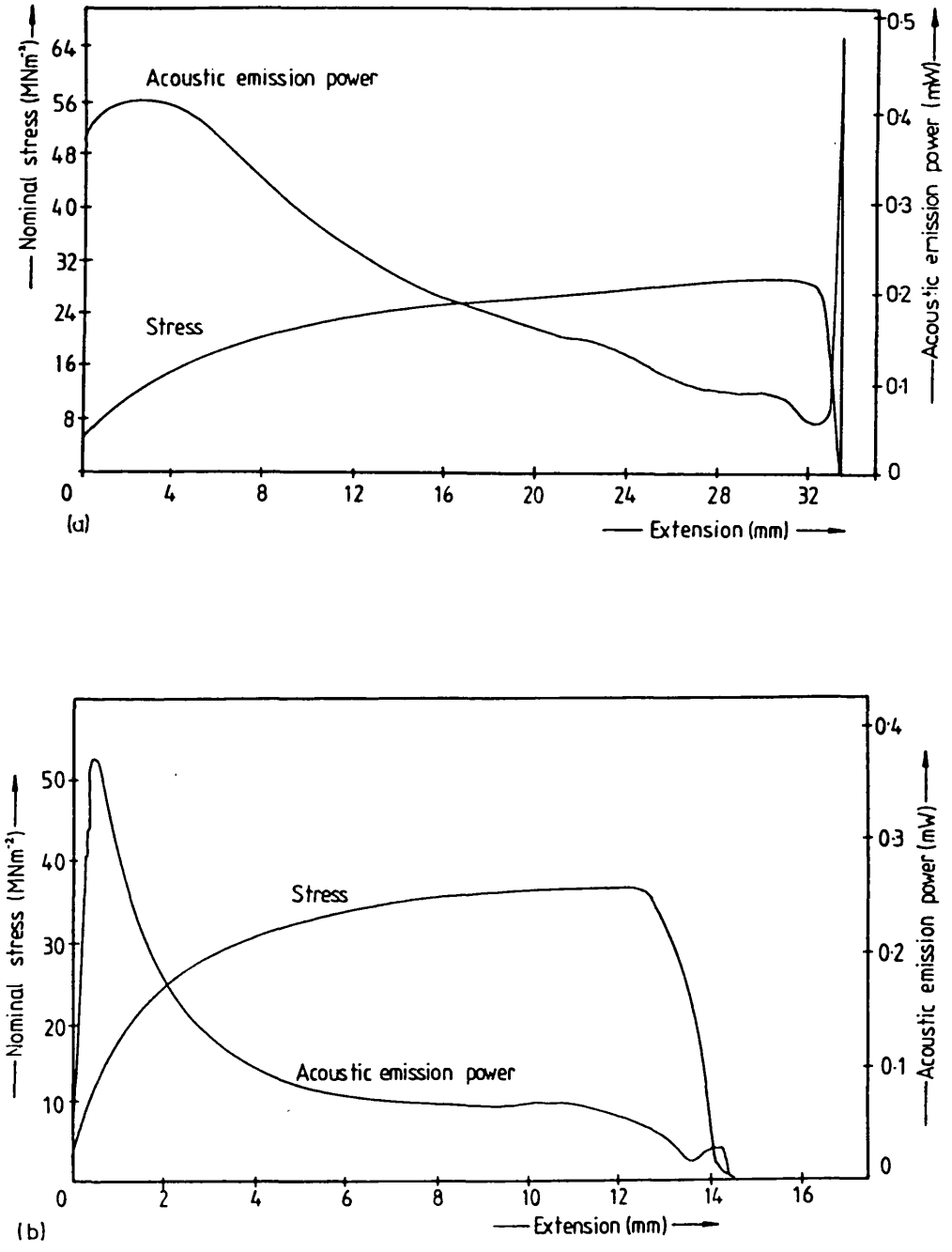

Fig 5.6 Acoustic emission power and stress as a function of extension for an aluminium (a) single crystal (b) a polycrystalline specimen with 660 micrometer grain size. (After Scruby et al Ref. 99)

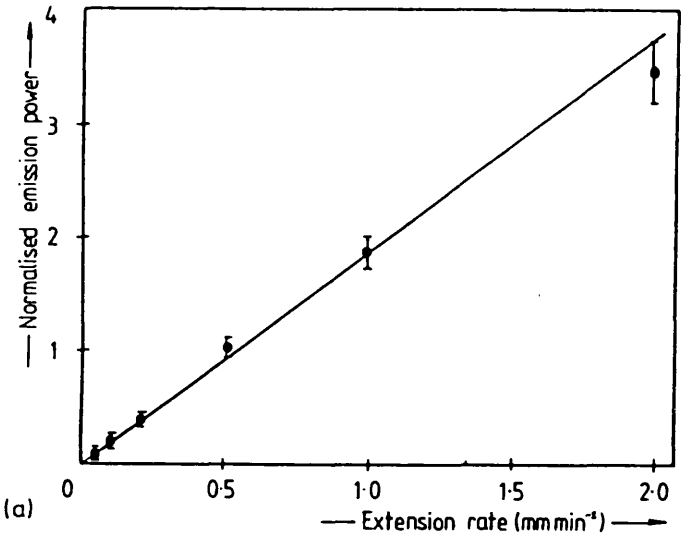

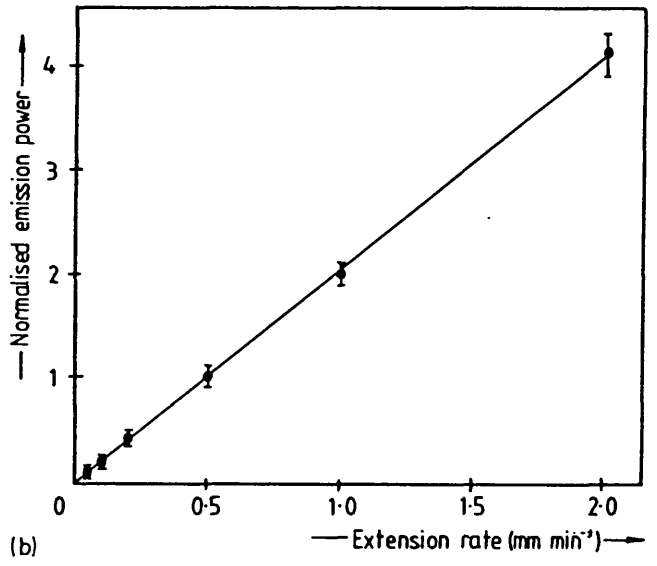

Fig 5.7 The extension rate dependence of the acoustic emission power from 99.999% aluminium (a) polycrystalline (b) single crystals. (After Scruby et al Ref. 99)

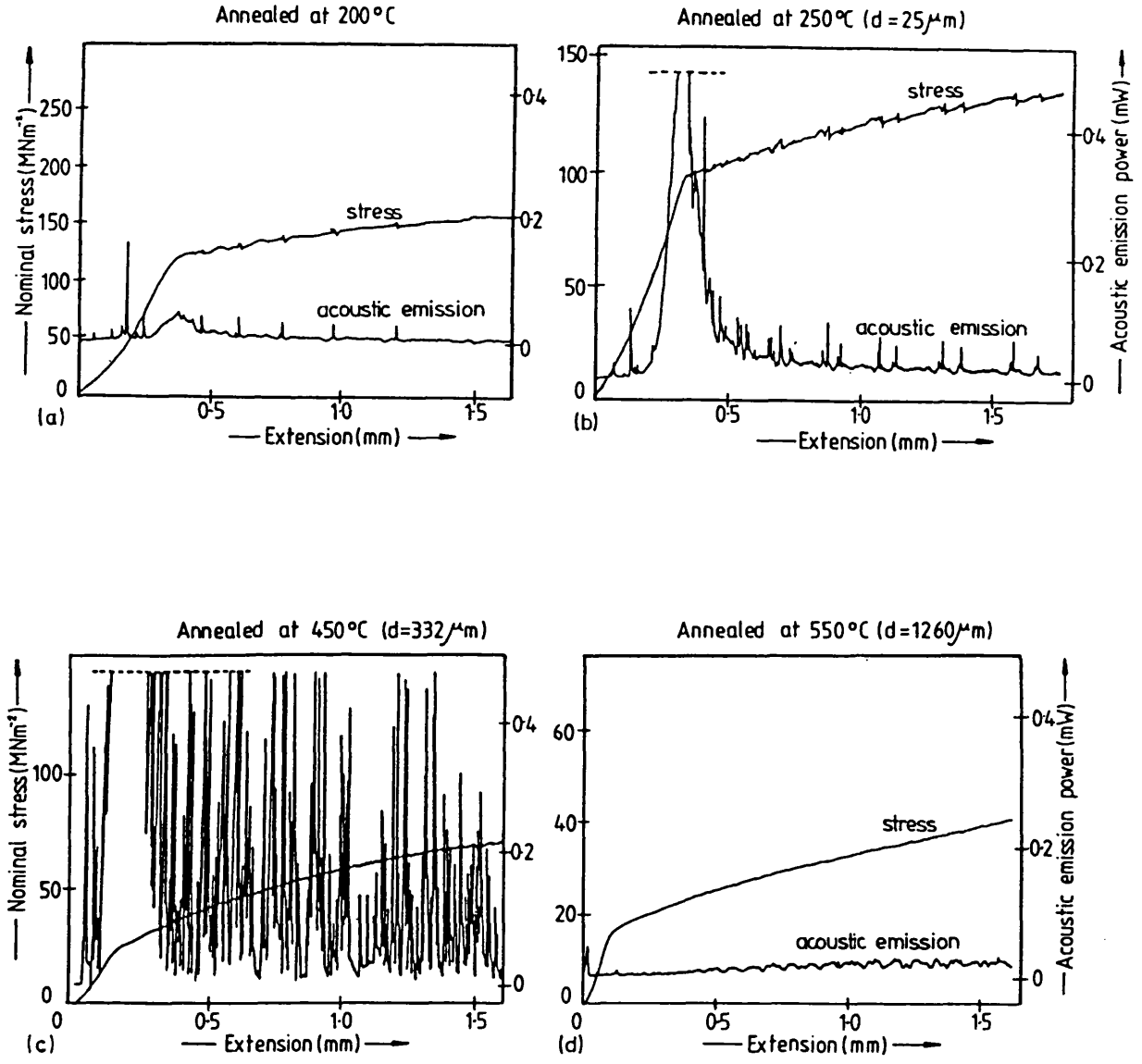

Fig 5.8 Acoustic emission power as a function of extension for AL 1.3 wt% Mg with four different grain sizes, (a) annealed at 200°C, (b) annealed at 250°C d<25 micrometer, (c) annealed at 450°C d=332 micrometer, (d) annealed at 550°C d=1260 micrometer. (After Scruby et al Ref. 99)

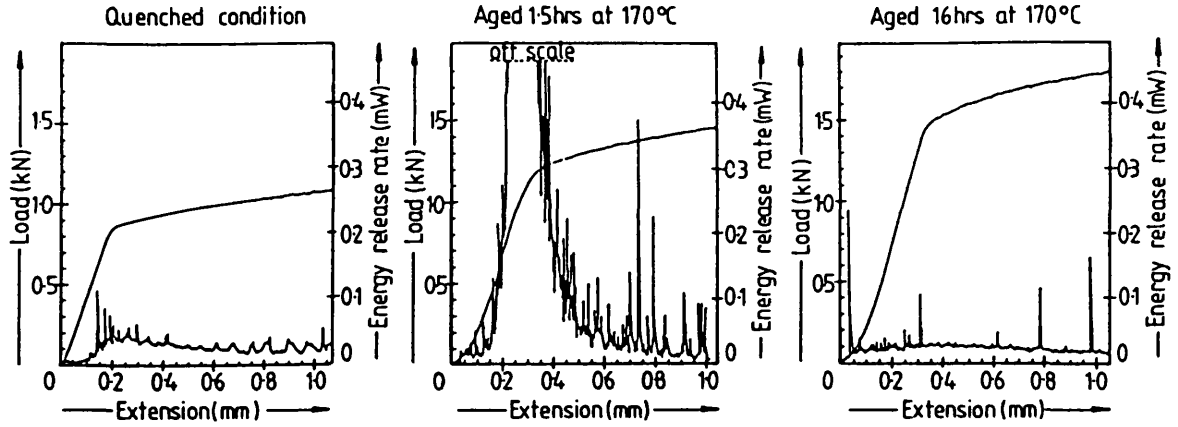

Fig 5.9 Acoustic emission as a function of extension for Al 4wt% Cu in the quenched condition and after ageing at 170°C. (After Scruby et al Ref. 100)

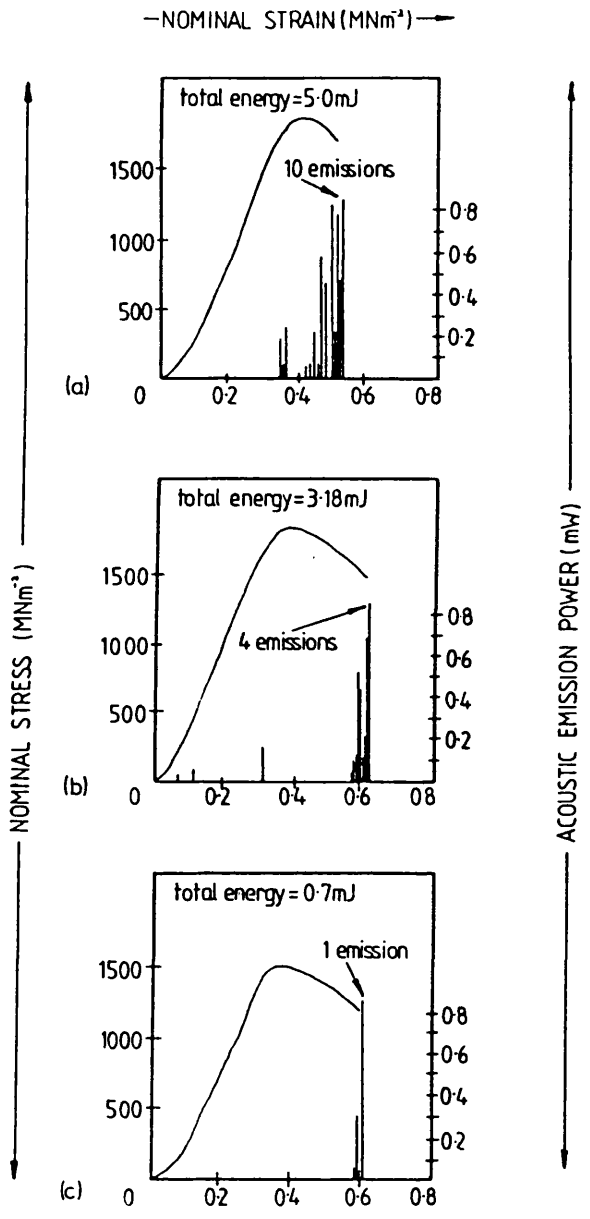

Fig 5.10 Strain dependence of stress and acoustic emission power for A533B steel austenitized 1 hour at 1000°C., and quenched in, (a) iced-brine, (b) water, (c) oil. (After Scruby et al Ref. 101)

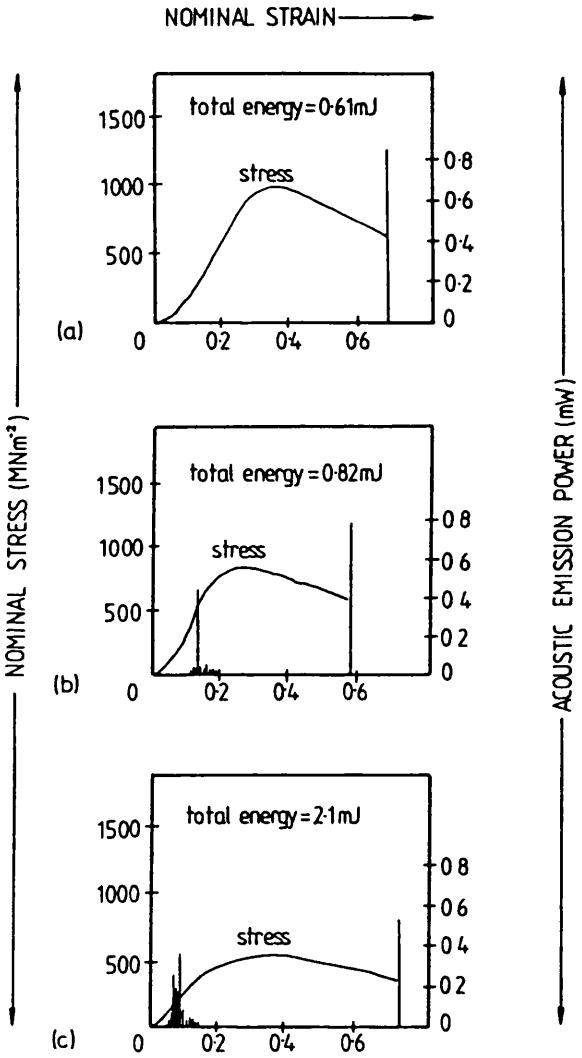

Fig 5.11 Strain dependence of stress and acoustic emission power for A533B composition steel, water quenched and tempered at 650°C for various times, (a) 6 minutes, (b) 8 hours, (c) 167 hours. (After Scruby et al Ref. 101)

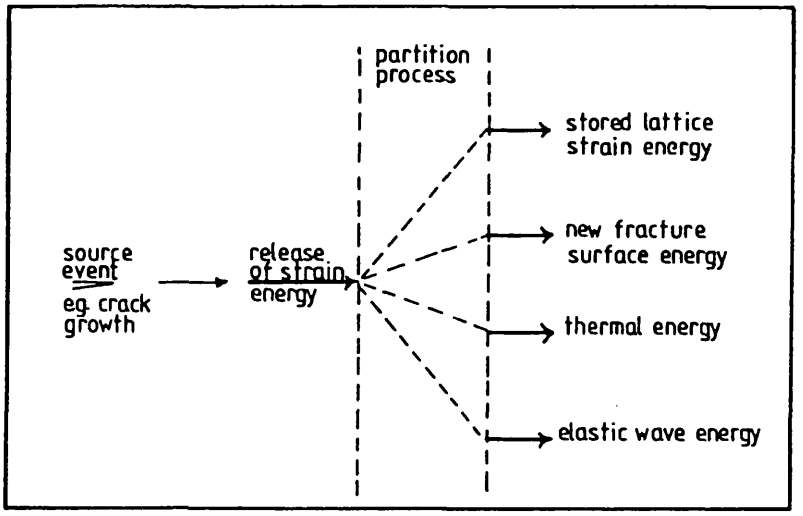

Fig 5.12 Distribution of released strain energy from a micromechanical event. (After Birchon Ref. 108)

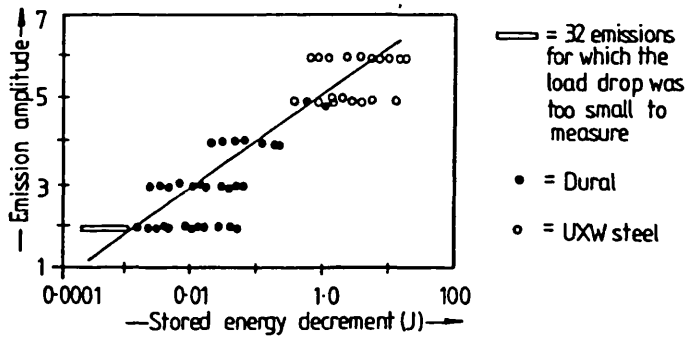

Fig 5.13 AE amplitude versus the mechanical energy released from discrete crack movements in UXW steel and 2014-T6 aluminium. (After Pollock Ref. 111)

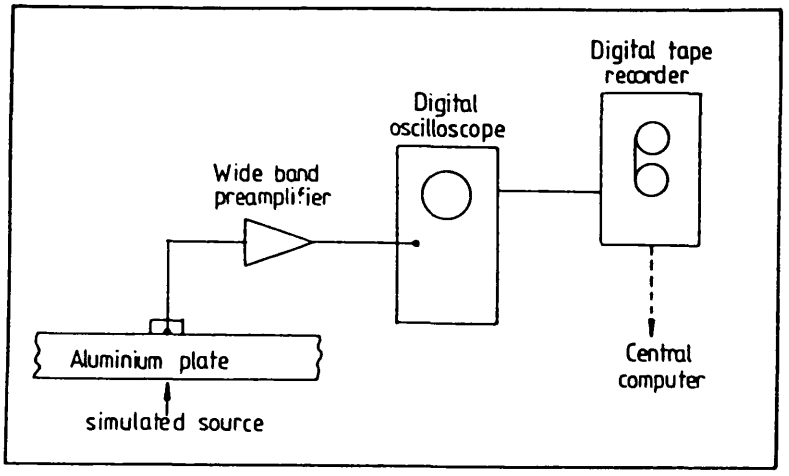

Fig 5.14 Schematic diagram of the experimental system used for AE signal analysis. (After Hsu et al Ref. 113)

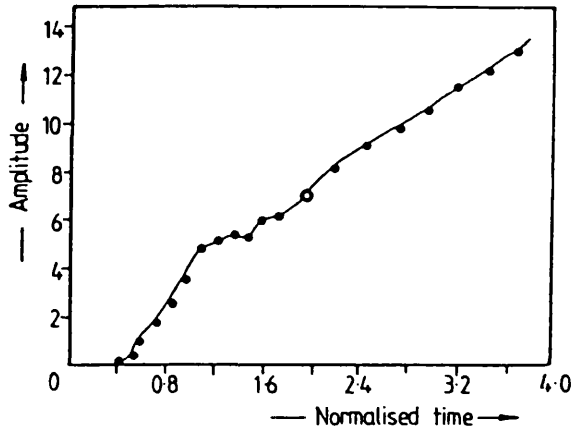

Fig 5.15 Comparison of the theoretical vertical displacements and the experimentally measured voltage output of the capacitative transducer at the epicenter of a large aluminium plate • experimental points, o scaling refrence point, - theoretical calculation. (After Hsu et al Ref. 113)

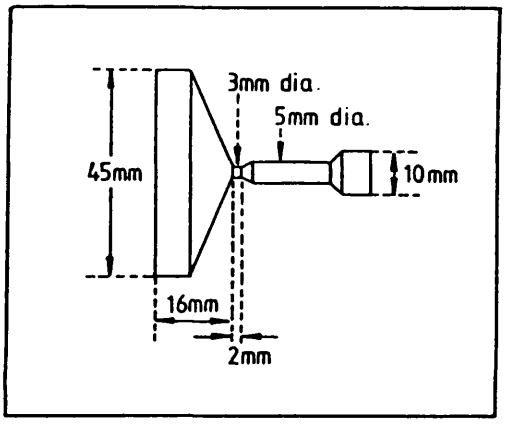

Fig 5.16 Yobell specimen used for measuring acoustic emission wave forms over a wide range of frequencies. (After Scruby et al Ref. 101)

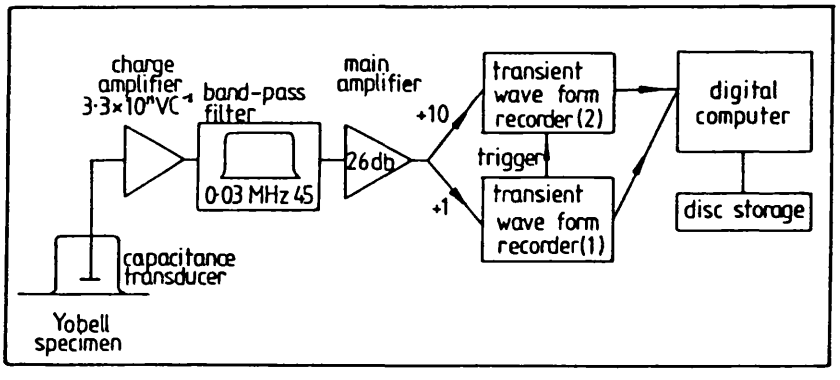

Fig 5.17 Schematic diagram of the AE detection system used by Scruby et al. (After Scruby et al Ref. 101)

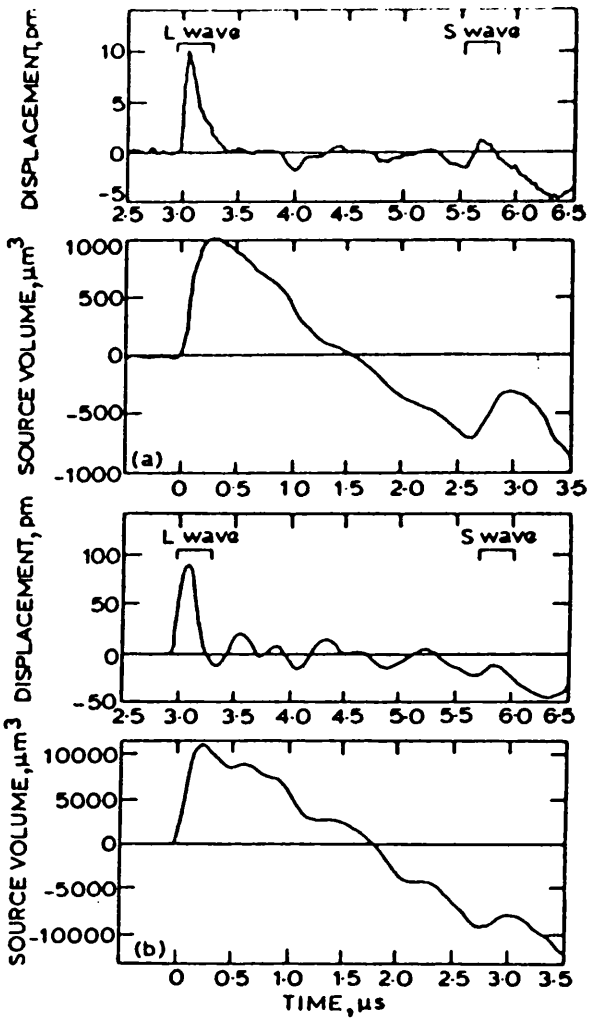

Fig 5.18 Examples of acoustic emission displacement wave forms for (a) an iced-brine quenced specimen (b) a water quenched specimen, corresponding source-volume-time histories were calculated by convolution with inverse transfer function. (After Scruby et al Ref. 101)

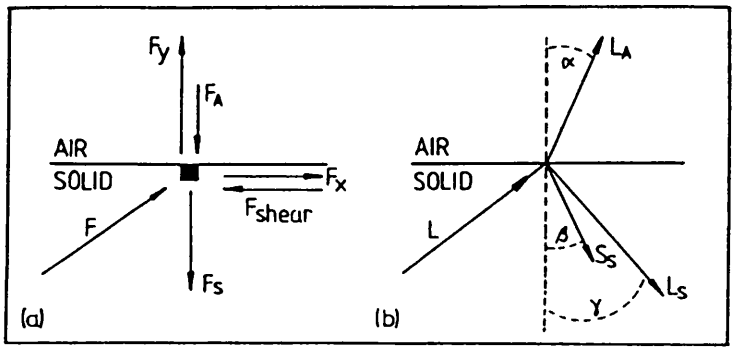

Fig 5.19 Mode conversion, (a) physical origin of phenomenon, (b) reflection and refraction of a logitudinal wave at a boundary.

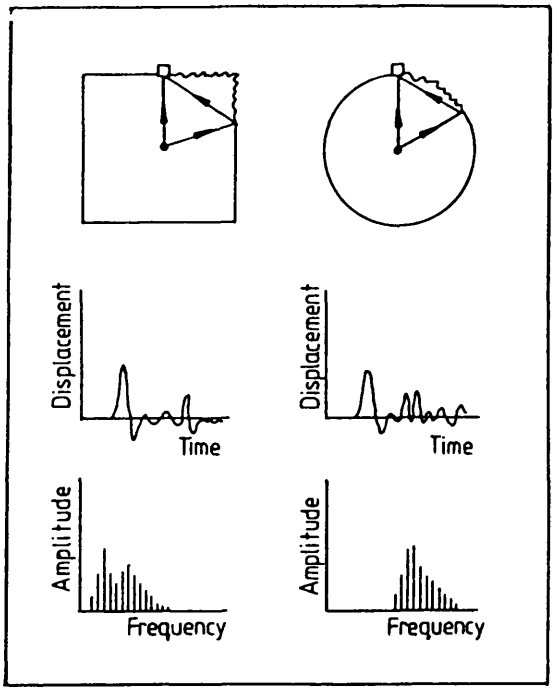

Fig 5.20 Schematic illustration of wave form and frequency spectrum modification of acoustic emission signal due to specimen geometry. (After Green Ref. 115)

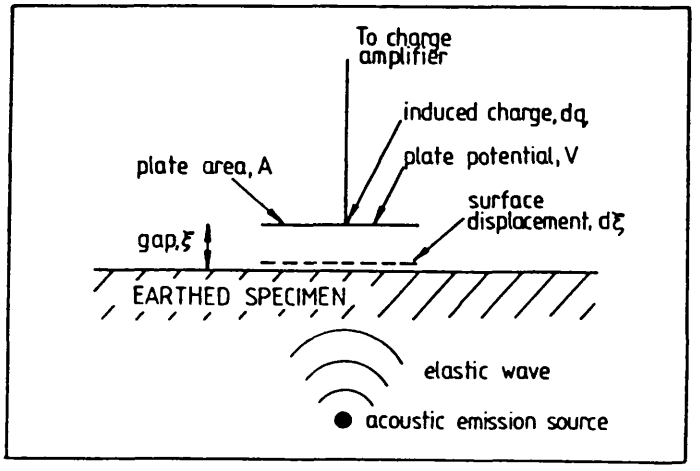

Fig 5.21 Schematic illustration of a capacitative transducer.

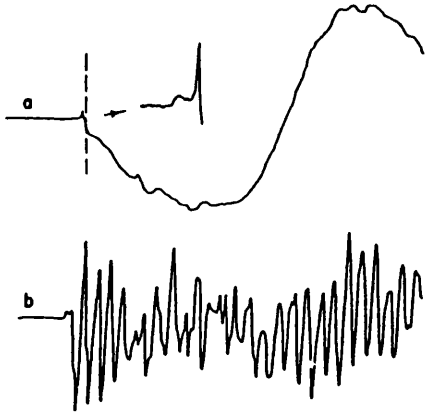

Fig 5.22 Comparison of detected signals for step function force with two different sensors, (a) capacitative displacement transducer, (b) piezoelectric transducer. (After Hsu et al Ref. 113)

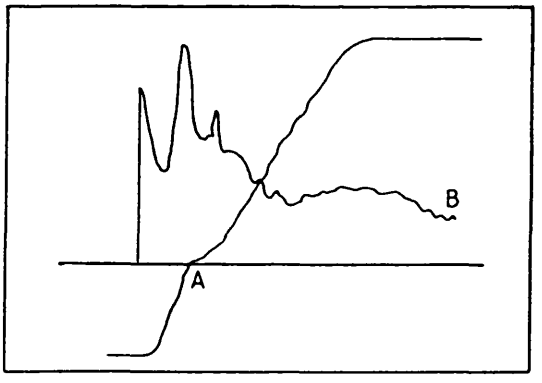

Fig 5.23 Comparison of waveforms from the fracture of a glass capillary as detected by (a) an optical transducer (b) a piezoelectric transducer. (After Green Ref. 115)

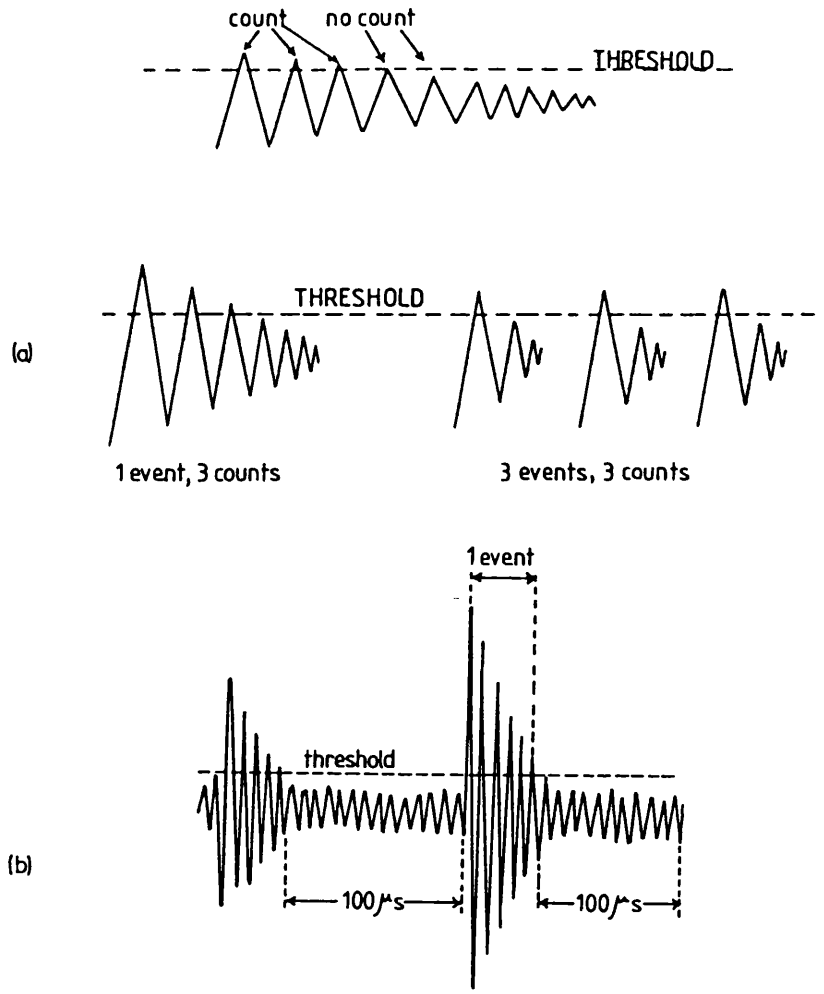

Fig 5.24 Schematic diagram of AE pulses showing (a) ring-down counts (b) event counts.

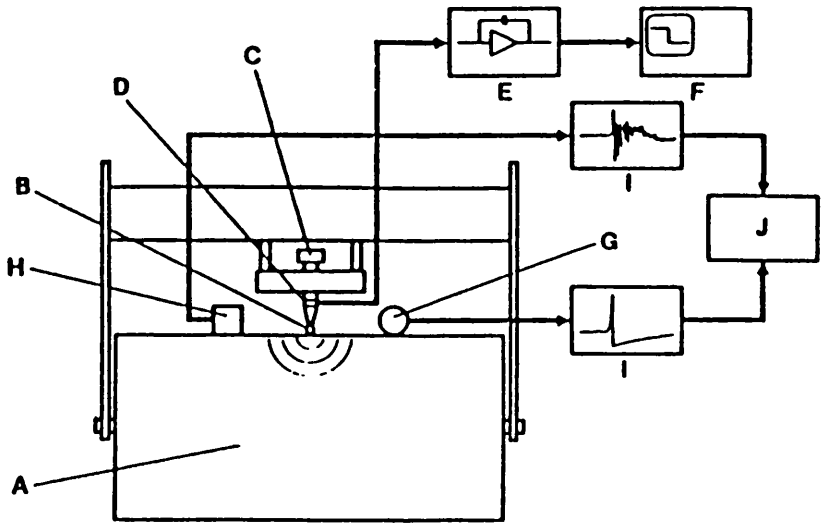

Fig 5.25 Schematic diagram of the experimental set up used for transducer calibration; a) test block; b) glass capillary; c) screw; d) load cell; e) amplifier; f) oscilloscope; g) capacitative transducer h) transducer under calibration; i) recorders; j) computer. (After Husu and Breckenridge Ref. 132)

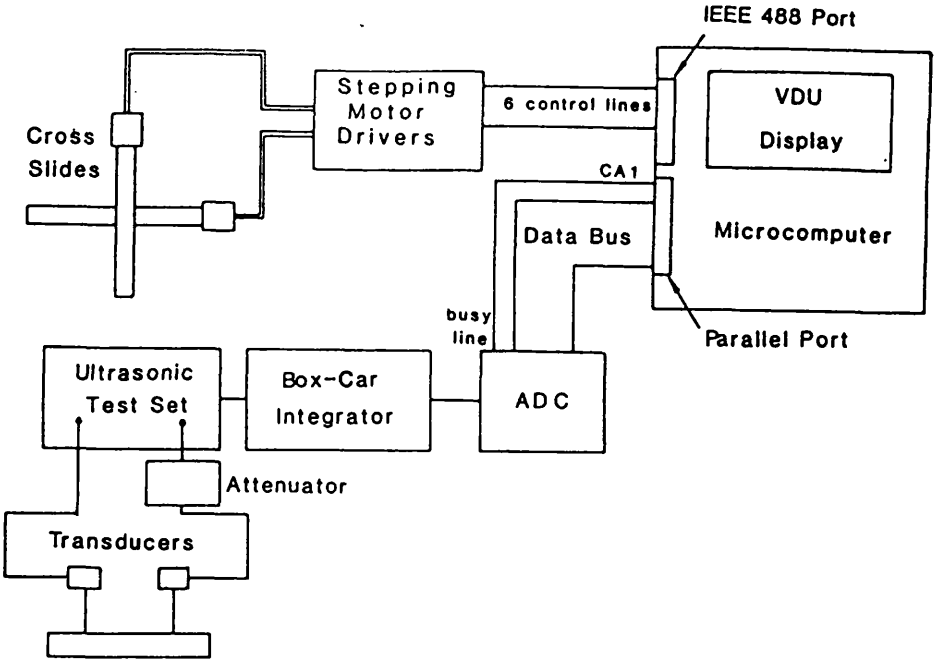

Fig 6.1 Block diagram of the C-scanner's measurement and control systems.

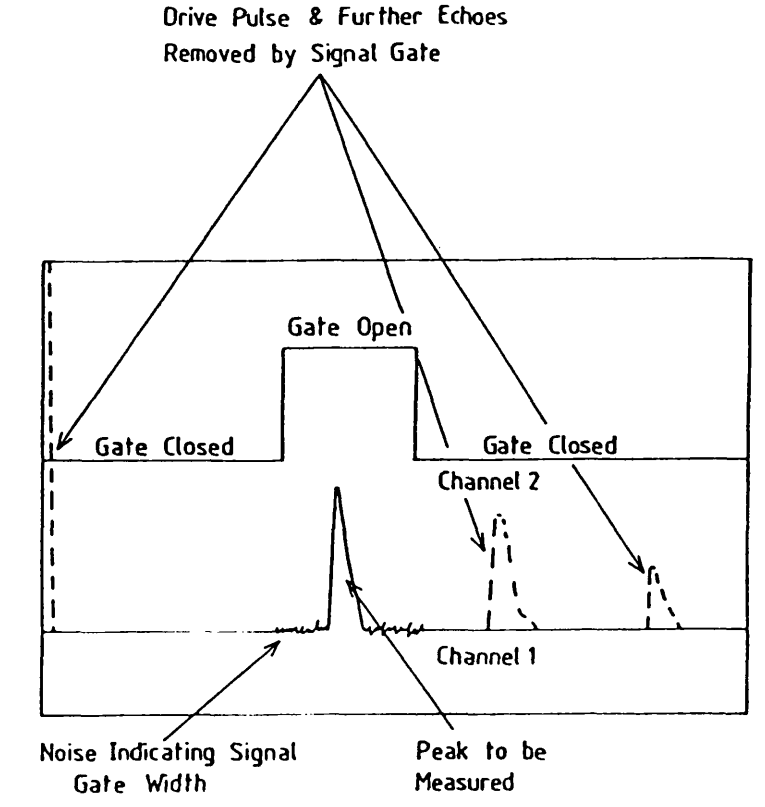

Fig 6.2 Schematic representation of gating operations.
Channel 1 displayed the gated Matec output signal
Channel 2 displayed the signal from the scan delay generator.

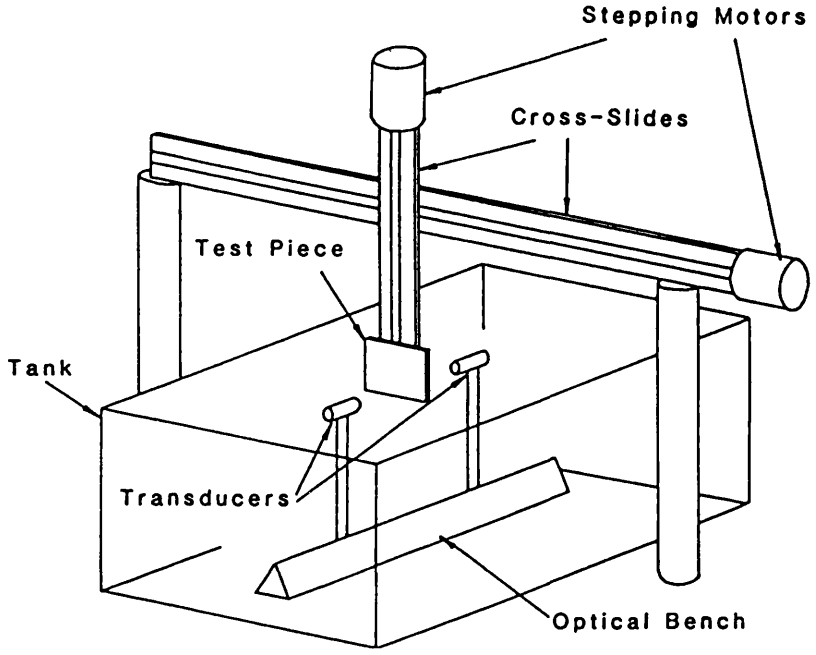

Fig 6.3 Schematic diagram of the C-scanner.

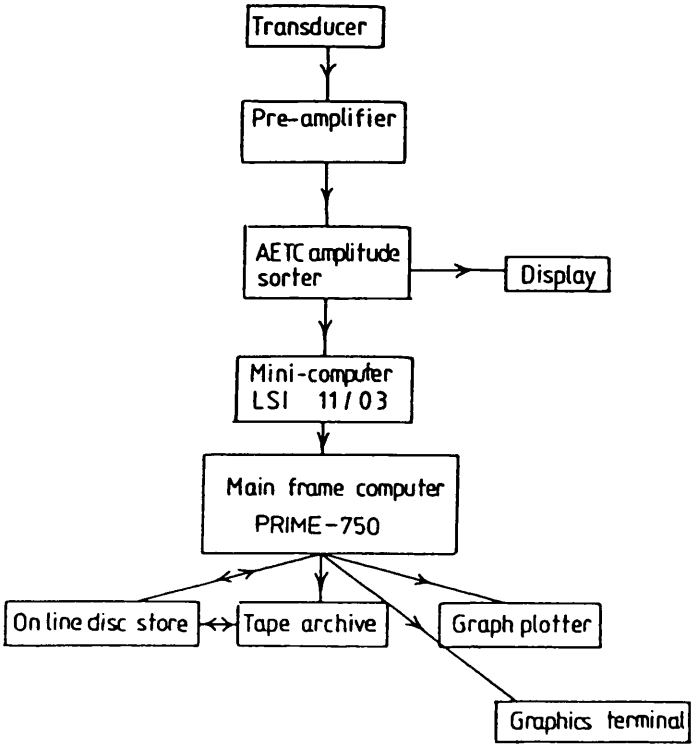

Fig 6.4 Block diagram of the AE testing rig.

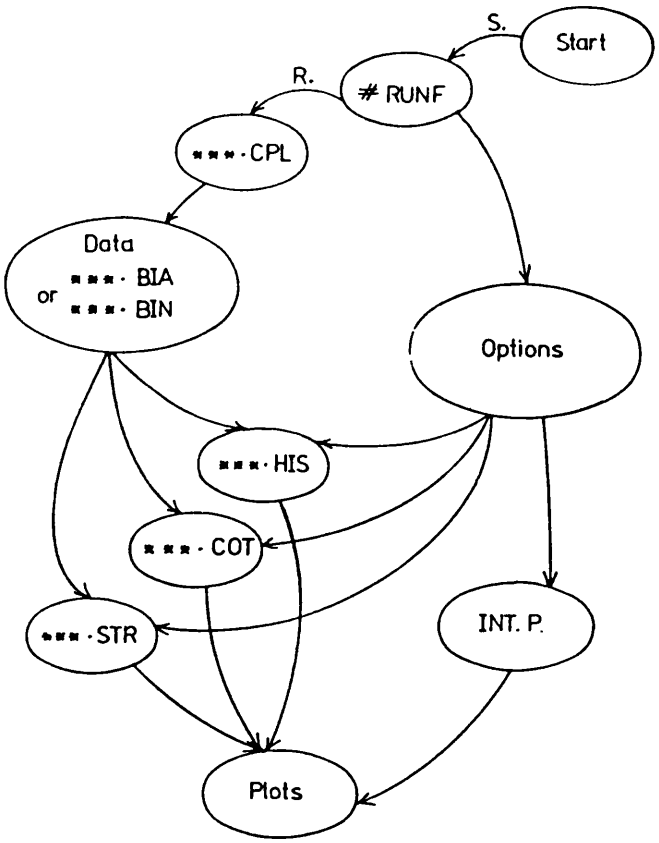

Fig 6.5 A block diagram of the AE analysis software used on PRIME-750 computer.

S. = SEG Run-file
R. = RUN Run-file
***.CPL = CPL Programme
***.BIA = Binary data file
***.BIN = Binary data file
***.HIS & ***.COT & ***.STR = Reformated data files
INT.P. = Interactive process.

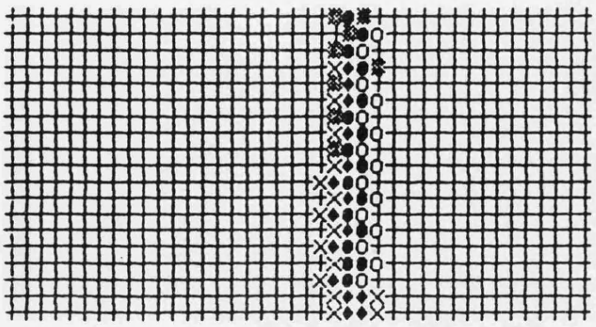

+...LESS THAN 23 DB DOWN FROM ORIGINAL SIGNAL.
×...BETWEEN 23 AND 25
o...BETWEEN 25 AND 27
⁂...BETWEEN 27 AND 29
♦...BETWEEN 29 AND 31
●...MORE THAN 31 DB

Fig 7.1 Acoustic image of a 1mm wide rubber band using 2.5 MHz ultrasound (25mm X 12.5mm).

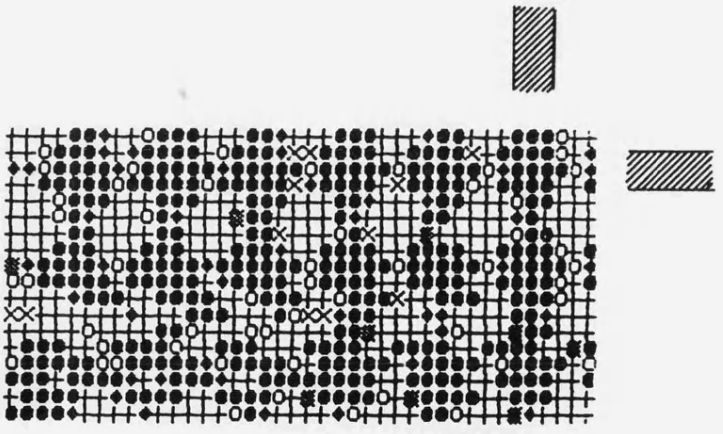

+...LESS THAN 149 DB DOWN FROM ORIGINAL SIGNAL.
×...BETWEEN 149 AND 148
o...BETWEEN 148 AND 147
⁂...BETWEEN 147 AND 146
♦...BETWEEN 146 AND 145
●...MORE THAN 145 DB

Fig 7.2 Acoustic image of a 1mm mesh size square gauze (25mm X 12.5mm) using 10 MHz ultrasound. The solid lines shows the position of the wires.

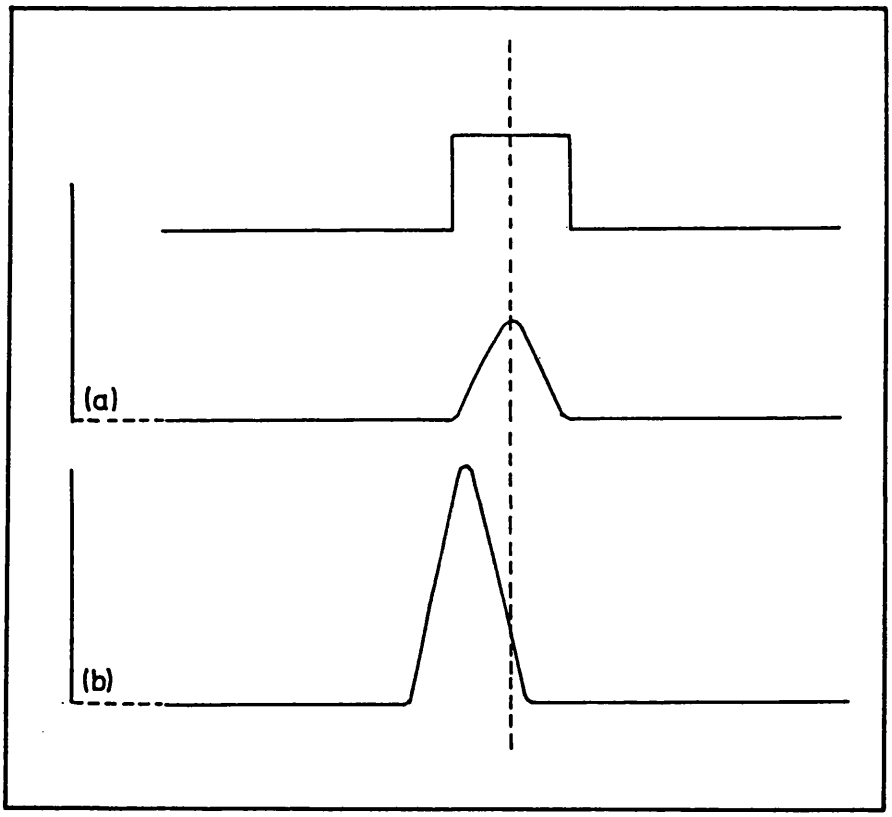

Fig 7.3 Schematic timing diagram of the transmission echo, (a) through a steel wire of diameter 1 mm, and (b) through water.

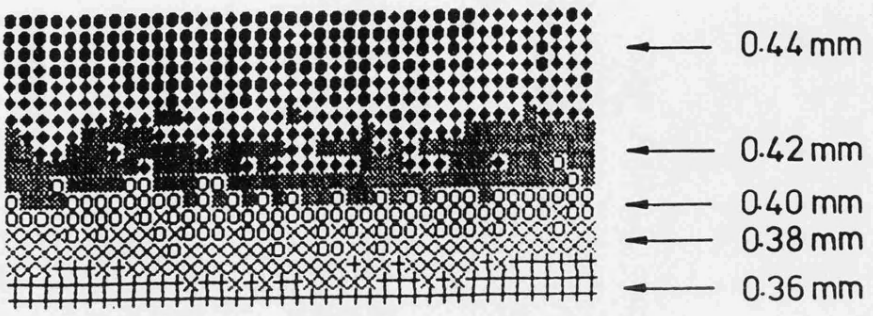

+...LESS THAN 30 DB DOWN FROM ORIGINAL SIGNAL.
×...BETWEEN 30 AND 32
o...BETWEEN 32 AND 34
⁂...BETWEEN 34 AND 36
♦...BETWEEN 36 AND 38
●...MORE THAN 38 DB

Fig 7.4a C-scan of a Mo63 coated sample (50mm X 25mm) with coating thickness variation as shown. The image was produced, using 10 MHz probes.

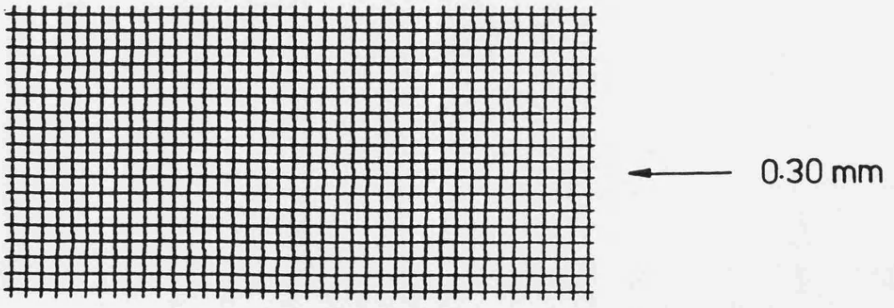

+...LESS THAN 22 DB DOWN FROM ORIGINAL SIGNAL.
×...BETWEEN 22 AND 24
o...BETWEEN 24 AND 26
⁂...BETWEEN 26 AND 28
♦...BETWEEN 28 AND 30
●...MORE THAN 30 DB

Fig 7.4b C-scan of the sample, shown in Fig 7.4a, after grinding to a uniform thickness, (10 MHz probes).

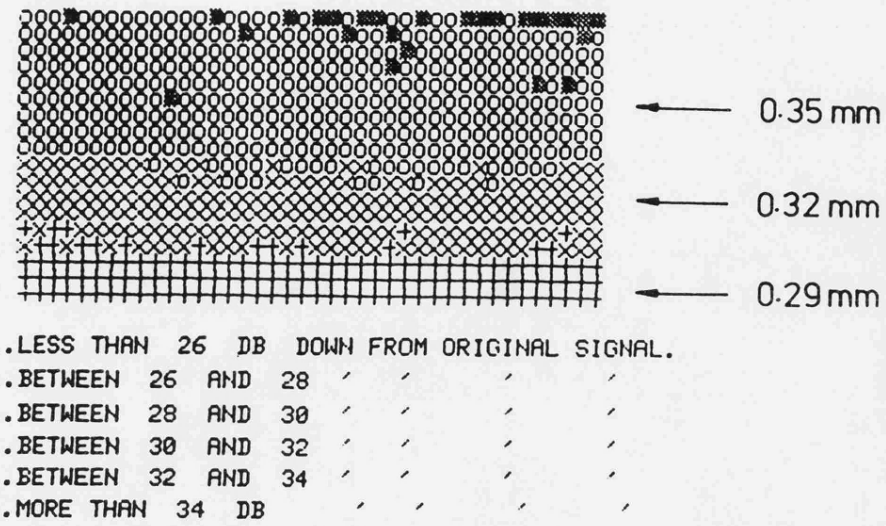

Fig 7.5 C-scan image of a Mo63 coated sample (50mm X 25mm), produced using 5 MHz ultrasound.

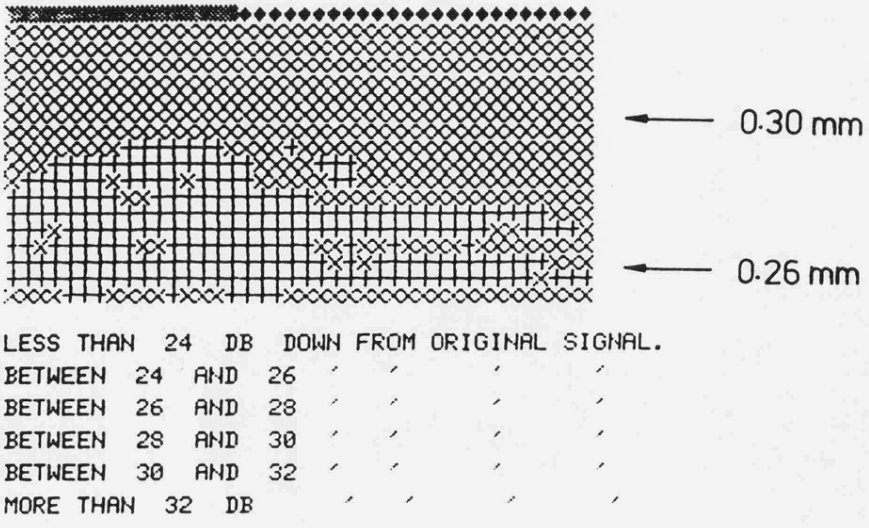

Fig 7.6 C-scan image of a Mo63 coated specimen (50mm X 25mm), produced using 2.5 MHz ultrasound.

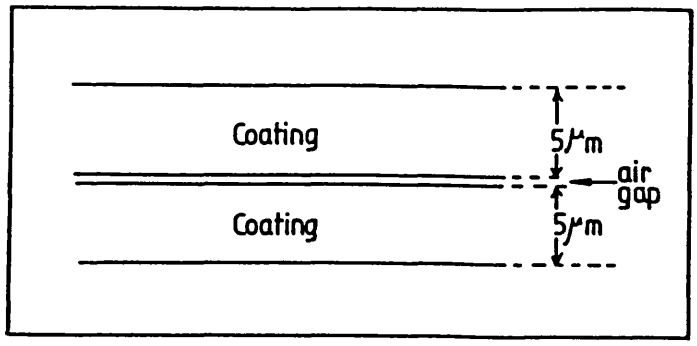

Fig 7.7 Model of a plasma sprayed coating, (After Patel and Almond 63).

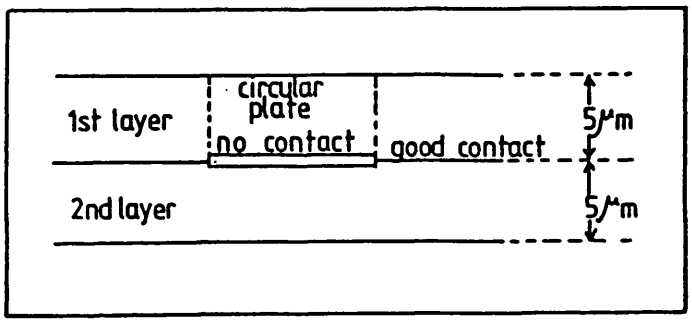

Fig 7.8 A schematic model of two lamellae in a plasma sprayed coating.

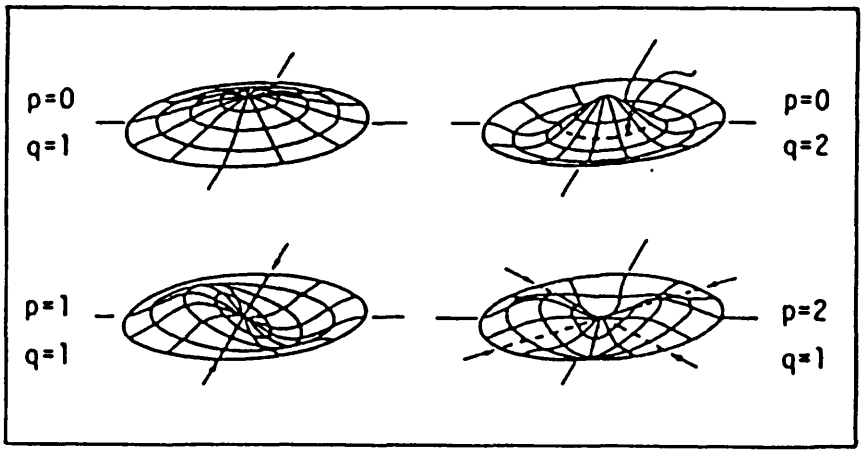

Fig 7.9 Four modes of vibration of a circular plate (After Stump Ref. 144).

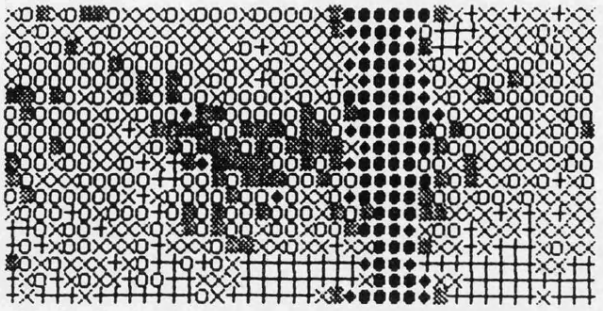

+...LESS THAN 34 DB DOWN FROM ORIGINAL SIGNAL.
×...BETWEEN 34 AND 36
o...BETWEEN 36 AND 38
▪...BETWEEN 38 AND 40
♦...BETWEEN 40 AND 42
●...MORE THAN 42 DB

Fig 7.10 C-scan image of an aluminium specimen with a line defect, produced using a pair of 10 MHz probes (50mm X 25mm).

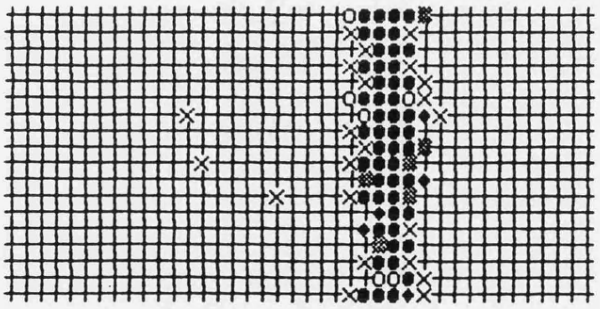

+...LESS THAN 40 DB DOWN FROM ORIGINAL SIGNAL.
×...BETWEEN 40 AND 42
o...BETWEEN 42 AND 44
▪...BETWEEN 44 AND 46
♦...BETWEEN 46 AND 48
●...MORE THAN 48 DB

Fig 7.11 An enhanced C-scan image of the sample shown in Fig 7.10, showing that by using micro-computer the effect of local variation can be masked (10 MHz probes).

(a)

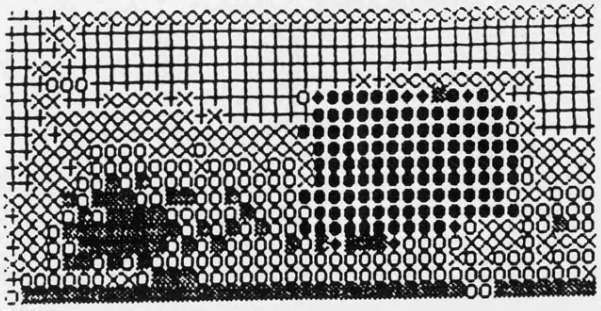

+...LESS THAN 30 DB DOWN FROM ORIGINAL SIGNAL.
×...BETWEEN 30 AND 32
o...BETWEEN 32 AND 34
⊠...BETWEEN 34 AND 36
♦...BETWEEN 36 AND 38
●...MORE THAN 38 DB

(b)

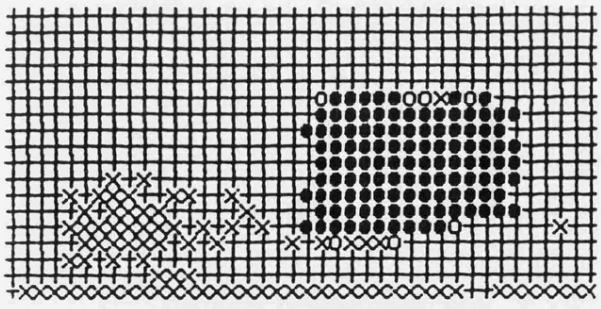

+...LESS THAN 34 DB DOWN FROM ORIGINAL SIGNAL.
×...BETWEEN 34 AND 36
o...BETWEEN 36 AND 38
⊠...BETWEEN 38 AND 40
♦...BETWEEN 40 AND 42
●...MORE THAN 42 DB

Fig 7.12 C-scan image of an aluminium coating with an artificial defect (50mm X 25mm). (a) As produced (b) Enhanced image, (10 MHz probes).

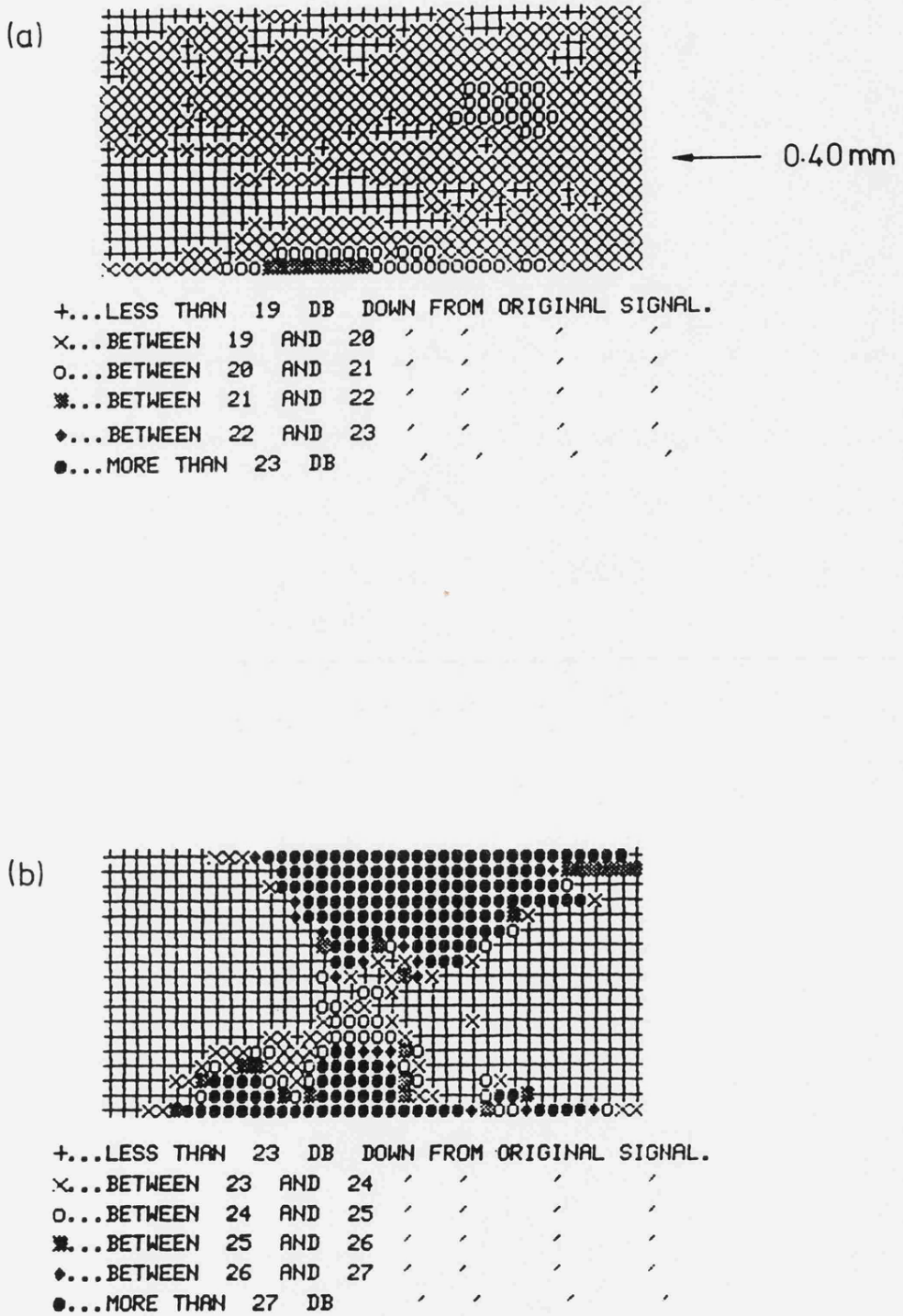

Fig 7.13 C-scan image of an aluminium coating (50mm X 25mm), (a) before and (b) after four point bending. The extent of the damage is clearly shown, (2.5 MHz probes).

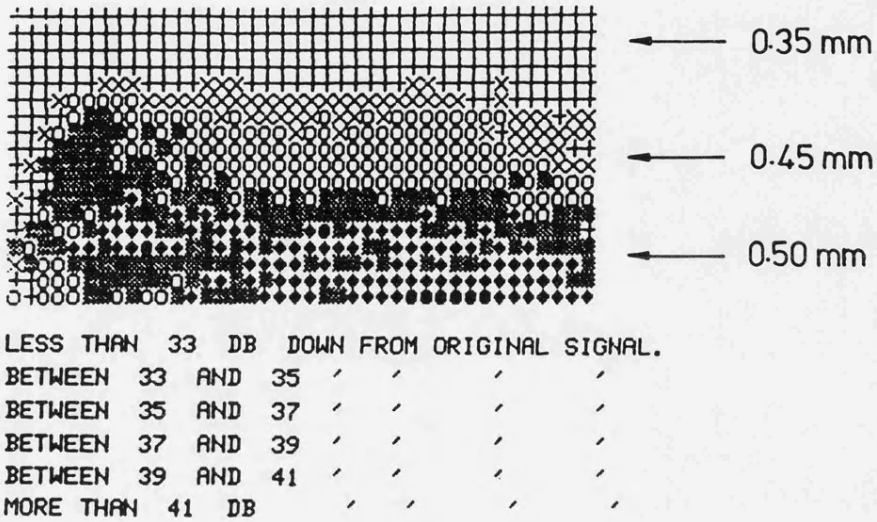

Fig 7.14 C-scan image of an alumina coating sprayed using Metco's recommended process variables, 10 MHz probes (50mmX 25mm).

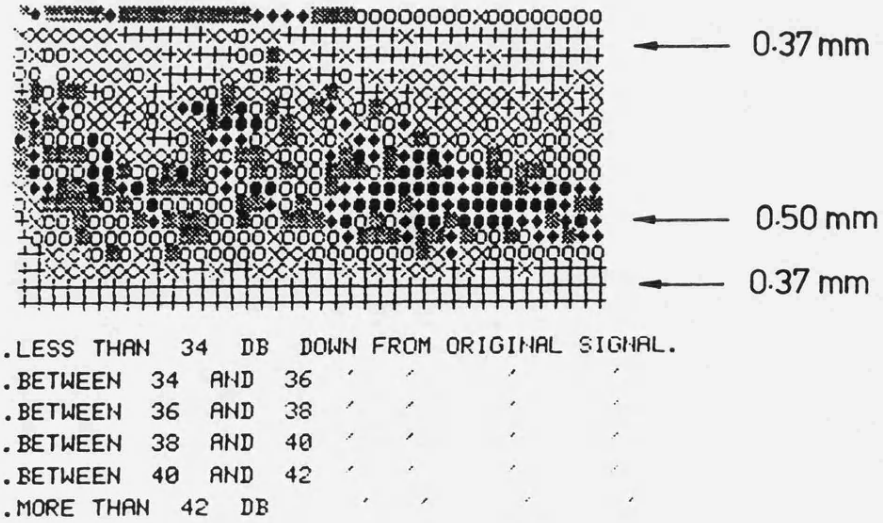

Fig 7.15 C-scan image of an alumina coating, sprayed onto a substrate that has had poor surface preparation, 10 MHz probes (50mm X 25mm).

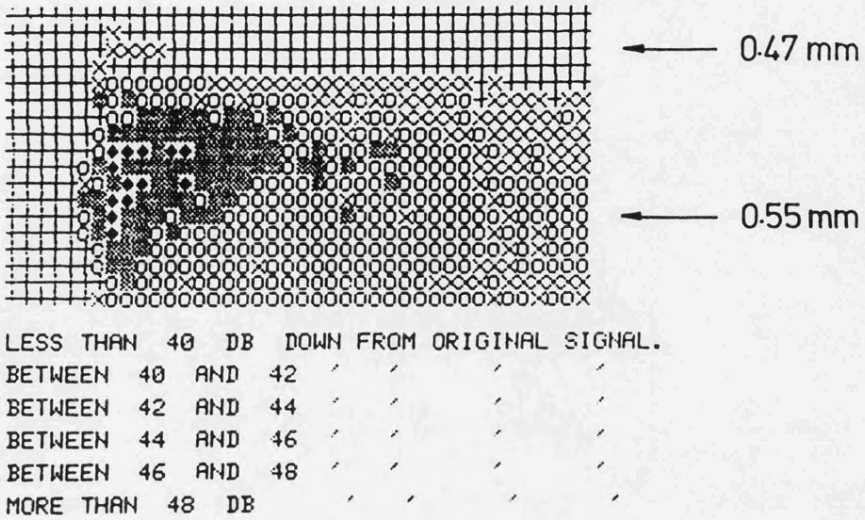

Fig 7.16 C-scan image of an alumina coating, sprayed with 20% less input power than recommended by Metco, 10 MHz probes (50mm X 25mm).

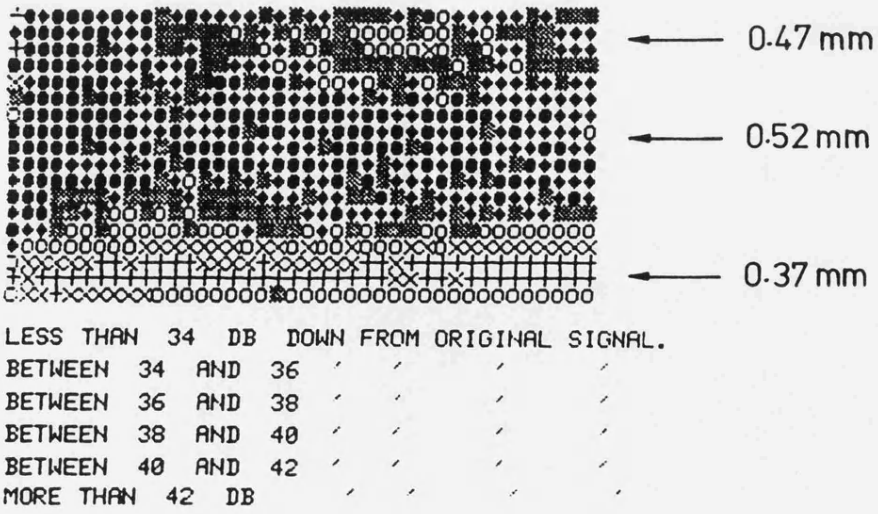

Fig 7.17 C-scan image of an alumina coating, sprayed using no cooling air, 10 MHz probes, (50mm X 25mm).

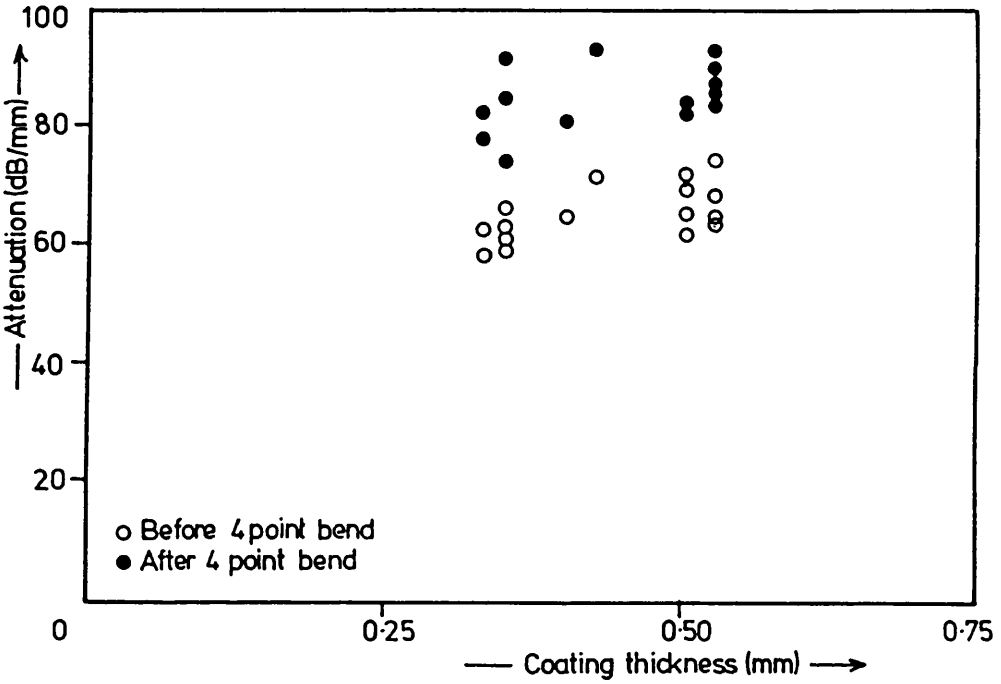

Fig 7.18 Graphical representation of the attenuation per unit thickness for an alumina coating, sprayed onto a substrate that has had poor surface preparation, before 4 point bending, after 4 point bending.

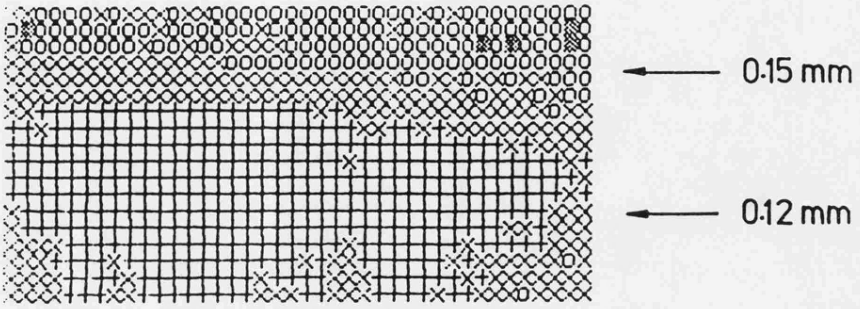

+...LESS THAN 22 DB DOWN FROM ORIGINAL SIGNAL.
×...BETWEEN 22 AND 24
o...BETWEEN 24 AND 26
▒...BETWEEN 26 AND 28
◆...BETWEEN 28 AND 30
●...MORE THAN 30 DB

Fig 7.19 C-scan image of a Mo63 coating sprayed following Metco's recommended practices, 10 MHz probes (50mm X 25mm).

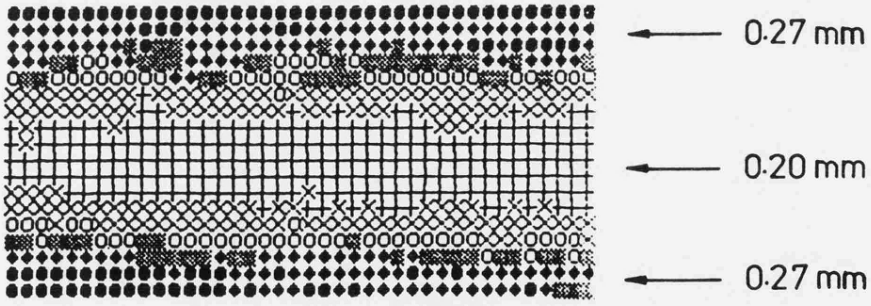

+...LESS THAN 28 DB DOWN FROM ORIGINAL SIGNAL.
×...BETWEEN 28 AND 30
o...BETWEEN 30 AND 32
▒...BETWEEN 32 AND 34
◆...BETWEEN 34 AND 36
●...MORE THAN 36 DB

Fig 7.20 C-scan image of a Mo63 coating sprayed with 20% less input power than recommended by Metco (50mm X 25mm).

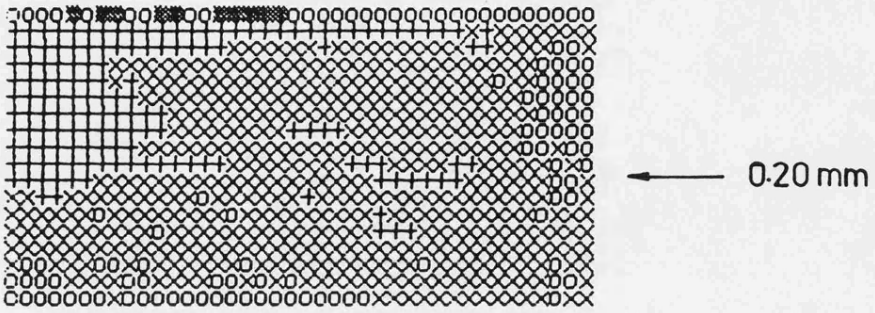

+...LESS THAN 24 DB DOWN FROM ORIGINAL SIGNAL.
×...BETWEEN 24 AND 26 ′ ′ ′ ′
o...BETWEEN 26 AND 28 ′ ′ ′ ′
▒...BETWEEN 28 AND 30 ′ ′ ′ ′
◆...BETWEEN 30 AND 32 ′ ′ ′ ′
●...MORE THAN 32 DB ′ ′ ′ ′

Fig 7.21 C-scan image of a Mo505 coating sprayed according to Metco's recommendations, 10 MHz probes (50mm X 25mm).

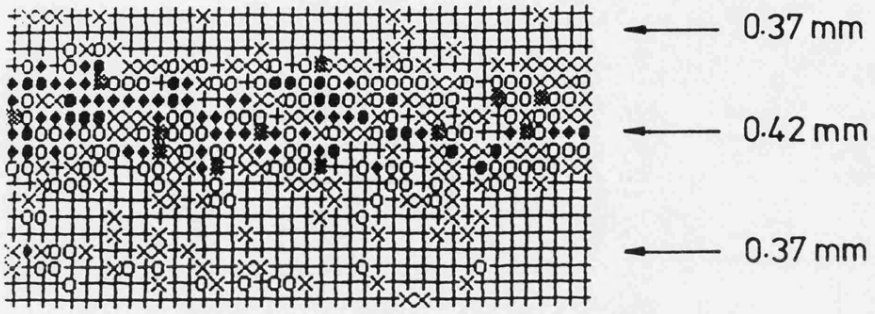

+...LESS THAN 40 DB DOWN FROM ORIGINAL SIGNAL.
×...BETWEEN 40 AND 42
o...BETWEEN 42 AND 44
⁂...BETWEEN 44 AND 46
♦...BETWEEN 46 AND 48
●...MORE THAN 48 DB

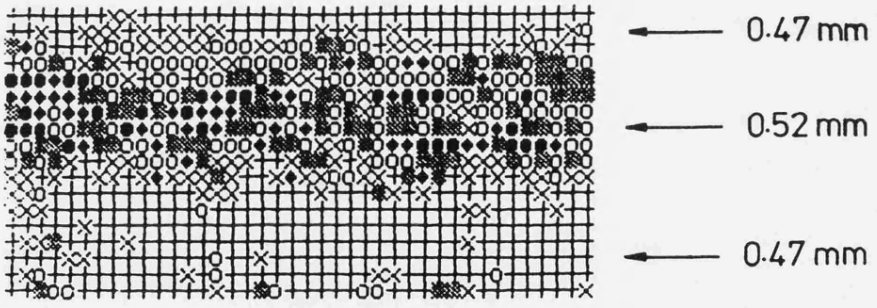

+...LESS THAN 36 DB DOWN FROM ORIGINAL SIGNAL.
×...BETWEEN 36 AND 38
o...BETWEEN 38 AND 40
⁂...BETWEEN 40 AND 42
♦...BETWEEN 42 AND 44
●...MORE THAN 44 DB

Fig 7.22 Two typical C-scan images of aluminium coatings sprayed according to the Metco's recommendations, 10 MHz probes (50mm X 25mm).

%... 14 >DB DOWN FROM ORIGINAL SIGNAL.
@... 15 >DB> 14
#... 16 >DB> 15
O... 17 >DB> 16
+... 18 >DB> 17
 ... 18 <DB

Fig 7.23 Four typical C-scan images of the samples provided by Phillips of Eindhoven (2.5 MHz probes).

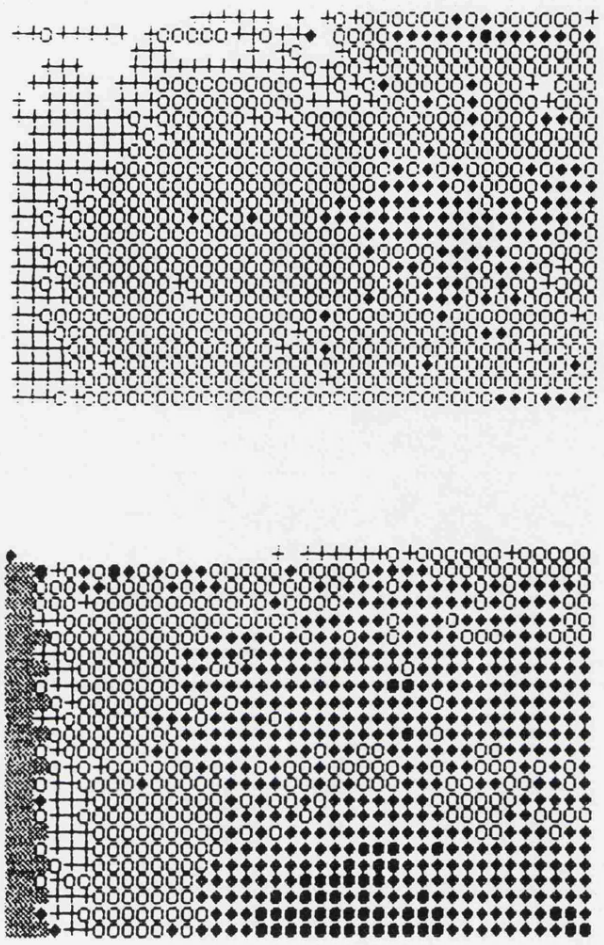

Fig 7.24 Two typical C-scan images of the samples provided by Phillips of Eindhoven (5 MHz probes).

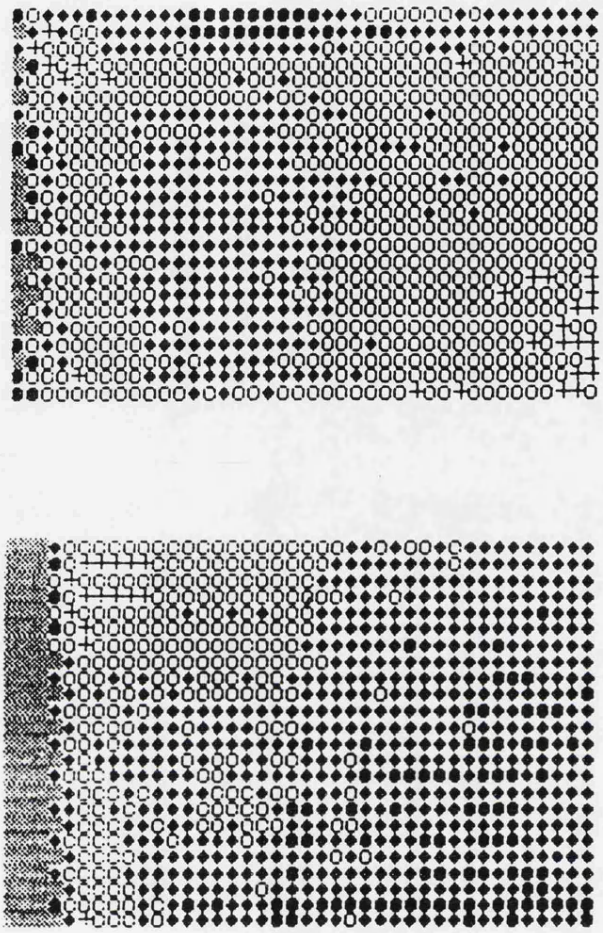

Fig 7.25 Two typical C-scans of the samples provided by Phillips of Eindhoven (10 MHz probes).

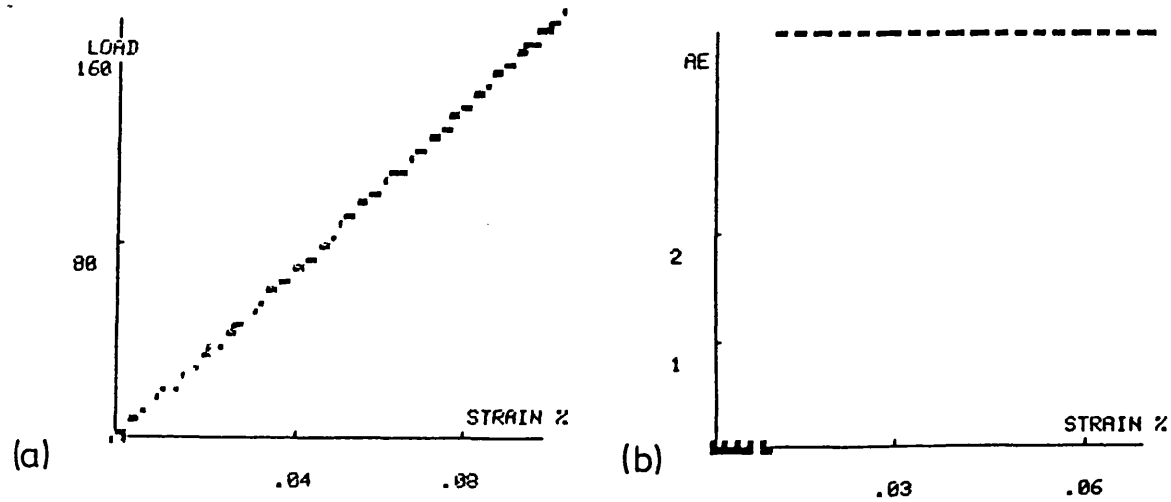

Fig 7.26 Load vs strain and acoustic emission (ring-down count) vs strain plots for a typical heat treated EN42 steel substrate.

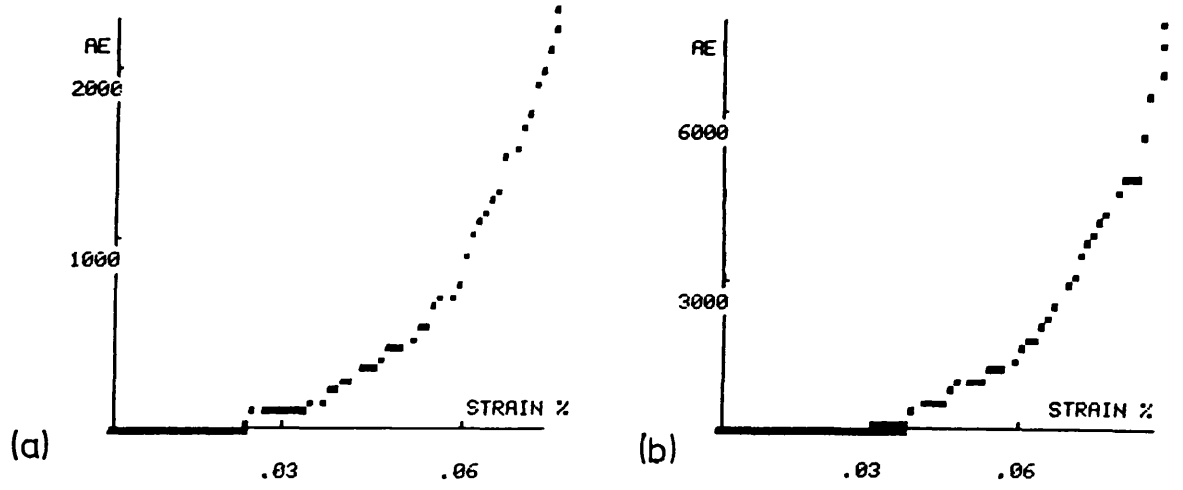

Fig 7.27 Two typical AE plots (ring-down vs strain) of control alumina coatings.

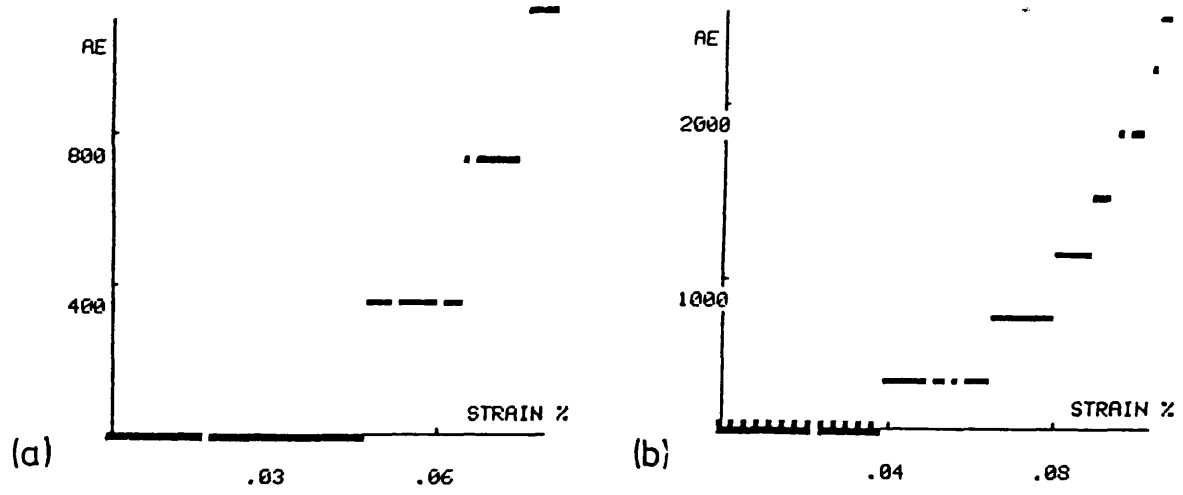

Fig 7.28 Two typical ring-down graphs of low input power alumina coatings. These samples were sprayed using 20% less power than recommended by Metco.

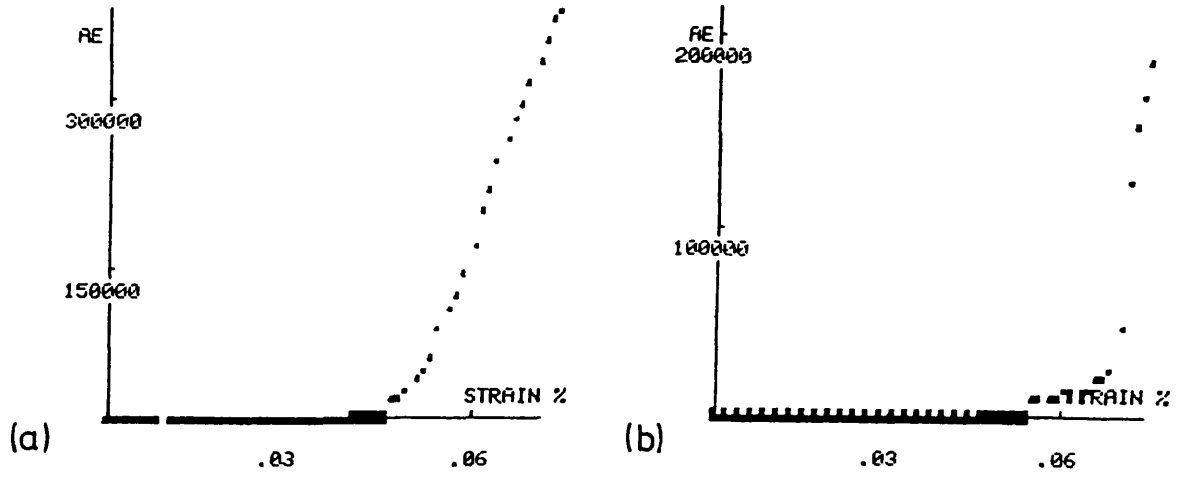

Fig 7.29 Two typical ring-down plots for over heated alumina coatings.

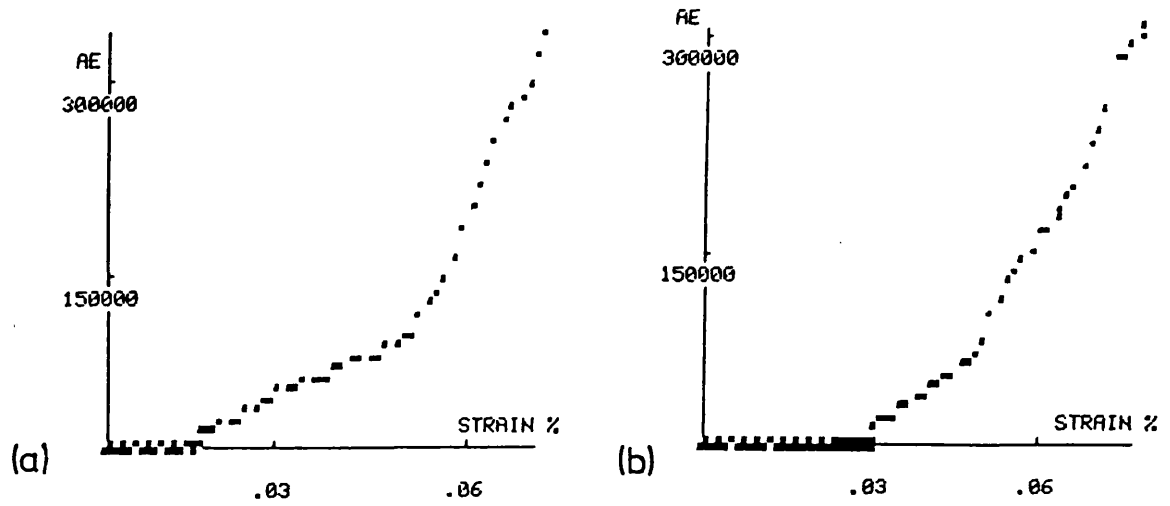

Fig 7.30 Two typical ring-down plots for alumina coatings, sprayed on to a substrate with poor surface preparation.

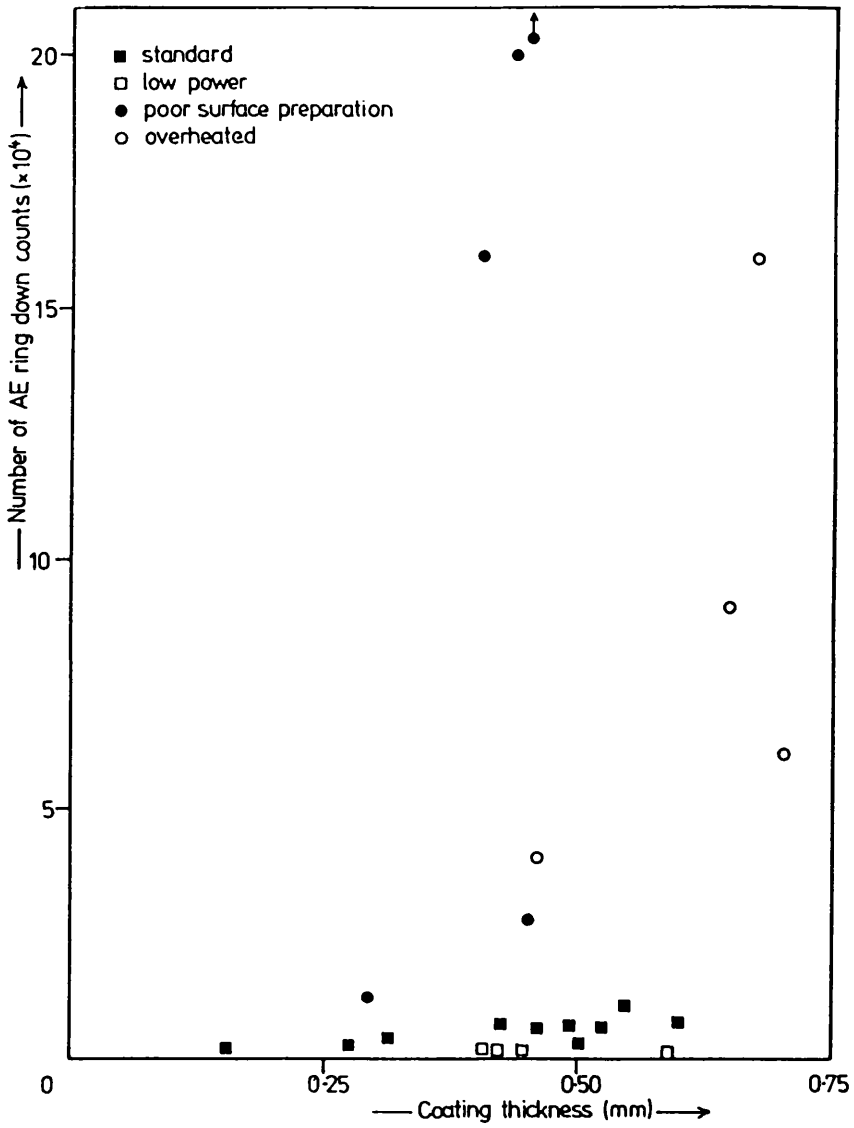

Fig 7.31 Graphical representation of the total number of ring-down counts recorded up to 0.06 percent strain from various alumina coatings with different thickness.

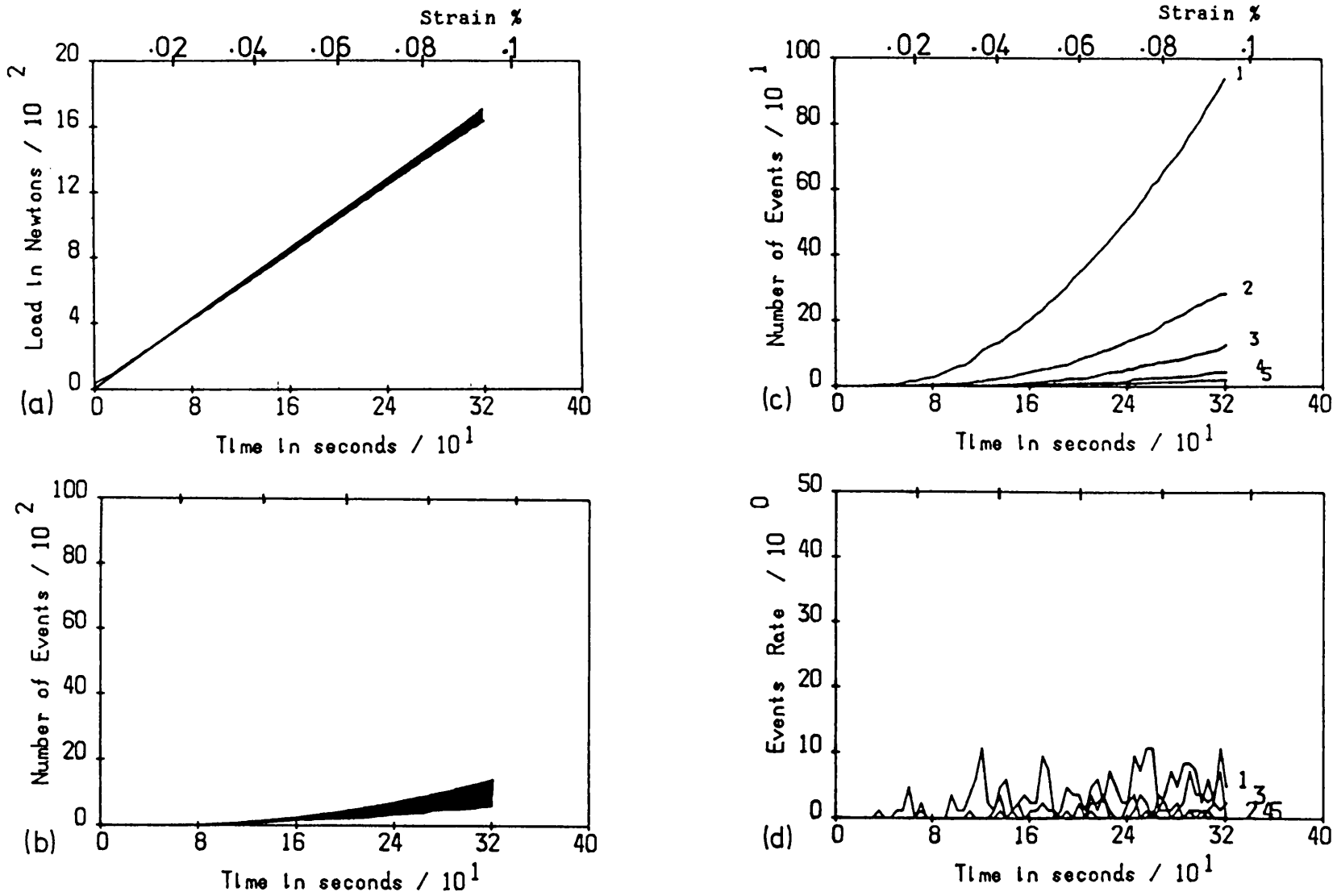

Fig 7.32 AE event curves for 9 alumina (Metco 105) control samples. a) Load vs time, b) Cumulative events vs time, c) Cumulative events in specified amplitude ranges vs time, d) Event rate in specified amplitude ranges vs time.

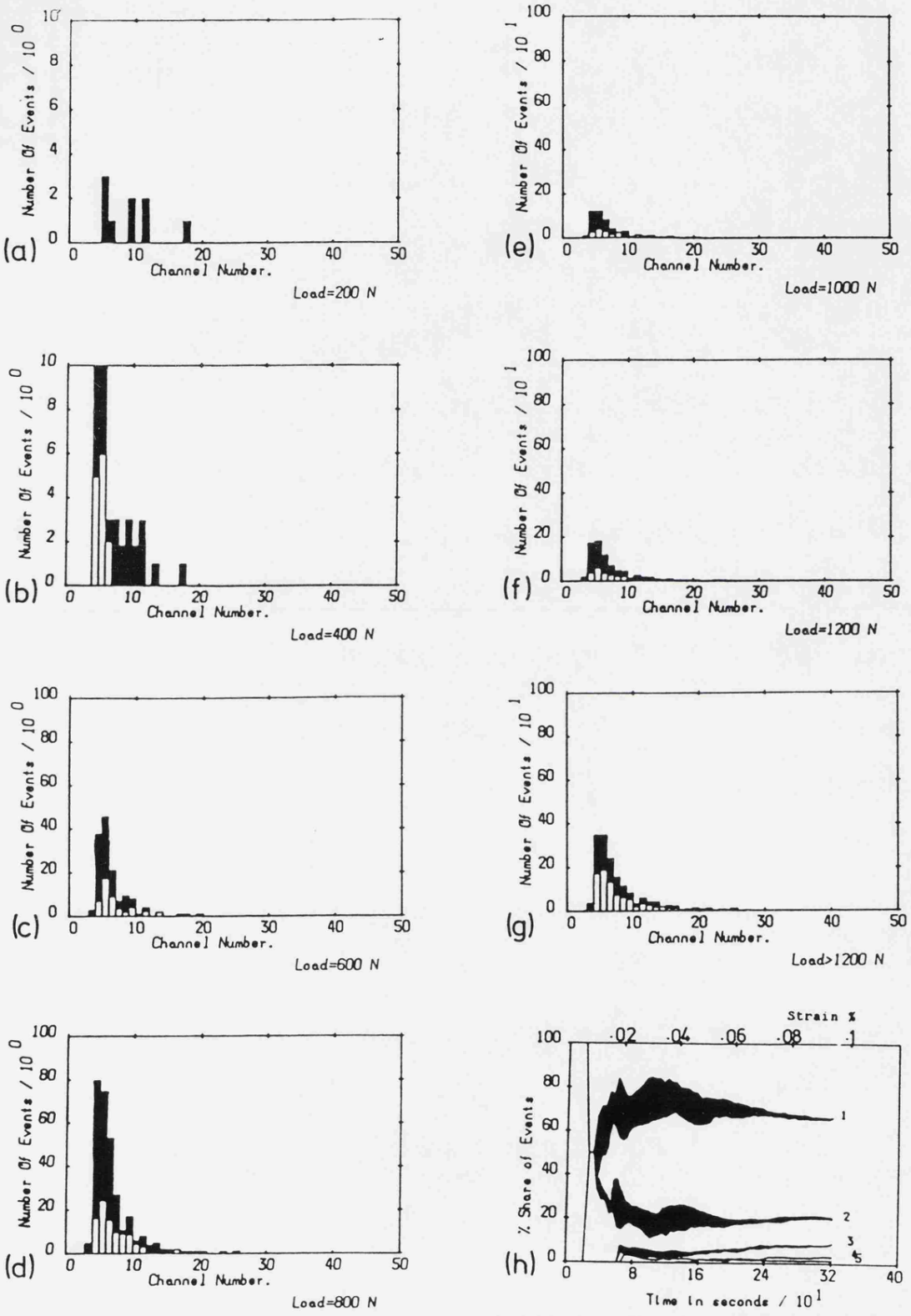

Fig 7.33 a-g) Amplitude distribution histograms at various load levels for alumina samples shown in Fig 7.32, h) percentage share of events in specified amplitude ranges vs time.

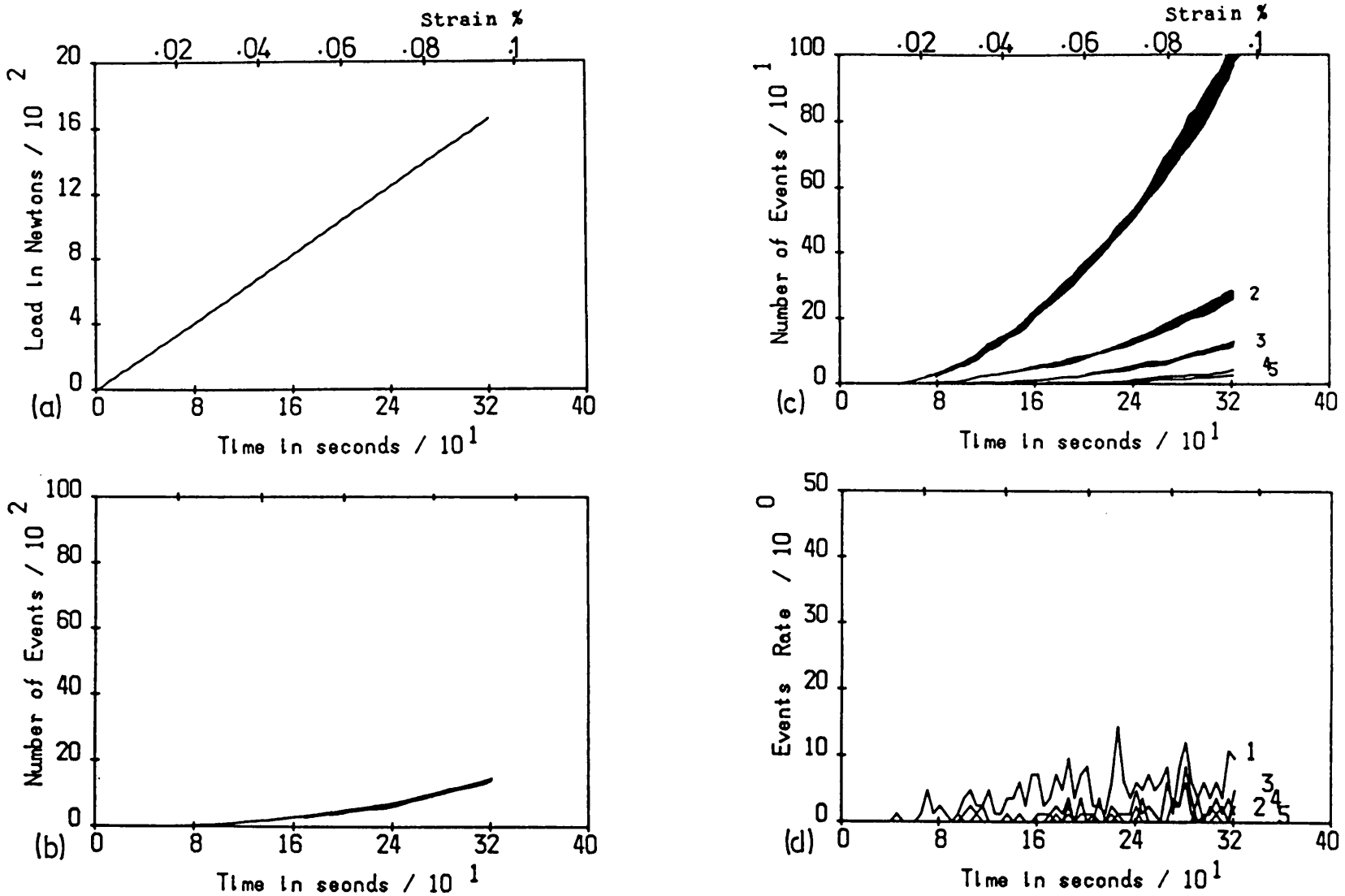

Fig 7.34 AE event curves for three replicate alumina control samples.

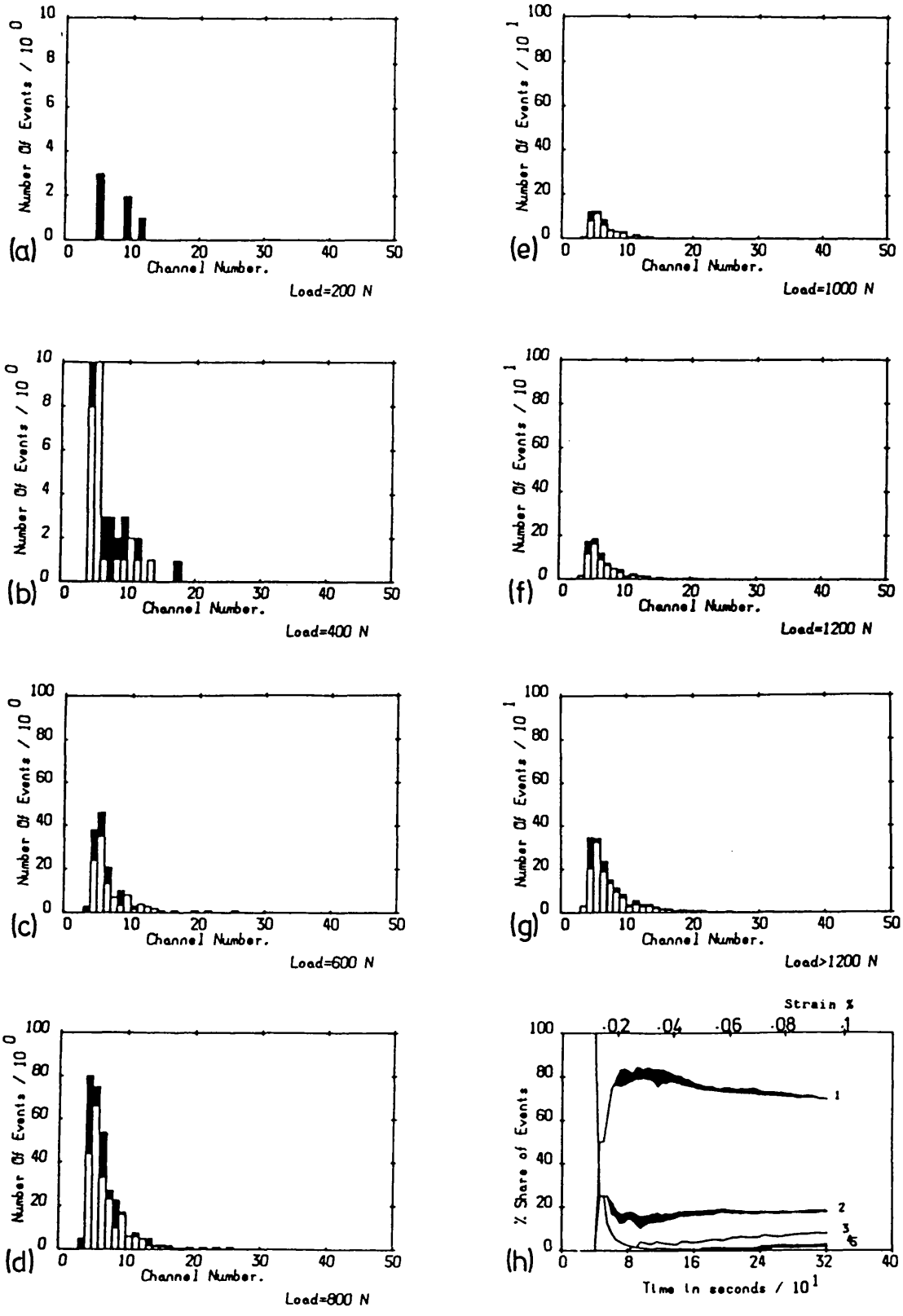

Fig 7.35 Amplitude distribution histograms and the percentage share graph for the alumina control samples shown in Fig 7.34

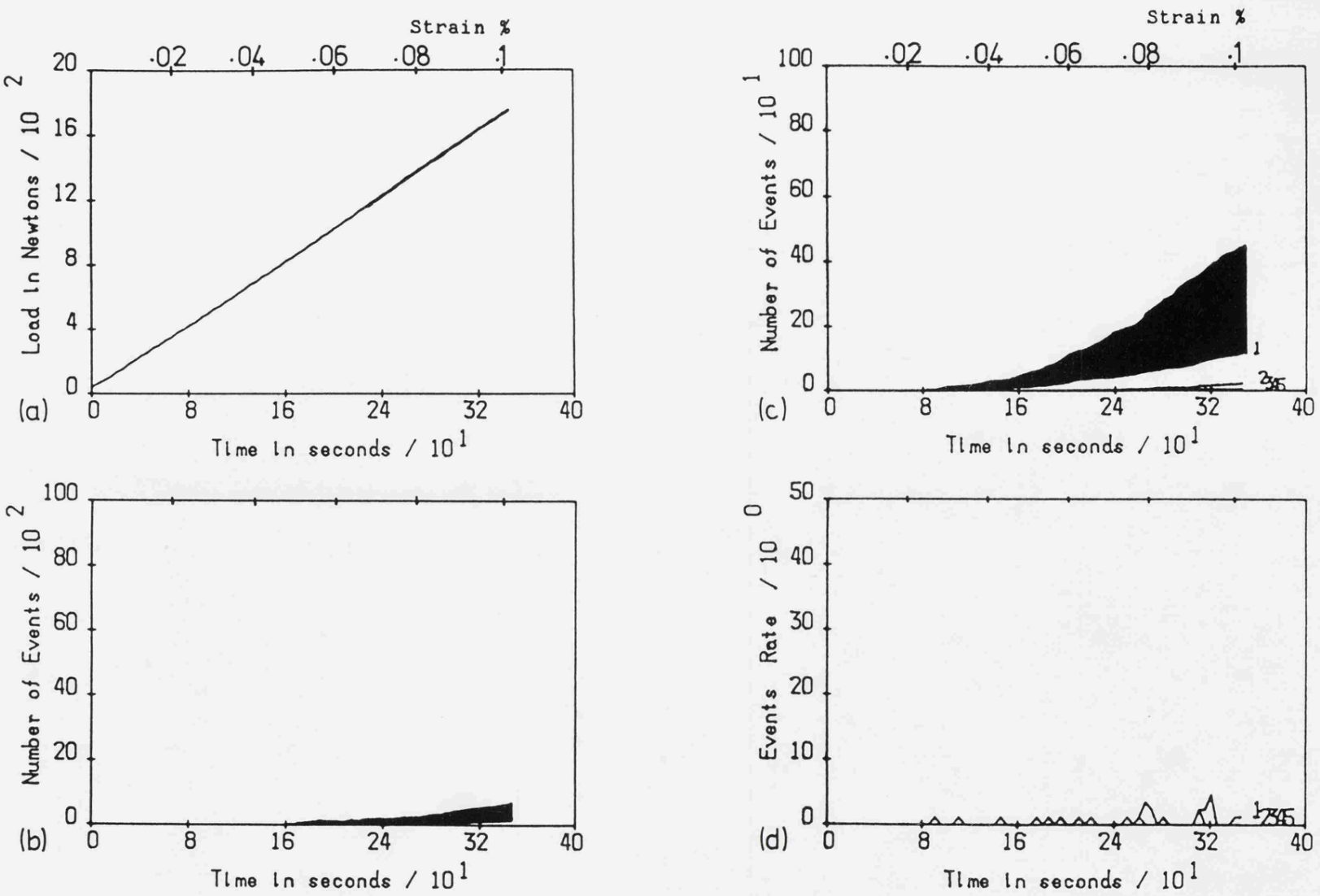

Fig 7.36 AE event curves for 10 low power alumina coatings.

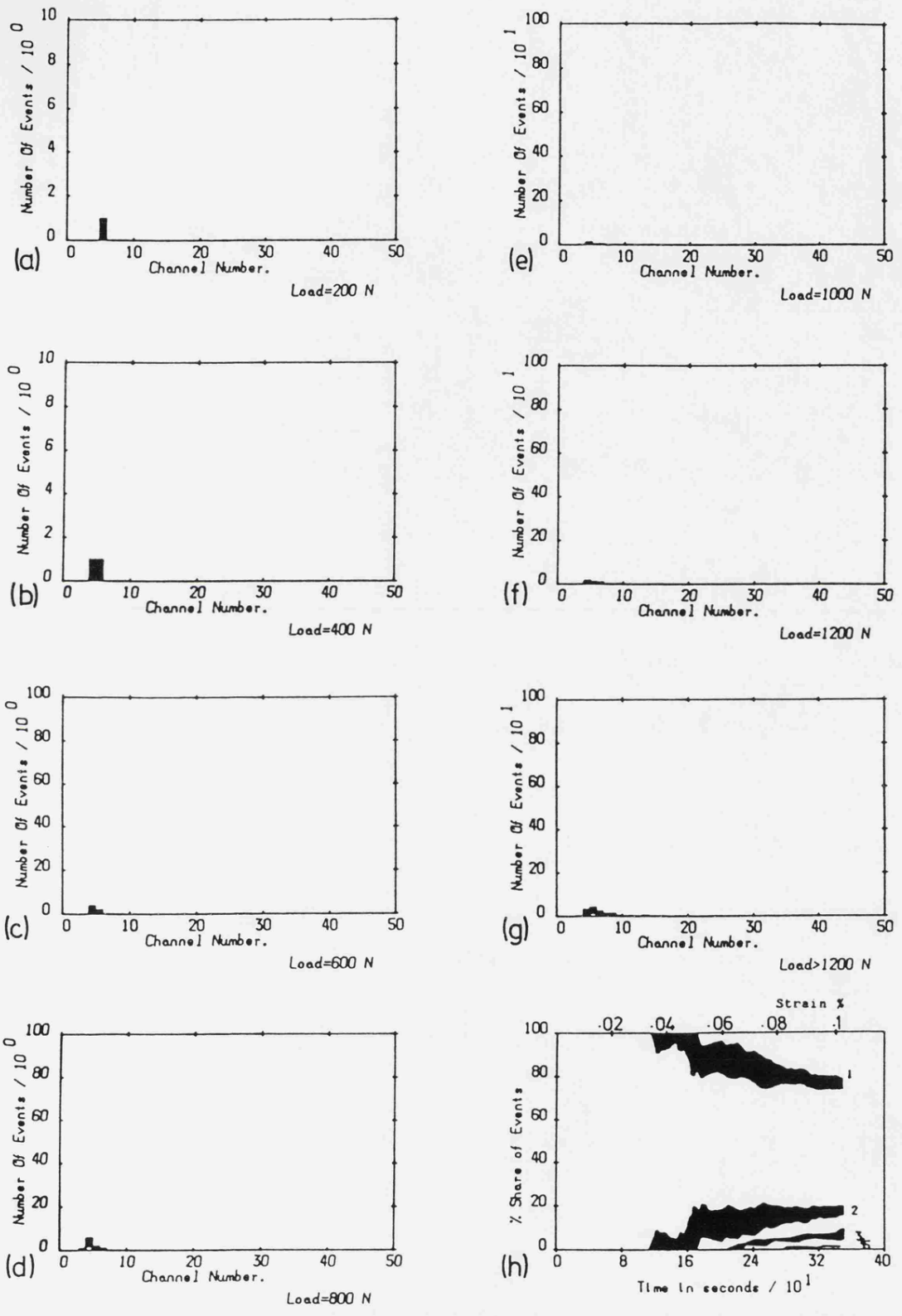

Fig 7.37 Amplitude distribution histograms and the percentage share graph for the low power alumina coatings shown in Fig 7.36.

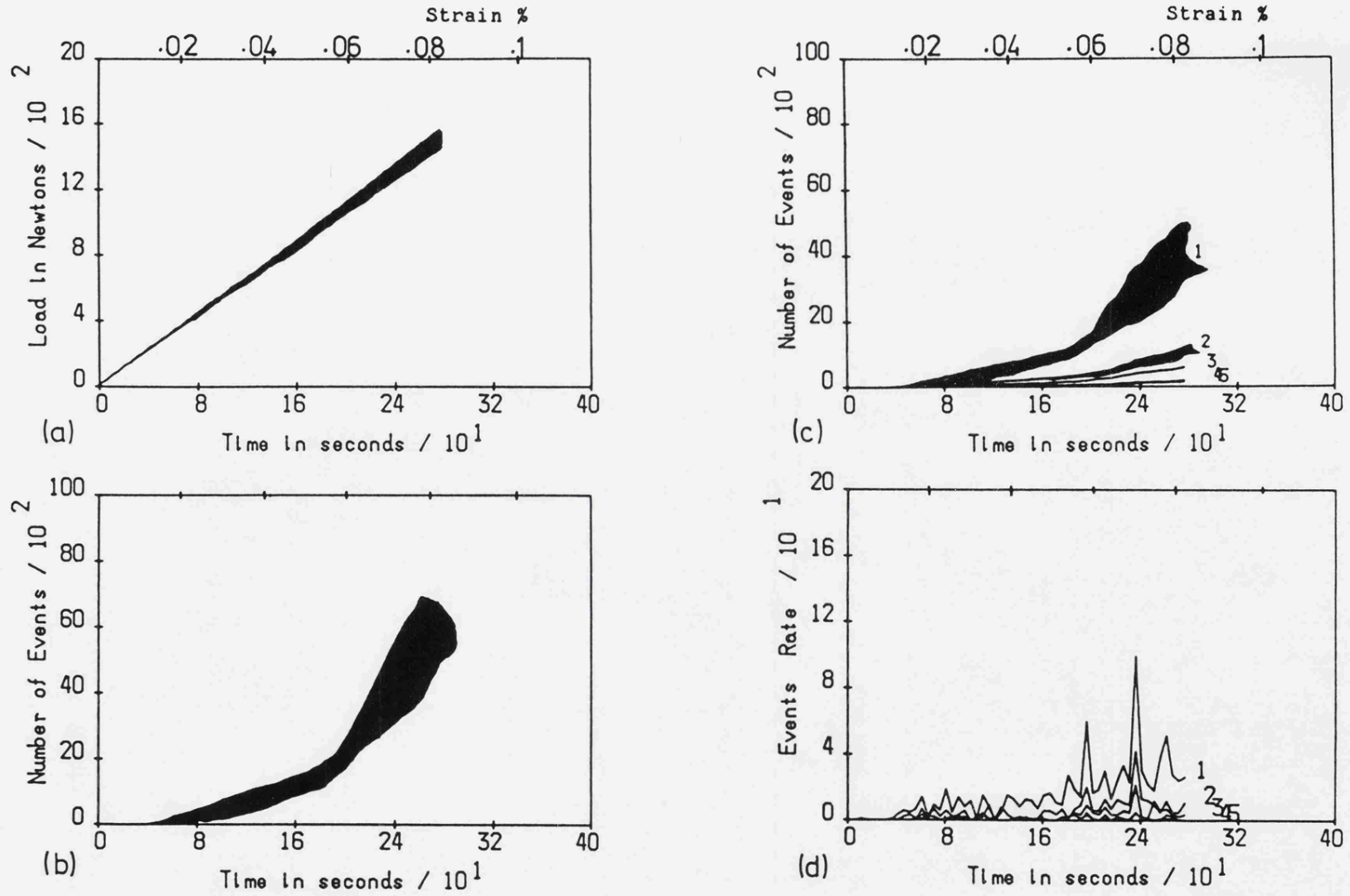

Fig 7.38 AE event curves for 10 alumina coatings sprayed on the substrate with poor surface preparation.

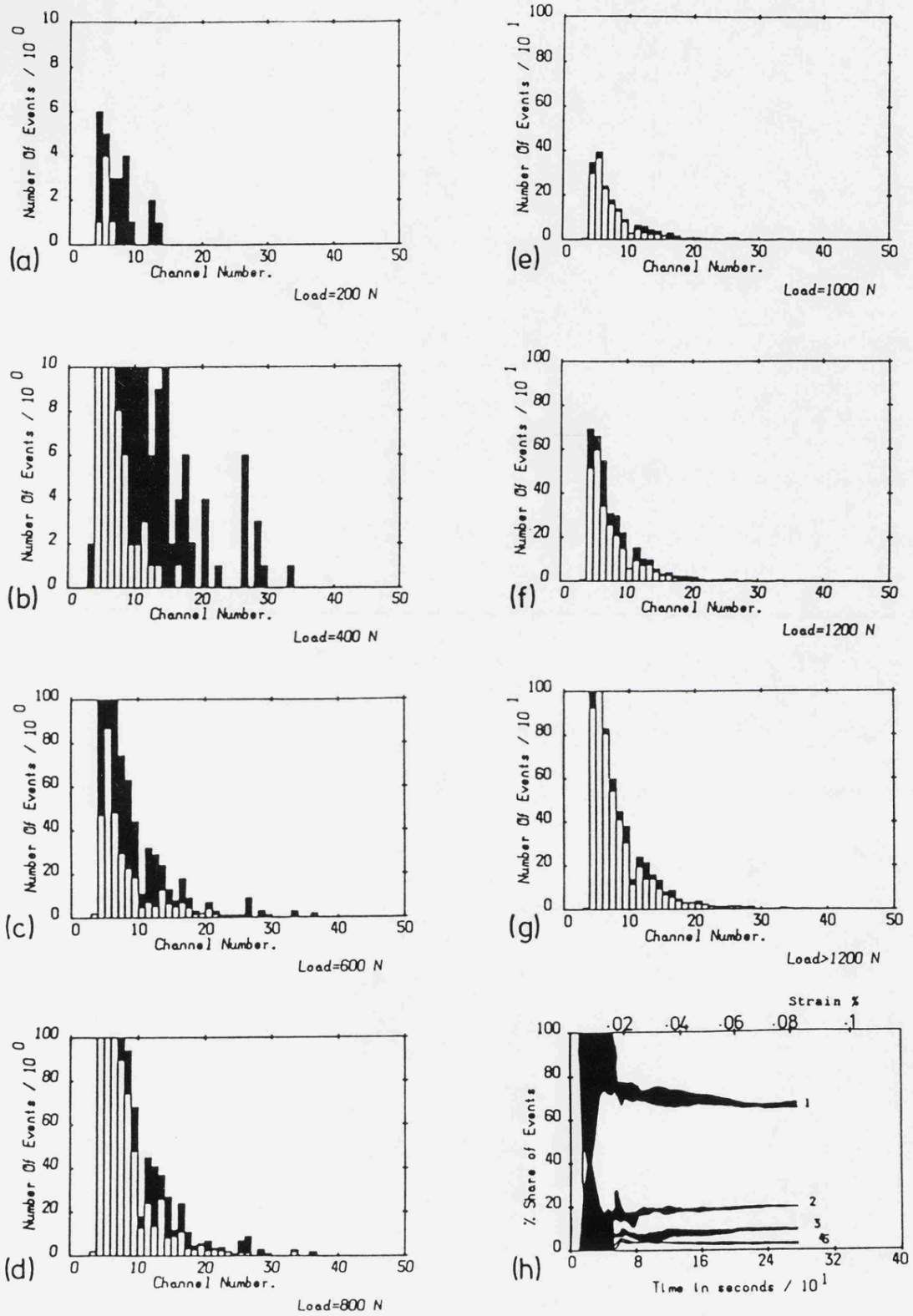

Fig 7.39 Amplitude distribution histograms and the percentage share graph for the poor surface preparation alumina coatings shown in Fig 7.38.

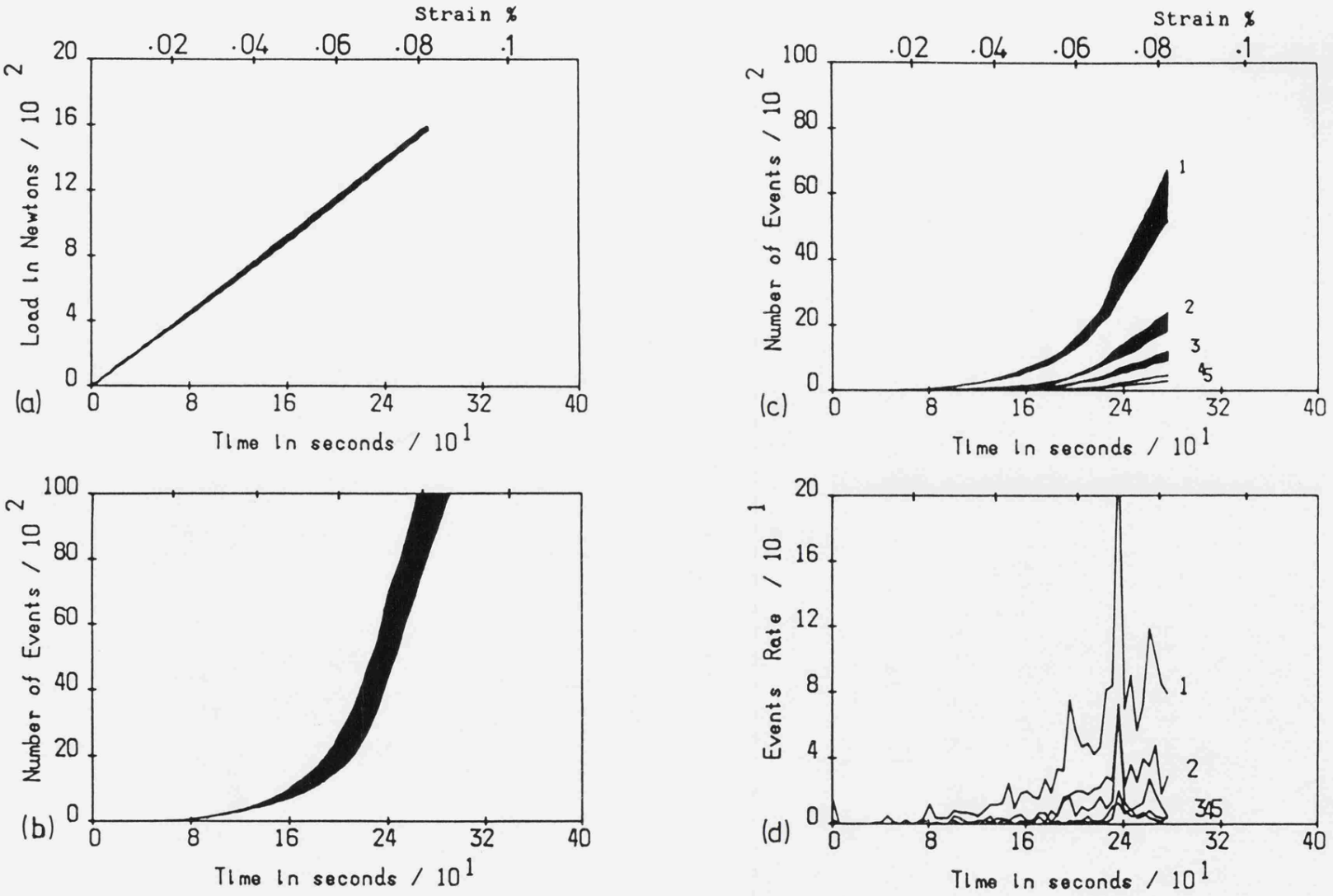

Fig 7.40 AE event curves for 10 alumina coatings sprayed with no coolant air.

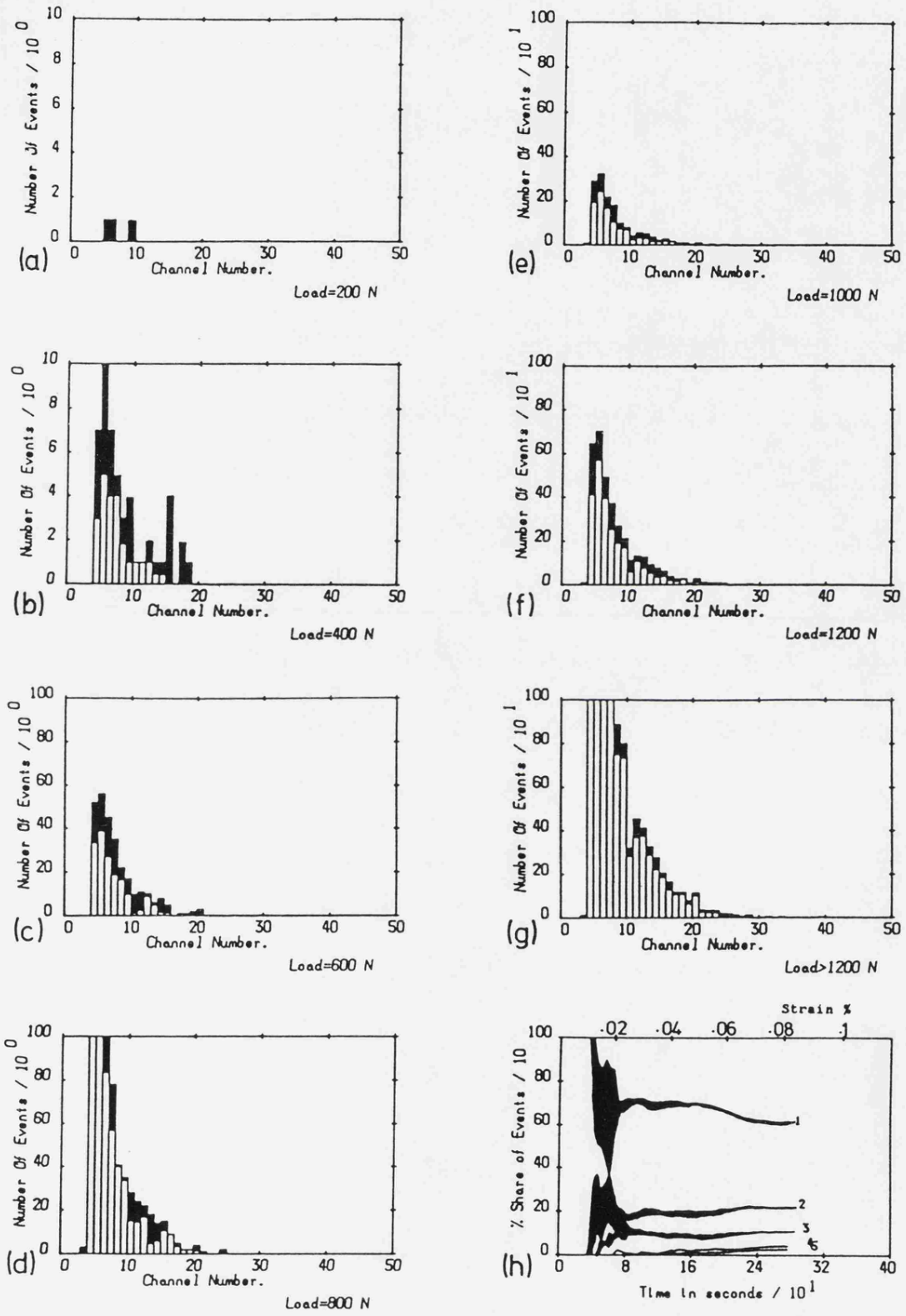

Fig 7.41 Amplitude distribution histograms and the percentage share graph for the over heated alumina samples shown in Fig 7.40

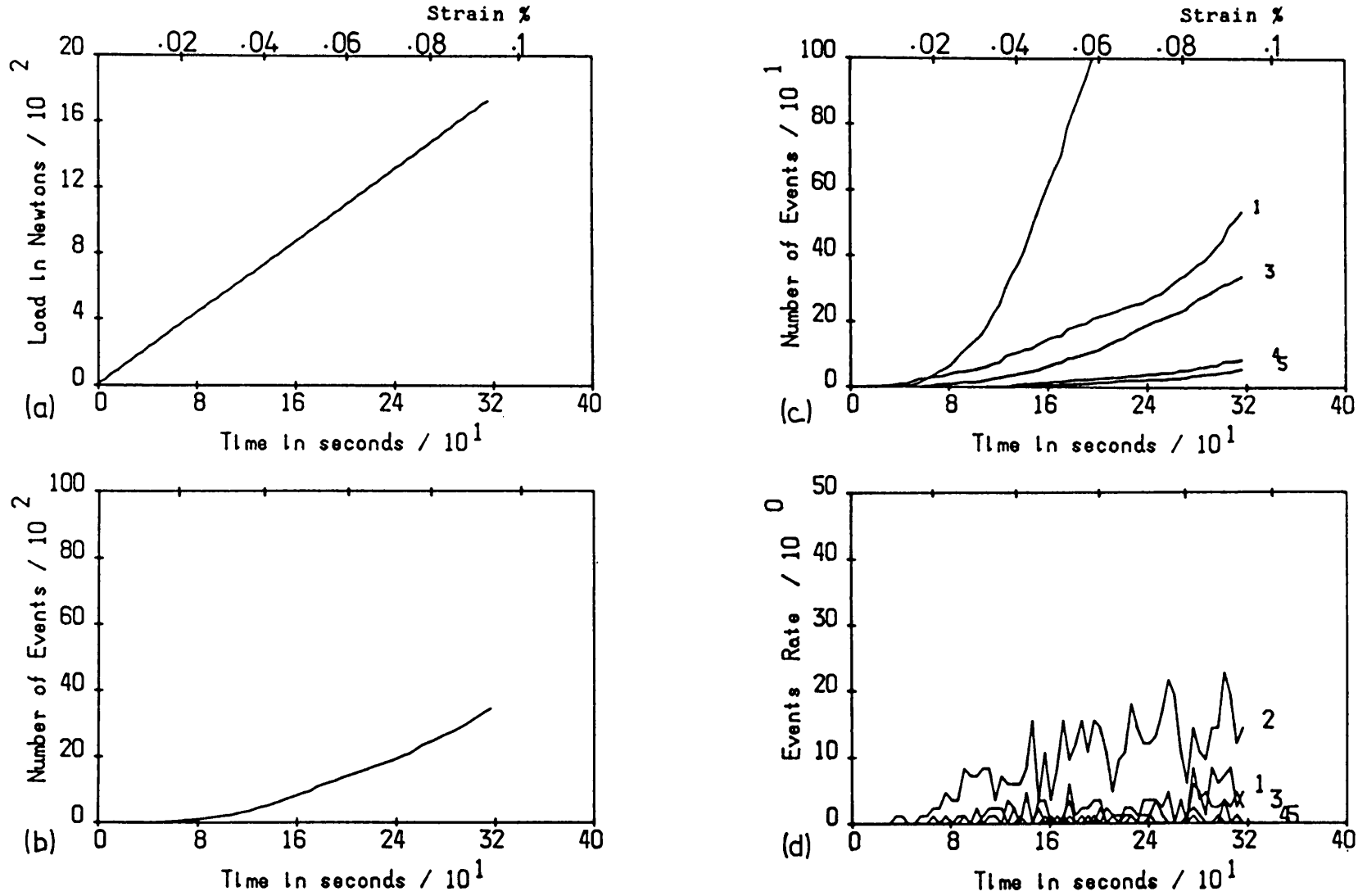

Fig 7.42 AE event curves for an alumina control sample, which showed more AE activity than the rest of the control ones (Fig 7.31).

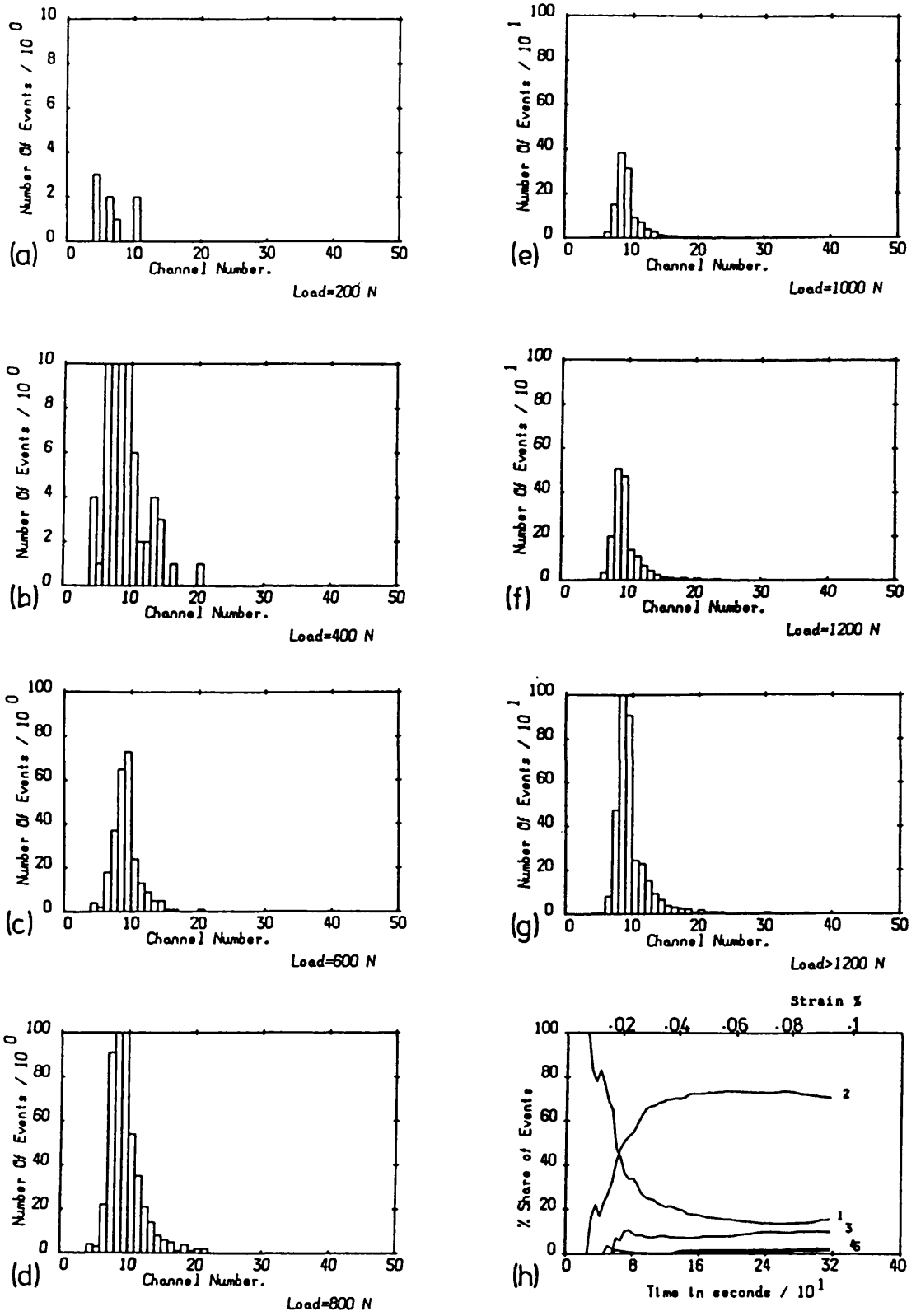

Fig 7.43 Amplitude distribution histograms and the percentage share graph for the alumina coatings shown in Fig 7.42.

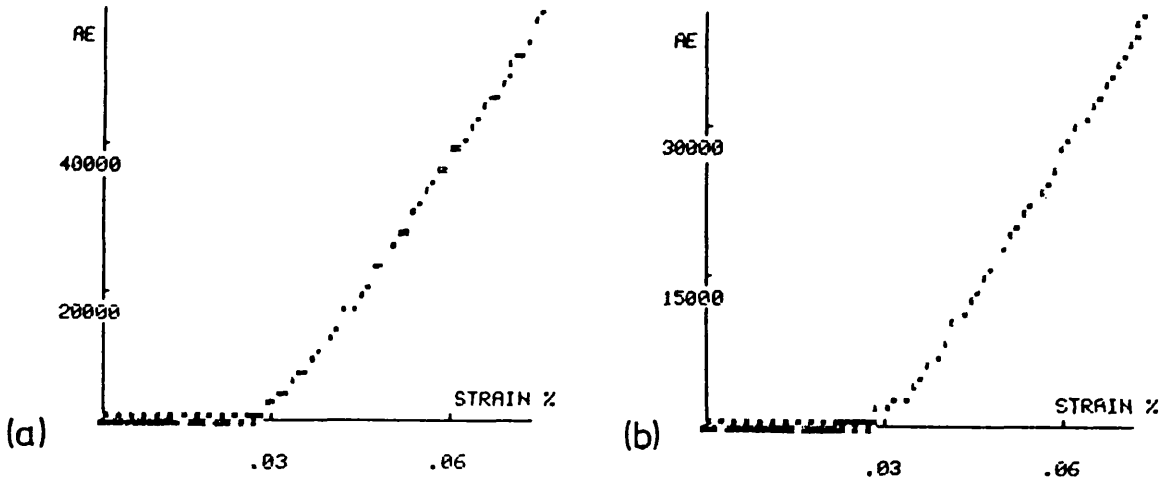

Fig 7.44 Two typical AE plots (ring-down vs strain) of Mo63 control coatings.

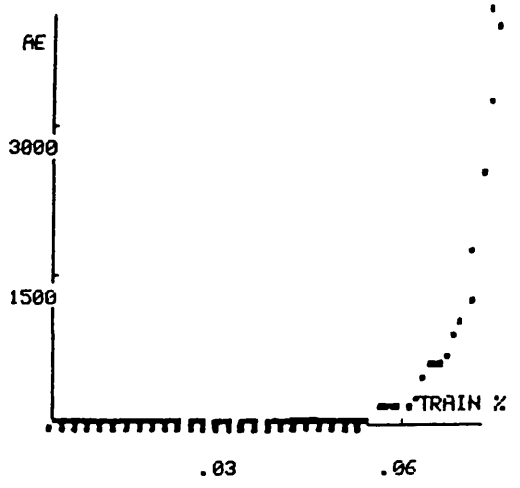

Fig 7.45 AE ring-down plot vs strain for reloading of the sample shown in Fig 7.44a.

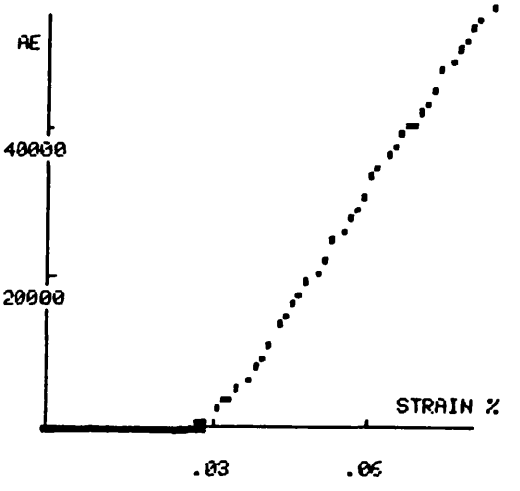

Fig 7.46 A typical ring-down plot for a Mo63 coating sprayed on a substrate which has had no surface preparation.

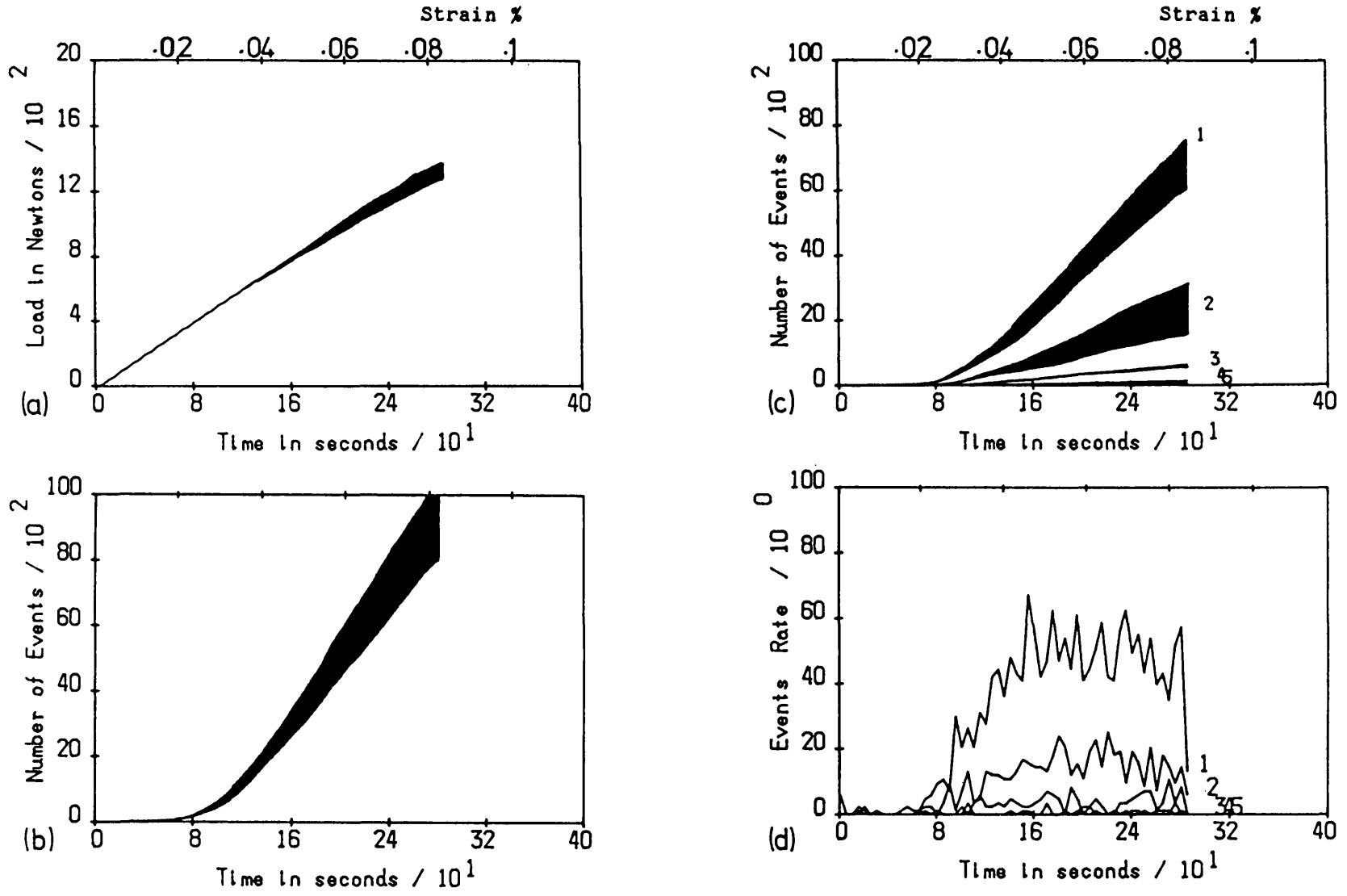

Fig 7.47 AE event curves for 9 replicate Mo 63 coatings (coating thickness 0.25 mm)

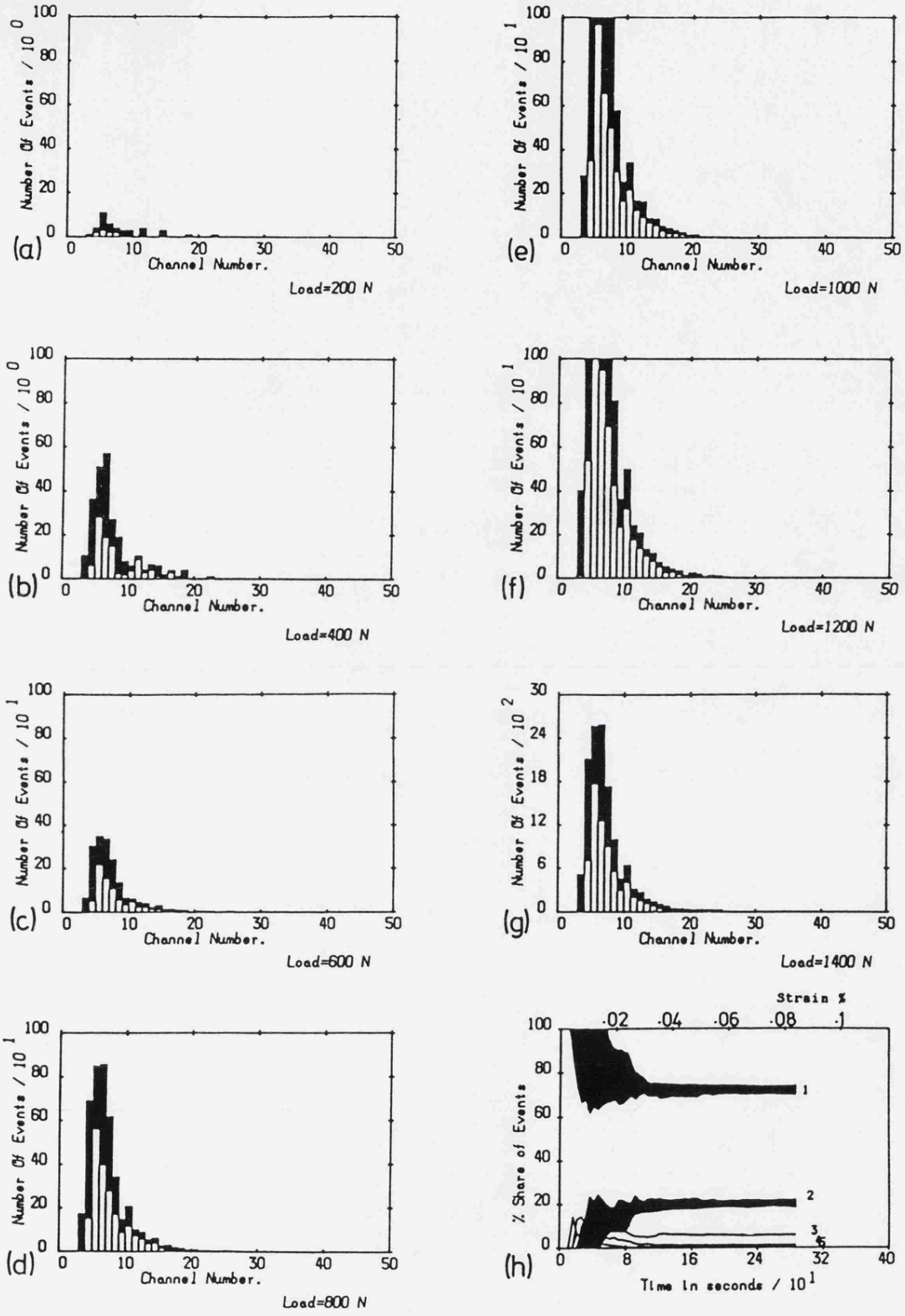

Fig 7.48 Histograms of the amplitude distributions and the percentage share graph for the samples shown in Fig 7.47.

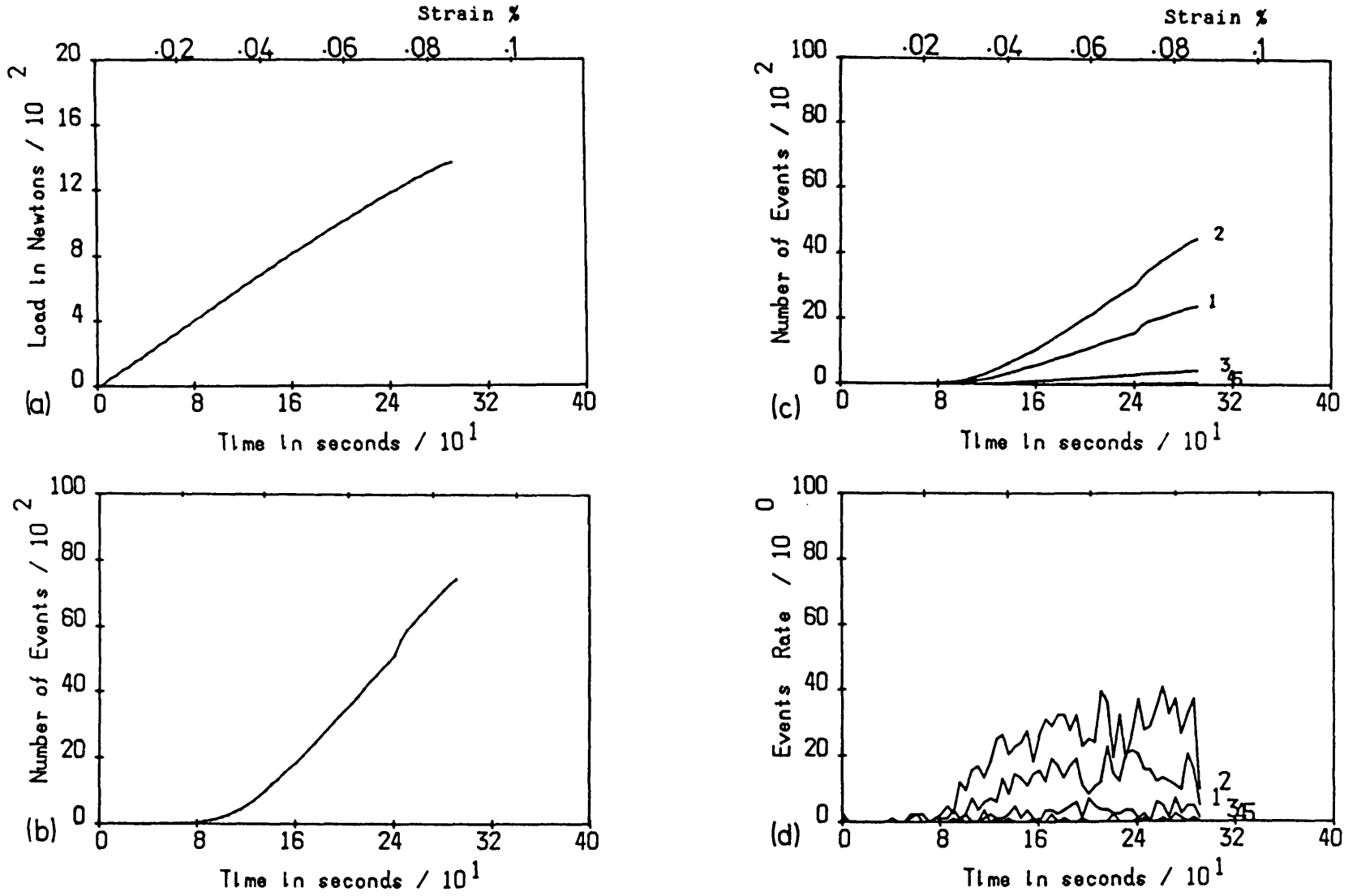

Fig 7.49 AE event curves for a Mo63 control specimen (coating thickness 0.19 mm).

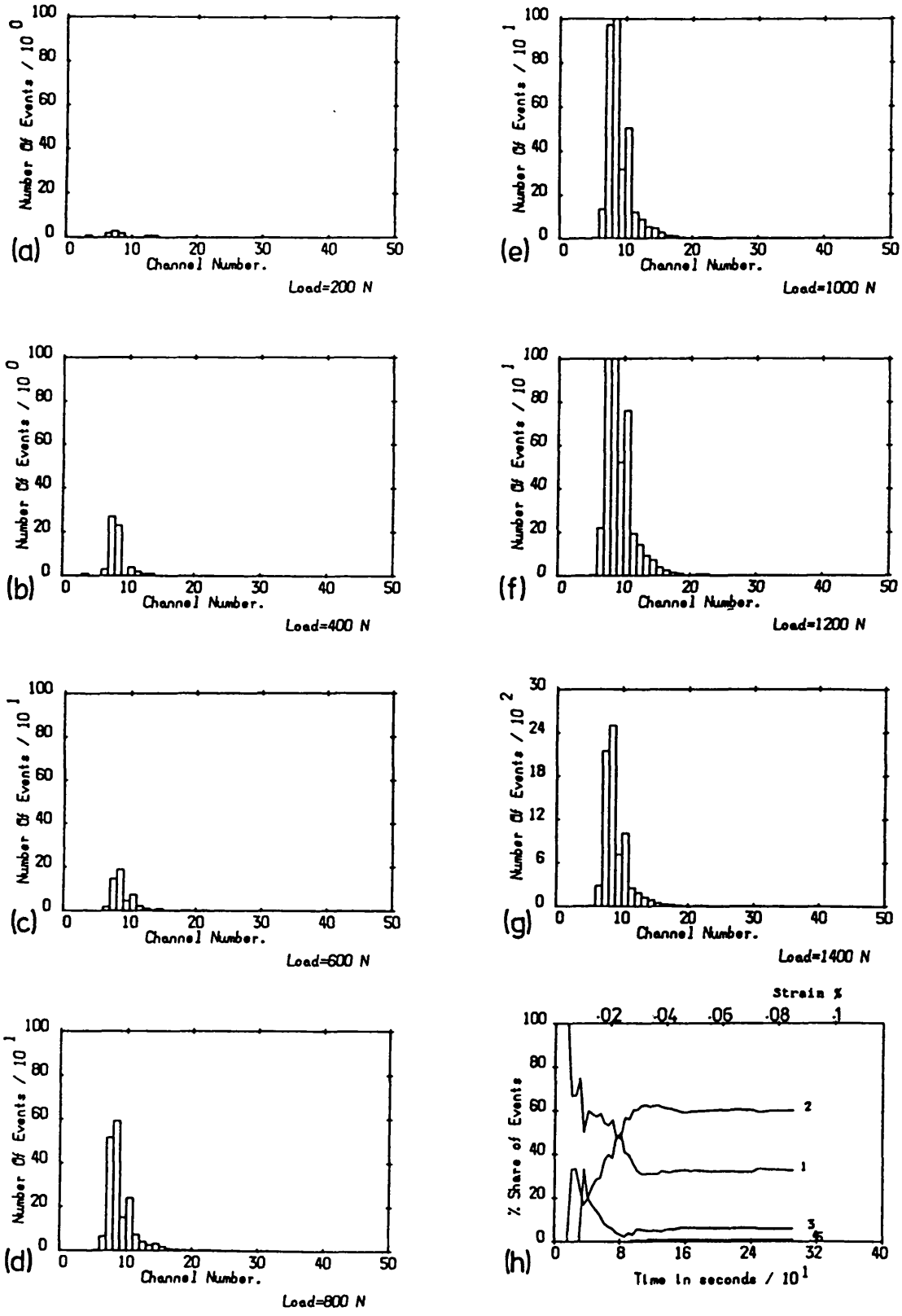

Fig 7.50 Histograms of the AE event amplitude distributions and the percentage share graph for the sample shown in Fig 7.49.

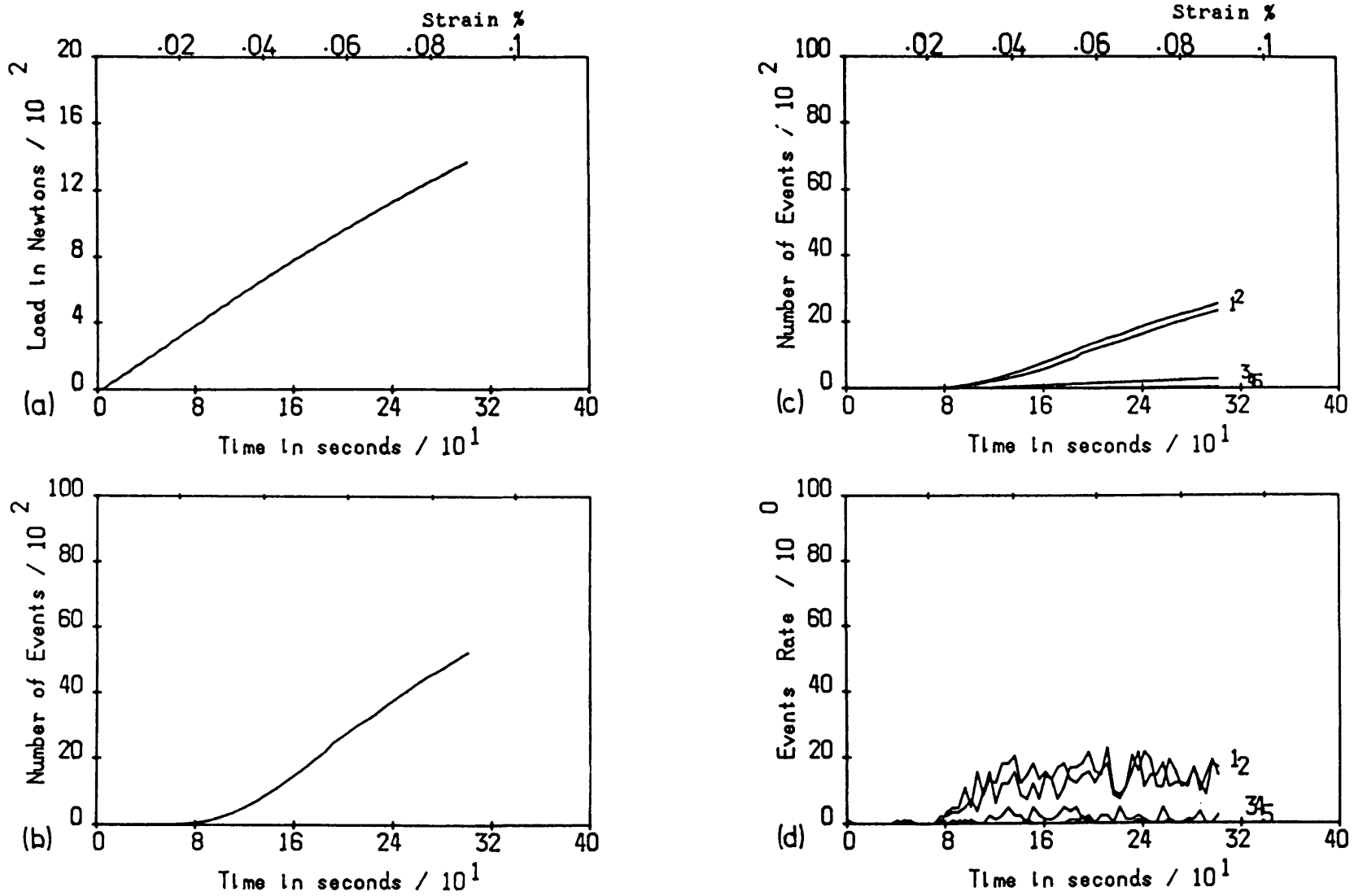

Fig 7.51 AE event curves for a Mo63 control sample (coating thickness 0.18 mm).

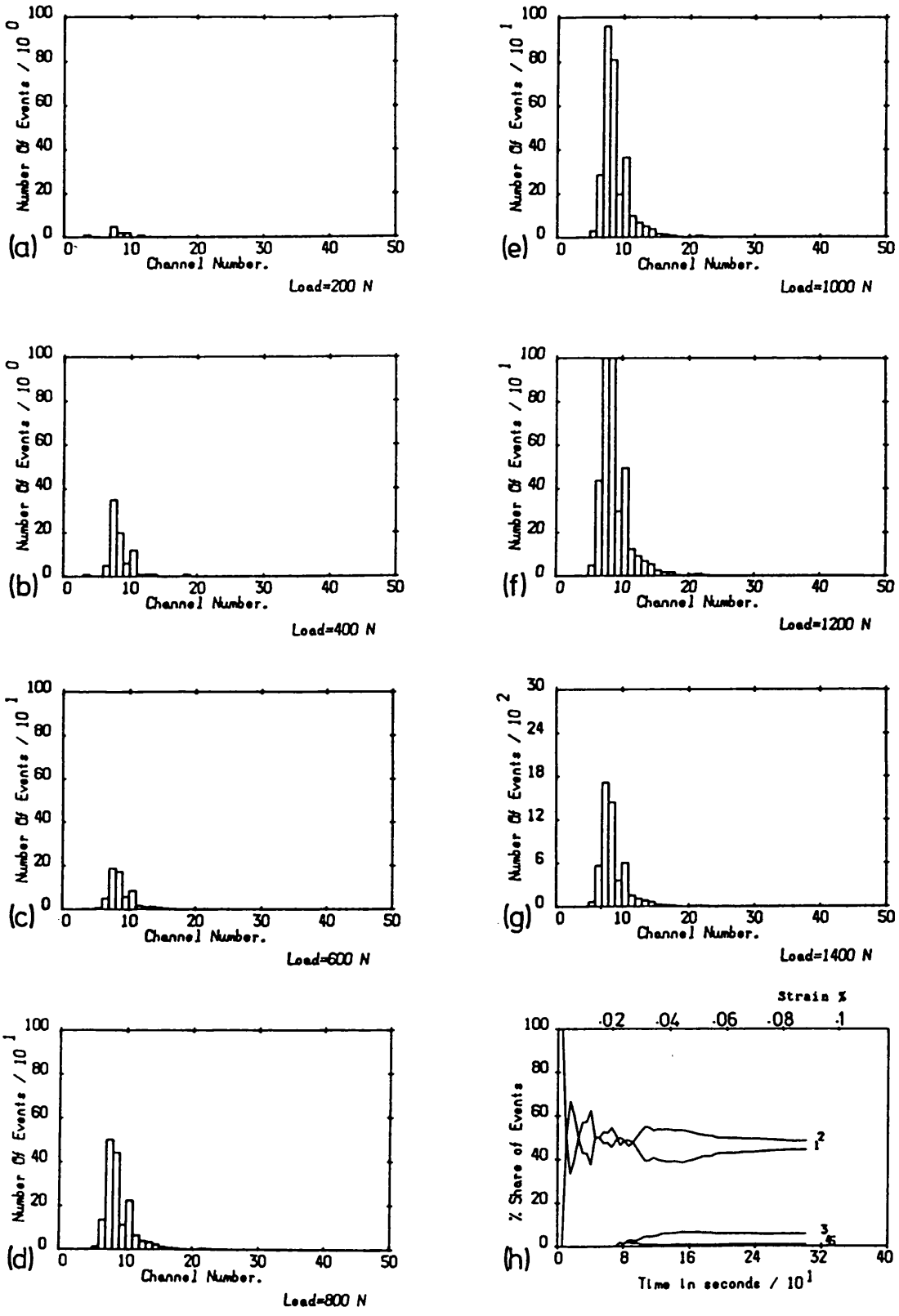

Fig 7.52 Histograms of the AE event amplitude distributions and the percentage share graph for the sample shown in Fig 7.51.

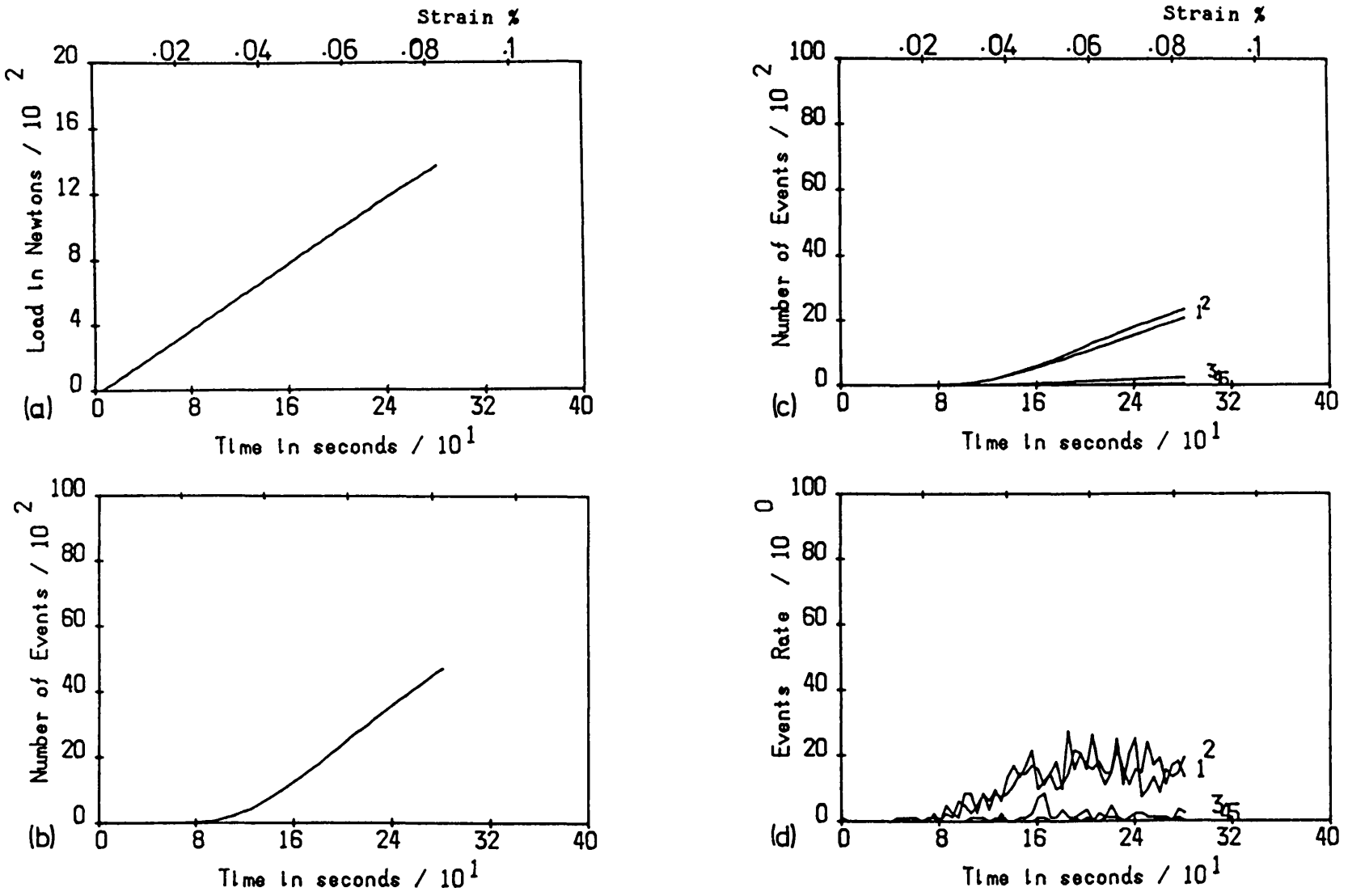

Fig 7.53 AE event curves for a Mo63 coating sprayed on a subatrate with no surface preparation (coating thickness 0.18 mm).

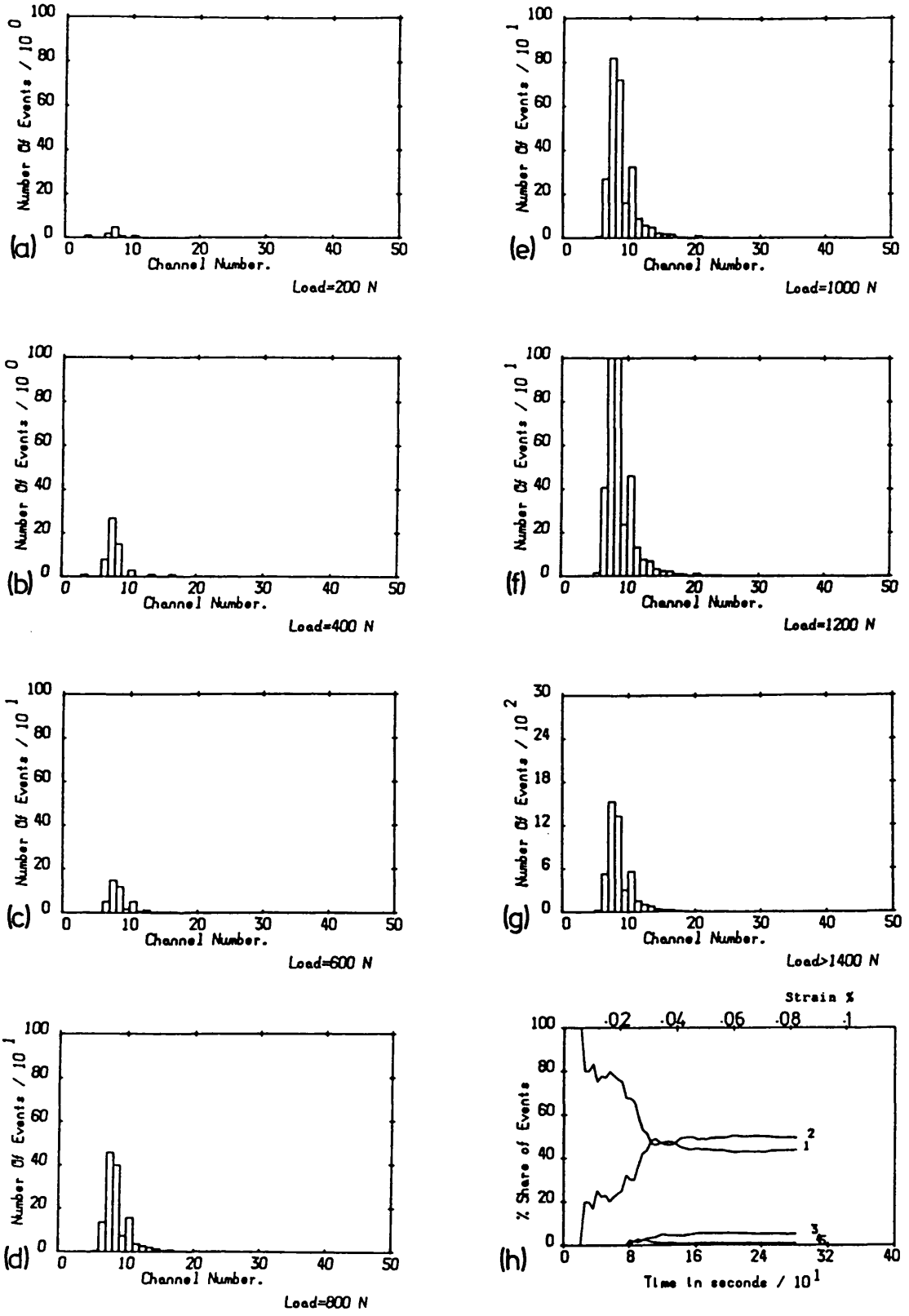

Fig 7.54 Histograms of the AE event amplitude distribution and percentage share graph for the sample shown in Fig 7.53.

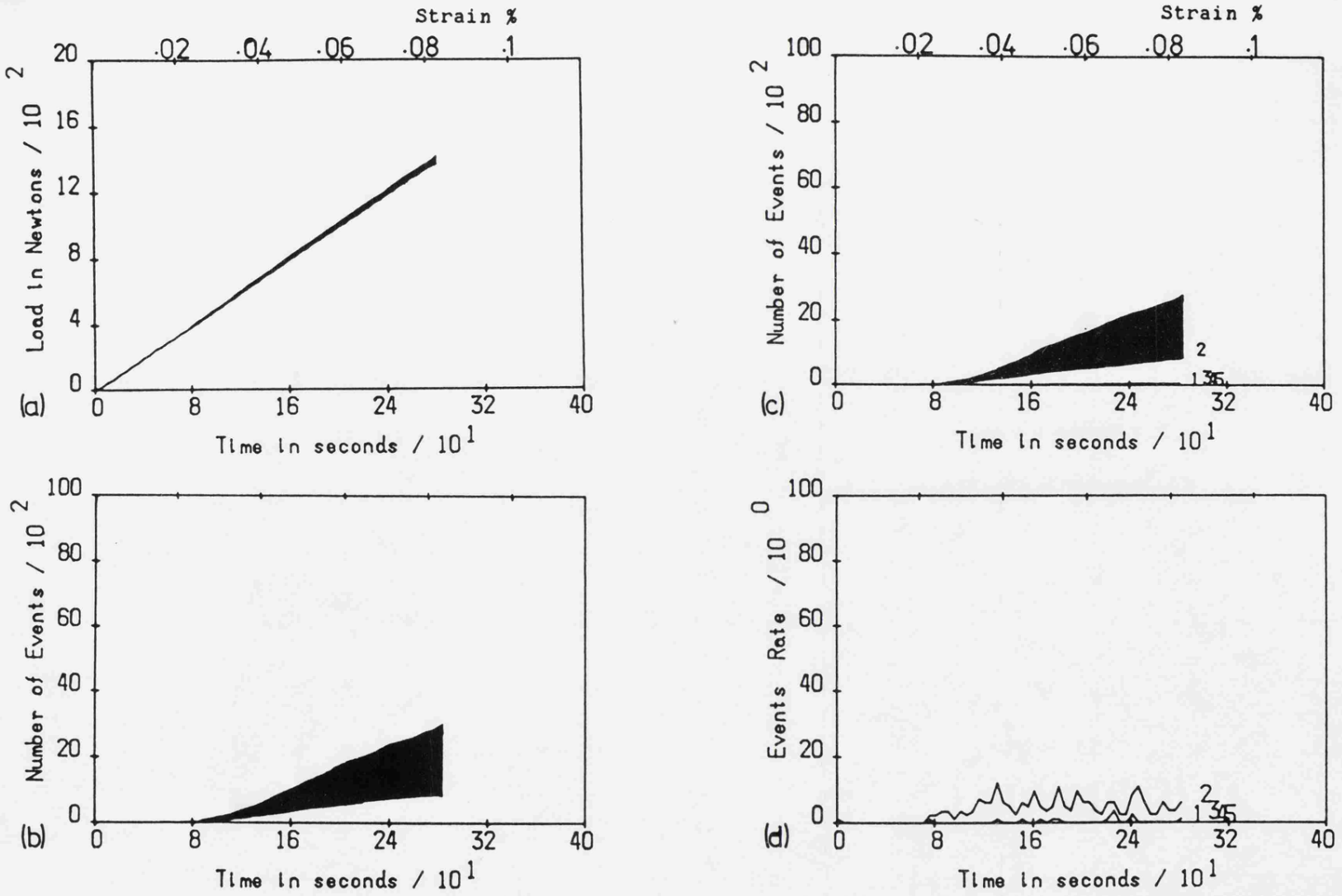

Fig 7.55 AE event curves for 4 replicate Mo63 coatings (coating thickness 0.14 mm).

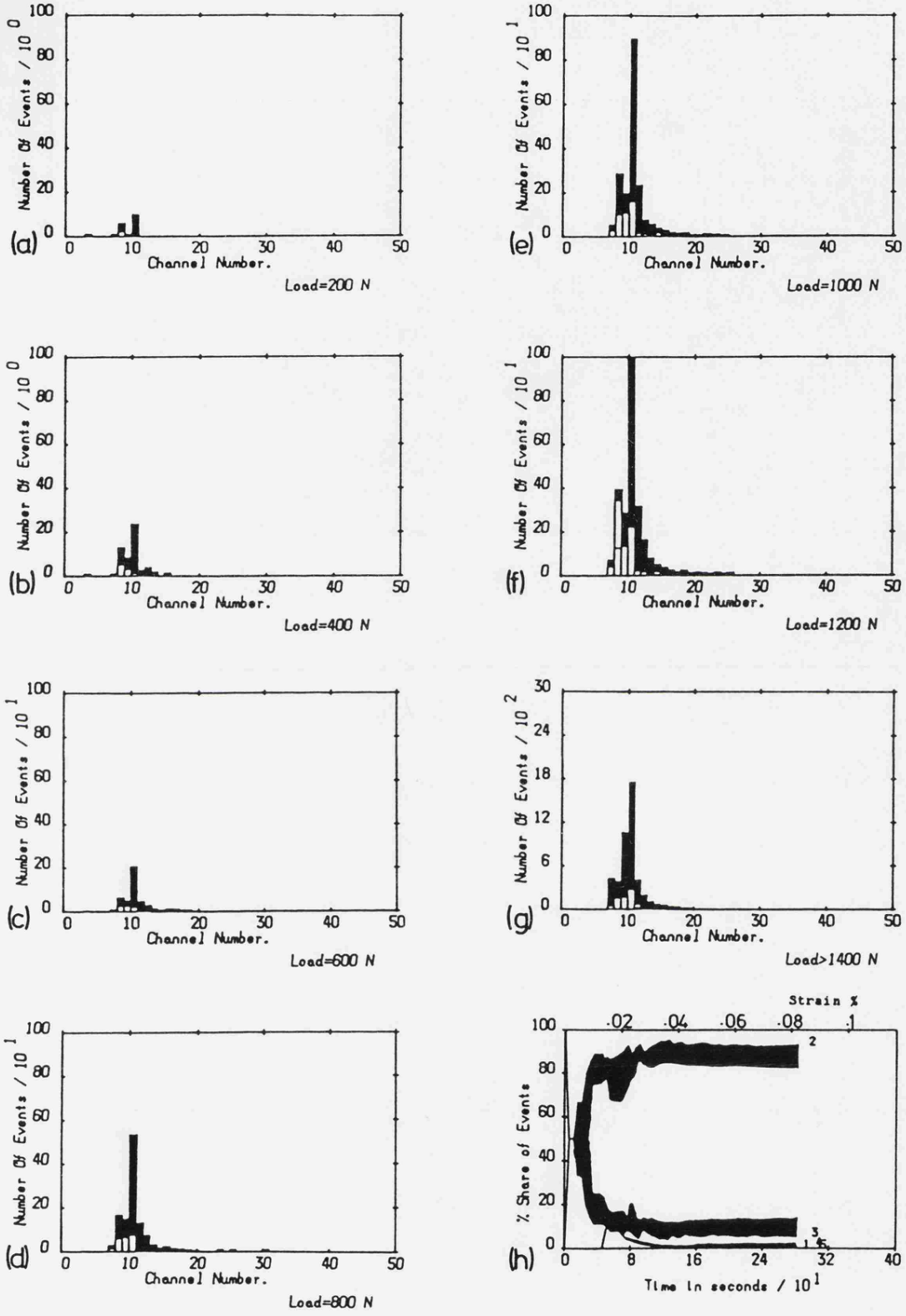

Fig 7.56 Histograms of the AE event amplitude distribution and the percentage share for the samples shown in Fig 7.55.

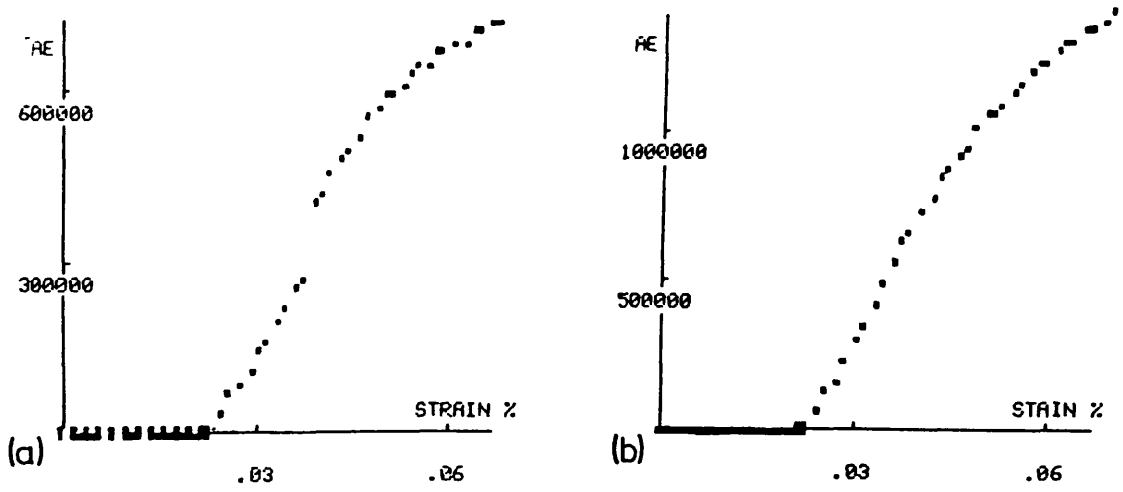

Fig 7.57 Two typical AE ring-down plots for Mo505 control coatings.

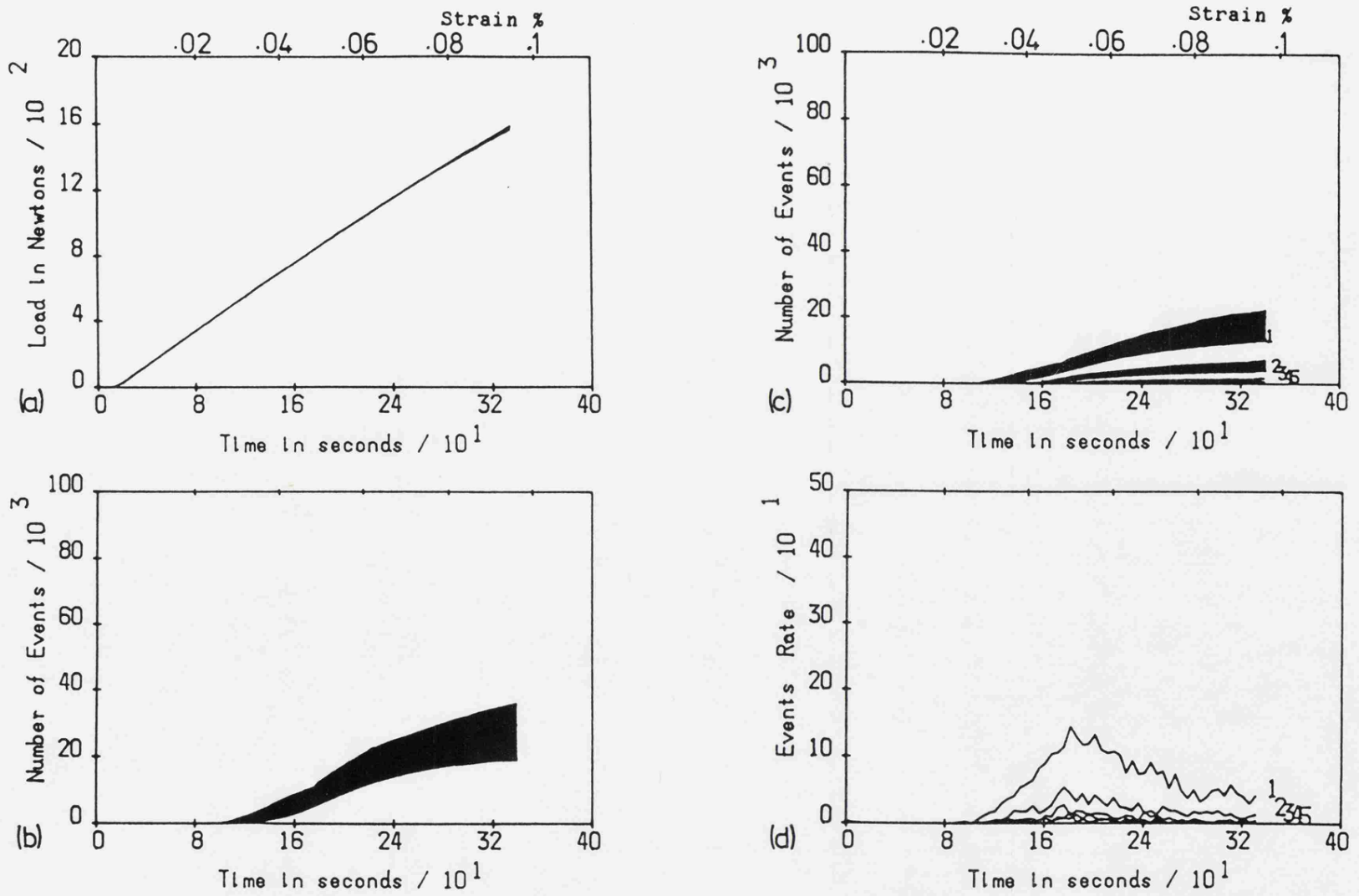

Fig 7.58 AE event curves for 6 replicate Mo 505 coatings (coating thickness 0.11 mm).

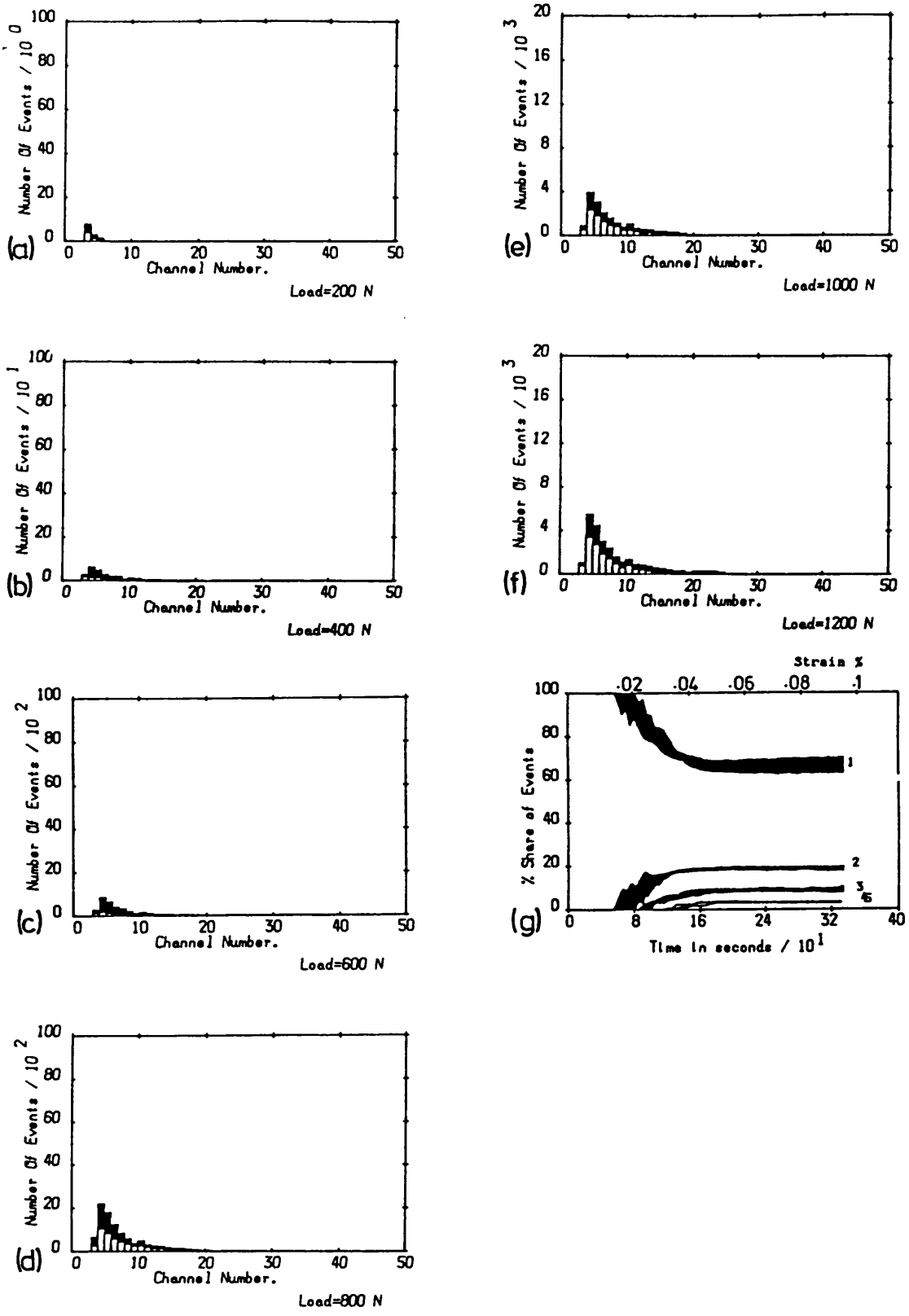

Fig 7.59 Histograms of the AE event amplitude distributions and the percentage share graph for the samples shown in Fig 7.58.

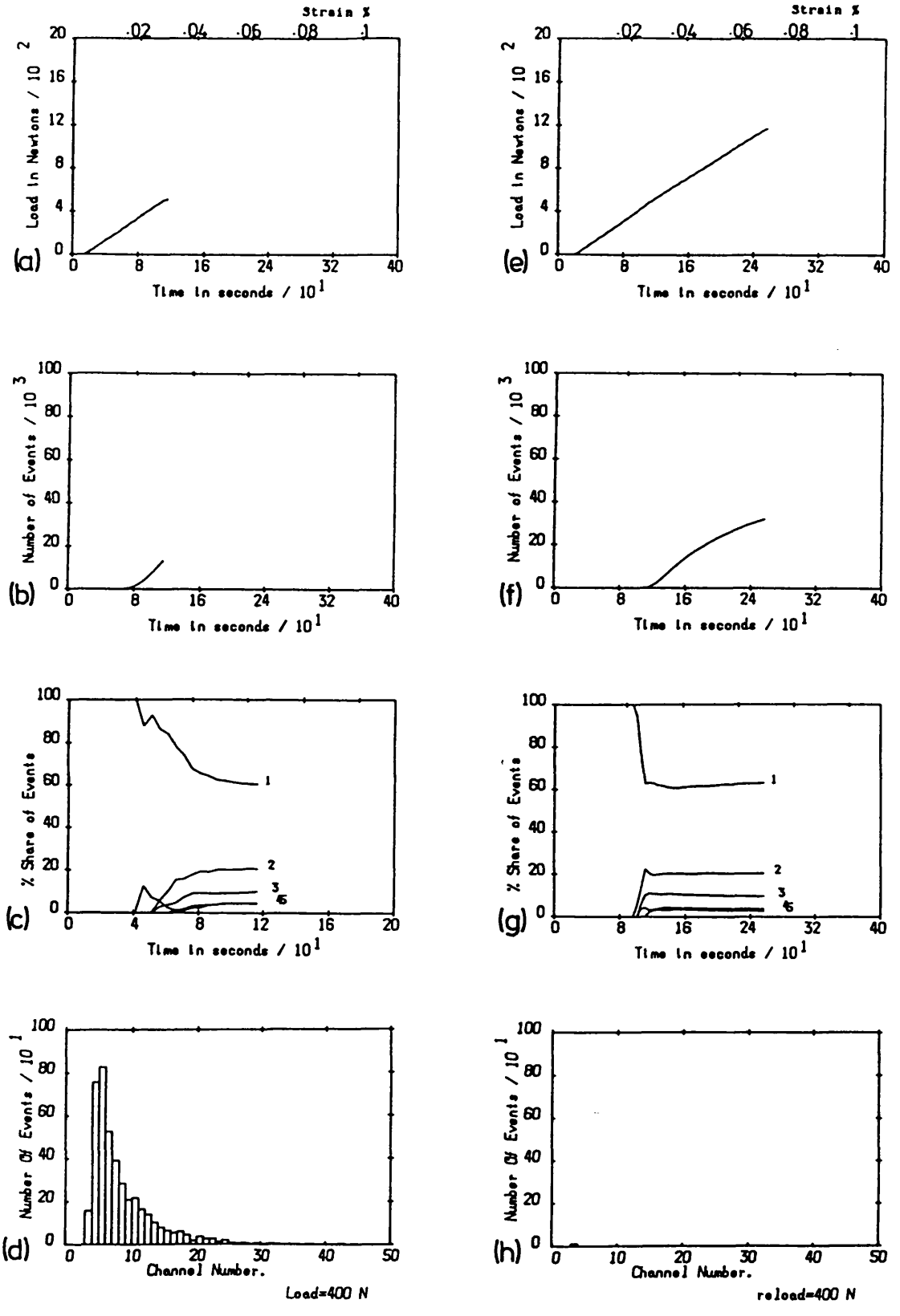

Fig 7.60 a, b, c&d AE response of a Mo505 coating upon first loading.
e, f, g&h AE response of the same sample upon second loading.

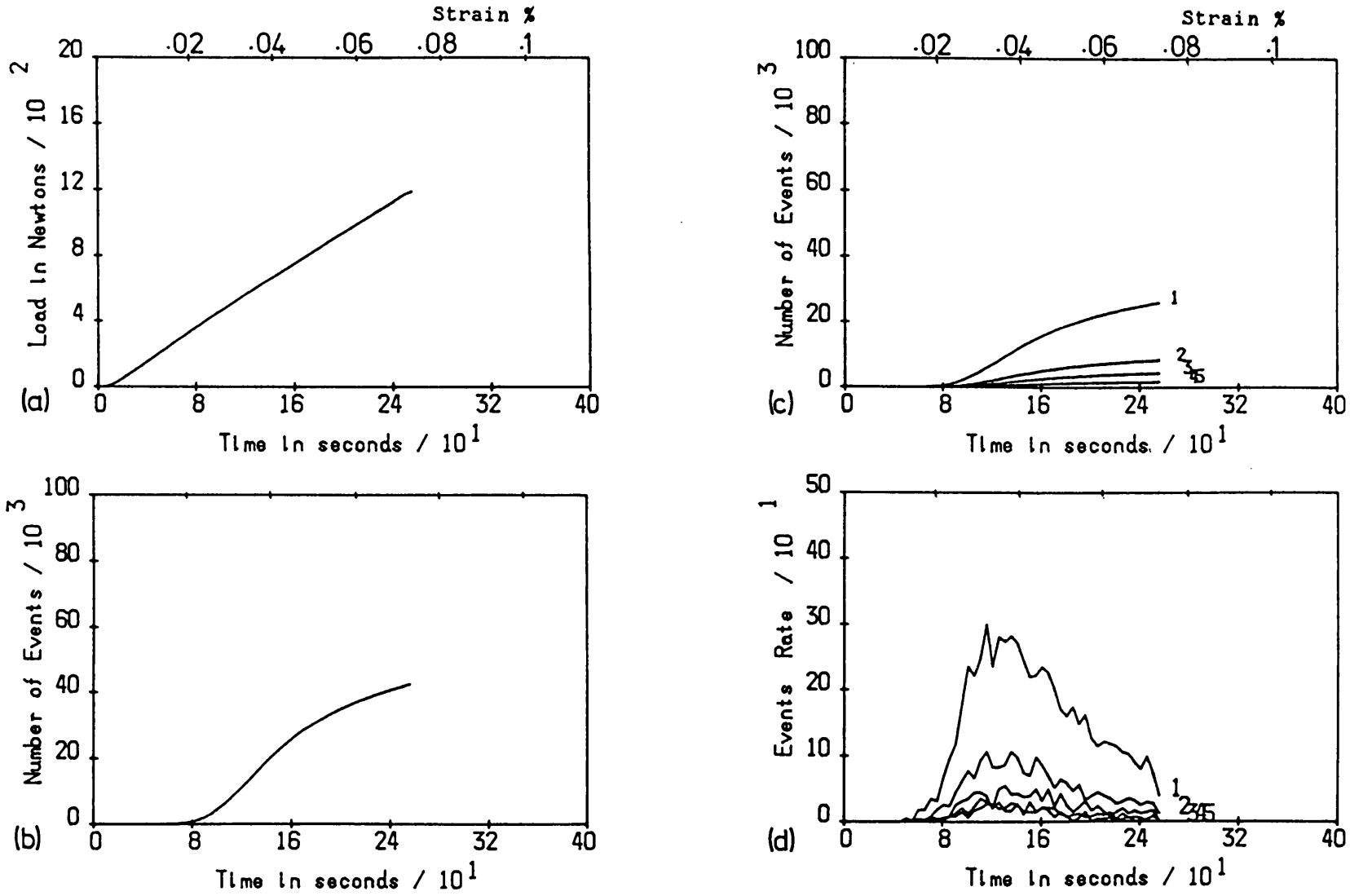

Fig 7.61 AE event curves for a Mo505 control sample (coating thickness 0.2 mm).

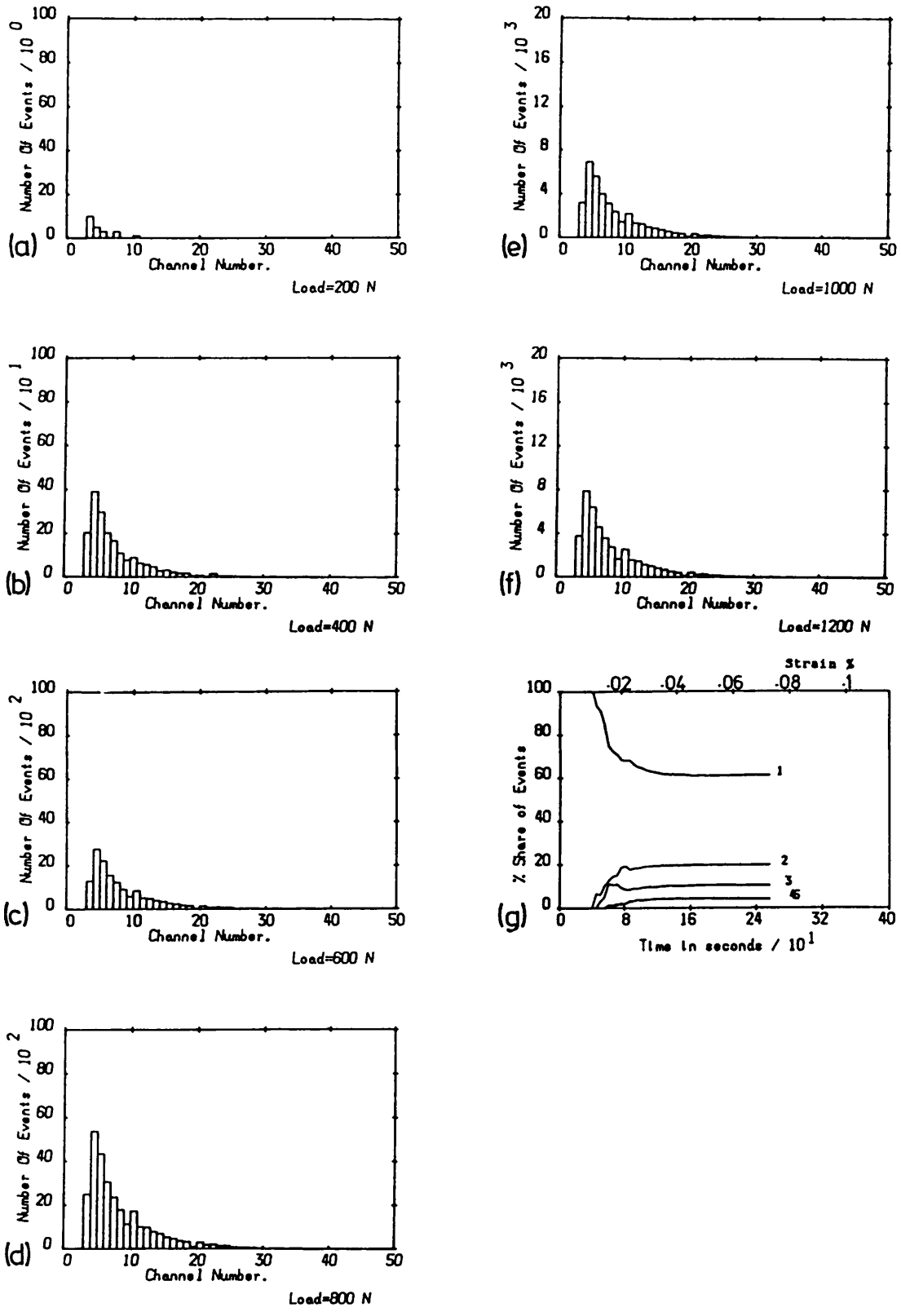

Fig 7.62 Histograms of the AE event amplitude distributions and the percentage share graph for the sample shown in Fig 7.61.

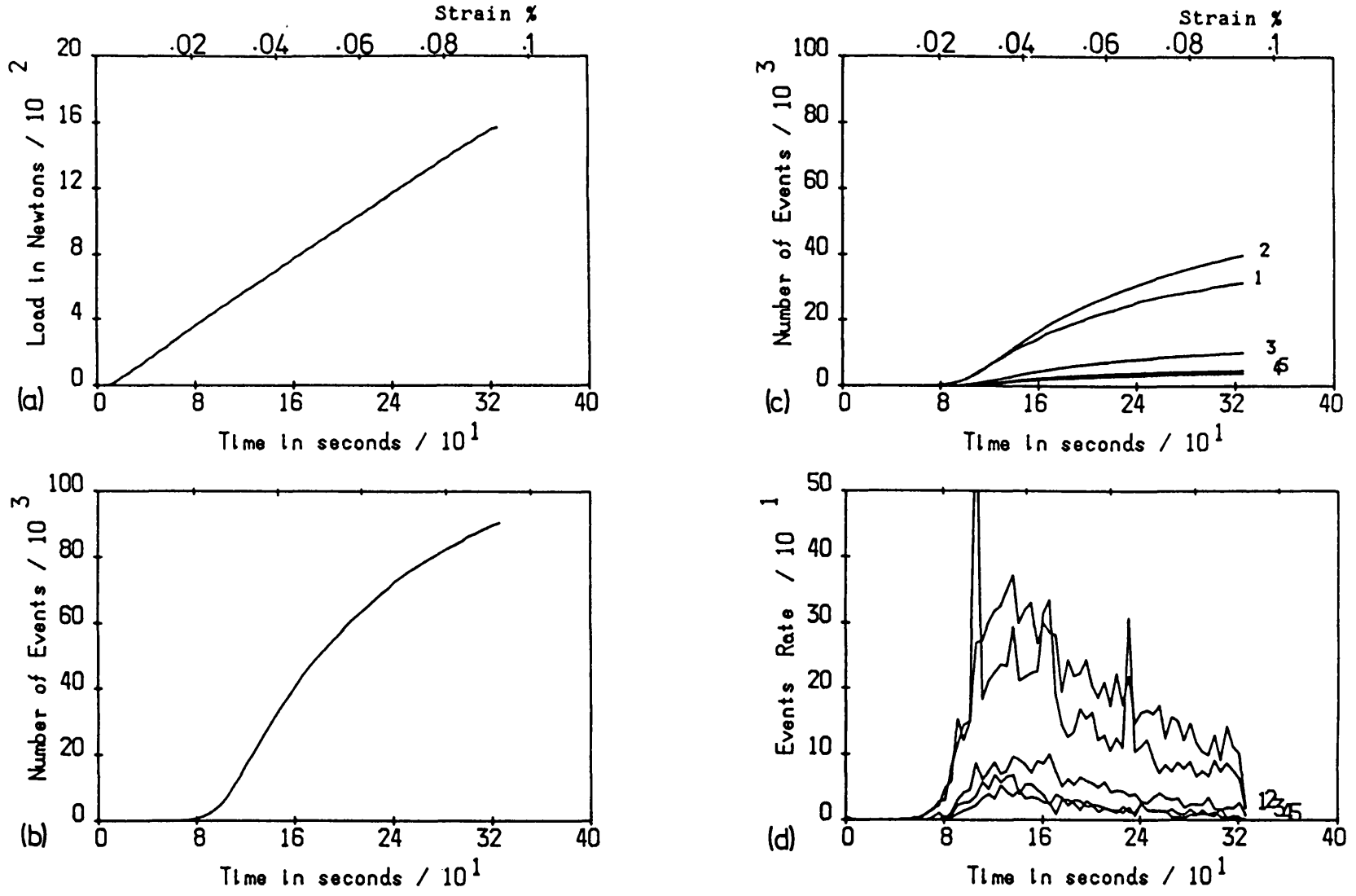

Fig 7.63 AE event curves for a 0.025 mm thick Mo505 control coating.

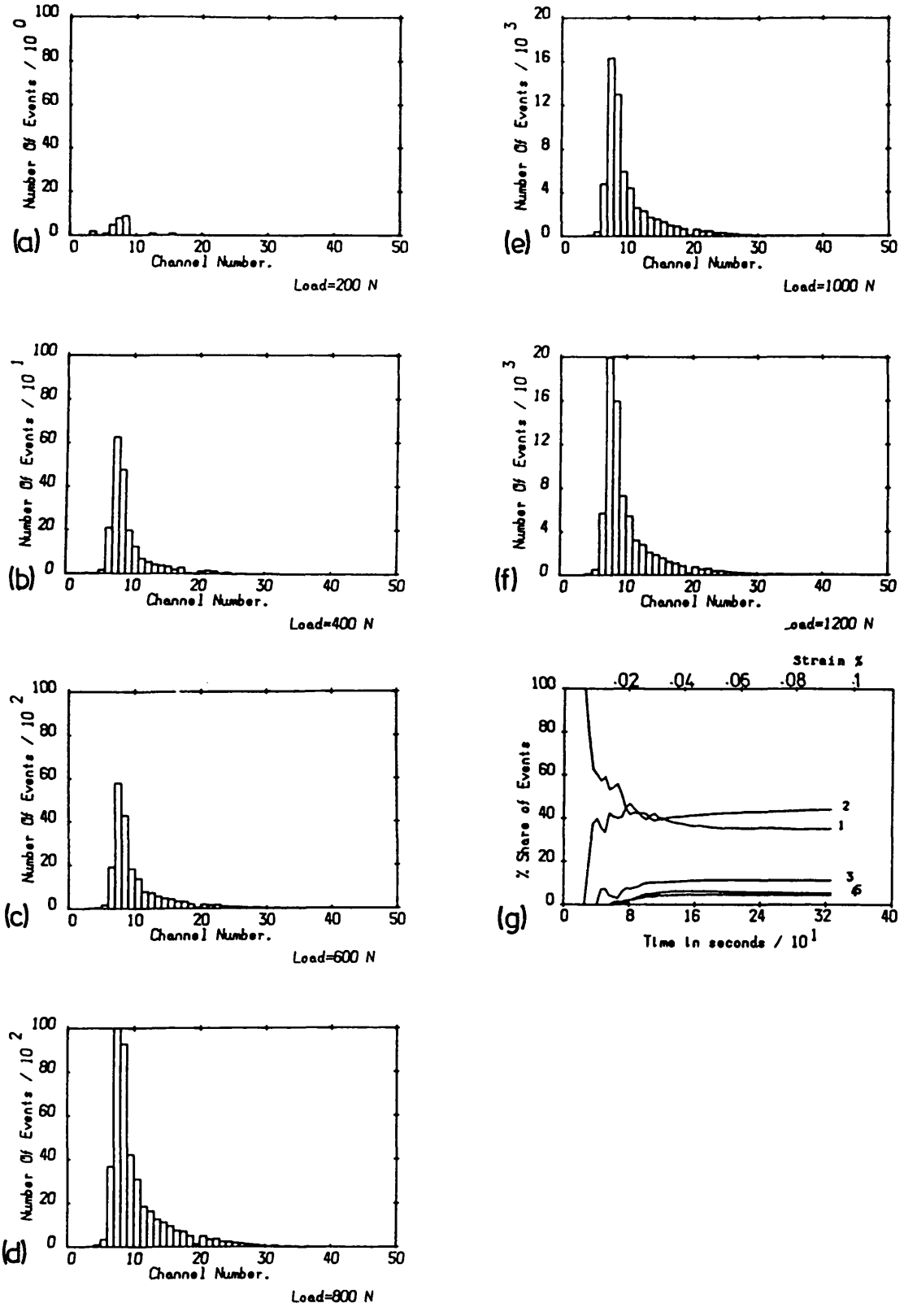

Fig 7.64 Histograms of the AE event amplitude distribution and the percentage share graph for the coating shown in Fig 7.63.

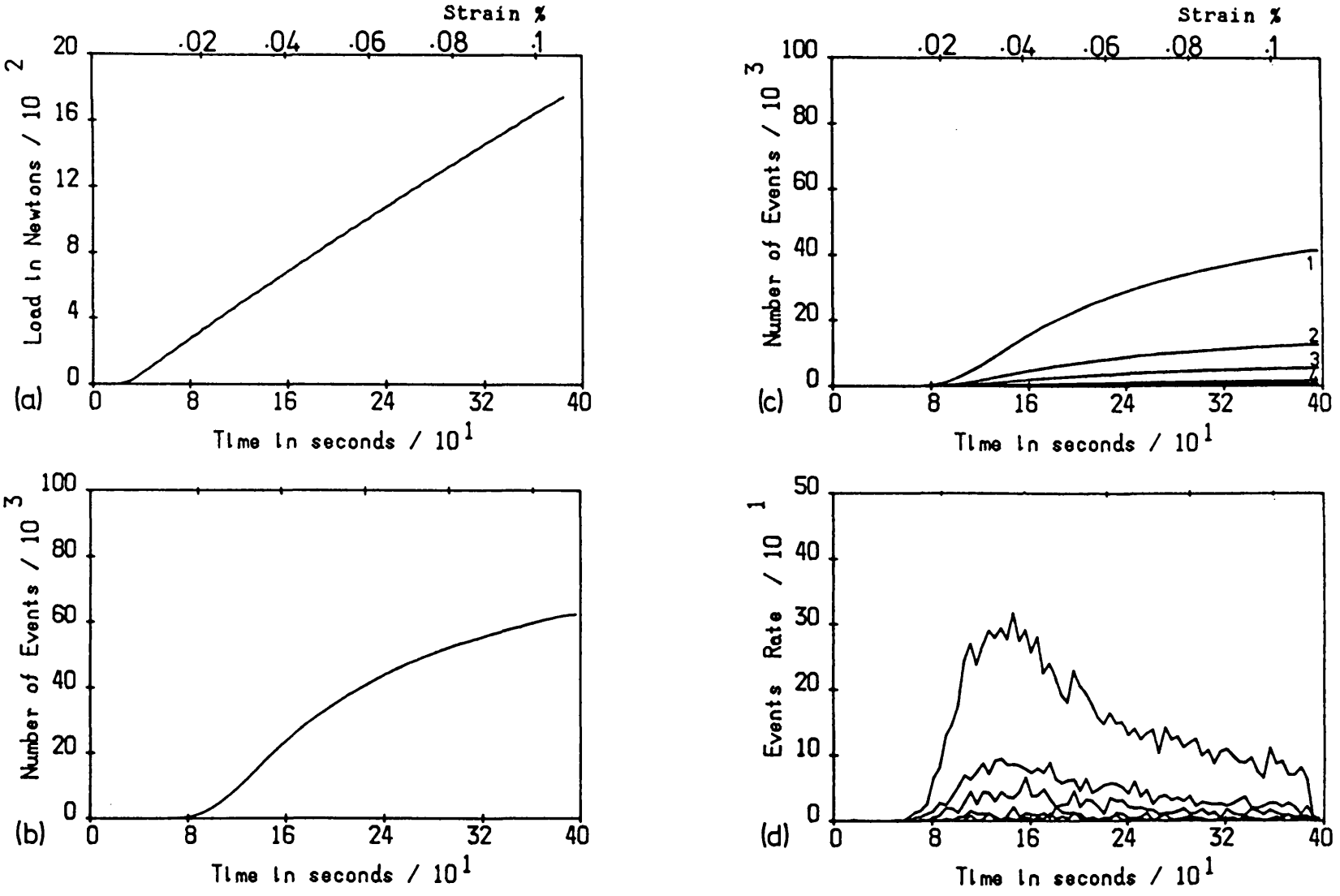

Fig 7.65 AE event curves for a 0.3 mm thick low power Mo505 coating.

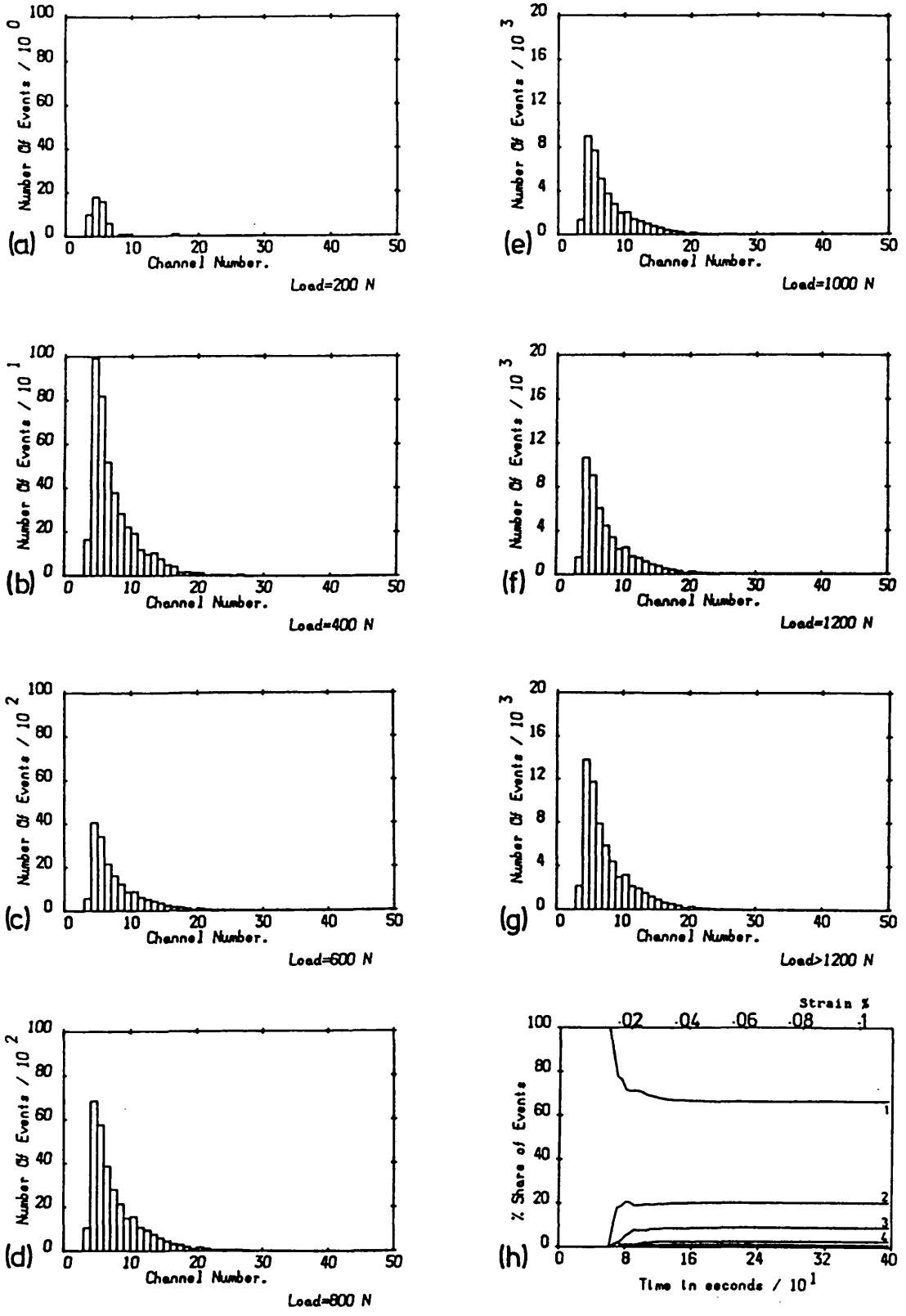

Fig 7.66 Histograms of the AE event amplitude distributions and the percentage share graph for the coating shown in Fig 7.65.

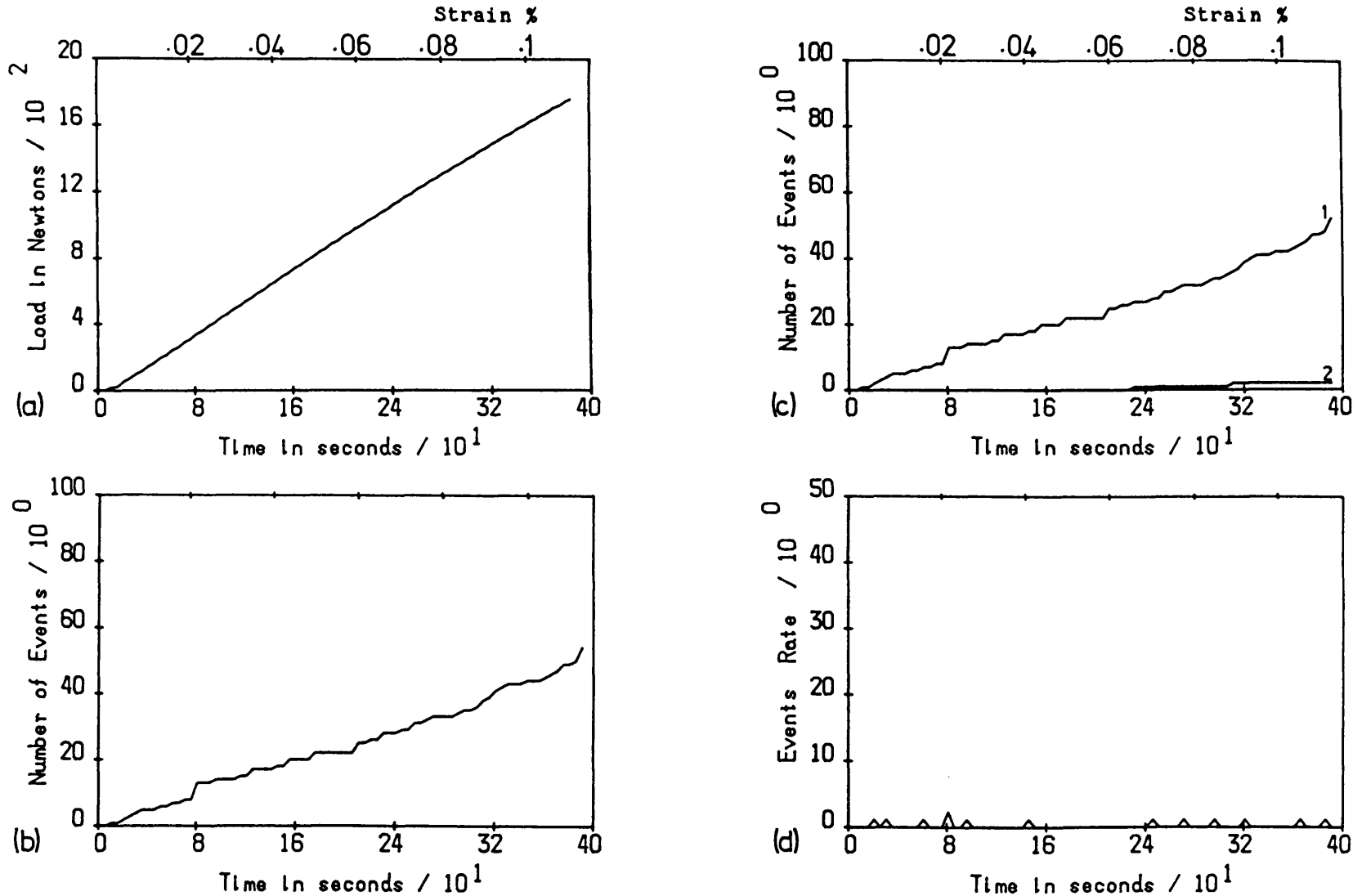

Fig 7.67 AE event curves for a typical aluminium control coating.

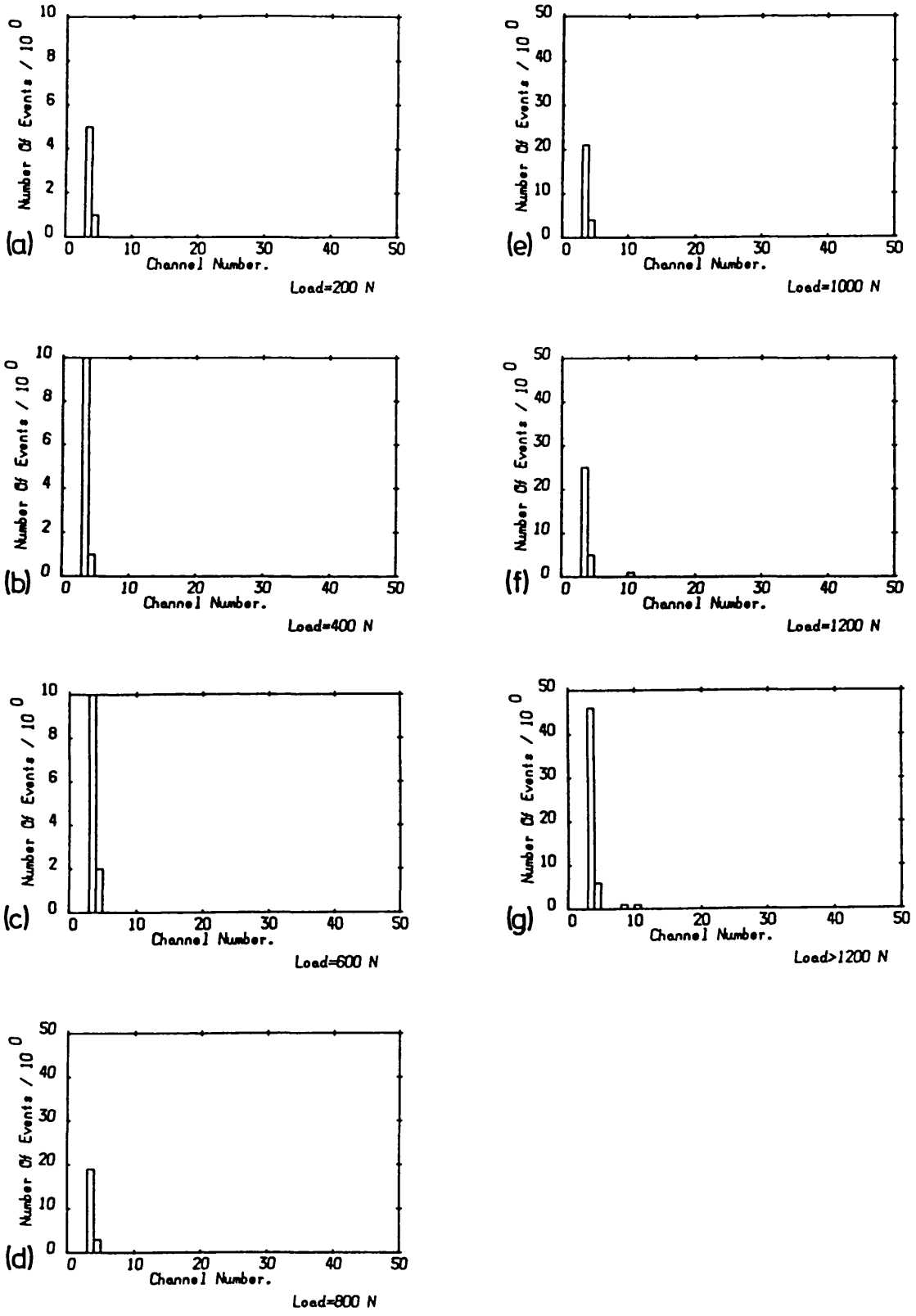

Fig 7.68 Histograms of the AE event amplitude distributions and the percentage share graph of the sample shown in Fig 7.67.

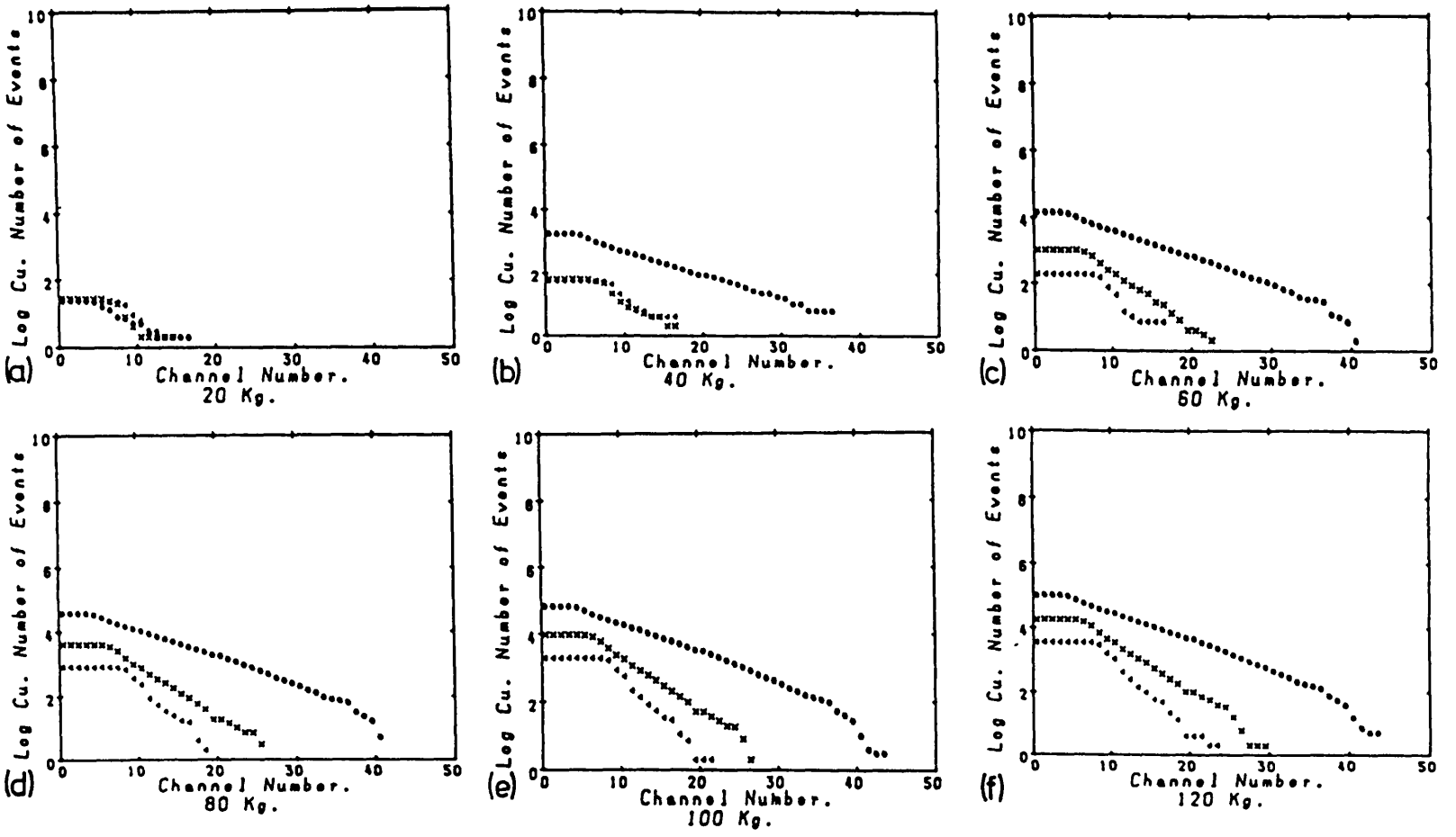

Fig 7.69 A typical group of b_plots for plasma sprayed coatings (, Mo63 standard; , Mo63 sprayed onto a substrate which had not been grit blasted; , Mo505 standard) tested at various loads: a) 20 Kgf; b) 40 Kgf; c) 60 Kgf; d) 80 Kgf; e) 100 Kgf; f) 120 Kgf.

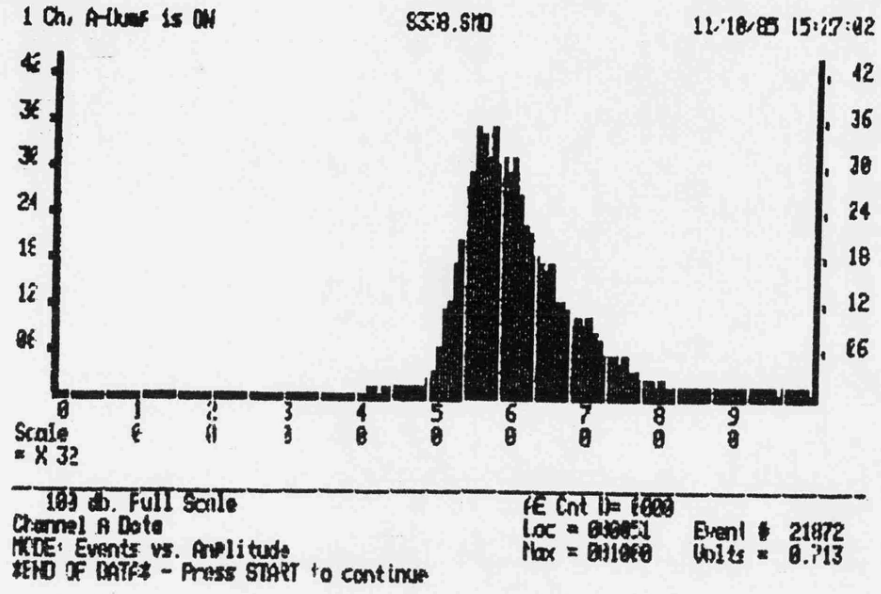

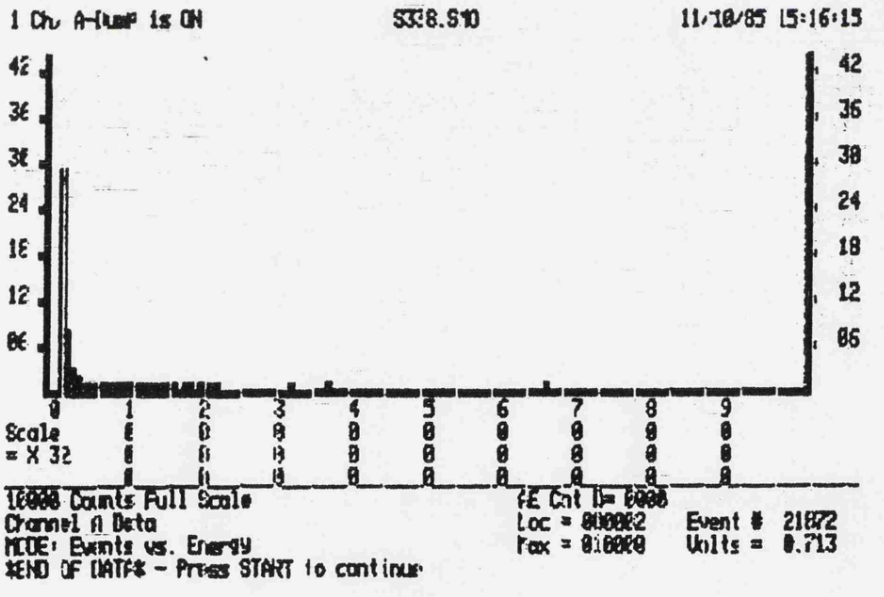

Fig 7.70 A typical AE event amplitude distribution and it's corresponding event vs energy distribution for a Mo505 coating, (PAC-3400).

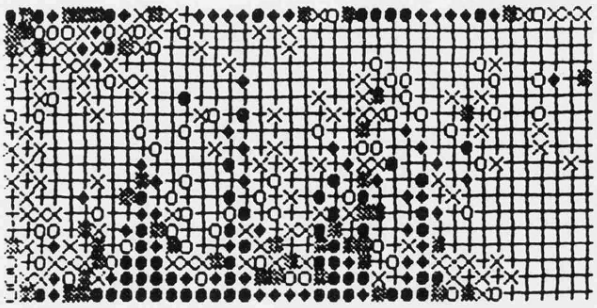

+...LESS THAN 38 DB DOWN FROM ORIGINAL SIGNAL.
×...BETWEEN 38 AND 40
o...BETWEEN 40 AND 42
⁂...BETWEEN 42 AND 44
♦...BETWEEN 44 AND 46
●...MORE THAN 46 DB

Fig 7.71 A typical C-scan of an alumina coating after AE test. The delaminations are clearly shown.

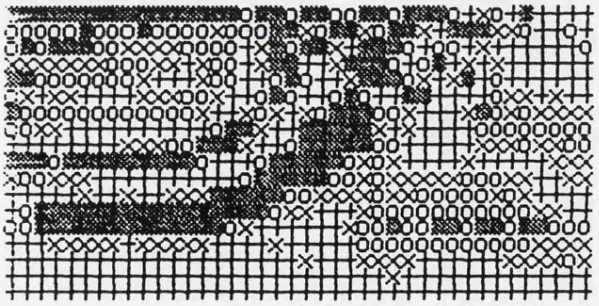

+...LESS THAN 44 DB DOWN FROM ORIGINAL SIGNAL.
×...BETWEEN 44 AND 46
o...BETWEEN 46 AND 48
⁂...BETWEEN 48 AND 50
♦...BETWEEN 50 AND 52
●...MORE THAN 52 DB

Fig 7.72 A typical C-scan of an alumina coating sprayed on a substrate which had not been grit blasted, showing large areas of delaminations.

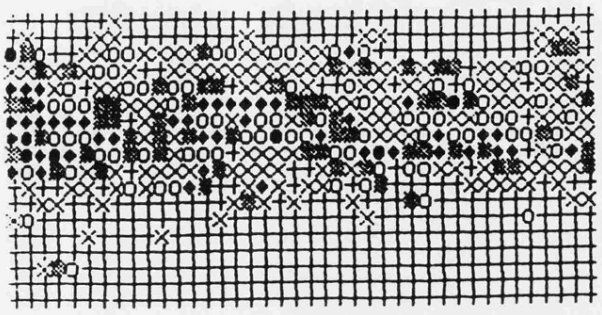

+...LESS THAN 36 DB DOWN FROM ORIGINAL SIGNAL.
×...BETWEEN 36 AND 38
o...BETWEEN 38 AND 40
▒...BETWEEN 40 AND 42
♦...BETWEEN 42 AND 44
●...MORE THAN 44 DB

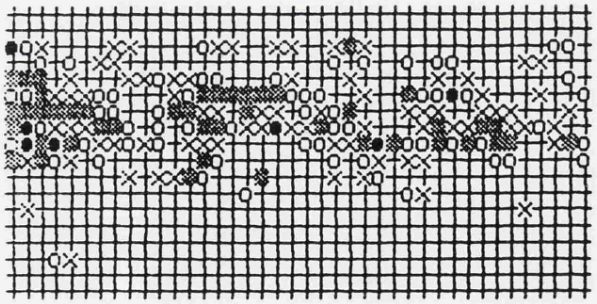

+...LESS THAN 40 DB DOWN FROM ORIGINAL SIGNAL.
×...BETWEEN 40 AND 42
o...BETWEEN 42 AND 44
▒...BETWEEN 44 AND 46
♦...BETWEEN 46 AND 48
●...MORE THAN 48 DB

Fig 7.73 A typical C-scan image of an aluminium coating after 4 point bend test. There was no detectable damage in the sample (see Fig 7.23).

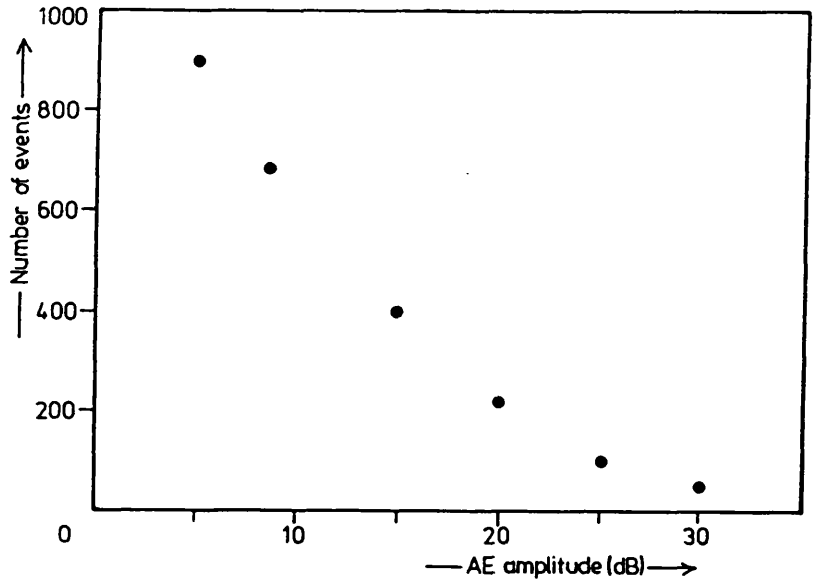

Fig 7.74 A histogram of the AE event amplitude distribution for an infinitly large layerd medium, (6 layers !).

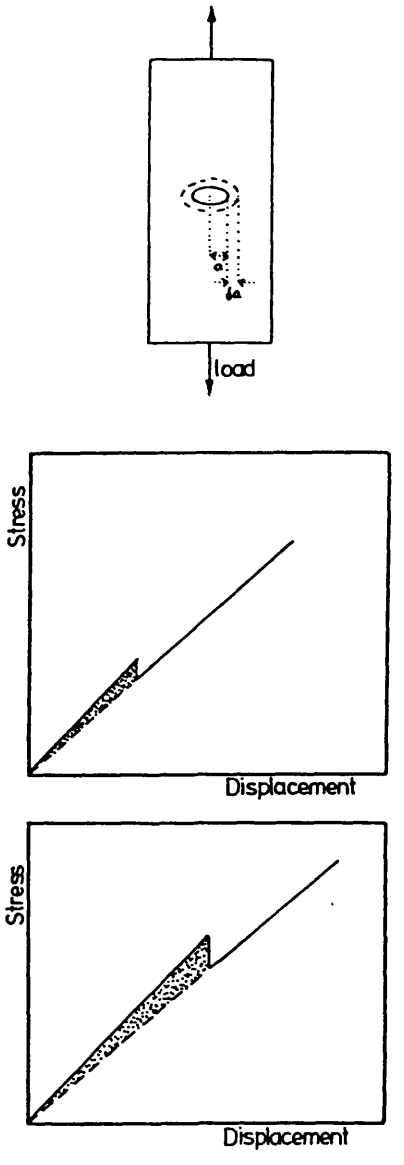

Fig 7.75 Schematic diagram of the energy released due to the extension of a crack in a constant displacement test.

Ratio (oxygen: fuel gas)	Temperature °C	Flame condition	result
1:1	3000	Carburizing	Insufficient heat
1:1	3000	Reducing	Good for some metals
1.1:1	3050	Neutral	Recommended for general use
1.1:1	3350	Oxidizing	Good for some ceramics

Table 2.1 Oxygen to fuel gas ratios and their corresponding flame temperature. (After James and Daryl Ref. 16)

Process Variables Listed by Category

Plasma
1. Power Input
2. Type of Arc Gas
3. Flow of Arc Gas
4. Plasma-torch Geometry

Powder
1. Composition
2. Physical Properties
3. Method of Manufacture
4. Powder Size
5. Particle Size Distribution

Powder Feed
1. Type of powder Feed System
2. Rate of Powder Addition to Carrier Gas
3. Type of Carrier Gas
5. Angle of Powder Entry into Plasma
6. Location of Powder Entry Port

Substrate
1. Composition
2. Surface-preparation Method
3. Surface Roughness
4. Temperature

Spraying Procedure
1. Torch-to-Work Distance
2. Traverse Rate
3. Angle of Torch with Work
4. Cover Gas
5. Spraying Atmosphere

Table 2.2 Classification of plasma sprayed vaiables. (After Mash Ref. 40)

Thickness	Adhesion to substrate
Evenness	Chemical Reactivity
Edge definition	Chemical composition
Surface finish	Thermal properties
Structure	Electrical properties
Porosity	Frictional properties
Hardness	Wear resistance
Cohesive strength	Machinability

Table 3.1 Potential criteria for coatings (After Smart Ref. 55)

Constants of Various Piezoelectric Materials* (From J. R. Frederick, *Ultrasonic Engineering*, John Wiley & Sons, New York. Reproduced by permission)

Physical property	Quartz 0° X-cut	Lithium sulphate 0° Y-cut	Barium titanate Type B	Lead zirconate-titanate PZT-4	Lead zirconate-titanate PZT-5	Lead meta-niobate	Units
Density ρ	2.65	2.06	5.6	7.6	7.7	5.8	10^3 kg/m^3
Acoustic impedance ρc	15.2	11.2	24	30.0	28.0	16	10^6 kg/m^{2}s
Frequency thickness constant ft	2,870	2,730	2,740	2,000	1,800	1,400	kHz mm
Maximum operating temperature	550	75	70–90	250	290	500	°C
Dielectric constant	4.5	10.3	1,700	1,300	1,700	225	—
Electromechanical coupling factor for thickness mode k_{33}	0.1	0.35	0.48	0.64	0.675	0.42	—
Electromechanical coupling factor for radial mode k_p	0.1	—	0.33	0.58	0.60	0.07	—
Elastic quality factor Q	10^6	—	400	500	75	11	—
Piezoelectric modulus for thickness mode d_{33}	2.3	16	149	285	374	85	10^{-12} m/V
Piezoelectric pressure constant g_{33}	58	175	14.0	26.1	24.8	42.5	$10^{-3}\frac{\text{V/m}}{\text{N/m}^2}$
Volume resistivity at 25 °C	$>10^{12}$	—	$>10^{11}$	$>10^{12}$	$>10^{13}$	10^9	—
Curie temperature	575	—	115	320	365	550	°C
Young's modulus E	8.0	—	11.8	8.15	6.75	2.9	10^{10} N/m^2
Rated dynamic tensile strength	—	—	—	24	27.6	—	10^6 N/m^2

*The properties of the ceramic materials can vary with slight changes in composition and processing, and hence the values that are shown should not be taken as exact.

Table 4.1 Constants of some piezoelectric materials. (After Szilard Ref. 64)

Measured variable:	Intensity	Intensity and phase	Intensity and Transit time	Transit time or Resonance frequency
Method	Intensity method Sound-image or Image-projection methods	Ultrasonic holography	Pulse transit-time or Pulse-echo methods	Transit-time or Resonance methods
Principal application	Image projection of flaws in plates	General 3-dimensional image projection of flaws	General flaw location and determination of size	Wall-thickness measurements and flaw determination in plates

Table 4.2 Classification of ultrasonic methods used in materials testing. (After Krautkramer Ref. 65)

Powder	Metco 63	Metco 505	Metco 105	Metco 54
Melting point	Mo 2610°C	Mo 2610°C Matrix 1025°C	2000°C	650°C
Typical size	+30 micron	+15 micron	+15 micron	+5 micron
Typical composition	99% Mo	75% Mo 4.25% Cr 0.8% B 1% Si 1% Fe 0.2% C % Ni	98.5% Al^2O^3 1% SiO^2	99.+% Al

Table 6.1 Powder properties. (Metco data sheet)

Substrate materials	En42	Mild steel	Aluminium
Dimensions (mm)	240 X 25 X 3	240 X 25 X 3	100 X 50 X 2

Table 6.2 Substrate materials and specimen dimensions used.

Condition	1. Standard (Recommended by Metco)			
Coating materials	Metco105	Metco505	Metco63	Metco54
Gun	3MB	3MB	3MB	3MB
Nozzle	G	G	G	G
Powder Port	2	2	1	
Gas Pressure PSi				
Primary	50	50	50	
Secondary	50	50	50	
Power				
Amps	500	350	400	
Volts	74-80	65-70	70-80	
Meter Wheel RPM	25	25	15	
Spraying Distance mm	50-100	50	75-125	
Condition	2. Low input power 20% less input electrical power			
Condition	3. No cooling air			
Condition	4. Poor or no surface preparation			

Table 6.3 Details of the Process variables used

AET-203 Calibration data

Cnannel No.	Channel Width (dB)	Channel No.	Channel Width (dB)
0	1.65	23	1.17
1	1.14	24	1.32
2	1.30	25	1.18
3	1.33	26	1.11
4	1.39	27	1.30
5	1.26	28	1.20
6	1.26	29	1.36
7	1.23	30	0.87
8	1.13	31	1.16
9	1.11	32	1.20
10	1.35	33	1.28
11	1.15	34	1.25
12	1.25	35	1.34
13	1.19	36	1.09
14	1.20	37	1.21
15	1.25	38	1.18
16	1.12	39	1.34
17	1.22	40	0.98
18	1.13	41	1.16
19	1.68	42	1.24
20	0.95	43	1.19
21	1.00		
22	1.25		

Table 6.4 Channel widths of the AET-203.

1. Load vs Time	6. Log AE vs Time	11. Stress vs Strain
2. Load vs Strain	7. Log AE vs Load	12. Percentage share vs Time
3. AE vs Load	8. Histograms (2d)	13. Percentage share vs Strain
4. AE vs Strain	9. Histograms (3d)	14. percentage share vs Load
5. AE vs Time	10. b_plot	

Table 6.5 Options available on the software package for the analysis of the AE data

Coating: Molybdenum (Mo63)	Test frequency: 10MHz	
Thickness mm	attenuation dB	attenuation dB/cm
0.36	45	1250
0.38	47	1236
0.40	49	1225
0.42	51	1214
0.44	53	1204
Differential Thickness and Attenuation:		
0.02	2	1000
After Ground:		
0.3	37	1233
	Test Frequency: 5 MHz	
0.29	18	620
0.32	20	625
0.35	22	628
Differential Thickness and Attenuation:		
0.03	2	666
	Test Frequency: 2.5 MHz	
0.26	14	538
0.30	16	533
Differential Thickness and Attenuation:		
0.04	2	500

Table 7.1 Attenuation per unit thickness of Mo63 coatings, calculated from the C-scan image

Area of no contact	$0.1A_o$	$0.2A_o$	$0.25A_o$	$0.5A_o$	$0.75A_o$
Attenuation dB/(20 micrometers)	0.9	1.9	2.5	6	12

Table 7.2 calculated results of the attenuation through a three layer media having different areas of good contact.

Material	Lamellae size (Radius μm)	f_{01} MHz	f_{11} MHz	f_{21} MHz	f_{02} MHz
Al	100	0.92	1.9	3.1	3.6
Al	50	3.7	7.6	12.5	14.3
AL	25	14.6	30.6	50.1	57.2
Al^2O^3	100	1.6	3.3	5.4	6.2
Al^2O^3	50	6.6	13.8	22.6	25.8
Al^2O^3	25	26.4	55.2	90.4	103.
Mo	100	0.9	1.9	3.1	3.5
Mo	50	3.74	7.8	12.8	14.6
Mo	25	14.9	31.3	51.2	58.4
Steel	100	0.8	1.67	2.7	3.1
Steel	50	3.4	7.1	11.6	13.3
Steel	25	13.5	28.2	46.2	52.8

Table 7.3 Calculated resonance frequencies of various lamellae (lamellae thickness 10 micrometers)

Frequency	2.5 MHz		5 MHz		10 MHz	
Materials	A.P. 10^5 N/m^2	x_{max} μ	A.P. 10^5 N/m^2	x_{max} μ	A.P. 10^5 N/m^2	x_{max} μ
Al	12.7	0.09	24.3	0.09	48.7	0.082
Mo	12.9	0.09	25.9	0.09	51.8	0.087
Steel	12.9	0.09	25.8	0.09	51.6	0.086
Al^2O^3	12.7	0.09	25.4	0.09	50.8	0.085

Table 7.4 Calculated deflections at resonance for aluminium, molybdenum, Steel and alumina lamellae. (A.P. acoustic pressure)

Coating: alumina (Metco105) Frequency 10 MHz

No.	Standard dB/cm	Low Power dB/cm	Poor Surface P. dB/cm	No Coolant dB/cm
1	640 ± 100	620 ± 80	720 ± 130	710 ± 120
2	620 ± 90	580 ± 100	660 ± 110	720 ± 140
3	630 ± 110	590 ± 110	690 ± 130	700 ± 110
4	600 ± 90	570 ± 70	650 ± 80	690 ± 120
5	630 ± 130	600 ± 90	700 ± 140	710 ± 100
6	590 ± 70	590 ± 120	650 ± 90	680 ± 90
7	600 ± 120	580 ± 90	670 ± 120	700 ± 130
8	600 ± 90	600 ± 110	640 ± 90	720 ± 80
9	620 ± 110	580 ± 100	680 ± 130	710 ± 90
10	610 ± 90	570 ± 80	660 ± 100	700 ± 100

Table 7.5 Attenuation per unit thickness of alumina coatings, produced with various process parameters.

Coating: Molybdenum (Mo63) Frequency 10 MHz

No.	Standard dB/cm	Low Power dB/cm	Poor Surface P. dB/cm	No Coolant dB/cm
1	1000 ± 80	920 ± 50	1100 ± 80	1100 ± 100
2	980 ± 60	930 ± 40	1,000 ± 70	1200 ± 90
3	1100 ± 90	950 ± 50	970 ± 60	980 ± 110
4	990 ± 70	900 ± 40	980 ± 80	1100 ± 90
5	980 ± 50	940 ± 50	960 ± 70	1200 ± 100
6	1000 ± 60	930 ± 60	990 ± 70	1000 ± 110
7	990 ± 50	920 ± 40	970 ± 80	990 ± 120
8	970 ± 60	920 ± 50	1100 ± 90	1200 ± 100
9	990 ± 60	910 ± 60	1000 ± 80	1100 ± 80
10	1100 ± 90	940 ± 50	980 ± 70	1000 ± 90

Table 7.6 Attenuation per unit thickness of Mo63 coatings produced with various process parameters.

Coating: Self-fusing molybdenum (Mo505) Frequency 10 MHz

No.	Standard dB/cm	Low Power dB/cm	Poor Surface P. dB/cm	No Coolant dB/cm
1	820 ± 50	810 ± 40	800 ± 60	840 ± 80
2	800 ± 40	850 ± 60	810 ± 40	870 ± 90
3	850 ± 60	800 ± 30	840 ± 60	850 ± 110
4	880 ± 50	830 ± 40	820 ± 50	830 ± 100
5	810 ± 40	780 ± 50	800 ± 30	860 ± 70
6	840 ± 60	820 ± 40	790 ± 60	880 ± 90
7	820 ± 80	800 ± 50	840 ± 70	840 ± 120
8	860 ± 70	770 ± 60	830 ± 60	860 ± 80
9	820 ± 40	810 ± 40	850 ± 40	890 ± 70
10	850 ± 60	820 ± 60	810 ± 80	840 ± 90

Table 7.7 Attenuation per unit thickness of Mo505 coatings produced with various process parameters.

Sample ID	Attenuation dB	Frequency 2.5 MHz
2X/1	15 - 18	
2X/3	17 - 19	
3X/2	16 - 18	
3X/4	17 - 18	
4X/1	15 - 17	
4X/2	15 - 18	
6X/3	16 - 18	
6X/4	15 - 17	
10X/1	15 - 17	
14X/1	16 - 18	
16X/3	15 - 17	
16X/4	16 - 18	

Table 7.8 Measured attenuation of the samples provided by Phillips of Eindhoven.

Sample ID	Attenuation dB	Frequency 5 MHz
2X/1	22 - 24	
2X/2	22 - 25	
4X/1	21 - 24	
6X/3	19 - 23	
10X/1	18 - 22	
14X/3	22 - 25	
16X/1	19 - 21	
16X/2	19 - 22	

Table 7.9 Measured attenuation of the samples provided by Phillips of Eindhoven.

Sample ID	Attenuation dB	Frequency 10 MHz
2X/1	30 - 34	
2X/2	24 - 32	
2X/3	27 - 33	
2X/4	29 - 35	
8X/1	26 - 30	
8X/2	26 - 30	
8X/3	24 - 30	
8X/4	26 - 30	
10X/1	30 - 34	
10X/2	28 - 32	
10X/3	28 - 32	
10X/4	28 - 32	
12X/1	26 - 30	
12X/2	28 - 32	
12X/3	28 - 32	
12X/4	26 - 32	
14X/1	26 - 30	
14X/2	26 - 30	
14X/3	24 - 28	
14X/4	26 - 32	
16X/1	28 - 32	
16X/2	26 - 30	
16X/3	24 - 28	
16X/4	26 - 30	

Table 7.10 Measured attenuation of the samples provided by Phillips of Eindhoven.

Samples 1-7 pure Mo coatings prepared as standards
Sample 8 pure Mo coatings grit blasting omitted

Load 20Kg			Load 40Kg			Load 60Kg		
Rank	Sample	χ^2	Rank	Sample	χ^2	Rank	Sample	χ^2
1	1	0	1	2	6	1	7	45
2	2	0	2	6	8	2	2	89
3	3	0	3	7	8	3	4	122
4	4	0	4	4	9	4	1	166
5	5	0	5	3	10	5	3	247
6	6	0	6	1	12	6	5	279
7	7	0	7	5	15	7	6	306
8	8	0	8	8	40	8	8	624
F = 7			F = 28			F = 77		

Load 80Kg			Load 100Kg			Load 20-100Kg		
1	7	189	1	7	348	1	7	1338
2	2	301	2	4	579	2	4	2239
3	4	315	3	2	600	3	2	2262
4	1	677	4	1	1197	4	3	4833
5	3	763	5	3	1460	5	1	4953
6	5	873	6	5	1481	6	5	6111
7	6	1129	7	6	2404	7	6	8448
8	8	2533	8	8	4537	8	8	15817
F = 105			F = 119			F = 1155		

(F = Degrees of Freedom)

Load Kg	20	40	60	80	100	120	140	160
% strain	0.002	0.009	0.02	0.036	0.056	0.08	0.1	0.14

Table 7.11 Measurements showing the variability of AE amplitude distributions between samples of plasma sprayed Mo under 4-point bending.

Samples 2-7 sprayed under standard conditions
Sample 1 sprayed with dusty grit

Load 80Kg			Load 100Kg			Load 100Kg		
Rank	Sample	χ^2	Rank	Sample	χ^2	Rank	Sample	χ^2
1	1	0	1	3	11	1	3	12
2	2	0	2	6	23	2	6	37
3	3	0	3	4	27	3	4	47
4	4	0	4	7	61	4	7	60
5	5	0	5	5	78	5	5	118
6	6	0	6	1	226	6	1	290
7	7	0	7	2	759	7	2	1263
F = 180			F = 42			F = 42		

Load 120Kg			Load 20-120Kg		
1	3	25	1	6	162
2	6	39	2	3	209
3	7	73	3	7	274
4	4	93	4	4	348
5	5	164	5	5	502
6	1	402	6	1	1258
7	2	1819	7	2	4325
F = 66			F = 504		

(F = Degrees of Freedom)

Table 7.12 Measurements showing the variability of AE amplitude distributions between samples of plasma sprayed alumina under 4-point bending.

```
INPUT DATA  X(I,J) .....
 200.00   180.00   160.00   140.00   100.00
 100.00    90.00    80.00    70.00    50.00
  50.00    45.00    40.00    35.00    25.00
  25.00    22.50    20.00    17.50    12.50

GRAND TOTALS .....
1462.50 1462.50

TOTALS FOR EACH ROW .....
 780.00   390.00   195.00    97.50

TOTALS FOR EACH COLUMN .....
 375.00   337.50   300.00   262.50   187.50

EXPECTATION FOR EACH CELL .....
 200.00   180.00   160.00   140.00   100.00
 100.00    90.00    80.00    70.00    50.00
  50.00    45.00    40.00    35.00    25.00
  25.00    22.50    20.00    17.50    12.50

CHI** FOR EACH BLOCK.....
   0.00     0.00     0.00     0.00     0.00
   0.00     0.00     0.00     0.00     0.00
   0.00     0.00     0.00     0.00     0.00
   0.00     0.00     0.00     0.00     0.00

CHI** FOR EACH ROW.....
   0.00     0.00     0.00     0.00

TOTAL CHI**....  >>       0.00
```

```
INPUT DATA  X(I,J) .....
 100.00    80.00    60.00    50.00    40.00
 102.00    52.00    62.00    52.00    42.00
  98.00    78.00    58.00    48.00    38.00
  96.00    76.00    56.00    46.00    36.00

GRAND TOTALS .....
1270.00 1270.00

TOTALS FOR EACH ROW .....
 330.00   310.00   320.00   310.00

TOTALS FOR EACH COLUMN .....
 396.00   286.00   236.00   196.00   156.00

EXPECTATION FOR EACH CELL .....
 102.90    74.31    61.32    50.93    40.54
  96.66    69.81    57.61    47.84    38.08
  99.78    72.06    59.46    49.39    39.31
  96.66    69.81    57.61    47.84    38.08

CHI** FOR EACH BLOCK.....
   0.08     0.43     0.03     0.02     0.01
   0.29     4.54     0.34     0.36     0.40
   0.03     0.49     0.04     0.04     0.04
   0.00     0.55     0.04     0.07     0.11

CHI** FOR EACH ROW.....
   0.57     5.94     0.64     0.78

TOTAL CHI**....  >>       7.93
```

Table 7.13 Chi-squared test appiled to two simple distributions.

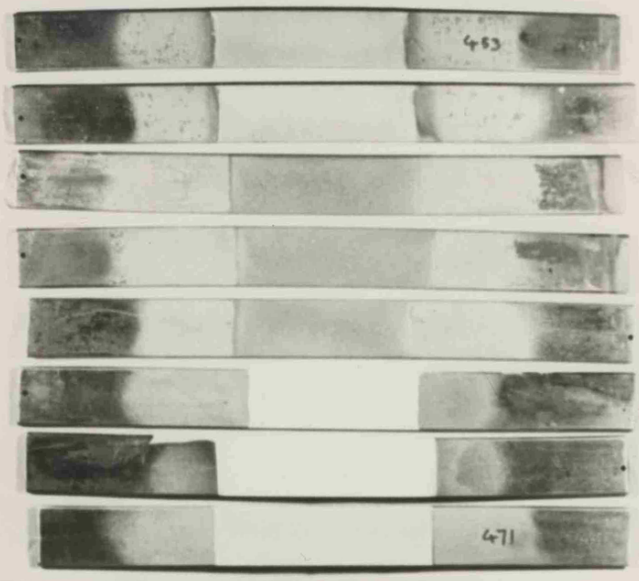

Plate 6.1 Typical plasma sprayed specimens.

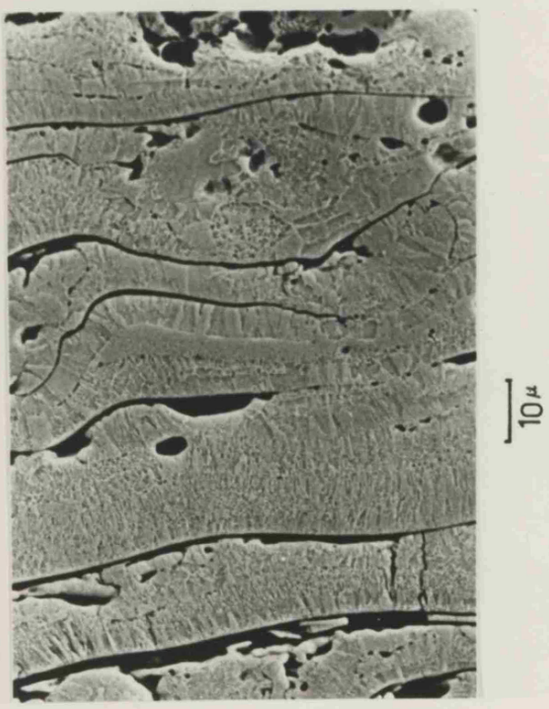

Plate 7.1 Scanning electron photo-micrograph of molybdenum (Mo63) coating , (X 1000) .

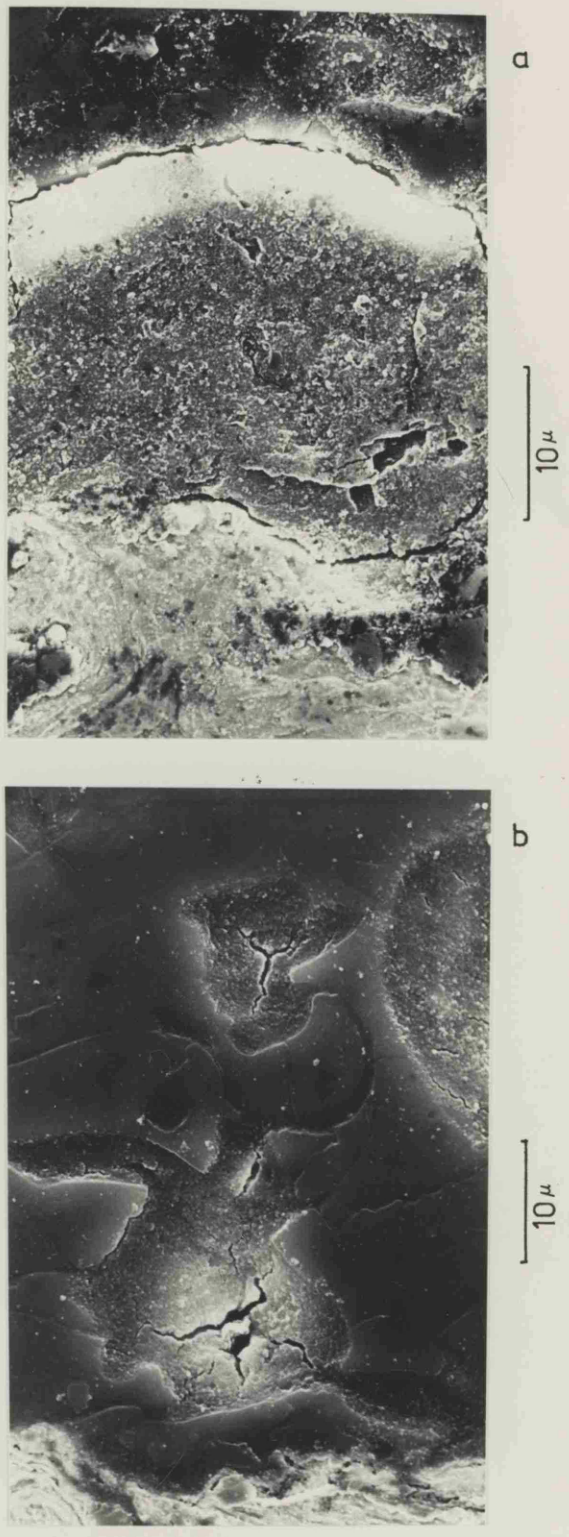

Plate 7.2 Scanning electron photo-micrograph of alumina (Metco105), showing the shrinkage cracks in the coating. a) X 2600 , b) X 2000 .

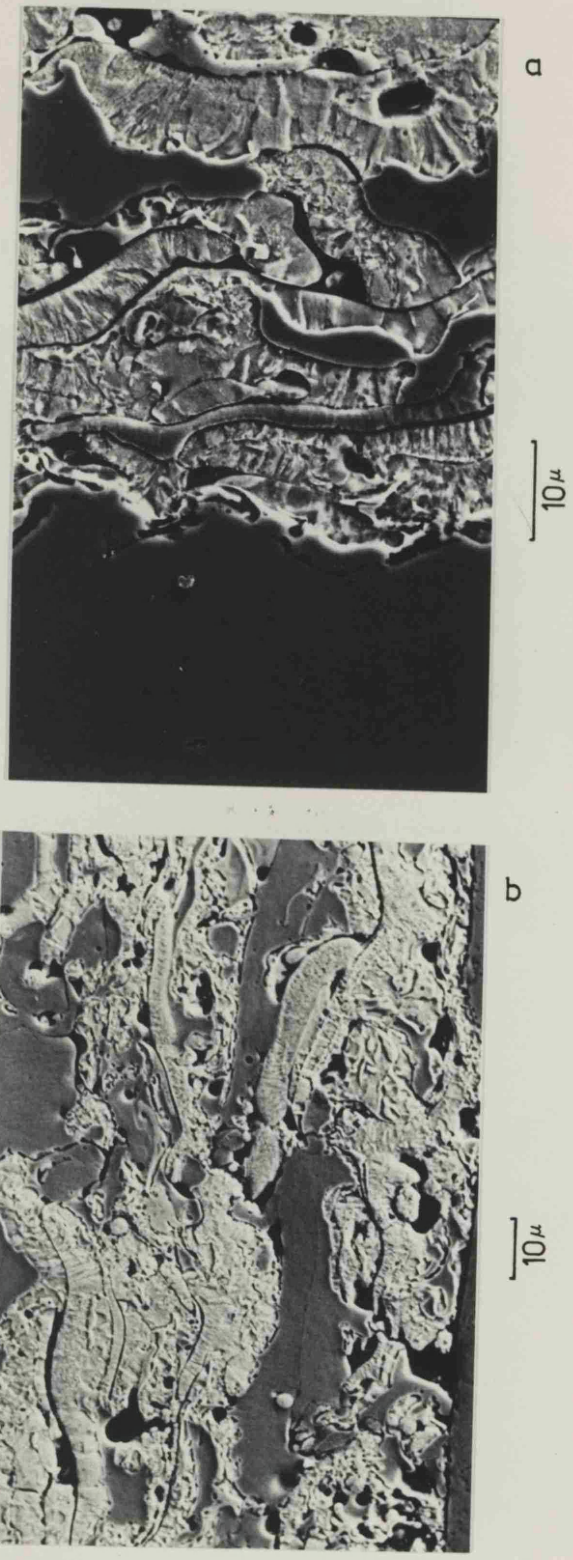

Plate 7.3 Scanning electron photo-micrograph of a self-fusing molybdenum (Mo505) coating, a) X 1500, b) X 900 .

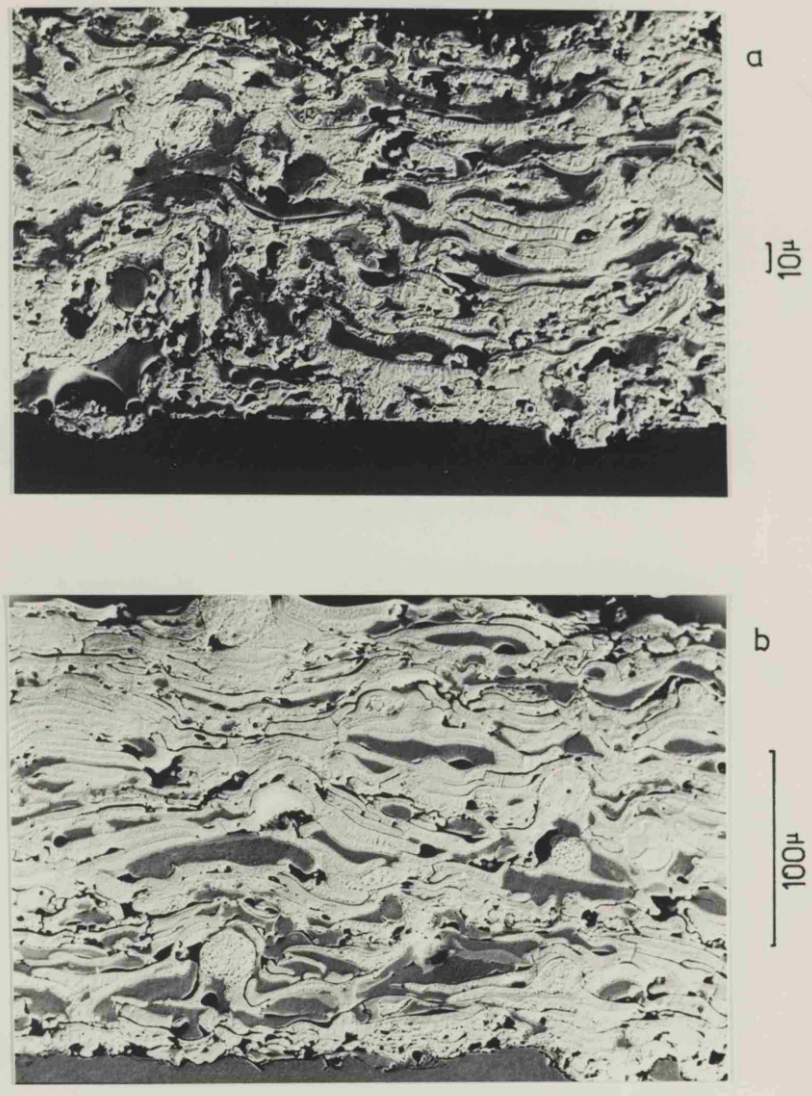

Plate 7.4 Scanning electron photo-micrograph of self-fusing molybdenum coating (Mo505), a) sprayed on a substrate with poor surface preparation, b) sprayed with 20 % less input power than normal. a) X 430, b) X 300 .

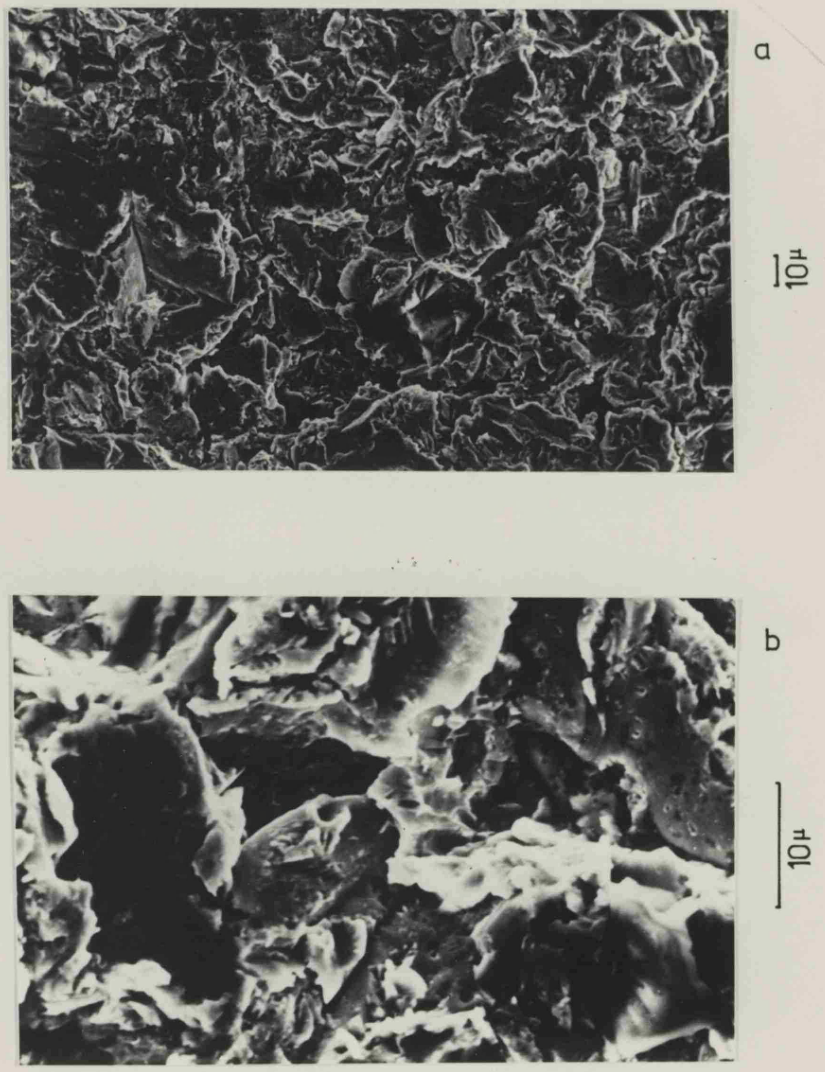

Plate 7.5 Scanning electron photomicrograph of the surface of a substrate after grit blasting (recommended practice). a) X 500, b) X 2000.

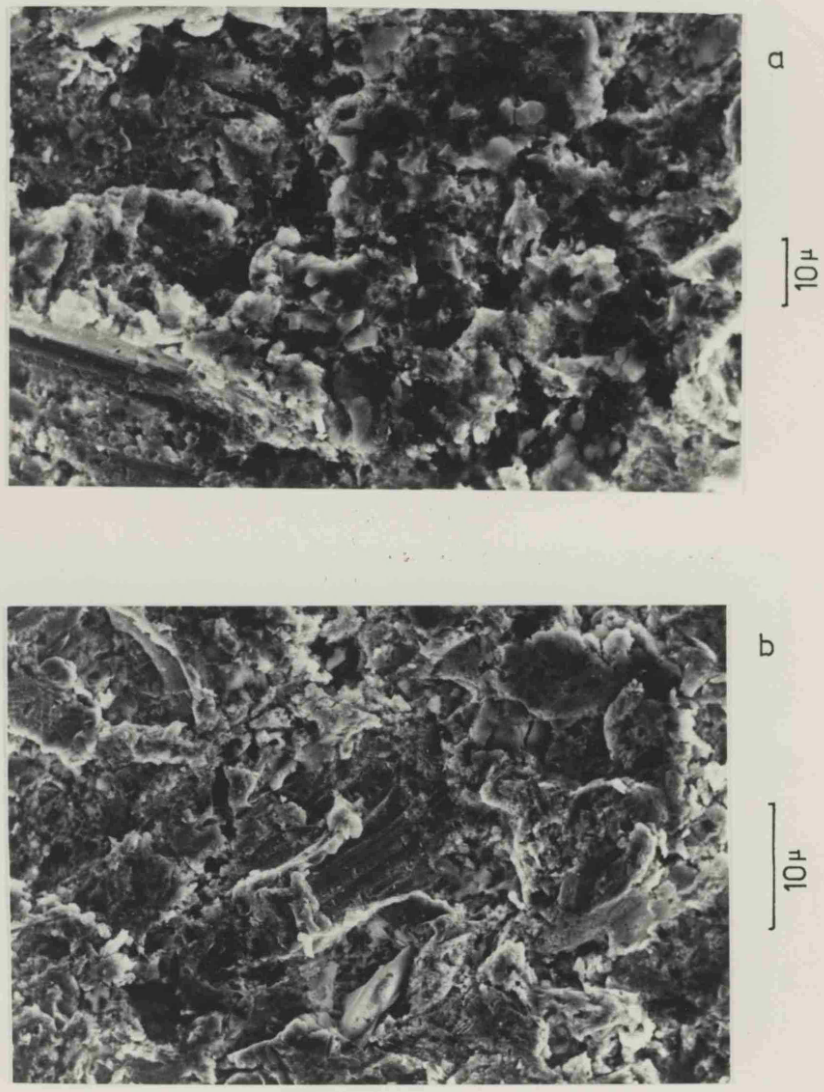

Plate 7.6 Scanning electron photomicrograph of the surface of a substrate after grit blasting, using dusty grit. a) X 1000, b) X 2000.

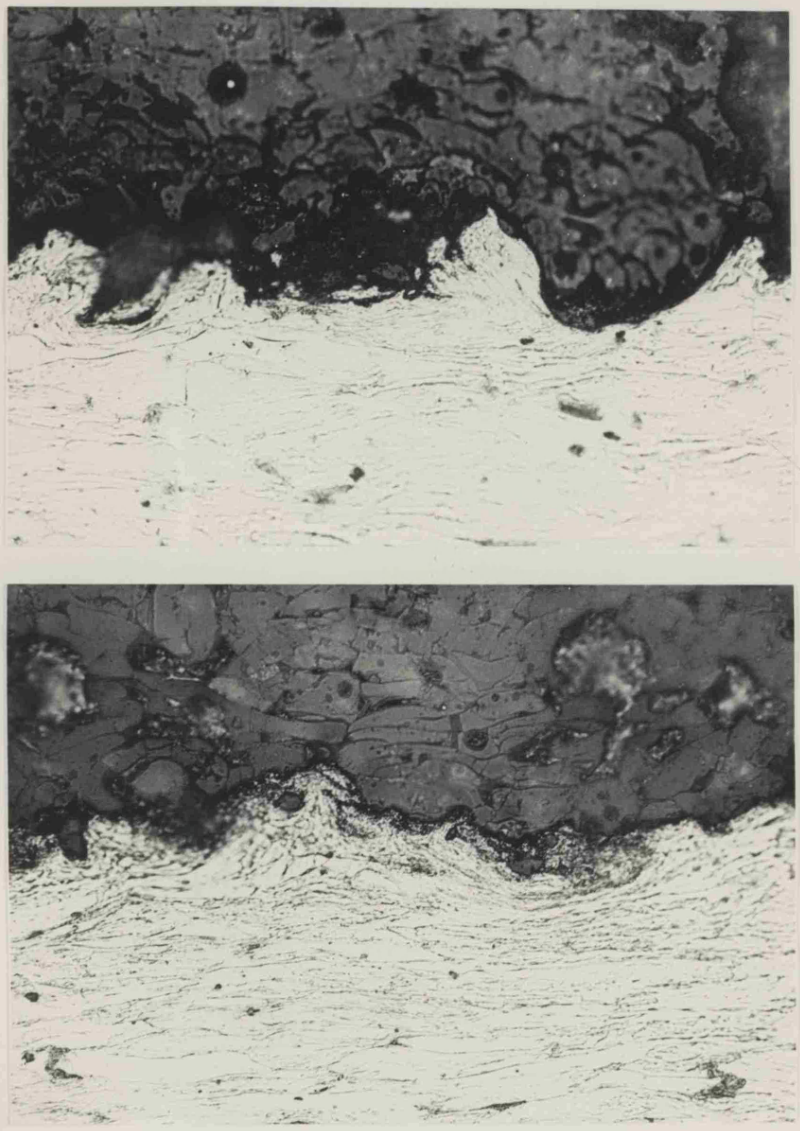

Plate 7.7 Photo-micrograph of the alumina coatings before AE test, a) control (X 400), b) poor surface preparation (X 400).

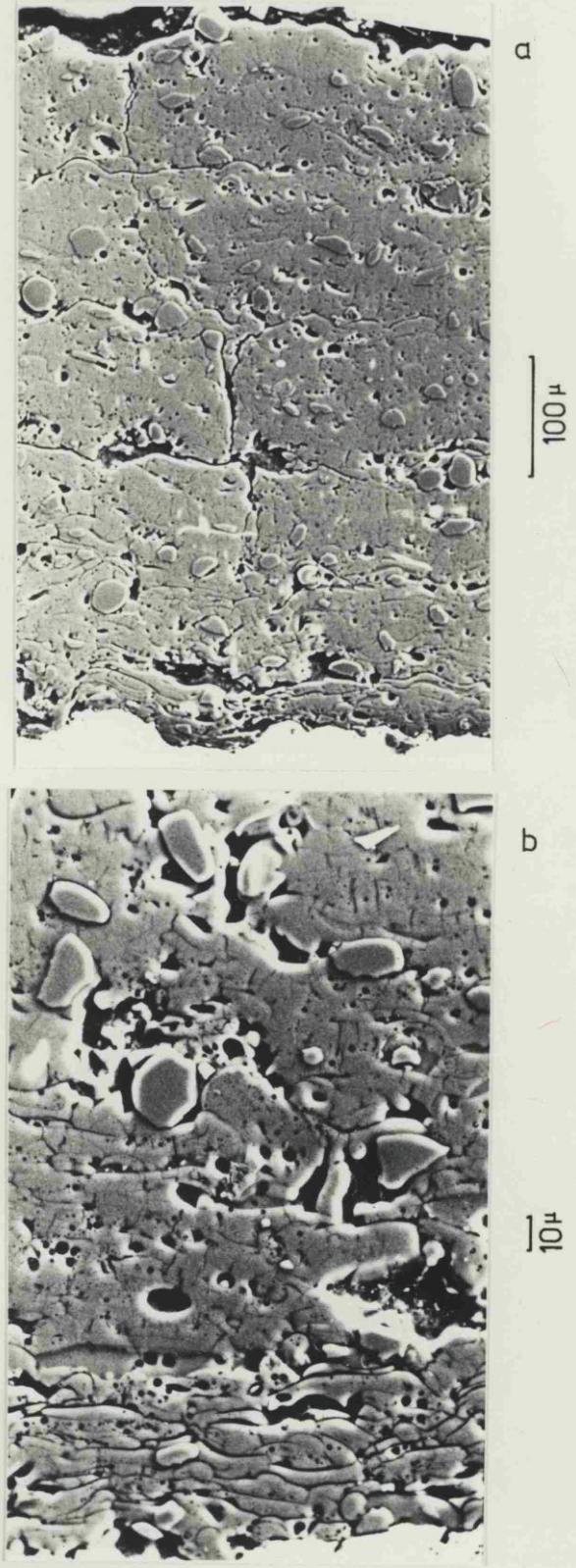

Plate 7.8 Scanning electron photo-micrograph of the over heated alumina coatings after 4 point bend test, a) X 180, b) X 500 .

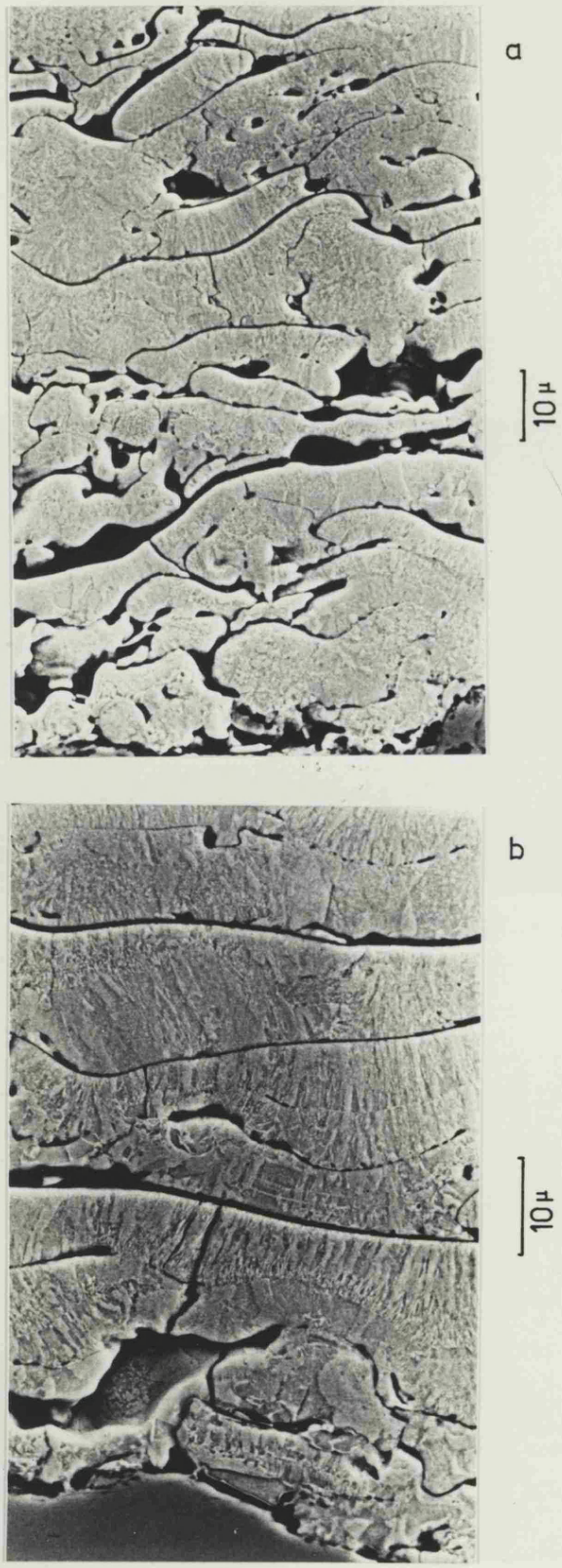

Plate 7.9 Scanning electron photo-micrograph of the over heated molybdenum (Mo63) coatings, a) X 1000, b) X 1500 .

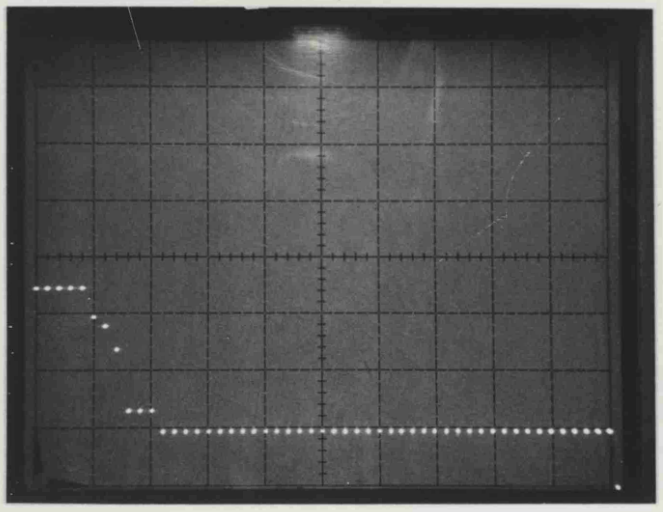

Plate 7.10 A typical cumulative amplitude distribution of a lead pencil breaking test (system calibration).

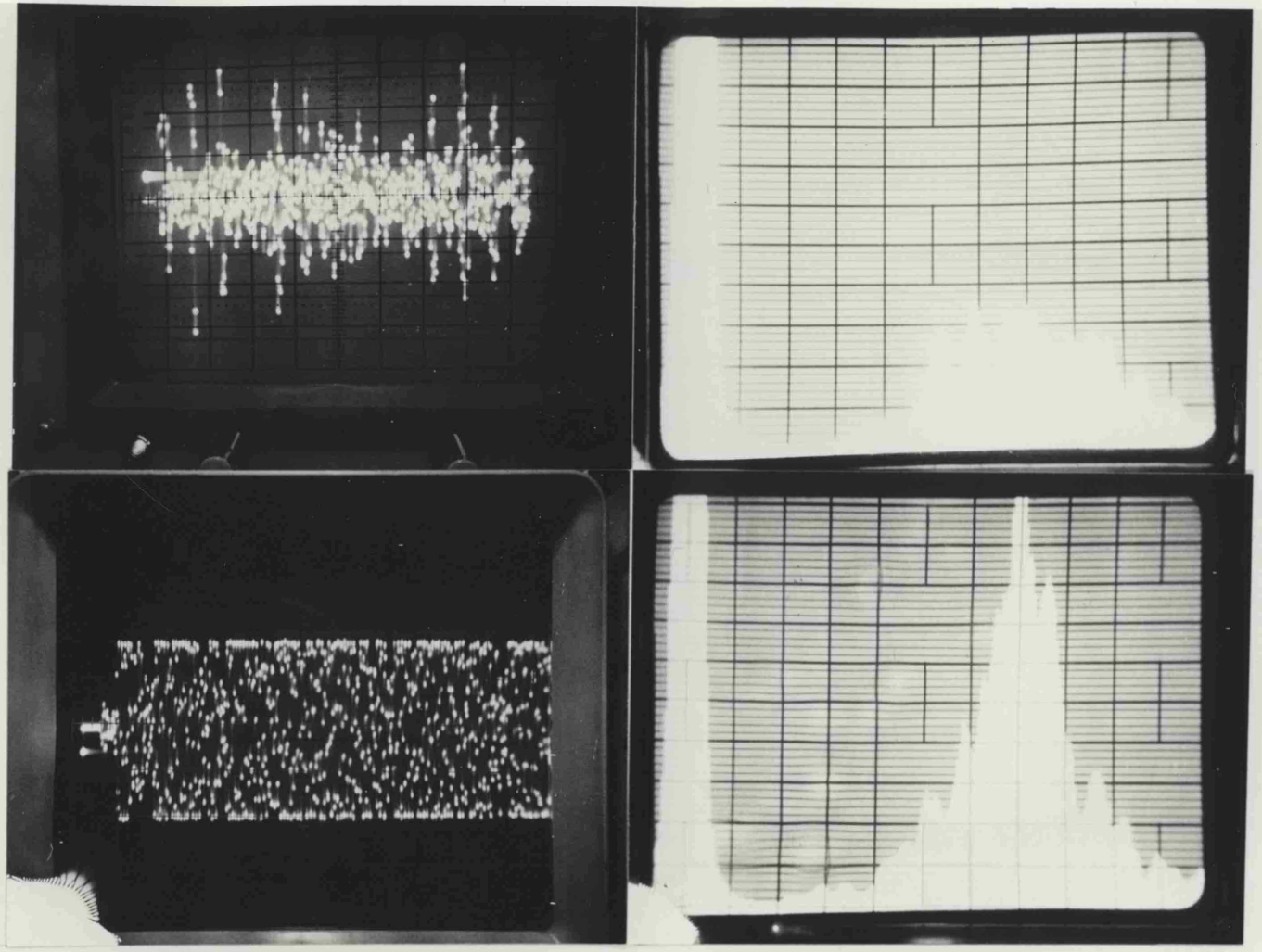

Plate 7.11 Typical acoustic emission signal generated from a lead pencil breaking test, a) detected by AET-203 system, b) detected by AECL-105 system.

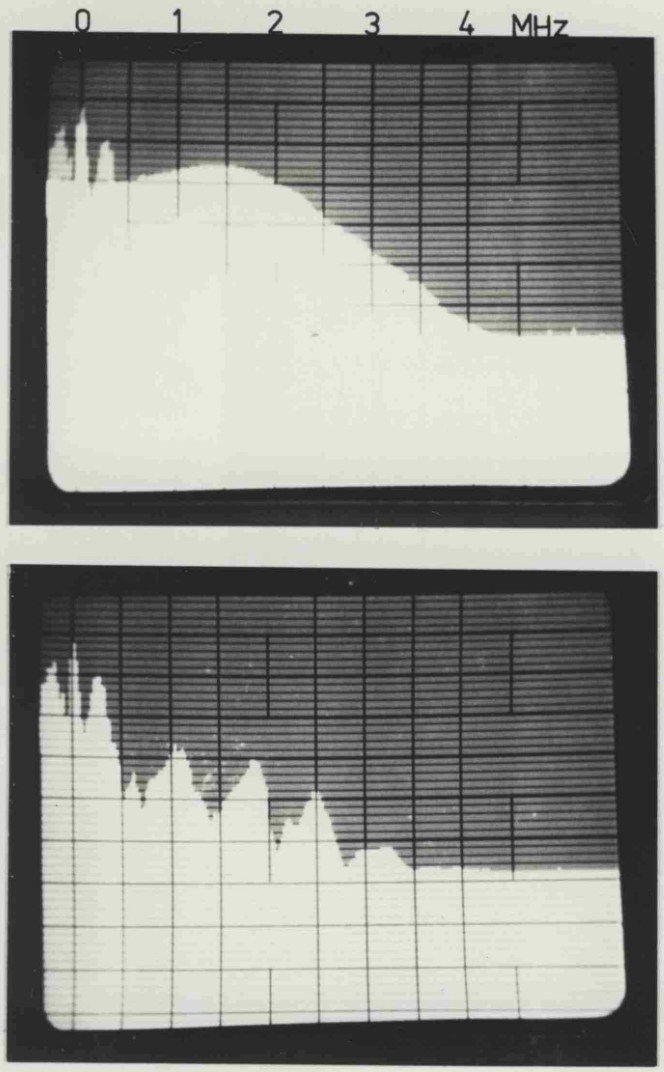

Plate 7.12 Frequency response of the AE transducers used, a) broad band, b) resonant .

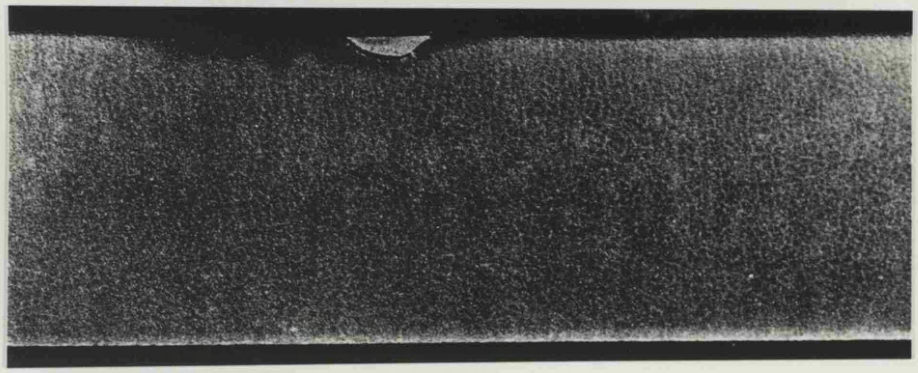

Plate 7.13 Cracks and delamination of an alumina coating after 4 point bend test, revealed using the dye pentrant.

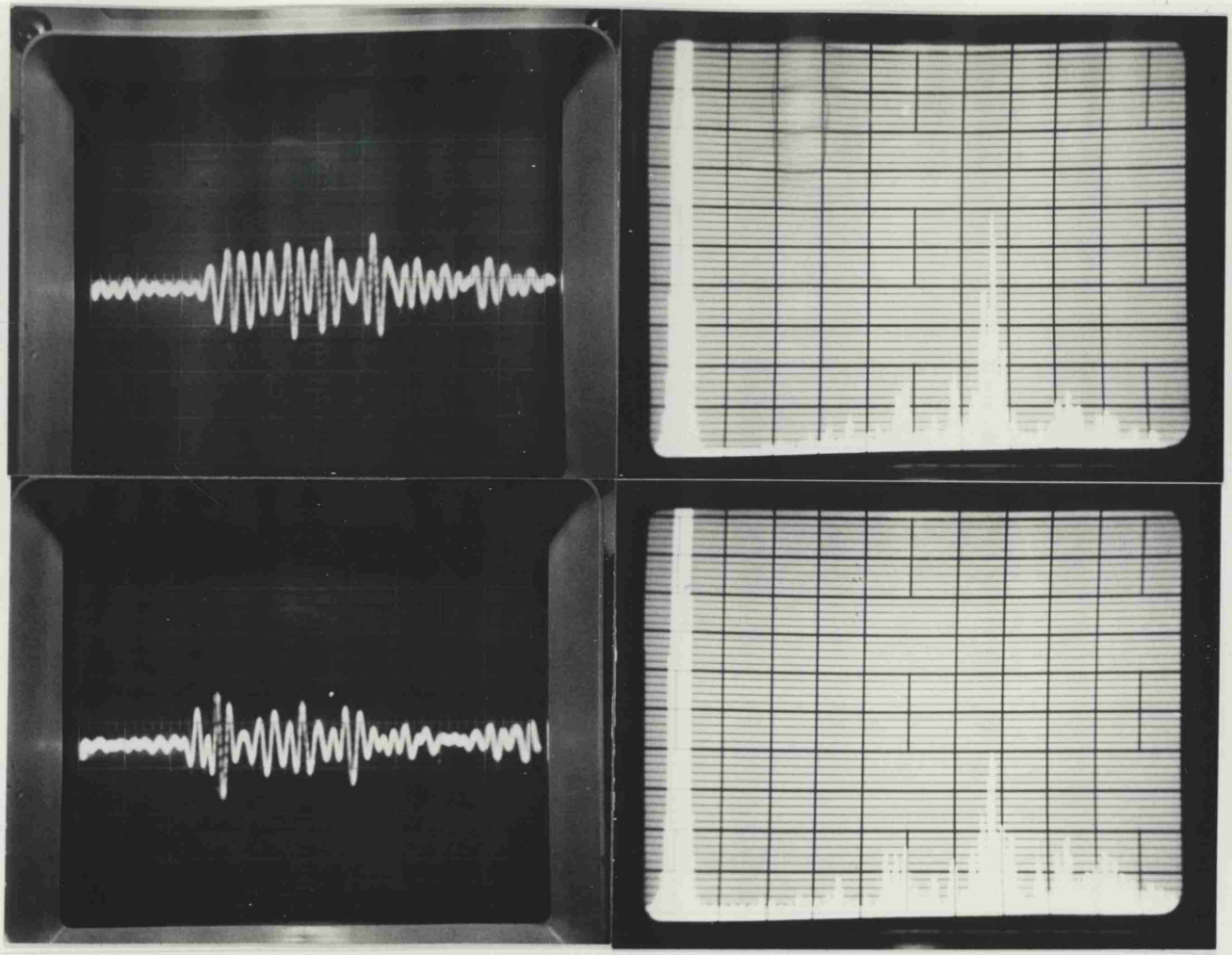

Plate 7.14 Two typical AE signals and their corresponding frequency components.

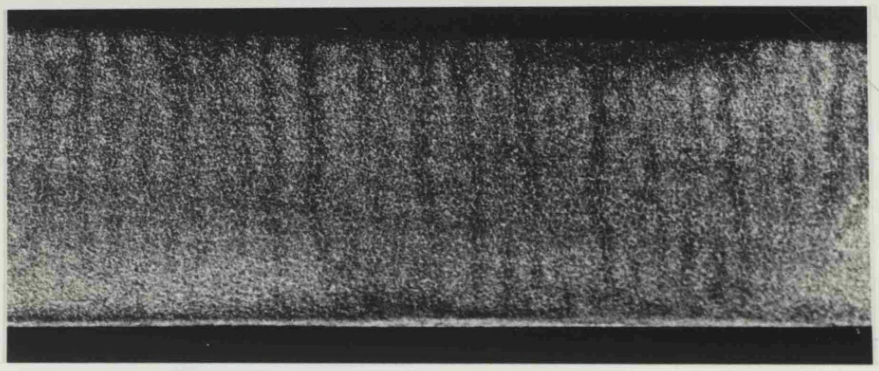

Plate 7.15 A typical surface of a plasma sprayed coating after 4 point bend test, showing the cracks across the coating, (using dye penetrant).

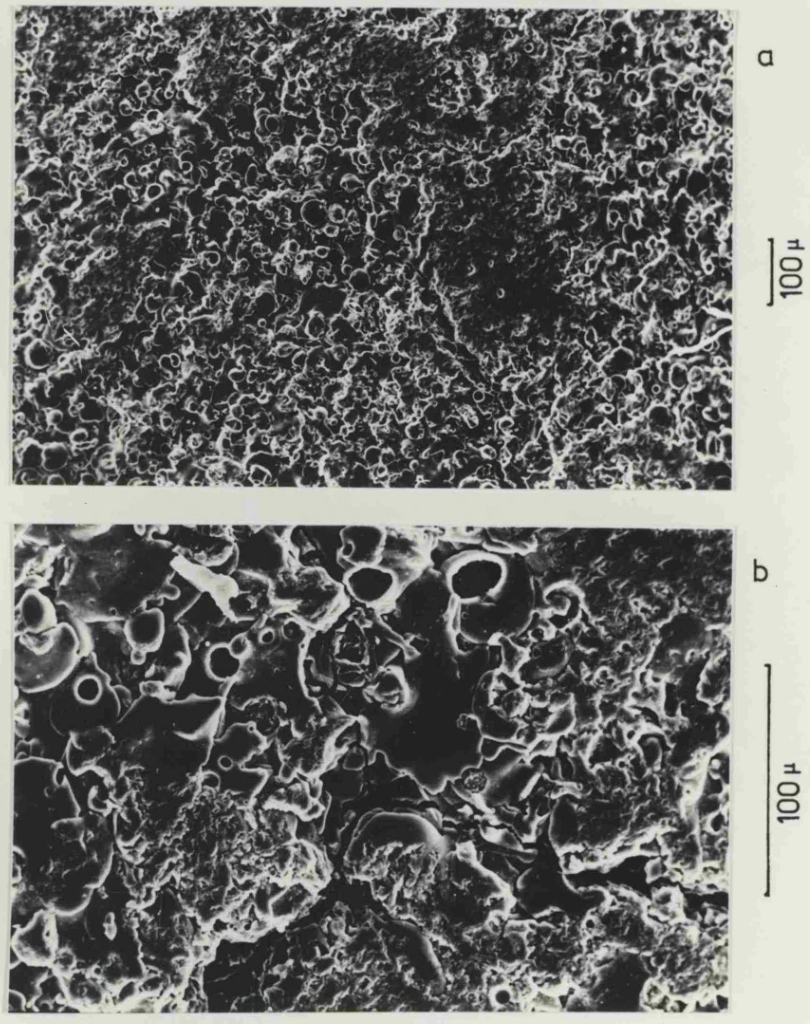

Plate 7.16 Scanning electron photo-micrograph of the cracks at the surface of an alumina coating after bending, a) X 100, b) X 360.

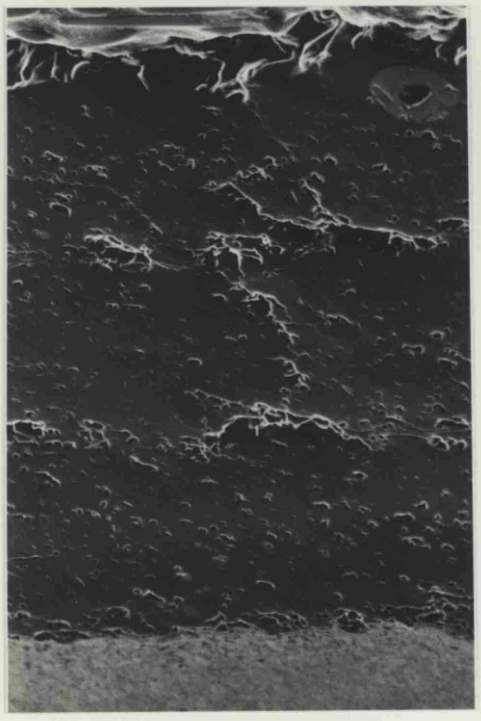

Plate 7.17 Scanning electron photo-micrograph of an alumina control coating after 4 point bend test, showing, interlamellar and translamellar cracks, X 240 .

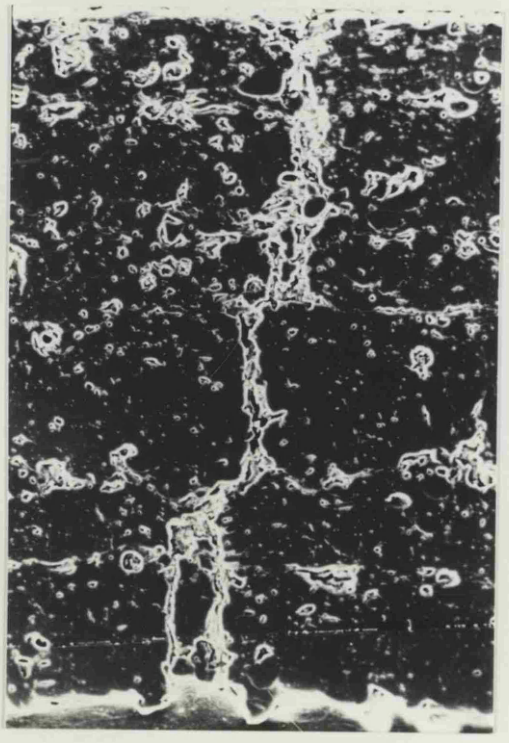

Plate 7.18 Scanning electron photo-micrograph of an alumina coating sprayed on a substrate which was blasted with worn grit, X 220.

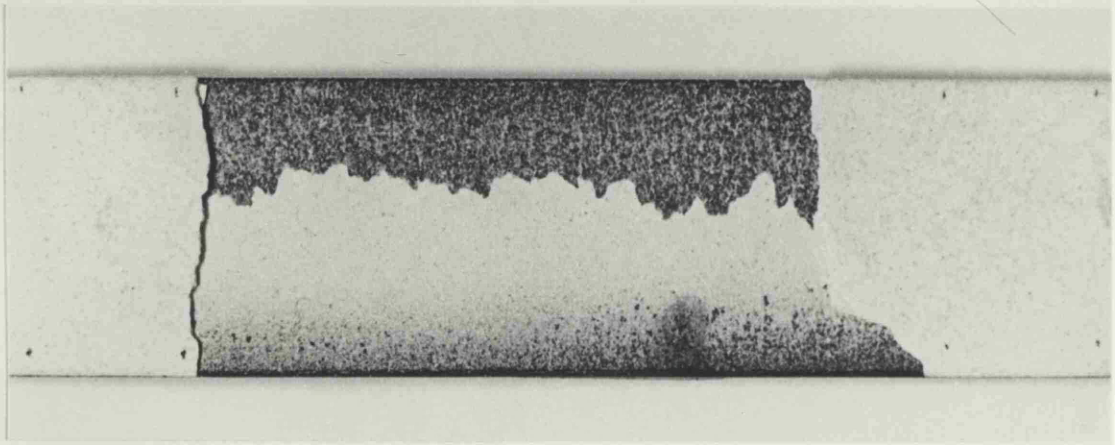

Plate 7.19 Fracture surface of an over heated alumina coating, showing the predominantly cohesive failure near the interface.

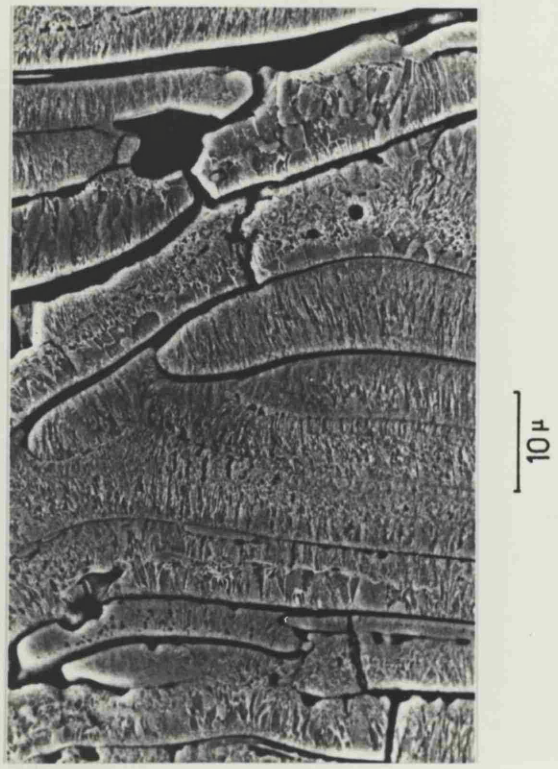

Plate 7.20 Scanning electron photo-micrograph of a Mo63 control coating after 4 point bend test, (X 1500).

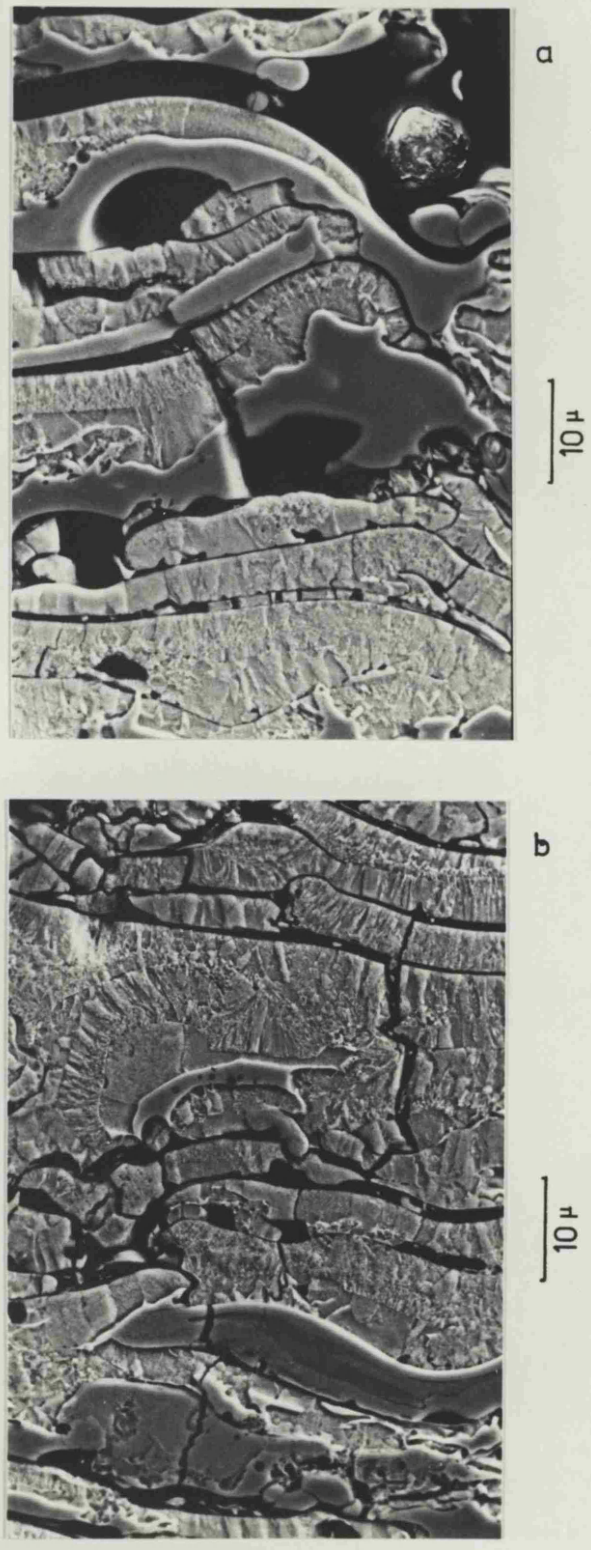

Plate 7.21 Scanning electron photo-micrograph of a Mo505 control coating afetr 4 point bend test, a) X 1500, b) X 1500 .

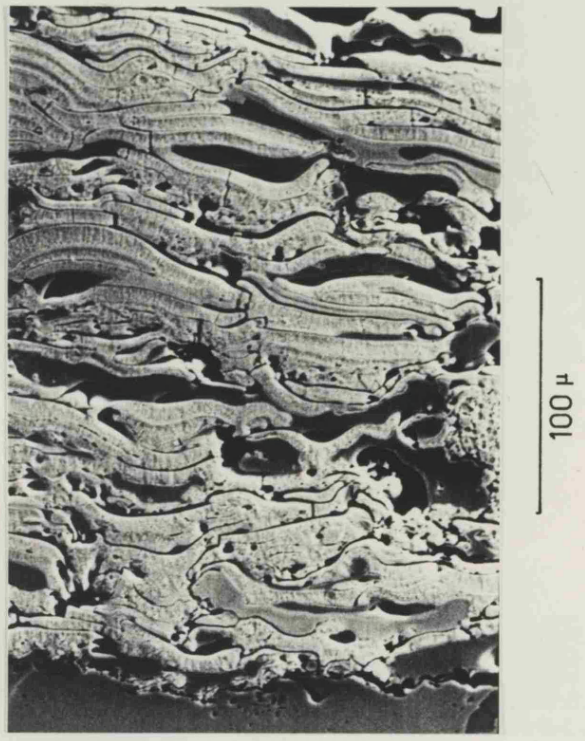

Plate 7.22 Scanning electron photo-micrograph of a Mo505 coating which was sprayed on a substrate without grit blasting, (after 4 point bend test).

Plate 7.23 Scanning electron photo-micrograph of the surface of a Mo505 control sample, (X 1000).

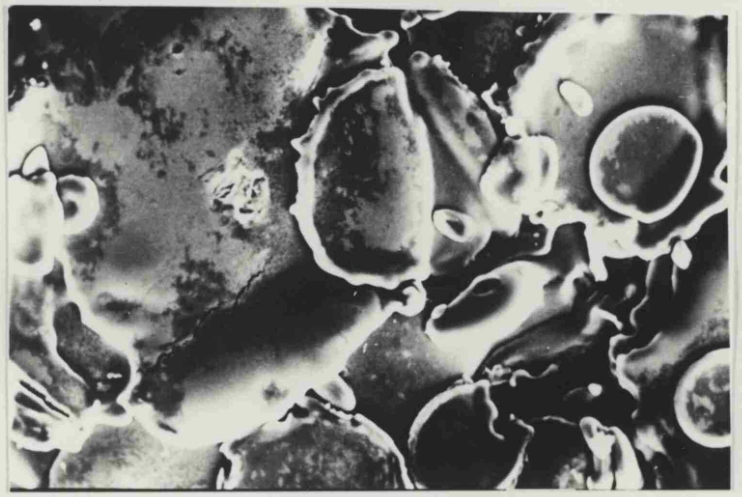

Plate 7.24 Scanning electron photo-micrograph of the surface of a low power Mo505 coating, (X 1000).

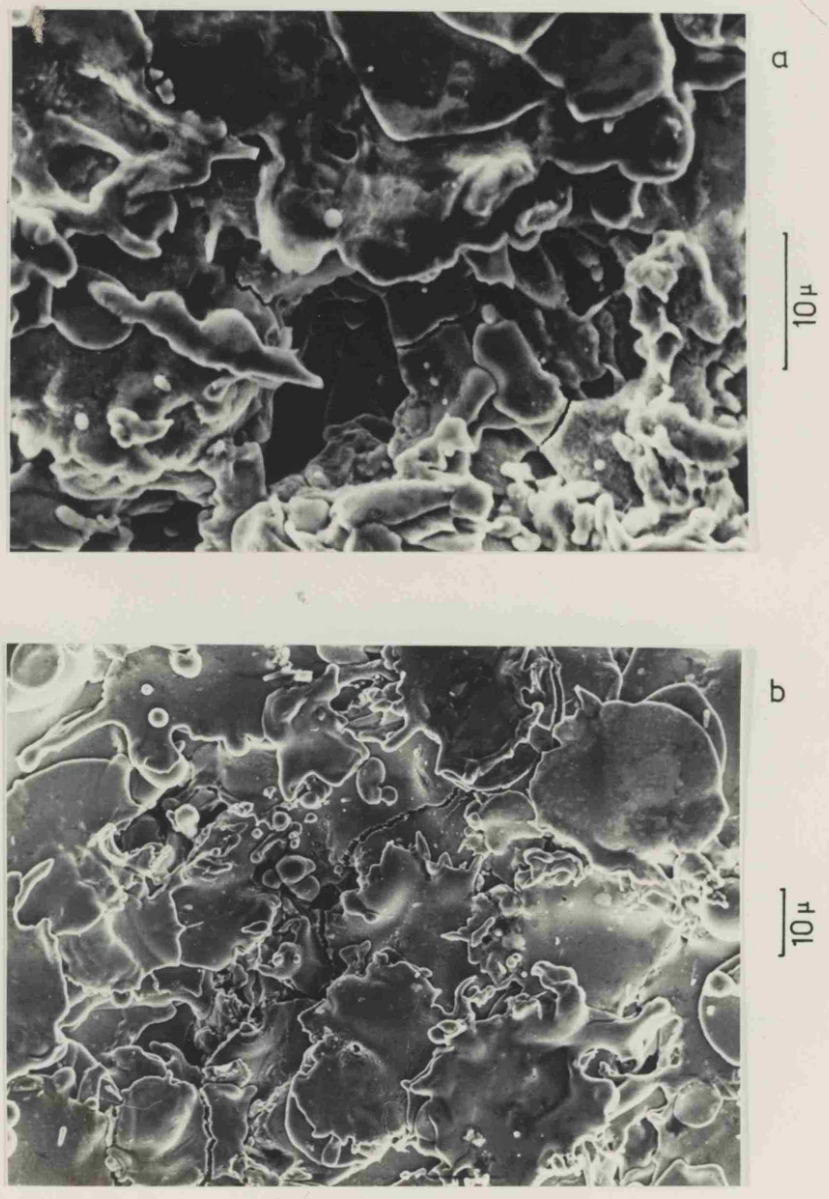

Plate 7.25 Scanning electron photo-micrograph of the cracks at the surface of the Mo505 coating, showing that the cracks usually start from a defect, a) control (Mag X 2000), b) low power (X 1000).